MARITIME FORWARD SCATTER RADAR

by

Liam Yannick Daniel

A thesis submitted to the University of Birmingham for the degree of
DOCTOR OF PHILOSOPHY

Electronic, Electrical and Systems Engineering
University of Birmingham
May 2016

ABSTRACT

This thesis is dedicated to the study of forward scatter radar (FSR) in the marine environment. FSR is a class of bistatic radar where target detection occurs at very large bistatic angle, close to the radar baseline. It is a rarely studied radar topology and the maritime application is a completely novel area of research. The aim is to develop an easily deployed buoy mounted FSR network, which will provide perimeter protection for maritime assets—this thesis presents the initial stages of investigation. It introduces FSR and compares it to the more common monostatic/bistatic radar topologies, highlighting both benefits and limitations. Phenomenological principles are developed to allow formation of forward scatter signal models and provide deeper understanding of the parameters effecting the operation of an FSR system. Novel FSR hardware has been designed and manufactured and an extensive measurement campaign undertaken. The outcome of this was the creation of the first comprehensive maritime FSR target and clutter signal database—results from which have been shown with preliminary analysis. Alongside experimental work, a sea surface model has been produced in order to estimate the effects of wave blocking in high sea states and assess FSR performance in these conditions.

DEDICATION

Firstly, I would like to express my gratitude to my academic supervisors Prof. Cherniakov and Dr. Gashinova. Thank you for your knowledge and expertise and your continuous support and friendship both during my Ph.D and in the times since.

I want to thank Dr. Edward Hoare, a constant source of useful information, appalling jokes and a good friend. I appreciate all your help and advice, both in relation to work (a good engineer would make one) and life (what's the worst that can happen).

Mother, I know you thought you would never see this thesis, Dad you knew it would come in the end and Nan, I know you have been holding on for this for a while. Thank you all for sticking with it and supporting me so extensively, both morally and monetarily…

I got there in the end!

Louise, my very patient wife. I think this PhD was more stressful for you than me (sorry)! You have provided me with limitless support throughout, taking up the slack during busy times and for this I am truly grateful—love you.

Finally, I dedicate this thesis to my son Seth, you are genuinely the most awesome little man I have ever had the pleasure to meet. You were the inspiration to finish this thesis, I hope I make you proud.

ACKNOWLEDGEMENTS

This PhD study was funded by the Engineering and Physical Sciences Research Council (EPSRC).

CONTENTS

LIST OF ABBREVIATIONS

ADC	Analogue-to-digital converter
AWG	Arbitrary waveform generator
BPF	Band pass filter
CA-CFAR	Cell averaging-constant false alarm rate
CDF	Cumulative distribution function
CFAR	Constant false alarm rate
COTS	Commercial off the shelf
DPO	Digital phosphor oscilloscope
DSA	Deterministic spectral amplitude
FDMA	Frequency domain multiple access
FS	Forward Scatter
FSCS	Forward scatter cross section
FSML	Forward scatter main lobe
FSR	Forward scatter radar
FWHM	Full width half maximum
GNSS	Global navigation satellite systems
HPF	High pass filter
IFFT	Inverse Fourier transform
JONSWAP	JOint North Sea WAve Project
LNA	Low noise amplifier
LOS	Line of sight
LPF	Low pass filter
MBV	Miller, Brown, Vegh

NLE	Non-linear element
NSA	Non-deterministic spectral amplitude
PDF	Probability density function
P-M	Pierson-Moskowitz
PO	Physical optics
PSD	Power spectral density
RAM	Radar absorbing material
RCS	Radar cross section
RF	Radio frequency
RSSI	Received signal strength indicator
Rx	Receiver/Receive
SCR	Signal-to-clutter ratio
SLD	Square law detector
SNR	Signal-to-noise ratio
SS	Sea state
TDMA	Time domain multiple access
Tgt	Target
Tx	Transmitter/Transmit
UWB	Ultra-wideband
WMO	World Meteorological Organisation

1 INTRODUCTION

Currently many systems may be used for the remote monitoring of the sea surface, each system with its own distinct capabilities and limitations. Installations fixed to the shore or offshore (e.g. oil rigs) are generally limited by the local horizon. Over-the-horizon HF radar operate against medium to large sized targets and require a large antenna installation. Air and ship-borne radars allow the surveillance of remote oceanic regions, however, permanent coverage of any large area is expensive and highly weather dependent. Radar imaging from satellites is an extremely powerful tool but suffers from lengthy revisit times. Electro-optical systems offer effective identification but are essentially weather dependent. Thus it is unlikely that any one system is able to solve all the issues related to the monitoring of the ocean with a resolution sufficient to permit the detection and automatic identification of small objects. It is envisaged that the general solution lies in a combination of systems, which can complement each other by providing additional information for data fusion. It is for this reason that the introduction of new tools, specifically those that are capable of filling the gaps in the existing security systems should be investigated.

This is where the introduction of forward scatter radar (FSR) comes into play—which is the topic of this thesis. FSR is a very rarely studied radar topology and the maritime application is a completely novel area of research. As will be explained within, FSR is a class of bistatic radar which has certain advantages over conventional radar. These include a dramatically increased cross section in the forward direction and long target coherent visibility times. FSR lends itself to the detection of low profile, small, generally low speed maritime targets in the high clutter maritime environment — targets such as inflatable boats, jet-skis and even semi-submerged objects such as lost shipping containers, which pose great hazards in shipping lanes.

The goal of the full term of this research topic, of which the work contained here is a contribution, is the development of a buoy mounted maritime FSR network. The network should form persistent perimeter protection for maritime structures of interest, such as harbours, wind farms and oil rigs and therefore be easily deployable both near to the coast and far off-shore. The maritime FSR concept is shown in Figure 1.1-1.

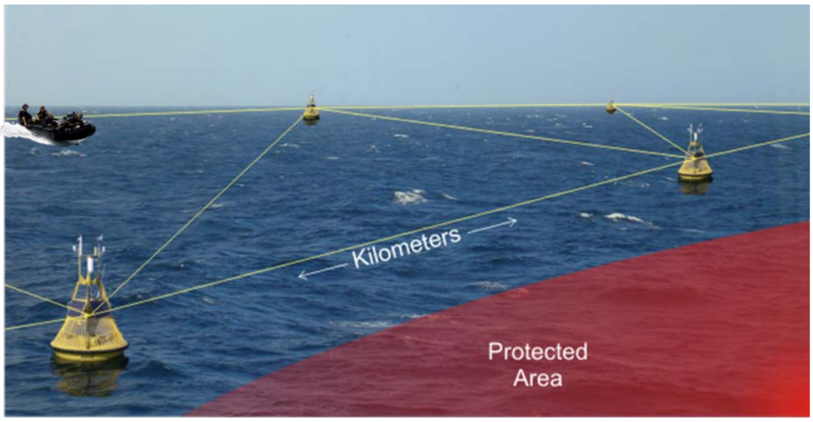

Figure 1.1-1. Example of buoy mounted maritime forward scatter radar network. Yellow lines show potential FSR baselines.

The network consists of multiple FSR baselines formed between buoys, shown by yellow lines. The configuration of the buoys and baselines in the figure is purely for illustrative purposes; this is in itself a whole area of study dedicated to determination of the optimum configuration for a given objective. The investigation of the network should start with consideration of a single baseline, one transmitter and one receiver system only. The performance of this single FSR link should be examined thoroughly and broken down itself into three stages:

1) Initially the scenario of stationary antennas spanning an area of sea surface should be studied. This is the simplest scenario to test (especially from a hardware/practical viewpoint) and should provide the reference performance for the maritime FSR system.

2) Investigation of single moving end. One stage higher in complexity than the stationary antenna case—transmitter or receiver should be mounted on a floating platform.
3) Transmitter and receiver both mounted on floating platforms.

Each stage above will inform the next. In general the main themes of research for each should be:

- Development of signal and simulation models based on phenomenological and physical principles of FSR.
- Design and creation or modification of test hardware to perform experimental trials.
- Use of measured data to verify or adapt models.
- Identification of parameters which may improve performance, an ongoing theme which may lead to further model and hardware development.
- Signal processing aspects
    - Using modelled and measured data to estimate and verify radar detection performance.
    - Development of target tracking and kinematic parameter estimation.
    - Development of processing methodologies for target identification and ultimately classification.

In due time, considerations should be made regarding the network aspect of the system, how it may be practically achieved and what performance benefits may be derived from it.

As this is the first investigation into the Maritime use of a relatively unstudied radar topology, we are essentially starting from the beginning. There is a fundamental lack of literature, experimental data and verified signal models.

The research undertaken and presented in this thesis aims to change this situation and lay the groundwork for continued study and development of maritime FSR. As such, at present this study relates to the condition of stationary antenna platforms. The research aims and outcomes within this thesis are summarised as follows:

1) Develop and understand the relationship between more traditional bi/monostatic radar topologies and FSR and thus understand the benefits and compromises of using an FSR system.
2) Develop a deeper understanding of the phenomenological principles of FSR and experimentally investigate them in controlled conditions. This is required to formulate target signature, power budget models and simulation methodologies.
3) Formulate signal models, such that future research can focus on verification and improvement of these using collected experimental data. Models may then be used (alongside real data) to estimate radar performance.
4) Design and build prototype forward scatter radar to enable experimental investigation.
5) Undertake an FSR measurement campaign to collect the first comprehensive database of measured maritime target and clutter signatures recorded in many conditions. This significant aspect of the research will provide a novel and unique dataset. Initially it will serve to prove if FSR is at least feasible in the maritime environment; in the future it will be used to verify the proposed signal models and provide data for estimation of radar performance.

6) Perform an initial analysis of results of the measurement campaign. This includes clutter analysis and qualitative analysis for a selection of representative target data, in order to relate results to what may be expected in FSR.
7) Develop a sea surface model and simulation strategy to begin to assess the functionality of the FSR system in high sea states and deep sea conditions. This has been done in order to substantiate the continued development of the buoy mounted system.

As such, the structure of this thesis is as follows. The thesis begins by explaining basic radar principles and terminologies related to the traditional monostatic and bistatic radars; concepts are introduced that are used later in the thesis. Forward scatter radar is then introduced and the related radar principles explained in the context of FSR. Next, in order to gain a deeper insight into forward scatter radar and allow the development of signal models, a section on forward scatter phenomenology is included. This discusses the forward scattering effect/ mechanism in the context of physical optics. A description of the power budget model for targets follows this, covering two propagation modes, free space and the two-ray path to incorporate important multi-path effects. Following this, a description of the maritime FSR network concept and experimental equipment design and fabrication is presented. This also describes more recent additions to the hardware that will be used for future studies, and the reasons behind these additions. A description of the trial methodologies is given and results are then presented, sea clutter analysis is summarised and measurement trial results are shown for a selection of collected maritime target signatures. The trial results are discussed qualitatively and some suggestions are given as to how to further the analysis into the area of target detection. The final section shows the results of a sea surface model used to estimate target line of sight visibility time in a buoy mounted maritime forward scatter radar. Finally a summary and conclusions are presented and proposed areas of future work derived from the research are explained.

Appendix A includes a list of the author's publications referred to in this thesis. All contributions to this thesis from these publications represent the author's work and contributions to these publications (unless otherwise stated) and are highlighted within the text (and Appendix A).

2 RADAR PRINCIPLES

This chapter provides an overview of radar principles in general, describing the common radar topologies of monostatic and bistatic radar, defining the most relevant principles and aspects of these topologies in relation to the content of this thesis. Following this, a description of the less common topology (which is the main subject of this thesis) of Forward Scatter Radar (FSR) is given along with a comparative discussion of the previously defined principles, but now placed in the context of FSR.

The monostatic and bistatic radar principles are mostly presented through basic definitions with little derivation, as generally much of the content is now commonplace knowledge to radar experts and has been frequently reproduced in general radar texts. The references drawn on here include such well-known texts as [1]–[4].

2.1 MONOSTATIC AND BISTATIC RADAR

The two main radar configurations are monostatic radar and bistatic radar. Monostatic radar can be further sub-divided into quasi-monostatic, where transmit and receive antennas are located in essentially the same position with regards to the point of view of the target and true monostatic radar which utilises the same or at least co-located antennas for both transmit and receive functions. In bistatic radar the transmitter and receiver are separated by a much larger relative distance (usually of the order of the distance to a target) [2]. The two topologies are pictured in Figure 2.1-1.

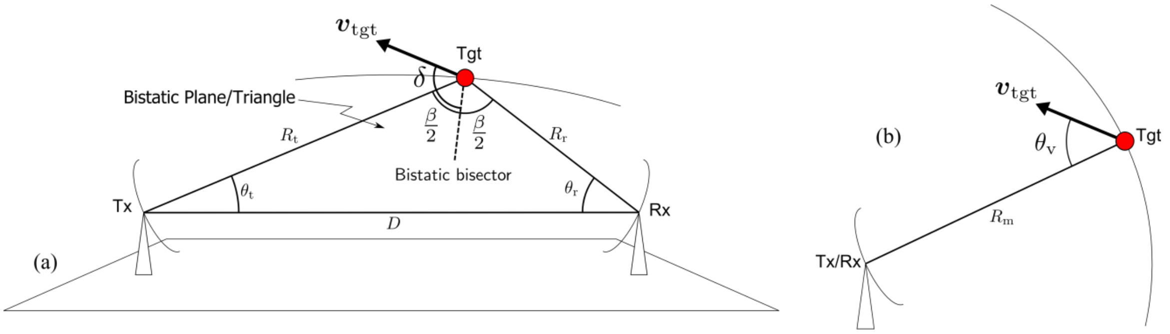

Figure 2.1-1. Bistatic (a) and monostatic (b) radar topologies.

In bistatic radar, Figure 2.1-1(a), there are two paths to consider. The transmitter (Tx) to target (Tgt) path with range $R_{\rm t}$ and the return path from target (Tgt) to the receiver (Rx) with range $R_{\rm r}$. These paths and the baseline D specify a plane in 3-D space, this is the bistatic plane (or triangle). There are three relevant angles on this plane, $\theta_{\rm t}$ and $\theta_{\rm r}$, which are the transmitter and receiver look angles, $\beta = 180 - (\theta_{\rm t} + \theta_{\rm r})$ is the bistatic angle. Also shown, but discussed later in Section 2.7 are the bistatic bisector and the angle δ between this and the target velocity vector $\boldsymbol{v}_{\rm tgt}$.

The monostatic radar case of Figure 2.1-1(b) can be seen as a contraction of the bistatic situation, where the baseline $D = 0$ and hence $\beta = 0$ with $R_{\rm t} = R_{\rm r} = R_{\rm m}$, where $R_{\rm m}$ is the monostatic target range (one way). Again, also shown but discussed later is the angle $\theta_{\rm v}$, which is the angle between the target velocity vector $\boldsymbol{v}_{\rm tgt}$ and the line joining antenna to target.

2.2 ANTENNA PARAMETERS

One of the key elements of any radar is the antenna. The radiation pattern of an antenna is a normalised far-field description of how the antenna distributes the radiated signal power in space, normally given as a function of azimuth and elevation angles, ϕ and θ, with respect to the plane of the antenna, as shown in Figure 2.2-1(a). An example of an antenna radiation pattern in one of the principle planes ($\phi = 0$) is shown in Figure 2.2-1(b).

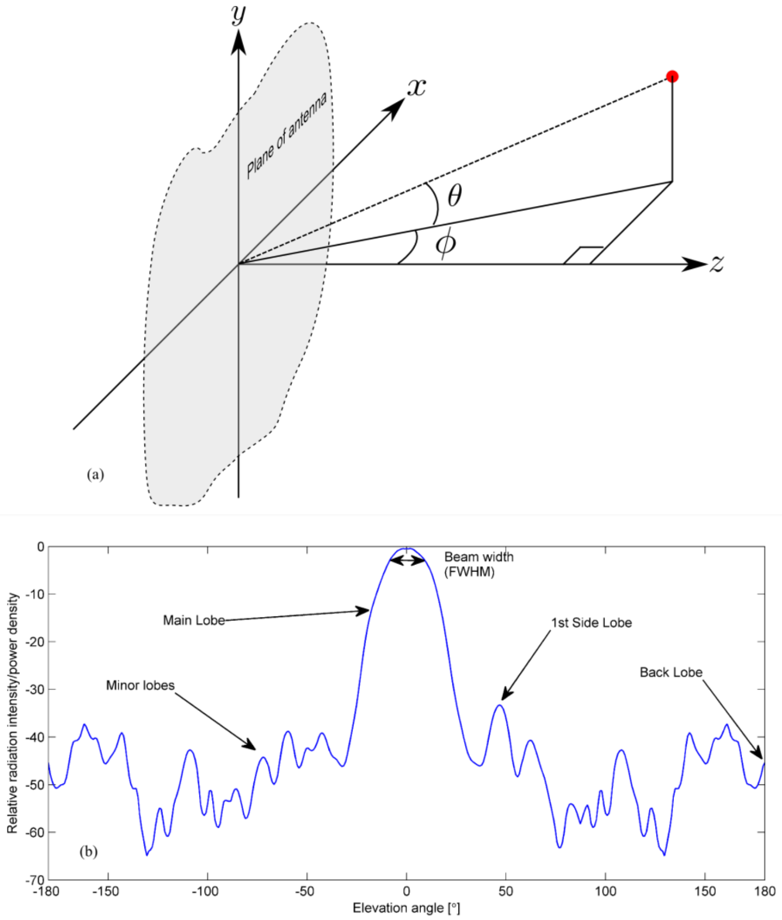

Figure 2.2-1. Co-ordinate system for antenna azimuth and elevation (a) and principle plane (elevation) antenna pattern (b).

The main lobe is the angular region in which the antenna provides the most directionality, from this the beam width θ_{B} can be measured – shown here as the full width at half maximum (FWHM) power, also referred to as the -3dB pattern. There are other subsidiary lobes in the structure; side lobes, minor lobes and the back lobe; commonly these are sought to be minimised. Side lobe reduction is accomplished in general through weighting of the antenna aperture. This is accomplished through the antenna design process, by producing a field distribution which is tapered (non-uniform) across the aperture. In the case of array antennas, where the antenna is formed from an array of radiating elements, tapering is performed across the combined array aperture as discussed in [5] and references therein. The reduction in side lobes is however generally at the expense of a broadened main lobe and a compromise between beam width, gain (discussed below) and side lobe level must be made.

The directive gain (or directivity) $D(\phi',\theta')$ of an antenna is defined as

$$D(\phi',\theta') = \frac{U(\phi',\theta')}{U(\phi,\theta)_{\mathrm{av}}} = \frac{4\pi}{P(\phi,\theta)_{\mathrm{tot}}} U(\phi',\theta') \ . \tag{2.2.1}$$

Where $\mathrm{U}(\phi',\theta')$ is the radiation intensity of the antenna [power/steradian] in a particular direction (ϕ',θ') and $\mathrm{U}(\phi,\theta)_{\mathrm{av}}$ is the average radiation intensity over the full 4π steradians of the sphere, which is equal to the total power radiated, divided by 4π. $\mathrm{P}(\phi,\theta)_{\mathrm{tot}}$ can be found by integrating the volume under the full 3D radiation pattern.

More commonly the power gain, G, is used, which rather than normalising to total radiated power, normalises to the antenna input power, $P_{\mathrm{ant}}^{\mathrm{in}}$ and thus accounts for losses in the antenna itself. It can be defined as,

$$G(\phi',\theta') = \frac{4\pi}{P_{\mathrm{ant}}^{\mathrm{in}}} U(\phi',\theta') \ . \tag{2.2.2}$$

Relating to the directive gain,

$$G = \rho_{\mathrm{r}} D \tag{2.2.3}$$

where ρ_{r} is the antenna radiation efficiency factor. Occasionally when mentioning the gain, what is actually implied is the maximum gain/directionality of the antenna, thus $U(\phi',\theta')$ can be replaced with $U(\phi,\theta)_{\mathrm{max}}$.

The above descriptions for determining gain are true definitions; in commonplace scenarios where absolute accuracy is not required, some simplified rules can be followed. The maximum gain of the antenna can be estimated using [6],

$$G_{\mathrm{max}} = \rho_r \frac{4\pi A_{\mathrm{eff}}}{\lambda^2} \approx \frac{4\pi}{\theta_{\mathrm{B}}\phi_{\mathrm{B}}} \ . \tag{2.2.4}$$

This relates the gain through the effective antenna area A_{eff} at a wavelength λ or alternatively to the approximate ‘beam area’, $\theta_{\mathrm{B}}\phi_{\mathrm{B}}$, where θ_{B} and ϕ_{B} are the -3dB antenna beam widths in the principle planes (in radians). This beam width could indeed be measured or estimated from the further approximation for aperture type antennas (which are relevant for future sections of this thesis) [7],

$$\theta_{\mathrm{B}} \approx \epsilon\lambda / D_\theta \ , \tag{2.2.5}$$

$$\phi_{\mathrm{B}} \approx \epsilon\lambda / D_\phi \ . \tag{2.2.6}$$

Where λ is the wavelength in meters, D is the antenna size in meters (for a particular principle plane) and ϵ is a coefficient which depends on a particular antenna type, but in the first approximation $\epsilon = 1$. The antenna patterns for aperture antennas (i.e. antennas which emit electromagnetic radiation through an opening) are generally calculated using the field equivalence principle and simplified by calculation in the far field region [8] - for non-infinite ground planes, edge diffractive effects then need to be accounted for. However, at small angles about the antenna boresight, these patterns can be approximated by the Fourier transform/Fraunhoffer diffraction pattern of the aperture function (where polarisation is neglected, but assumed constant) [9]–[11]. For simple apertures these patterns are well known analytic functions and can be calculated relatively easily. The cases of rectangular and elliptical apertures will be discussed here without derivation. For apertures which are large in relation to wavelength, much of the energy is concentrated in the small angle region and the approximation works well; it should be noted the solutions only provide patterns for the forward direction.

2.2.1 RECTANGULAR APERTURE ANTENNA

A rectangular aperture antenna with uniform aperture field intensity distribution has a pattern described by [10]–[12]:

$$I(\theta,\phi)=\left(\frac{\sin\left(\frac{ka}{2}\sin\theta\right)}{\frac{ka}{2}\sin\theta}\right)^2\left(\frac{\sin\left(\frac{kb}{2}\sin\phi\right)}{\frac{kb}{2}\sin\phi}\right)^2, \tag{2.2.7}$$

with k being the wave number of the radiation, and θ, ϕ, a and b as described in Figure 2.2-2.

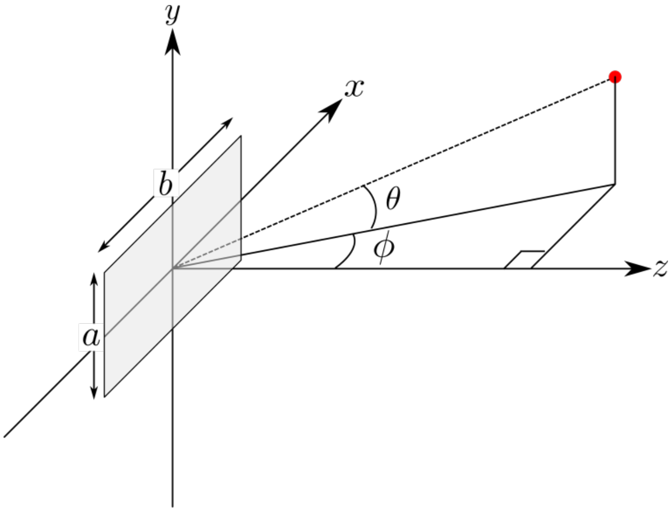

Figure 2.2-2. Rectangular aperture antenna definitions.

Taking one of the principle planes, i.e. the elevation plane, $I(\theta, \phi = 0)$, the pattern is then given by,

$$I(\theta)=\left(\frac{\sin\left(\frac{ka}{2}\sin\theta\right)}{\frac{ka}{2}\sin\theta}\right)^2 \tag{2.2.8}$$

which is shown (in dB) in Figure 2.2-3, with respect to the argument,

$$x=\frac{ka}{2}\sin\theta \tag{2.2.9}$$

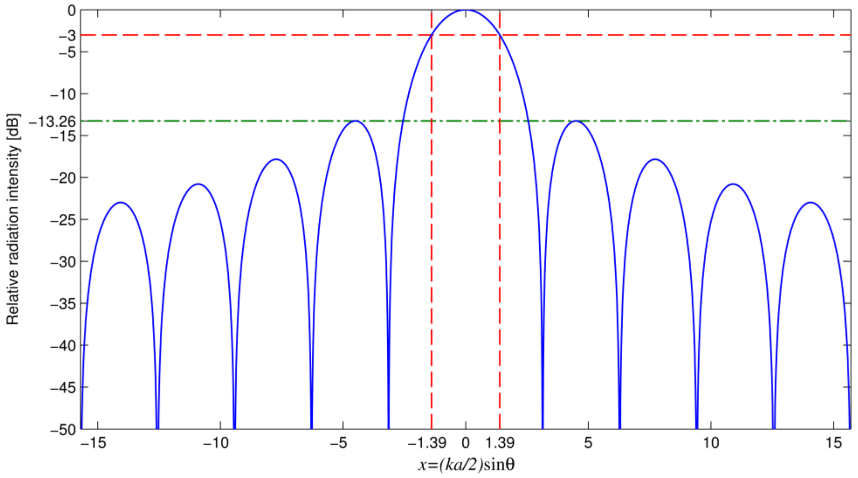

Figure 2.2-3. Approximate pattern from rectangular aperture antenna.

As for the most common patterns, the half power points and side lobe levels are tabulated in the literature [10], in the case of the rectangular aperture, the half power (-3 dB) points can be found by solving numerically,

$$\frac{1}{\sqrt{2}}=\frac{\sin(x)}{x}\ , \tag{2.2.10}$$

resulting in $x = 1.39$, as shown by the red dashed lines in Figure 4 and thus the -3 dB beam width, θ_{B} (rads) is given (from (2.2.9)) by,

$$\sin\frac{\theta_{\mathrm{B}}}{2}=\frac{2x}{ka}=\frac{x\lambda}{\pi a} \tag{2.2.11}$$

$$\Rightarrow\theta_{\mathrm{B}}=2\arcsin\left(0.44\frac{\lambda}{a}\right)\underset{\text{small }\theta_{\mathrm{B}}}{\rightarrow}\theta_{\mathrm{B}}=0.88\frac{\lambda}{a}\,. \tag{2.2.12}$$

Which relating back to (2.2.5), gives a value of ϵ of 0.88.

The side-lobe levels of the pattern can be found from the roots of the derivative of the pattern function, and the level of the first side-lobes are found to be approximately -13 dB with respect to the main lobe peak. In practically used antennas with a rectangular aperture the first side-lobe usually -16 to -20 dB order – this can be achieved with non-uniform/tapered illumination at the expense of a wider main lobe [7].

2.2.2 ELLIPTICAL AND CIRCULAR APERTURE ANTENNAS

For an elliptical aperture, the intensity pattern takes the form of [13],

$$I(\theta,\phi)=\left[\frac{2J_1\left(k\sqrt{a^2\sin^2\theta+b^2\sin^2\phi}\right)}{k\sqrt{a^2\sin^2\theta+b^2\sin^2\phi}}\right]^2. \tag{2.2.13}$$

Where k is the wave number, a is the radius of the aperture and $J_1$is the Bessel function of first kind and first order. a is the semi-axis in the elevation plane and b in the azimuth plane, the angles are defined as in Figure 2.2-4.

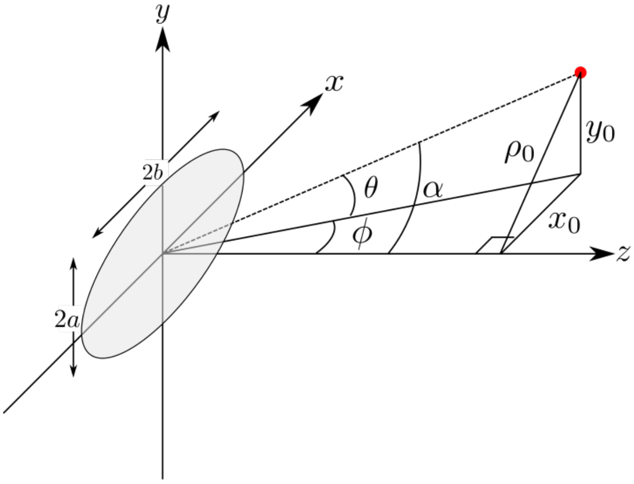

Figure 2.2-4. Elliptical aperture antenna definitions.

Taking for example the elevation principle plane, where $\phi = 0$, it can be seen that the pattern for an elliptical aperture reduces to,

$$I(\theta) = \left[\frac{2J_1(ka \sin \theta)}{ka \sin \theta} \right]^2 \tag{2.2.14}$$

which is the same as that of the 'principle plane' intensity pattern of a circular aperture of radius a. Indeed as a sanity check, it is useful to see that if the values of the semi-axes for the ellipse are set equal, the we retrieve the pattern for a circular aperture, thus with $a = b$ in (2.2.13) then,

$$I(\theta, \phi) = \left[\frac{2J_1\left(ka\sqrt{\sin^2 \theta + \sin^2 \phi}\right)}{ka\sqrt{\sin^2 \theta + \sin^2 \phi}} \right]^2 \tag{2.2.15}$$

and from the geometry of Figure 2.2-4, it can be seen that

$$\sin \phi = \frac{x_0}{z}\ ; \sin \theta = \frac{y_0}{z}; \sin \alpha = \frac{\rho_0}{z} \tag{2.2.16}$$

and

$$\rho_0 = \sqrt{{x_0}^2 + {y_0}^2}\,, \qquad (2.2.17)$$

thus

$$\sin\alpha = \sqrt{\sin^2\theta + \sin^2\phi} \qquad (2.2.18)$$

Substituting (2.2.18) into (2.2.15) gives,

$$I(\alpha) = \left[\frac{2J_1(ka\sin\alpha)}{ka\sin\alpha}\right]^2 \qquad (2.2.19)$$

which is the well-known Airy disc pattern for the circular aperture originally derived in [14], with α being the angle between boresight and the point in question . The principle plane pattern of (2.2.13) with the substitution $x = ka\sin\theta$, gives the plot in Figure 2.2-5.

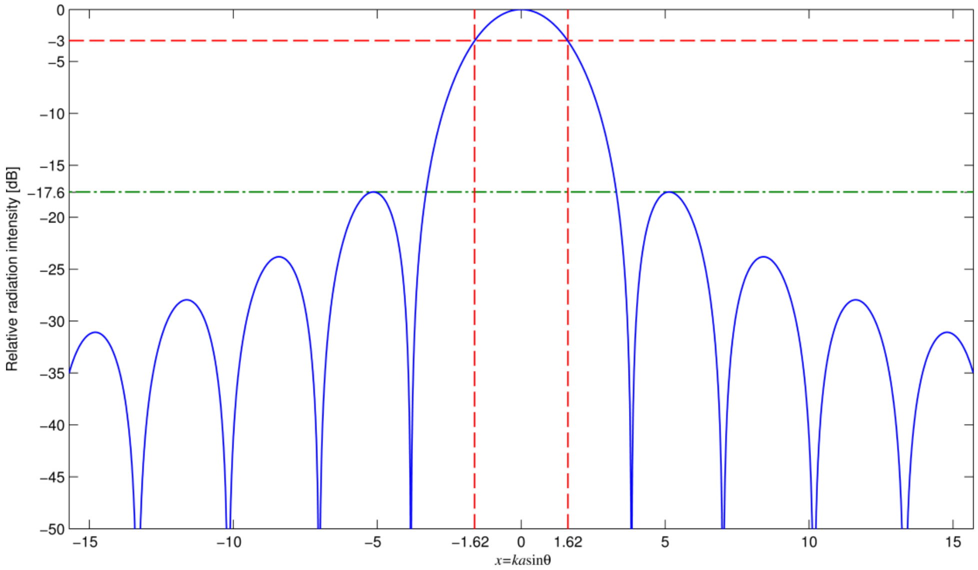

Figure 2.2-5. Elliptical antenna pattern approximation.

The half power point is at $x = 1.62$ (solved numerically - dashed red line in Figure 6), which for small angles, gives the -3 dB beam width (rads) (from $x = ka \sin \theta$) as,

$$\theta_{\mathrm{B}} = 0.51 \frac{\lambda}{a} \tag{2.2.20}$$

Remembering that a is half of the full aperture dimension, thus for the full dimension d of the aperture in that specific plane,

$$\theta_{\mathrm{B}} = 1.02 \frac{\lambda}{d} \tag{2.2.21}$$

Again relating back to the beam width approximation of (2.2.5) for this aperture type, $\varepsilon = 1.02$. The first side lobe position is at $x = 5.14$ [12], and has an intensity of -17.6 dB with respect to the main lobe maxima (dashed green line in Figure 2.2-5).

2.3 TARGET RADAR CROSS SECTION

The radar cross section (RCS) of a target σ is a measure of how the target redistributes incident power into surrounding space and as such, it can be defined generally in a way similar to that of antenna directivity/gain, as:

$$\sigma\left(\beta\right)=4\pi\frac{U_{\mathrm{R}}}{P_{\mathrm{D}}}=4\pi R\frac{P_{\mathrm{R}}\left(\beta\right)}{P_{\mathrm{D}}}. \tag{2.3.1}$$

R is the range from the target to the receiver in the far field (this is sometimes emphasised by the introduction of a limit as $\mathrm{R}\rightarrow\infty$ in (2.3.1). U_{R} is the radiation intensity at the receive antenna, P_{R} the power density at the receiver, and P_{D} is the power density of the intercepted signal. (2.3.1) is actually a general case applicable to bistatic or monostatic radar, dependent on the bistatic angle β. The scenario for both situations is shown in Figure 2.3-1.

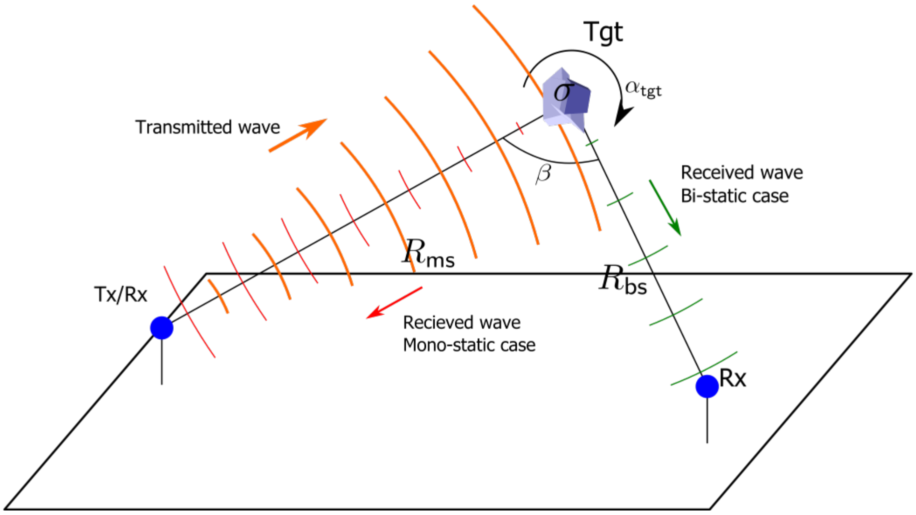

Figure 2.3-1. Target RCS definition geometry.

In bistatic radar, the received power density is a function of the bistatic angle, in monostatic radar $\beta = 0$. The appropriate ranges are also defined, $R = R_{\mathrm{ms/bs}}$ for either the monostatic or bistatic case. The significance of the rotation angle α_{tgt} is to emphasise that in all cases, the RCS is a function of the aspect under which the target is illuminated (except for example, a sphere). In general, the RCS is also a function of the transmitted and received wave polarisation and can (if required) be presented as a RCS scattering matrix:

$$\boldsymbol{\sigma} = \begin{bmatrix} \sigma_{\mathrm{HH}} & \sigma_{\mathrm{VH}} \\ \sigma_{\mathrm{HV}} & \sigma_{\mathrm{VV}} \end{bmatrix}. \tag{2.3.2}$$

Where for example σ_{HV} is the cross section for transmitted horizontal polarisation and vertical receive. The RCS has dimensions of m^2 (dBm^2 or more commonly denoted dBsm on a logarithmic scale) and can be seen as a fictional area that intercepts and re-radiates the transmitted energy. The RCS is defined over all 4π steradians of a sphere (centred on the target) for a given illumination direction.

Only a few ‘simple’ shapes have an analytic RCS. An informative, well used example is that of the sphere, which can be calculated by a Mie series [15] and the result is found in many texts e.g. [16]. Figure 2.3-2 shows the monostatic RCS σ_{ms} for a perfect electrically conducting sphere of radius a_{s} normalised to the physical area of the sphere as a function of the radius normalised to the wavelength $\frac{2\pi a_s}{\lambda}$. The main scattering regions are highlighted, Rayleigh ($\lambda \gg \text{target dimension}$), which shows an RCS dependence $\propto \lambda^4$, the Mie/Resonance region ($\lambda \approx \text{target dimension}$) where the RCS fluctuates about the mean and Optical ($\lambda \ll \text{target dimension}$) where the RCS becomes independent of the wavelength of illumination. For simulation of more complex targets computer packages such as CST Studio Suite (Microwave Studio) [17] are available, which use a number of numerical solving techniques. The technique used depends largely on the electrical size of the object under simulation and its material composition, in general RCS simulations tend to be of objects of larger electrical size (i.e. upper Mie and optical scattering regimes). Therefore full volume 3D meshing of a target object to use, for instance, finite difference based techniques to solve

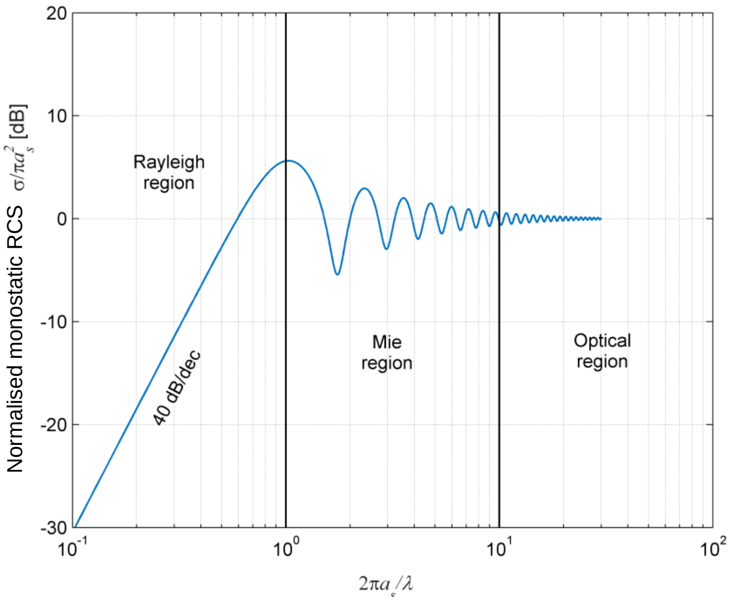

Figure 2.3-2. Normalised monostatic RCS for PEC sphere.

Maxwell's equations become highly computationally expensive and time consuming. Approximate techniques which only require electromagnetic calculation on the objects surface are then used, these include methods such as: integral equation solvers using the Method of Moments and Multilevel Fast Multipole Methods, Physical Optics solvers, Shooting Bouncing Ray and Geometric Optics solvers; which may all be used for metallic and dielectric structures. Uniform theory of diffraction solvers may be used for very large perfectly conducting structures.

2.3.1 RADAR CROSS SECTION FLUCTUATIONS

A target with complex shape, may be regarded as being composed of multiple point scatterers. The resulting field at a distance from the target and indeed therefore the RCS depends on the addition of the relative phases of the field scattered from each point. Targets and radar in many practical cases are moving relevant to each other, so over any reasonable time we may expect target rotation with respect to the view of the radar. As the result target RCS is not constant, but fluctuates. There are many models and descriptions of the fluctuations in RCS, well known versions are the ‘Swerling Cases’ [18], [19]. To highlight the dependencies related to the fluctuation in cross section, a simple example of a two point scatterer target is shown in Figure 2.3-3.

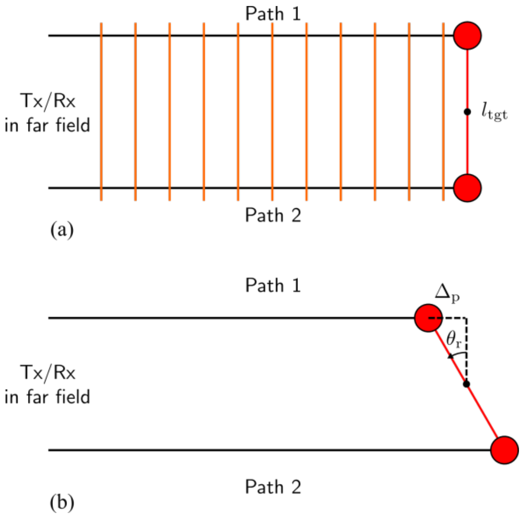

Figure 2.3-3. A target composed of two point scatterers. (a) Path lengths 1 and 2 are the same, leading to constructive interference at the receiver, (b) rotation of the target causes a phase difference in the paths, producing fluctuation in the RCS.

In Figure 2.3-3(a) it can be seen that there is no difference in the path length of path 1 and path 2 and so in the far field the received waves will add in phase. In (b), due to target rotation angle of θ_{r}, the path length of both path 1 and path 2 will be altered by Δp from the original un-rotated scatterers, where:

$$\Delta p = \frac{l_{tgt}}{2} \sin \theta_{\mathrm{r}}, \tag{2.3.3}$$

l_{tgt} is the separation of the point scatterers, or ‘target length’. This can be written in terms of the phase difference between the two paths $\Delta\phi$, in which each path is traversed twice, there and back in the monostatic case, thus:

$$\Delta\phi = \frac{4\pi}{\lambda} l_{\mathrm{tgt}} \sin \theta_{\mathrm{r}} \tag{2.3.4}$$

If this phase difference is an integer number of 2π then constructive interference will occur. However it can be seen that for a moving target with changing aspect, this phase term will fluctuate over time, with the fluctuation speed and therefore spectrum depending on wavelength, target size and the angular rotation rate. The time over which the radar returns may be integrated (summed up) effectively to improve the signal-to-interference ratio, is called the coherent analysis time, this is determined by the phase fluctuation. The fluctuation spectrum bandwidth Δf_{mr} and coherent analysis time $\Delta\tau_{\mathrm{mr}}$ for monostatic radar are related by [1]:

$$\Delta f_{\mathrm{mr}} \approx \left(\frac{l_{\mathrm{tgt}}}{\lambda}\right)\left(\frac{\Delta\phi}{\Delta t}\right) \quad \text{and} \quad \Delta\tau_{\mathrm{mr}} = 1/\Delta f_{\mathrm{mr}} \,. \tag{2.3.5}$$

In which l_{tgt} is the characteristic target length and $\Delta\phi/\Delta t$ is the rate of change of aspect angle with respect to the Tx/Rx. The

2.4 THE RADAR EQUATION

Now that the parameters of antenna gain and RCS have been specified, it is now possible to introduce the radar equation. The radar equation is a power balance equation for the radar system which gives an indication of the range performance of the radar. The equation itself can be written in many forms of varying complexity depending on how specifically the losses and gains of the system are defined. A simple form of the bistatic radar equation in can be written as below,

$$P_{\mathrm{R}} = \frac{P_{\mathrm{T}} G_{\mathrm{T}} G_{\mathrm{R}} \sigma_{\mathrm{BS}} \lambda^2}{(4\pi)^3 R_{\mathrm{T}}{}^2 R_{\mathrm{R}}{}^2 L_{\mathrm{BS}}} \,. \tag{2.4.1}$$

Where:

- P_{R} is the peak power at the input to the receiver.
- P_{T} is the transmitter peak power into the antenna.
- G_{T} is the gain of the transmitting antenna.
- G_{R} is the gain of the receiving antenna.
- σ_{BS} is the bistatic RCS.
- λ is the frequency of the radar signal.
- R_{T} is the transmitter to target range.
- R_{R} is the receiver to target range.
- L_{BS} is a general loss term (>1).

From this a maximum detection range product can be defined, if a minimum detectable signal power is chosen S_{MIN}, then:

$$P_{\mathrm{R}} = S_{\mathrm{MIN}} = \frac{P_{\mathrm{T}} G_{\mathrm{T}} G_{\mathrm{R}} \sigma_{\mathrm{BS}} \lambda^2}{(4\pi)^3 {R_{\mathrm{T}}}^2 {R_{\mathrm{R}}}^2 L_{\mathrm{BS}}} \tag{2.4.2}$$

$$\Rightarrow (R_{\mathrm{T}} R_{\mathrm{R}})_{\mathrm{MAX}} = \sqrt{\frac{P_{\mathrm{T}} G_{\mathrm{T}} G_{\mathrm{R}} \sigma_{\mathrm{BS}} \lambda^2}{(4\pi)^3 S_{\mathrm{MIN}} L_{\mathrm{BS}}}} \tag{2.4.3}$$

The difference between the bistatic and monostatic radar equation is purely the target ranges as before, $R_T = R_{\mathrm{R}} = R_{\mathrm{M}}$, and relabeling of the cross section and losses, such that for the monostatic case (2.4.1) becomes:

$$P_{\mathrm{R}} = \frac{P_{\mathrm{T}} G_{\mathrm{T}} G_{\mathrm{R}} \sigma_{\mathrm{MS}} \lambda^2}{(4\pi)^3 R_{\mathrm{M}}^4 L_{\mathrm{MS}}}, \tag{2.4.4}$$

and thus the equivalent maximum range product becomes,

$$R_{\mathrm{MS}}^{\mathrm{MAX}} = \sqrt[4]{\frac{P_{\mathrm{T}} G_{\mathrm{T}} G_{\mathrm{R}} \sigma_{\mathrm{MS}} \lambda^2}{(4\pi)^3 S_{\mathrm{MIN}} L_{\mathrm{MS}}}}\ . \tag{2.4.5}$$

In bistatic radar the round trip distance for a signal to travel from Tx → Tgt → Rx is $R_{\mathrm{T}} + R_{\mathrm{R}}$. If the round trip time delay between transmission and reception is τ_{d}, then given that the signal propagates at a speed c, the bistatic target range R_{BS} (range sum) is given by,

$$R_{\mathrm{BS}} = R_{\mathrm{T}} + R_{\mathrm{R}} = c\tau_{\mathrm{d}} . \tag{2.4.6}$$

In the monostatic case $R_{\mathrm{T}} = R_{\mathrm{R}} = R_{\mathrm{M}}$, the monostatic target range R_{M} is then given by,

$$R_{\mathrm{MS}} = \frac{c\tau_{\mathrm{d}}}{2} \tag{2.4.7}$$

Due to the topology of the bistatic radar having two foci, a given value of bistatic range can be formed from many combinations of R_{T} and R_{R}, producing confocal ellipsoidal iso-range surfaces with constant range sum, $R_{\mathrm{BS}} = R_{\mathrm{T}} + R_{\mathrm{R}}$. Conforming to standard ellipse definitions, the semi-major axis a of an ellipse lying in the bistatic plane is described by,

$$2a = R_{\mathrm{T}} + R_{\mathrm{R}} \tag{2.4.8}$$

The semi-minor axis b is defined by,

$$b^2 = a^2 - \left(\frac{d}{2}\right)^2 \tag{2.4.9}$$

$$b^2 = a^2 - \left(\frac{d}{2}\right)^2 \tag{2.4.10}$$

It should be noted from (2.4.10), for the monostatic case, $d = 0$ and therefore $a = b$ which implies the ellipse becomes a circle of radius $a = \frac{R_{\mathrm{T}}+R_{\mathrm{R}}}{2} = R_{\mathrm{MS}}$, as expected from a central focus point. In reality, even though defined through an ellipse here, the iso-range contours are actually not contours, but surfaces which are ellipsoidal. Due to symmetry in the topology the defined ellipse is essentially rotated about the baseline (volume of revolution) i.e. an ellipsoid in which the semi-principle axes b and c are equal. Examples of iso-range surfaces are shown in Figure 2.4-1

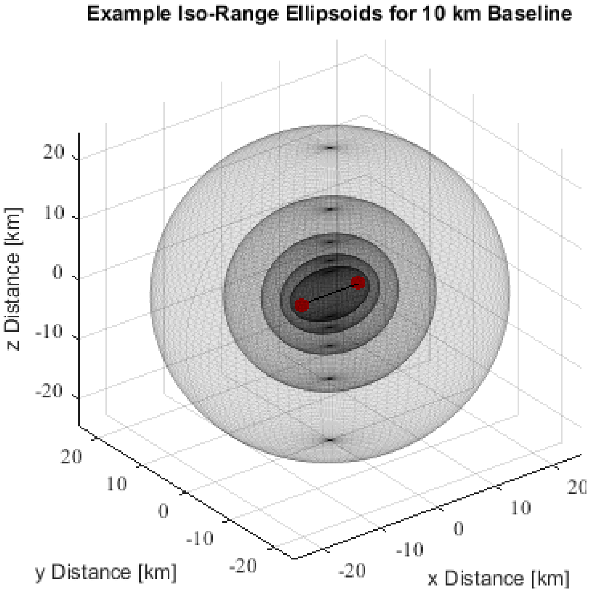

Figure 2.4-1 Iso-range ellipsoid surfaces for an example 10 km base line. Red dots indicate transmitter and receiver.

It can also be noted that as the bistatic range increases such that the antenna spacing becomes small in comparison, the system tends towards the monostatic case and the iso-range surfaces/contours become more spherical/circular.

2.5 RANGE RESOLUTION

Range resolution relates to the ability of the radar to separate/detect multiple targets in terms of their ranges or identically the receive delay time. Conventionally a minimum separation in time between returns of τ_P is used, where τ_P is the pulse width at the output of the matched filter. This is generally defined as the -3 dB pulse width i.e. full width at half the maximum of the pulse power.

In the monostatic case, take the example of two targets each positioned on a different iso-range contour separated by a range difference ΔR_{MS}, as shown in Figure 2.5-1. Then the extra round trip distance travelled by the pulse to the furthest target is $2\Delta R_{\mathrm{MS}}$. The equivalent required distance separation relating to the time separation τ_{P} is $c\tau_{\mathrm{P}}$, thus the minimum value of range separation for two targets to be resolved is given by,

$$\Delta R_{\mathrm{MS}} = \frac{c\tau_{\mathrm{P}}}{2} = \frac{c}{2B} \tag{2.5.1}$$

where B is the signal bandwidth.

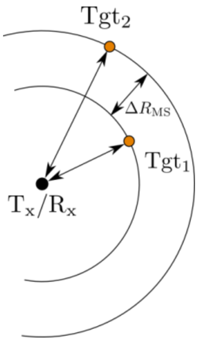

Figure 2.5-1. Monostatic range resolution.

The equivalent case for bistatic radar must take into account that the separation between iso-range ellipsoids in bistatic radar is not constant, but dependent on the bistatic angle β. The scenario for bistatic radar is shown in Figure 2.5-2.

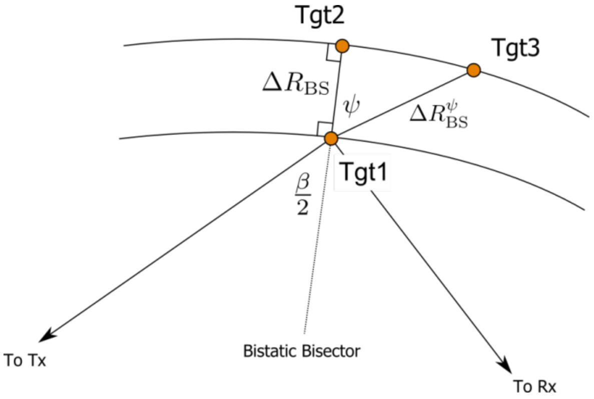

Figure 2.5-2. Bistatic range resolution, target 1 and 2 (Tgt1 and Tgt2) occupy the same extended bistatic bisector, target 3 (Tgt3) lies away from this, but on the same range contour as Tgt 2.

The equivalent of ΔR_{MS} for the bistatic case is ΔR_{BS} which is the separation between bistatic iso-range ellipsoids. This separation is defined along the extended bistatic bisector upon which targets Tgt1 and Tgt2 are located and which is perpendicular to the tangents of the ellipses. Tgt 3 is a target located on the same range contour as Tgt2, but at some angle ψ to the bisector and a distance $\Delta R_{\mathrm{BS}}^{\psi}$ from Tgt1. In order to resolve Tgt1 from Tgt2, it can be shown that ΔR_{BS} must be at least,

$$\Delta R_{\mathrm{BS}} = \frac{c\tau_{\mathrm{P}}}{2\cos\frac{\beta}{2}} \tag{2.5.2}$$

And from Figure 2.5-2 it can be seen that the minimum distance for Tgt1 to therefore be resolved from Tgt3, $\Delta R_{\mathrm{BS}}^{\psi}$, is approximately given by,

$$\Delta R_{\mathrm{BS}}^{\psi} \approx \frac{\Delta R_{\mathrm{BS}}}{\cos\psi} = \frac{c\tau_{\mathrm{P}}}{2\cos\frac{\beta}{2}\cos\psi} \tag{2.5.3}$$

It should be noted here, that for a particular iso-range contour (on which would be situated Tgt1) and particular value of ψ, the minimum values for the range resolution occurs when the target is on the extended baseline. This is sometimes known as the quasi-monostatic region where Tx, Rx and Tgt1 all lie along a single line.

The above discussion and equations derived for range resolution are truly only valid for separating returns from two equal-sized point targets. If, for example, one target response was much larger in amplitude, the larger response would mask the smaller, high noise levels would serve to effectively smear the responses in range. In both situations the separation distance required to resolve them would be larger than predicted. In general the range resolution is dependent on parameters such as target reflectivity/RCS, target dimensions and the signal-to-noise ratio (SNR) of the return.

2.6 ANGULAR RESOLUTION

The previous subsection briefly discusses matters relating to range and the determination of target range in radar, however a particular measured target range is not associated with a single position in space. In order to find this position, knowledge of the angular orientation of the antennas is required and essentially the combination of this and the antenna beam width defines the accuracy of the angular measurement.

Equivalent to range resolution, the angular resolution is an estimate of required target separation to resolve individual targets in angle. In monostatic radar the angular resolution is defined to be the -3dB (one way) beam width of the antenna pattern, $\Delta\theta_{\mathrm{M}}$ and thus a minimum physical target cross-range separation $\Delta R_{\mathrm{MS}}^{\theta}$, given by,

$$\Delta R_{\mathrm{MS}}^{\theta} \geq \Delta\theta_{\mathrm{M}} R_{\mathrm{MS}} \tag{2.6.1}$$

In the bistatic case, there is no enhancement due to a two-way beam pattern, Tx and Rx beam widths at the target range may be different both through differing ranges R_{T} and R_{R}, but also through differing antenna pattern widths $\Delta\theta_{\mathrm{T}}$ and $\Delta\theta_{\mathrm{R}}$. For the case where only the receiver contributes to the angular resolution (i.e. very wide transmitter beam width), the separation required to resolve two targets would be the receive antennas theoretical null to null beam width. This is approximated as $2\Delta\theta_{\mathrm{R}}R_{\mathrm{R}}$ for two targets on the same iso-range contour and this occurs when the target separation $\Delta R_{\mathrm{BS}}^{\theta}$ is,

$$\Delta R_{\mathrm{BS}}^{\theta} \approx \frac{2\Delta\theta_{\mathrm{R}} R_{\mathrm{R}}}{\cos\frac{\beta}{2}} \tag{2.6.2}$$

2.7 THE DOPPLER SHIFT AND DOPPLER RESOLUTION

The Doppler (non-relativistic) frequency shift f_D is related to the time rate of change of the range of a target with respect to the radar antenna or antennas.

In bistatic radar, this (in relation to parameters in Figure 2.1-1(a)) is given by,

$$f_{\mathrm{D}}^{\mathrm{BS}} = \frac{1}{\lambda}\left[\frac{d\left(R_{\mathrm{T}} + R_{\mathrm{R}}\right)}{dt}\right] = \frac{2v}{\lambda}\cos\delta\cos\frac{\beta}{2}\,. \tag{2.7.1}$$

In monostatic radar this (in relation to Figure 2.1-1(b)) is given by,

$$f_{\mathrm{D}}^{\mathrm{MS}} = \frac{2}{\lambda}\frac{\mathrm{d}R_{\mathrm{MS}}}{\mathrm{d}t} = \frac{2v}{\lambda}\cos\theta_{\mathrm{V}} \tag{2.7.2}$$

In order to resolve two Doppler frequencies in the receiver, f_{D_1} and f_{D_2}, the required separation is defined to be,

$$\left| f_{D_1} - f_{D_2} \right| = \frac{1}{T_c} \tag{2.7.3}$$

Where T_c is the coherent processing interval of the receiver. In terms of a target velocity difference, for bistatic radar, ΔV_{BS}, combining (2.7.1) and (2.7.3),

$$\Delta V_{BS} = \left| v_1 \cos\delta_1 - v_2 \cos\delta_2 \right| = \frac{\lambda}{2T_c \cos\frac{\beta}{2}}\ , \tag{2.7.4}$$

on the assumption the targets occupy approximately the same bistatic bisector, as shown in Figure 2.5-2. For monostatic radar, the velocity resolution ΔV_{MS} can be found by setting $\beta = 0$ in (2.7.4) or indeed by combining (2.7.2) and (2.7.3),

$$\Delta V_{MS} = \left| v_1 \cos\theta_{V_1} - v_2 \cos\theta_{V_2} \right| = \frac{\lambda}{2T_c}\,. \tag{2.7.5}$$

As with the equations for range resolution discussed in Section 2.5, the equations stated here for Doppler resolution are only approximate. The required separation in (2.7.3) is generally defined by the - 3dB bandwidth of the spectra of equal target returns. This approximately equates to $1/T_c$ in the case that the signals are a pair of truncated sinusoids of length T_c. The frequency resolution will be affected as with range resolution, if one signal is of higher power and masks the other. High levels of noise and target accelerations during the integration period both serve to smear spectral responses, requiring larger separation. Any windowing applied to the signal will also broaden the spectral response, reducing the frequency resolution.

2.8 CLUTTER

Clutter is the unwanted returns received by the radar. Depending on the type and mission of the radar, these may come in the form of distributed volume or surface clutter. Volume clutter includes returns from rain, snow, chaff and surface from vegetation, ocean etc.

For the case of monostatic radar, the single antenna geometry makes it relatively simple to calculate the clutter volumes and surface areas (for at least certain nominal conditions). However in the bistatic case, there are many more degrees of freedom—transmit and receive antenna beam widths may differ, the beam intersection geometry varies with bistatic angle, as does the intersection with the ellipsoidal range resolution cells and with the ground. The calculation of clutter areas is usually restricted to very specific circumstances and in most cases of any complexity is numerically evaluated [2]. The calculation of clutter volumes, as with areas, is a function of many radar parameters (as described above) and as such is performed for the specific cases requiring investigation. For this reason clutter volumes in bistatic radar are not derived here.

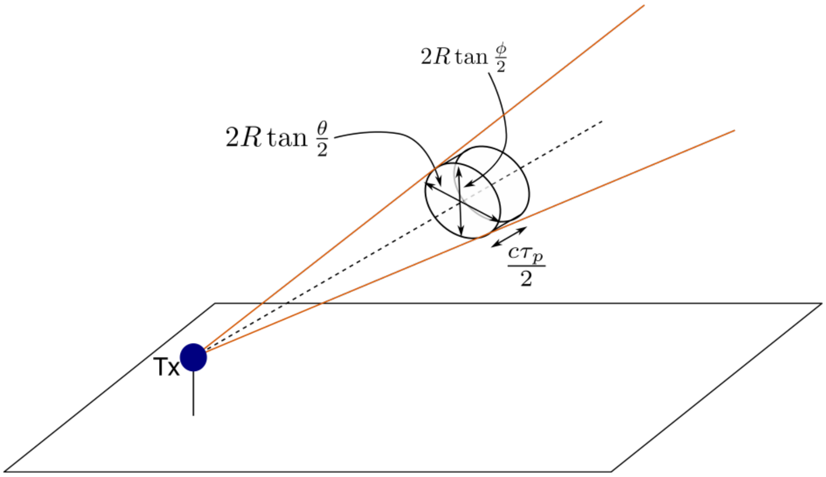

Figure 2.8-1. Volume clutter in monostatic radar.

The case for the monostatic radar clutter volume calculation is shown in Figure 2.8-1. To a first approximation, the volume can been estimated as an elliptical cylinder, with major and minor diameters defined by the angular/cross range resolution (2.6.1) in the antenna azimuth and elevation planes. The cylinder length is defined by the range resolution. Thus the clutter volume V_c is given by [7],

$$V_c = \pi R \tan\frac{\theta}{2} R \tan\frac{\phi}{2}\frac{c\tau_P}{2} = \frac{1}{2}\pi c\tau_P R^2 \tan\frac{\theta}{2}\tan\frac{\phi}{2} \tag{2.8.1}$$

For longer pulse widths and/or wider antenna beams, the volume is an elliptical conic frustrum.

There are two scenarios for calculation of the monostatic clutter area A_c, these are known as the beam width limited case and the range/pulse width limited case [4]. Essentially in the beam width limited case, the illuminated ground area dimension is smaller than the range resolution in this direction. The other case implies that the illumined dimension is larger than a single range cell on the ground. The two regimes can be mathematically defined, in accordance with Figure 2.8-2.

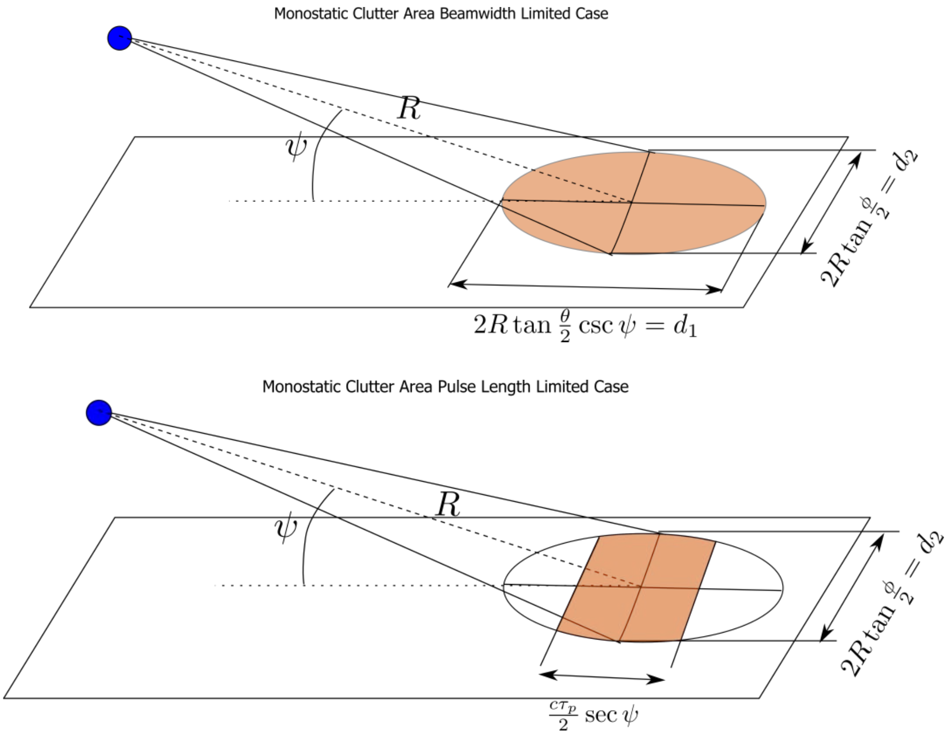

Figure 2.8-2. Beam and pulse width limited clutter areas in monostatic radar.

Figure 2.8-2(a) shows the beam width limited case, such that

$$\tan\psi > \frac{2R\tan\frac{\phi}{2}}{c\tau_\mathrm{p}/2}\ , \tag{2.8.2}$$

the clutter area is the area of the illuminated ground ellipse related to the cross range resolution in the azimuth and elevation planes of the antenna (2.6.1),

$$A_\mathrm{c} = \pi R^2 \tan\frac{\theta}{2}\tan\frac{\phi}{2}\csc\psi\ . \tag{2.8.3}$$

Figure 2.8-2(b) describes the pulse width limited case, which occurs under the conditions of:

$$\tan\psi < \frac{2R\tan\frac{\phi}{2}}{c\tau_\mathrm{p}/2}, \tag{2.8.4}$$

the clutter cell area is the estimated area of the strip related to the azimuthal cross range resolution and the pulse length,

$$A_c = c\tau_P R \tan\frac{\theta}{2}\sec\psi \,. \tag{2.8.5}$$

As an example of bistatic clutter area estimation, the case from [2] for small grazing angles and large range sums $R_t + R_r \gg D$ is reproduced. This is shown pictorially for both beam width and pulse width limited cases in Figure 2.8-3.

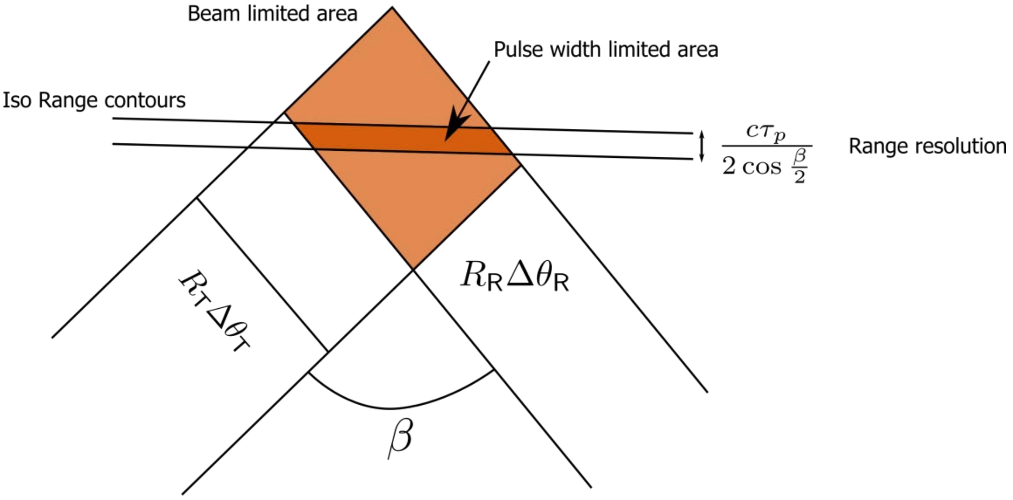

Figure 2.8-3. Beam and pulse width limited surface clutter in bistatic radar (special case).

The figure shows the intersection of the two antenna beams (approximated by a parallelogram) to give the beam width limited area and the corresponding intersection of this with a surface range resolution cell (intersection of constant range ellipsoids with ground surface). The cell boundaries are assumed to be parallel across the beam intersection and the separation is given by (2.5.2), thus forming another parallelogram for the pulse length limited cell.

2.8.1 NORMALISED AREA AND VOLUME CLUTTERS

Once the areas and volumes are found for the specific system, it is then possible to calculate the equivalent RCS of this patch/volume of the distributed clutter sources. This is performed through the use of a (pre-determined) normalised reflectivity [7], η_v – the volume clutter reflectivity [m^2/m^3] and σ_0 – the surface clutter reflectivity [m^2/m^2]. Such that to calculate the RCS of a volume of clutter σ_c ,

$$\sigma_c = V_c \eta_v \text{ ,} \tag{2.8.6}$$

where V_c is the aforementioned clutter cell volume. Equivalently the RCS of a clutter patch is given by

$$\sigma_c = A_c \sigma_0 \tag{2.8.7}$$

2.9 DETECTION OF SIGNALS IN NOISE – THE MATCHED FILTER RECEIVER

Conventionally in radar, any form of signal processing occurs in the intermediate frequency stages after down conversion from RF. In modern system it is done by means of digital signal processing in baseband usually presented by in-phase and quadrature channels. It is assumed that before this stage, the receiver is of large bandwidth and the actual frequency response $H(f)$ of the whole receiver will be defined by the filtering/amplification in the IF stage. The magnitude of the frequency response in the IF stage, $|H(f)|$ defines the bandwidth of the system, inside this band exists both system noise and received target returns. Figure 2.9-1(a) shows a pictorial example of a generic frequency response with bandwidth B_n for an arbitrary receiver/IF filter. Figure 2.9-1(b) illustrates the power spectral density (PSD), at the filter input, of both white noise - defined by a constant spectral density N_0 [W/Hz] and that of a target signature which may occupy this band—$|H(f)|$ has been overlaid for clarity.

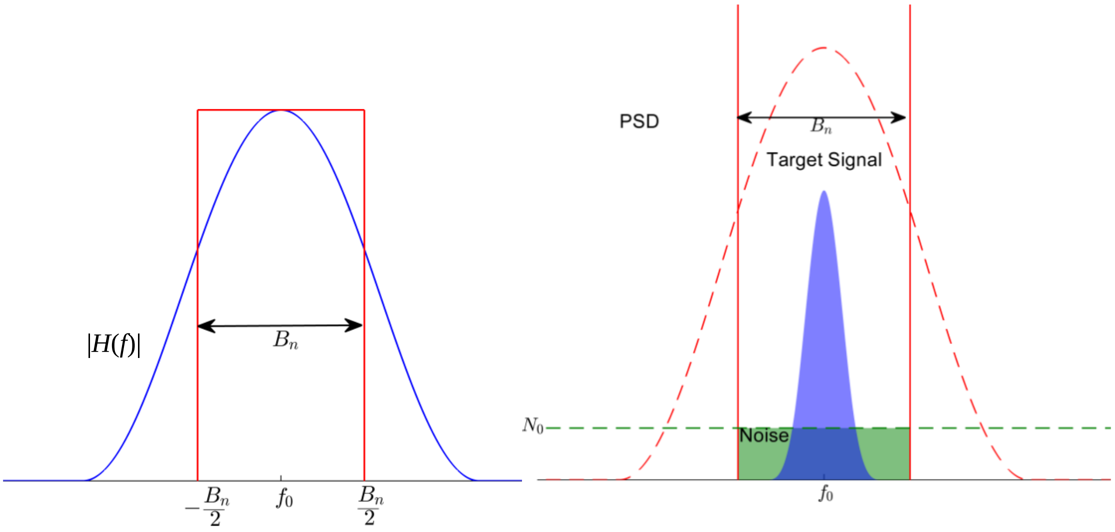

Figure 2.9-1. Example of noise bandwidth of system (a) and this bandwidth being occupied by signal (filled blue) and noise (filled green) (b).

It should be noted here that the bandwidth B_n specified in (a) is not the common definition of bandwidth as defined by the FWHM (-3dB) power, but for consideration of system noise, this is the integrated or noise equivalent bandwidth, given by [6], [7],

$$B_n = \frac{\int_{-\infty}^{\infty} |H(f)|^2 \mathrm{d}f}{|H(f_0)|^2} . \tag{2.9.1}$$

B_n is the bandwidth of the equivalent brick-wall filter which gives the same noise power output as the actual filter. Now as can be deduced from Figure 2.9-1 if the receiver noise bandwidth is overly large, the effective input noise power (which is the area of the green region in Figure 2.9-1)

$$N_{\text{in}} = N_0 B_n , \tag{2.9.2}$$

will increase with respect to the signal power and if it is too small, signal energy will be reduced as well as noise. The task here is to calculate the response $H(f)$ such that its effect on the input signal and input noise gives optimum signal output. This filter for the detection of targets in white noise is known as the matched filter [20]. The output of the matched filter gives the maximum available peak instantaneous signal power to mean white noise power ratio at its output, i.e. it maximises M where,

$$M = \frac{\left|s_{out}(t)\right|_{\max}^{2}}{N}, \tag{2.9.3}$$

with $s_{out}(t)$ being the output signal voltage of the filter and N is the average noise power output. The problem can be solved using the Schwartz inequality and is outlined in standard texts [6]. The outcome being that the frequency response of the matched filter is given by,

$$H(f) = G_a S^*(f) e^{-i2\pi f t_1}. \tag{2.9.4}$$

Where G_a is the matched filter gain (normally unity, has no effect on SNR at output), $S^*(f)$ is the complex conjugate of the received/input signal spectrum and t_1 is the time at which the signal $s_{out}(t)$ is a maximum – essentially the exponent part is a constant time delay to ensure causality. Along with this result comes the conclusion that the maximum value for M in (2.9.3) and thus the maximum possible relation of peak output signal power to average output noise power is given by:

$$M_{\max} = \frac{2E}{N_0}. \tag{2.9.5}$$

Where $E$is the input signal energy.

2.9.1 MATCHED FILTER FOR NON – WHITE NOISE

In the case where the noise at the input to the matched filter is not white, but the spectrum is a function of frequency i.e $N_{\mathrm{in}}(f)$, the optimum filter here is known as the non-white noise matched filter, and is defined as [1]

$$H(f)=\frac{G_a S^*(f)e^{-i2\pi f t_1}}{\left|N_{\mathrm{in}}(f)\right|^2}=\frac{1}{N_{\mathrm{in}}(f)}G_a\left(\frac{S(f)}{N_{\mathrm{in}}(f)}\right)^* e^{-i2\pi f t_1}, \tag{2.9.6}$$

with the definitions as for (2.9.4). The second equality expresses how the non-white noise filter can be expressed as two filters, where the term ${}^{1}\!/_{N_{\mathrm{in}}(f)}$ is a whitening filter, which as its name suggests, converts the noise to a uniform white noise spectrum and then is processed by a slightly modified standard matched filter.

2.9.2 MATCHED FILTER RELATION TO CORRELATION

The output $y_{\mathrm{out}}(t)$ of a filter with an impulse response $h(t)$ is given by the convolution of the impulse response with the input signal $s_{\mathrm{in}}(t')$, which contains both target signal and noise,

$$y_{\mathrm{out}}(t)=\int_{-\infty}^{\infty} s_{\mathrm{in}}(t')h(t-t')\mathrm{d}t'. \tag{2.9.7}$$

The impulse response for the matched filter is given by the Fourier transform of the frequency response (2.9.4), which corresponds to the reverse of the received signal (noiseless) $s(t)$ in time,

$$h(t)=G_a s(t_1-t) \tag{2.9.8}$$

$$\Rightarrow h(t-t')=G_a s(t_1-t+t'). \tag{2.9.9}$$

Where t_1 is as defined as for (2.9.4); the time at which the filter output signal $s_{out}(t)$ is a maximum. Thus (2.9.7) becomes,

$$\begin{aligned} s_{\mathrm{out}}(t) &= \int_{-\infty}^{\infty} s_{\mathrm{in}}(t') h(t-t') \mathrm{d}t' \\ &= G_a \int_{-\infty}^{\infty} s_{\mathrm{in}}(t') s(t_1 - t + t') \mathrm{d}t' = G_a X(t - t_1) \end{aligned}, \qquad (2.9.10)$$

where $X(t - t_1)$ is the cross-correlation function. In summary, the matched filter output is proportional to the cross correlation between the noisy received signal and a time delayed, time reversed, complex conjugated replica of the transmitted signal.

2.10 FORWARD SCATTER RADAR OVERVIEW

The previous sub-sections have discussed radar principles in relation to the two classic radar topologies of monostatic and bistatic radar. This section is a brief overview of the radar topology and parameters that are the main focus of this thesis – Forward Scatter Radar (FSR).

2.10.1 TOPOLOGY

FSR can be seen as a specific case of bistatic radar. In general the true definition of FSR is when the bistatic angle is 180°, though it will be shown in following chapters that it does not need to be that restrictive. The forward scatter topology lends itself towards systems where antennas face each other (when considering directional antennas) and target detection occurs at angles on or very close to the baseline; as depicted in Figure 2.10-1. The figure shows the transmit and receive antennas, Tx and Rx and the bistatic angle β, which is 180° in this case of FSR. The target crosses the baseline with some velocity v_{Tgt} at bistatic ranges of R_{T} and R_{R} from the transmit and receive antennas respectively and thus the total bistatic range sum is equal to the baseline distance d. It should be noted that for low profile/low height surface targets, the system functions at a very low grazing angle.

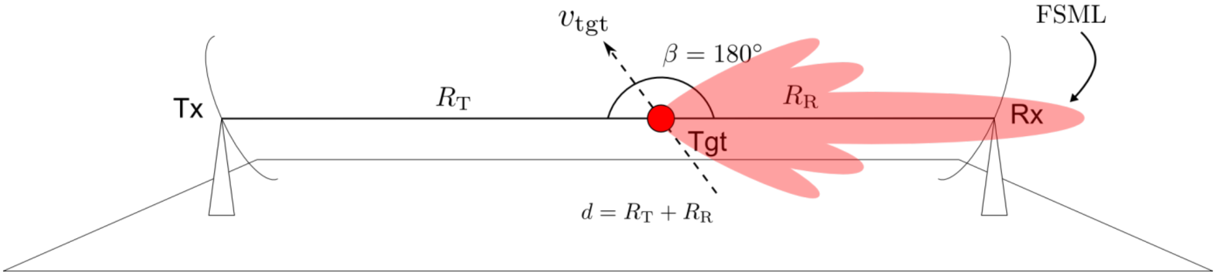

Figure 2.10-1. FSR topology.

2.10.2 FORWARD SCATTER RADAR CROSS SECTION

Though the general topology for FSR may seem restrictive in that detection can only occur in a specific spatial region, one of the major advantages of the use of FSR is the enhanced radar cross section in the forward direction [21], [22]—from hereon in termed the Forward Scatter Cross Section (FSCS).

Analytical solutions for the FSCS are only available for certain convex shapes for optical and sub-optical scattering regions [23], [24]. In the Rayleigh region the diffraction mechanism is more sophisticated and correct analytical solutions are only available for the sphere and infinitely long cylinder. However all is not lost, the Physical Theory of Diffraction gives an approximate method of calculating the FSCS.

The FSCS pattern for a target of a given three-dimensional shape can be calculated by replacing the silhouette of the target in the transmitter beam with an equivalently shaped radiating aperture antenna as is pictorially demonstrated in Figure 2.10-2. This replacement derives from the *shadow contour theorem* [22], [25] and the field in the FS direction is actually termed the shadow field, as it occupies the region of space in the 'shadow' of the target. This will be explained more thoroughly in a future chapter 3.1. This specifically describes the main field component for small angular deviations about the Forward Scatter (FS) direction, in the upper Mie and Optical scattering regimes (as described in Section 2.3). At wider angles bistatic scattering additionally comes into consideration.

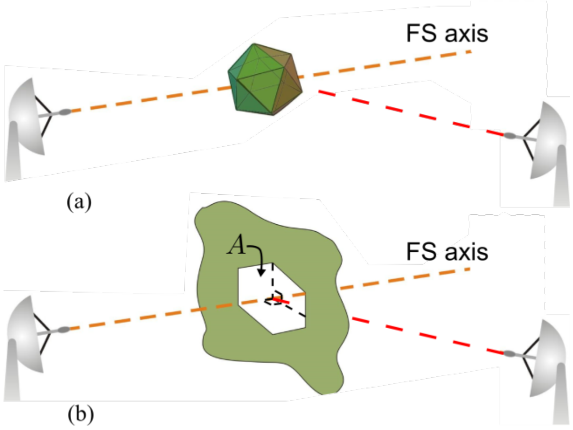

Figure 2.10-2. To estimate the forward scatter radar cross section pattern, a complex target shape (a) can be replaced by equivalent silhouette aperture of area A perpendicular to the incoming wave beam (b).

The FSCS is generally independent of the material of the target object, be it metallic or dielectric, and thus this system is ideally suited for the detection of stealth targets. The magnitude of the maximum FSCS of the target, $\sigma_{\mathrm{fs}}^{\max}$, i.e. the cross section at a bistatic angle of 180°, along the FS axis, is given in [1], [21] for these higher frequency limits by,

$$\sigma_{\mathrm{fs}}^{\max} = 4\pi\left(\frac{A}{\lambda}\right)^2 \ [\mathrm{m}^2]. \tag{2.10.1}$$

Where A is the physical area of the silhouette of the target intersecting the beam (perpendicular to the beam) as shown in Figure 2.10-2 and λ is the illumination wavelength. As the target is essentially treated as an aperture antenna, all of the general parameters relating to such antennas can be applied to the FSCS, like the forward scatter main lobe

(FSML) (Figure 2.10-1), with corresponding -3 dB width, denoted by $\theta_{\mathrm{fs}}^{\mathrm{ml}}$, and expressed by (2.2.5) or (2.2.6),

$$\theta_{\mathrm{fs}}^{\mathrm{ml}} = \varepsilon\lambda / D. \qquad (2.10.2)$$

D is the characteristic dimension of the target (in a particular plane of which we wish to find the lobe width), ε is a scaling factor depending on the aperture shape and λ is the signal wavelength—all previously shown in Section 2.2. This idea of a FS lobe relaxes the constraint to have the target exactly crossing the baseline in order to take advantage of the increase in FSCS.

To show the enhancement of the FSCS magnitude over that of the monostatic RCS in the upper Mie and optical regions, and to give an idea of the main lobe width relationship, a reproduction of the plot in Figure 2.3-2 showing the normalised monostatic RCS of a sphere of radius a_{s} is shown below in Figure 2.10-3. Here the FSCS and $\theta_{\mathrm{fs}}^{\mathrm{ml}}$ calculated from the area and dimension of the corresponding circular silhouette using (2.10.1) and (2.10.2) are added. As to is the FSCS calculated from the Mie approximation for comparison to the approximation. It can be seen that the FSCS enhancement begins to occur as stated before, in the Mie scattering region. Therefore in this region the approximations of FSCS and thus $\theta_{\mathrm{fs}}^{\mathrm{ml}}$ become valid, as can be seen by the similarity of the FSCS's. The gain in cross section for the FS case is obviously increasing as the electrical dimension of the sphere increases, i.e. a 6 dB increase in FSCS for 2× frequency increase; with this increase however comes a proportional 2× narrowing of the main lobe width. There is a trade-off between the gain in FSCS and its spatial/angular extent. The concept of the FSML width and indeed its narrowing, places restrictions on the antenna heights used in ground based FSR systems to ensure the FSML impinges on the receiver, making use of the increased FSCS.

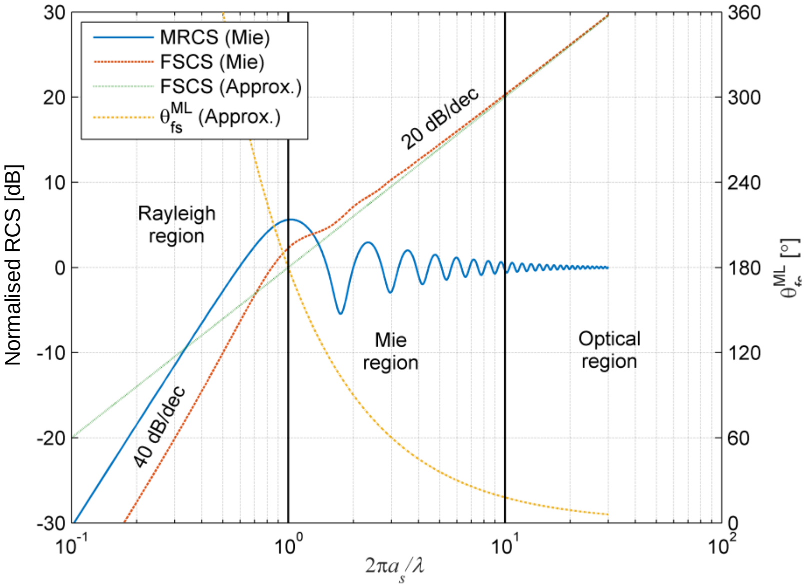

Figure 2.10-3. Normalised cross sections for sphere (relates to left y-axis). Blue shows monostatic RCS (labelled MRCS) and red the FSCS, both from Mie theory. Green gives the estimated FSCS from the circular silhouette. The yellow line corresponds to estimated FSML width (associated with right y-axis).

2.10.3 SPATIAL RESOLUTION PARAMETERS IN FSR

One disadvantage of the use of FSR is that it lacks ranging ability and therefore range resolution. We can see that a target has crossed the baseline, but we generally do not know where along its length and we cannot separate targets in range if they cross simultaneously. The lack of ranging is obvious in that the range sum from transmit to target and target to receiver is equal to the baseline D (as shown in Figure 2.10-1). This is a constant no matter the baseline crossing point, this is also therefore the reason for lack of resolution. This can also be shown mathematically by considering the range resolution equation for bistatic radar (2.5.3), reproduced here,

$$\Delta R_{\mathrm{BS}}^{\psi} \approx \frac{\Delta R_{\mathrm{BS}}}{\cos\psi} = \frac{c\tau_{\mathrm{P}}}{2\cos\frac{\beta}{2}\cos\psi}\ . \tag{2.10.3}$$

If the bistatic angle $\beta \rightarrow 180°$, then $\cos\frac{\beta}{2} \rightarrow 0$, this implies very large $\Delta R_{\mathrm{BS}}^{\psi}$, where targets require infinite separation to be resolved. All is not lost however—due to the predictable nature of the target signatures in FSR (Section 3.1), it is possible to use correlation processing to infer target trajectory parameters. This processing was part of the author's contribution to the work contained in [26], and will be explained in more detail in Section 5.2.6.

There is however be a form of angular resolution available to the FSR system, this is due to the distinct nature of the FSML as discussed in the previous sub-section. Depending on the electrical size of the target, the lobe is generally narrow and acts here as an equivalent directional antenna. This scenario is depicted in Figure 2.10-4.

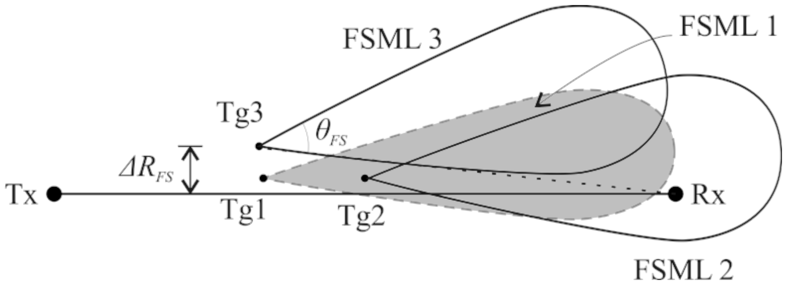

Figure 2.10-4. A form of range resolution in FSR, imposed by the target FSML acting as an effective directional antenna as it crosses the baseline (plan view of topology).

Tg3 is separated from the receiver due to the narrow FSML, even in the case of a wide beam receive antenna. The FSML's from targets Tg1 and Tg2 are directed towards the receive antenna and hence the FS signal is detected. On traversing the baseline, Tg3 will be resolved from Tg1 and Tg2 in distance. The distance resolution ΔR_{fs}, in Figure 2.10-4 could be estimated for narrow regions (small angles) around the baseline as,

$$\Delta R_{\mathrm{fs}} \approx R_R \frac{\theta_{\mathrm{fs}}^{\mathrm{ml}}}{2} \tag{2.10.4}$$

where $\theta_{\mathrm{fs}}^{\mathrm{ml}}$ is the FSML width (given by (2.10.2)). Or indeed the angular resolution of two targets with respect to the receiver can be described by $\Delta\theta_{\mathrm{fs}} = \theta_{\mathrm{fs}}^{\mathrm{ml}} / 2$.

2.10.4 FREQUENCY RESOLUTION AND DOPPLER SHIFT IN FORWARD SCATTER RADAR

The lack of true range resolution is a drawback; however a benefit of FSR is that this absence of range resolution gives rise to a non-fluctuating target signal. Additionally, the target equivalent antenna shape remains mostly unchanged in the target visibility region, further leading to low fluctuation levels in received signature envelopes. This means that the coherent processing time for the target, can be its full visibility time, greatly improving frequency resolution of FSR systems. As an approximation, if a perpendicular baseline crossing is considered at a velocity v_{tgt}, then this visibility time $\Delta\tau_{\mathrm{fs}}$ can be estimated by,

$$\Delta\tau_{\mathrm{fs}} = 2\frac{R_{\mathrm{cp}}}{v_{\mathrm{tgt}}}\tan(\alpha). \tag{2.10.5}$$

R_{cp} is the distance of the crossing point distance from the receiver and α is the maximal considered diffraction angle of the target from the receiver (in the ground plane) as pictured in Figure 2.10-5.

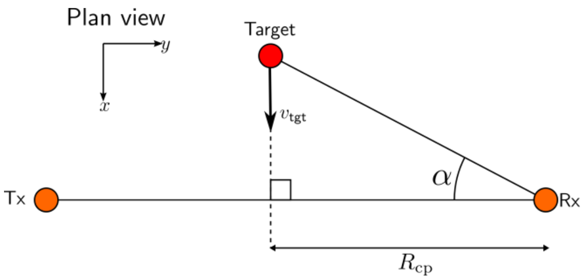

Figure 2.10-5. Geometry for estimation of target visibility/coherent time.

If it is chosen to define the coherent time by the -3 dB width of the FSCS main lobe pattern then, using (2.2.5),

$$\Delta\tau_{\mathrm{fs}} = 2\frac{R_{\mathrm{cp}}}{v_{\mathrm{tgt}}}\tan\left(\frac{\lambda}{2l_{t\mathrm{gt}}}\right), \tag{2.10.6}$$

with $l_{t\mathrm{gt}}$ being the target length, for small angles,

$$\Delta\tau_{\mathrm{fs}} = \frac{R_{\mathrm{cp}}\lambda}{v_{\mathrm{tgt}}l_{t\mathrm{gt}}}. \tag{2.10.7}$$

Thus the frequency resolution Δf_{fs} is inverse to this:

$$\Delta f_{\mathrm{fs}} = \frac{1}{\Delta\tau_{\mathrm{fs}}}. \tag{2.10.8}$$

Table **2.10-1** shows a comparison of coherent times/frequency resolution for monostatic radar and FSR (last two columns) at different wavelengths, for a Predator UAV.

Table 2.10-1. Maximum coherent time in monostatic radar and FSR for 'Predator' like UAV target (reproduced from [27]**) .**

$\Delta\varphi$ / Δt	**Monostatic**						**FSR**	
(°/s) →	**0.2**		**0.4**		**0.8**		**Baseline = 40km** **v_{Tg} = 50m/s**	
λ (m) ↓	Δf_M	$\Delta\tau_M$	Δf_M	$\Delta\tau_M$	Δf_M	$\Delta\tau_M$	Δf_{FS}	$\Delta\tau_{FS}$
3.0	0.8	1.25	1.6	0.63	3.2	0.31	0.013	75
1.5	1.6	0.63	3.2	0.31	6.4	0.16	0.026	37.5
0.75	3.2	0.31	6.4	0.16	12.8	0.09	0.053	18.8
0.3	8.0	0.13	16.0	0.06	32.0	0.03	0.13	7.5
0.1	24.0	0.04	48.0	0.02	96.0	0.01	0.4	2.5
0.03	80.0	0.01	160.0	0.006	320.0	0.003	1.3	0.75

The table is reproduced from [27] and is part of the author's contribution to the publication. In the FSR case, the target crosses the mid-point of a 40 km FSR baseline at 50 ms^{-1}. In the monostatic case, the target has a varying rate of change of aspect angle of 0.2, 0.4 or 0.8 $°s^{-1}$ and the coherent time is given by (2.3.5). The table indicates the huge increase in the potential time for coherent integration in FSR over monostatic radar, due to the absence of phase fluctuations. This fundamentally allows the development of effective target classification algorithms based on shadow inverse synthetic aperture synthesis and target profile reconstruction [28]–[30].

Figure 2.10-5 also allows the estimation of a maximal observed Doppler frequency, using (2.7.1), it can be seen that, the maximal FS Doppler

$$f_{\mathrm{d}}^{\max} = \frac{2v_{\mathrm{tgt}}}{\lambda}\sin\left(\alpha\right). \tag{2.10.9}$$

Again, if considering the angles defined by the -3dB FSML width, can be estimated by:

$$f_{\mathrm{d}}^{\max} = \frac{2v_{\mathrm{tgt}}}{\lambda}\sin\left(\frac{\lambda}{2l_{\mathrm{tgt}}}\right) \approx \frac{v_{\mathrm{tgt}}}{l_{\mathrm{tgt}}}. \tag{2.10.10}$$

Which indicates an independence on wavelength for very narrow FSML widths, and is presented in [27].

3 FORWARD SCATTER RADAR FOR SURFACE TARGETS

This section discusses more in depth the phenomenology behind the FS effect and shadow radiation, to give an insight to the underlying scattering principles of FSR. From this, the operating region of FSR, calculation of FSCS and fundamentals of the target signature formation in FSR are presented. Results from controlled anechoic chamber experiments are presented to experimentally verify the FS phenomenon. Target power budget models are also derived, which include important multi-path effects of scattering from the underlying conductive sea surface. The signal/power budget models are introduced here such that future work (not considered in this thesis) can focus on further validation against the collected experimental data described in Section 5.

3.1 PHENOMENOLOGY OF DOPPLER FORWARD SCATTER RADAR

This section describes important aspects of the phenomenology behind FSR in more depth. In Section 2.10 introducing FSR, general statements were made concerning the FS effect/phenomenon and estimation of the FSCS, which are found in generic radar texts. Here a broader overview will be given of the FS effect in terms of the Physical Optics (PO) approximation. This gives enough theory to then permit a description of the target signature formation in an FSR system, i.e. one where the FS main lobe actually impinges on the receiver and in which we can describe as receiving fully shadow radiation (as opposed to a combination of bistatic scattering and shadow field). The content here is an extension of part of the author's contribution to [26]. We begin with an overview of the forward scattering phenomenon, an outline of its theoretical formulation in the context of physical optics and its application to the calculation (or at least estimation) of FSCS. Then the formation of target signatures, the extraction of the useful phase information and the effect of the forward scatter cross section are described. Finally some measured results are shown to highlight and emphasise the FS phenomenology.

3.1.1 THE FORWARD SCATTER EFFECT

As mentioned in Section 2.10, FSR is a variant of bistatic radar which restricts the systems spatial operational area to regions in the vicinity of the radar baseline, but in exchange, it allows for enhanced target detection in these areas due to a dramatic increase in RCS in the forward direction. This is known as the FS effect [22], [31]. The phenomenon is observed in the Mie and optical scattering regimes and indeed was first discussed in a published work by Mie [32]. Much study has been carried out in optics [33] and more appropriate here is investigation in relation to radar and the estimation of the bistatic RCS of objects. One of the key contributors in this area being Ufimtsev who through his work on RCS reduction techniques [34] not only developed the Physical Theory of Diffraction [25] as an extension of physical optics, but also formalised the key ideas of shadow radiation and the shadow contour theorem related to FS. The concept of the shadow radiation was well known beforehand, from studies of black body scattering [35], but not defined in the context of PO.

In PO the total scattered field E_{sc} of an object can be separated into two constituent fields, the reflected field E_{ref} and the shadow field E_{sh} [22], [36] such that,

$$E_{\mathrm{sc}} = E_{\mathrm{ref}} + E_{\mathrm{sh}} \,. \tag{3.1.1}$$

The shadow field is so termed because the field is most prominent (though by all means not necessarily confined) in the spatial regions which are geometrically shielded (or shadowed) by the target, i.e. about the axis directly behind the target in the FS direction. Figure 3.1-1 gives a pictorial overview of the concept. The figure shows an opaque body being illuminated by an incoming plane wave and indicates the reflected radiation and the shadow region. The shadow contour Γ defines the geometric boundary between the illuminated and non-illuminated sides of the object—it should be highlighted that the object is truly a 3-D volume and the contour is a planar shape.

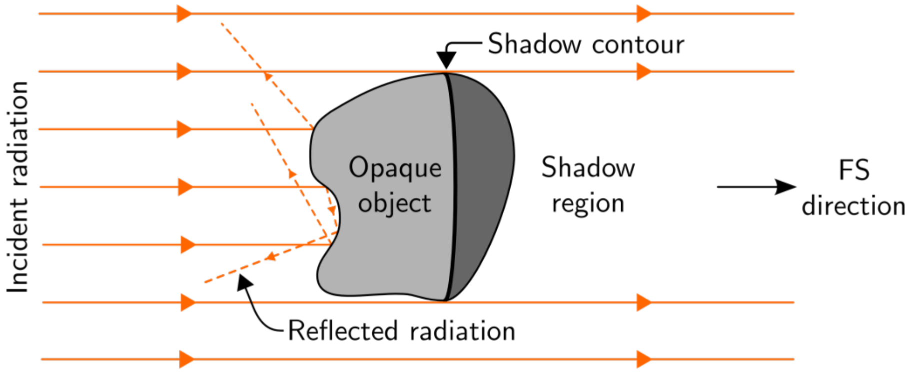

Figure 3.1-1. Plane wave illumination of an opaque body, indicating incident and reflected radiation and the region of geometric shadow where shadow field concentrates.

No attempt to indicate the shadow field structure is given in the figure and indeed there will be no rigorous theoretical derivations here, they can be found or are summarised in the following references, [25], [37], [38] and references therein. However, general statements relevant to use in the development of FSR signal models can be made from the theory. Firstly, the shadow field structure is purely determined by the shadow contour, Γ, of the target object, not its full 3-D shape. This was summed up by Ufimtsev in the '*Shadow Contour Theorem*':

> *'The shadow radiation does not depend on the whole shape of the scattering object, and is completely determined only by the size and the geometry of the shadow contour'*

Moreover, the shadow field description (in the scalar theory) is identical to the Kirchoff approximation for the field scattered by a planar absorbing plate with shape defined by the shadow contour. Secondly, from black body theory [38], the shadow field is independent of the material (and hence electromagnetic) properties of the target object. If the target were completely absorbing (true black body), the shadow field would be the only scattered field present—no reflected component would exist. Both the fact that the shadow radiation doesn't depend on the target 3-D shape or material provides major limitations in application of RCS reduction techniques such as the use of radar absorbing materials (RAM) or target surface shaping. Ultimately if considering a perfect electrically conducting target object, the best that can be achieved by a perfect RAM coating is a reduction of one half of the total scattered power—such limitations and techniques are discussed in more detail in [37]. Thirdly some statements can be made about the asymptotic forms of the shadow field. In the shadow region close to the target object, the field forms as a result of diffraction processes in the vicinity of the shadow boundary and is composed of creeping waves, surface diffracted waves or edge waves, dependant on the object shape. In this region (and indeed at asymptotically high frequency) the radiation can be considered as a wave that approximately cancels the incident field, i.e.

$$E_{\text{sh}} \approx -E_{\text{inc}} \tag{3.1.2}$$

Now in the far field, the shadow radiation is interpreted as a result of co-phased interference of waves arising from the vicinity of the shadow boundary; the shadow field concentrates in the forward direction close to the FS axis, which is the focal line. It is this concentration of the shadow field that is perceived as the forward scatter effect. Figure 3.1-2 (adapted from [25]) shows an example of the total PO scattered field for a cylinder (illuminated at 45° to the length), along with the shadow radiation component of this field. It clearly highlights the concentration of the shadow field around the forward scatter axis, and indeed the fact that the shadow radiation forms the major component of the field over a certain angular range about the forward direction. It is apparent in the figure and can be again shown from the theory [22], that in the direct FS direction (45° in Figure 3.1-2) the field is entirely composed of shadow radiation and in the backscatter direction (225° in the figure) the field is entirely composed of reflected radiation.

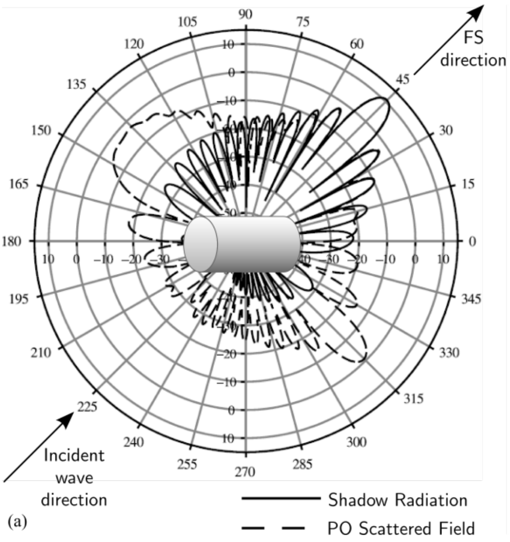

Figure 3.1-2. The total physical optics scattered far field of a cylinder, showing the contribution from shadow radiation which is focussed in the FS direction (45° **in this figure)—adapted from** [22], [25]**.**

3.1.2 RELATION OF SHADOW RADIATION/FORWARD SCATTER EFFECT TO FORWARD SCATTER CROSS SECTION

It can be shown [22] that if the incident field on a target, E_{inc}, is described by a plane wave travelling in the z direction i.e.

$$E_{\text{inc}} = E_0 e^{ikz}, \tag{3.1.3}$$

where E_0 is the field strength and k is the wavenumber, then exactly on the z axis (FS axis) on the shadow side of the target, the shadow far field has its maximum value $E_{\text{sh}}^{\max}$, given by

$$E_{\text{sh}}^{\max} = E_0 \frac{iA}{\lambda} \frac{e^{ikz}}{z} = \frac{iA}{\lambda z} E_{\text{inc}}. \tag{3.1.4}$$

A is the area of the shadow contour. The imaginary amplitude in (3.1.4) implies that the shadow far field on the FS axis has a $\pi/2$ rad phase difference to the incident field; this is important for the next section when considering the formation of the FSR target signature. Using (3.1.4), and (2.3.1), it is therefore possible to write the equation for the maximum FSCS,

$$\sigma_{\text{fs}}^{\max} = 4\pi z^2 \frac{\left|E_{\text{sh}}^{\max}\right|^2}{\left|E_{\text{inc}}\right|^2} = 4\pi z^2 \left|\frac{iA}{\lambda z}\right|^2 = 4\pi\left(\frac{A}{\lambda}\right)^2 . \quad (3.1.5)$$

The variables in the equation have been defined previously. This corresponds to the earlier stated formula in Section 2.10. The shape of the field and thus FSCS pattern can be approximated by considering what was stated in the previous sub section; the shadow radiation takes an identical form to that of an illuminated absorbing plate with shape defined by the shadow contour. Through application of *Babinet's principle* [11], which fundamentally states that the diffracted field from an opaque screen and its complimentary screen i.e. a screen which is transparent where the other is opaque and vice-versa, are the same except for a change of sign. It is possible therefore to treat the problem as one of diffraction from an aperture in a screen of which the aperture shape is given by the shadow contour. The process of reducing the problem from a volumetric target object through to diffraction from an aperture is pictorially described in Figure 3.1-3. It is seen (which was only stated in Section 2.10) that the shadow field and therefore the FSCS pattern can now be described by what is effectively an aperture antenna power pattern, with the far field main lobe maxima along the FS axis given by (3.1.5). Analytical power patterns for the far field of rectangular and elliptical apertures were given in Section 2.2. As mentioned previously, as the electrical dimensions of the target increase, the FS enhancement increases via (3.1.5),

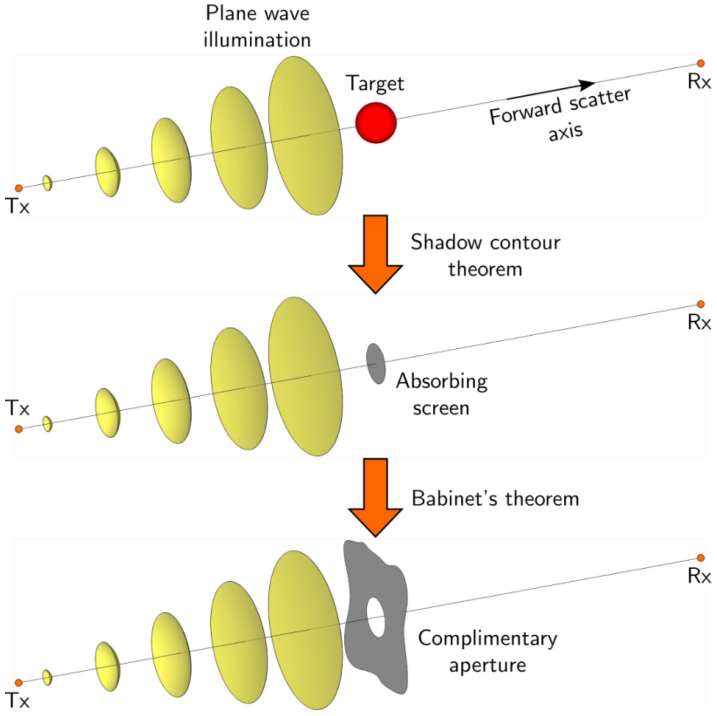

Figure 3.1-3. Reduction of problem of calculating the FS shadow field of a volumetric target body. The application of the shadow contour theorem allows replacement of the target with an absorbing screen with shape defined by the target shadow contour. Subsequently the application of Babinet's principle allows further replacement by a complimentary aperture in an infinite screen.

however, the FSML width narrows as the pattern is related to the Fourier transform of the aperture. If the shadow contour can be found for an arbitrary shaped target, the FSCS pattern could be estimated using the Fourier Transform of the equivalent co-phasal aperture defined by the contour, i.e.

$$\sigma_{fs}(\vec{r}_0) = \lim_{R\to\infty} 4\pi R^2 \left(|E_{sh}|^2 / |E_{inc}|^2 \right) = \frac{4\pi}{\lambda^2} \left| \int_{A_{SH}} \exp\left[j\left(2\pi/\lambda\right)\vec{\rho}\vec{r}_0 \right] dS \right|^2 . \qquad (3.1.6)$$

In which, $\vec{\rho}$ is a radius vector to point P_A on the aperture, $\vec{r}_0$ is the unit vector towards the evaluation point P and $\vec{R}$ is the radius vector to that point, A_{SH} is the area of the aperture. The notations and coordinates are depicted in Figure 3.1-4

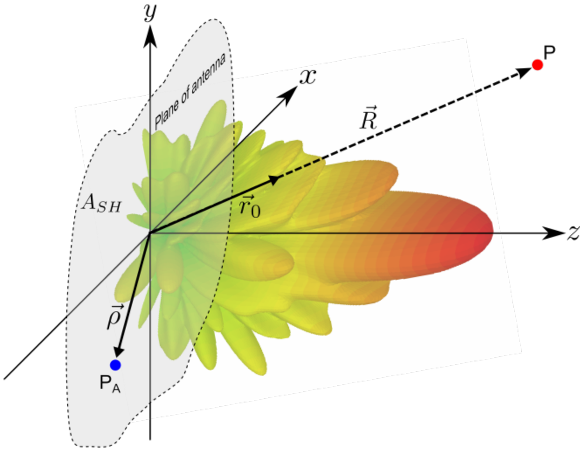

Figure 3.1-4. FSCS pattern calculation using Fourier Transform from approximation by equivalent aperture antenna.

3.1.3 FORWARD—BISTATIC SCATTERING BOUNDARY

When a target is traversing through an FSR system as in Figure 3.1-5, it has to approach from bistatic angles β which are much less than $180°$, therefore the angle α_r between the FS axis and the receiver can be large.

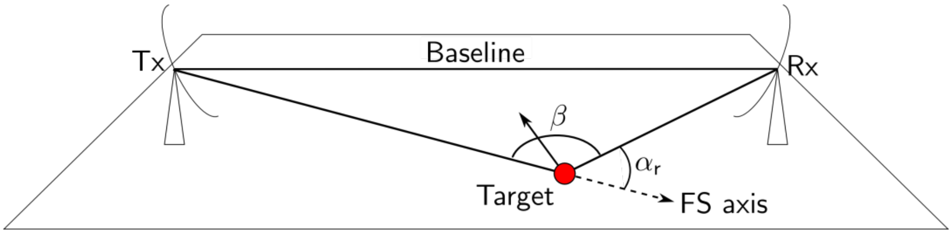

Figure 3.1-5. A target approaching and crossing the FSR baseline, will approach from a bistatic angle $< 180°$. In these regions, the angle from the FS axis to the receiver is large and the received scattered signal will be composed of both shadow and reflected radiation.

As shown before with reference to Figure 3.1-2, at angles away from the FS axis the scattered field at the receiver is not necessarily purely shadow field, it only is when the target is on the baseline at zero bistatic angle or in the case of a true black body. Therefore, scattering will also be composed of bistatic reflections from the target, which will vary with target electrical size and indeed shape and material. The replacement of target by aperture method will give the shadow field contribution, but in order to model FSR systems it is useful to know over what range of angles near FS in which shadow radiation is dominant and when does an appreciable field contribution from bistatic scattering start to occur. Also it would be of interest to know the range of target electrical sizes the theory is applicable for in general, even though this is generally thought of as an optical approximation. Now this could be forgone if it was possible to accurately predict the full 3-D scattered electric field patterns of our targets, unfortunately this is only possible in certain cases as explained previously, or indeed we could use EM packages to calculate this. However for the investigation of many trajectories, EM simulation would take a long time to compute over many incident angles. In order to draw some gross conclusions it is possible to use the reference target of a perfect electrically conducting sphere, for which the Mie series [15] is a 'complete' analytical solution—complete in that it still requires a sum to infinity for precise results. Sum terms can however be limited according to some rules. The Mie series gives the complete scattered far field (vector field), whereas the aperture antenna approximation will give the (scalar) component of this related to the shadow field and thus the 'FS effect'. Figure 3.1-6 shows a comparison of the calculated Mie and circular aperture FSCS's for different scattering regimes or electrical size of the sphere. (a) shows the Rayleigh scattering regime, where the sphere diameter $D_s = 0.5\lambda$, (b) the Mie region $D_s = 10\lambda$ and (c) the optical region where $D_s = 100\lambda$. It is clear from (a) that the aperture estimation of the FSCS fails to some extent, it does not define the FSCS at 0° appropriately or the lobe structure—as expected in the Rayleigh region, where indeed the scattering mechanism is not described by the shadow contour theorem. In the Mie region (b) it is clear that for the main lobe the three curves coincide well, inferring that the main lobe is formed primarily by the shadow field component, this could also be concluded to a lesser degree for the first side lobes. It is also apparent that this is true for both wave polarisations. The larger electrical dimension sphere (c) shows similar conclusions, however

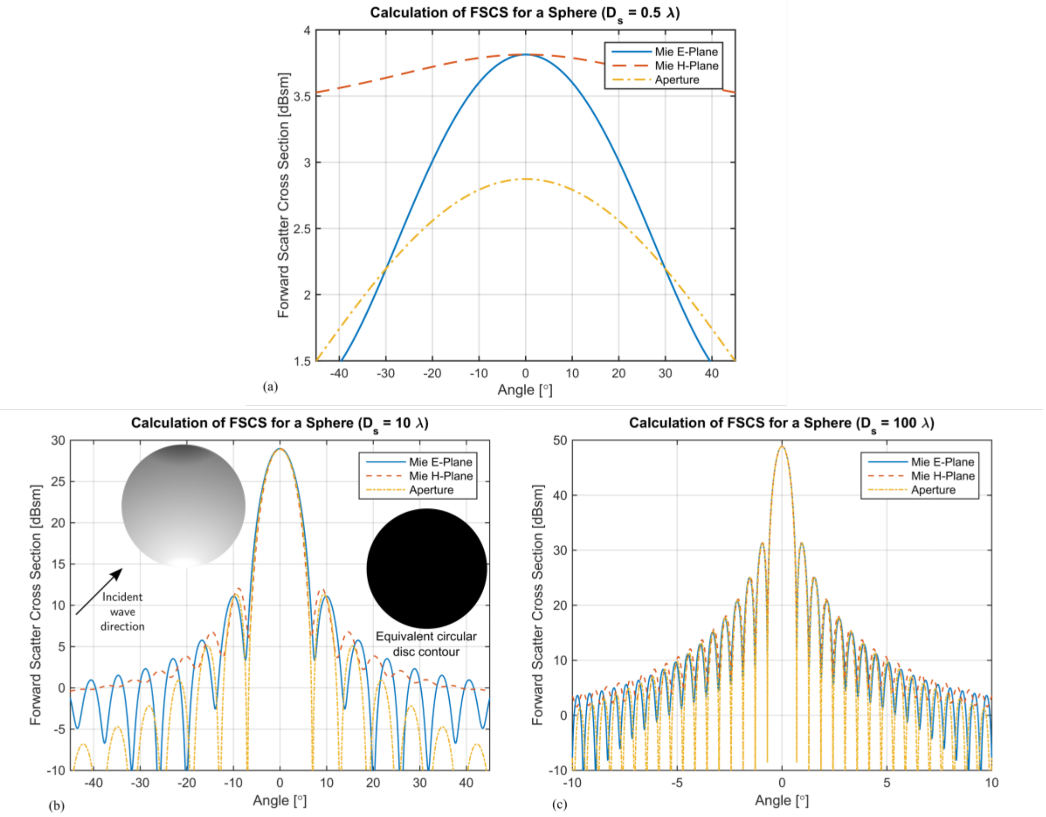

Figure 3.1-6. Comparison of FSCS's of a sphere as calculated by Mie series (full field) and circular aperture approximation (shadow field) for different electrical sizes. Sphere diameters are: (a) 0.5λ (Rayleigh), (b) 10λ (Mie) and (c) 100λ (Optical).

in this case the shadow field dominates many side lobes ($\approx 5-6$), though the extent of the dominance of the shadow field is not necessarily any larger in absolute angle that the case of (b). In any case, it is clear that the FSML can be treated to be composed solely of the shadow field.

3.1.4 TARGET SIGNATURE FORMATION IN FORWARD SCATTER RADAR

In essence the target signature in FSR can be thought of as a composition of both the phase signature due to a point like target traversing the FSR baseline over time, and an amplitude modulation imposed upon this by the FSCS and any present propagation effects. The next sub-sections will describe the phase/Doppler signature, followed by the effect of the

FSCS. Only once this generalised form of the signature is described will propagation effects be introduced to give a full signal model.

3.1.4.1 *TARGET PHASE/DOPPLER SIGNATURE*

As a target moves through (or indeed in the vicinity of) the baseline, two main signals play a role in forming the target phase signature at the receiver of an FSR system, these are highlighted in Figure 3.1-7. The first signal, resulting from the topology of FSR, is the strong unobscured direct path signal from transmitter to the facing receiver (otherwise known as the leakage signal).

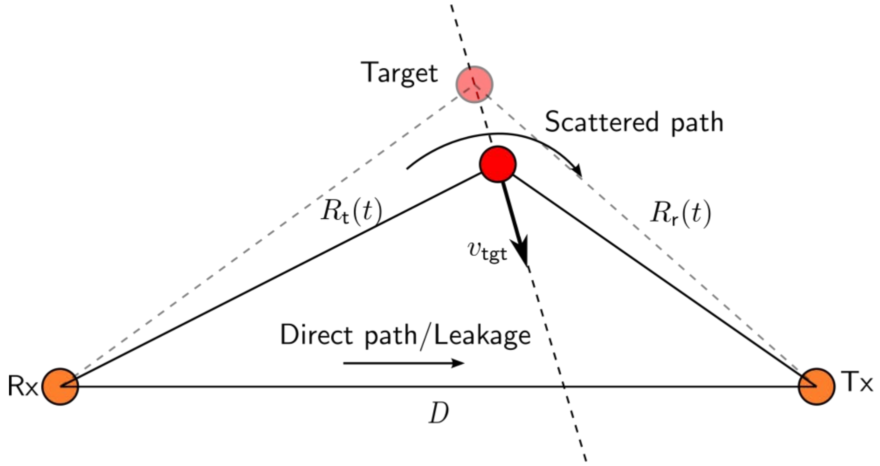

Figure 3.1-7. Received components forming the fundamental target phase signature in FSR. Highlighting direct path (leakage) and delayed scattered (shadow) signal from the target and the changing ranges as the target moves on its trajectory.

The second is the weaker signal scattered from the target and in the case of FSR is formed by the shadow field of the target being cast over the receiver. It is the interference of these two signals which forms the target phase signature. Thus, at the receiver the input signal $S_{in}(t)$ can be treated as the sum of the direct path $S_{dp}(t)$ and the delayed signal scattered from the target $S_{tgt}(t)$,

$$S_{in}(t) = S_{dp}(t) + S_{tgt}(t) = A_{dp}\cos(2\pi f_0 t) + A_{tgt}(t)\sin\left[2\pi f_0\left(t + t_{tgt}(t)\right)\right]. \qquad (3.1.7)$$

Where A_{dp} and $A_{\mathrm{tgt}}(t)$ are the amplitudes of the direct path and target signals respectively. In the case of FSR with stationary antennas the direct path amplitude A_{dp} is stable, the target amplitude $A_{\mathrm{tgt}}(t)$ will change with time due to propagation effects. f_0 is the carrier frequency and $t_{\mathrm{tgt}}(t)$ is the delay time of the scattered signal in relation to the direct path, which may[1] vary with time for the moving target, providing the phase modulation (Doppler shift). Initial phases are omitted with no loss of generality due to the coherency of both signals as they arise from the same source. It should be noticed that in (3.1.7) the target signal, being shadow radiation, is an additional $\pi/2$ radians phase shifted in relation to the direct path transmitted signal (as shown by (3.1.4)), hence the use of one cosine and one sine term. When away from the baseline, the target signal may also contain bistatic reflection components. As noted in Section 3.1.3, the magnitude of these bistatic components in relation to the shadow field depends on the target electrical size (Figure 3.1-6)—the larger the target, the wider the scattering angle over which the shadow field dominates. This signal model based on pure shadow radiation would therefore be valid over a wider range of scattering angles when representing targets in the Mie and optical scattering regimes.

The experimental hardware built for the research presented in this thesis uses what is termed a 'self-mixing heterodyne' receiver to extract the Doppler by means of a non-linear transformation of the input signal. As explained in Section 2.10, due to the large bistatic angles encountered in FSR, the Doppler frequencies involved are very low, in the order of Hz. This type of receiver fundamentally enables the extraction and measurement of these very low frequencies, which may otherwise be masked in the background of transmitter phase noise;

---

[1] The term 'may' is used in recognition that in some special cases e.g. motion around iso-range contours or along the FSR baseline, motion will not produce a varying delay.

further descriptions of the hardware and discussion of phase noise can be found in Section 4.2.1 and its subsection 4.2.1.1 respectively.

Commonly in bistatic radar, the direct path signal is considered to be a source of unwanted interference, for FSR however, it is vital. In such a ‘self-mixing’ receiver, the direct path signal component acts as a reference waveform, one which is however combined with the target returns at the receiver input and is not used independently. A detector with a quadrature characteristic, or ‘square law’ detector (SLD) is considered here, acting on the input waveform $S_{\text{in}}\left(t\right)$, which after passing through a low pass filter (LPF) gives (using standard trigonometric identities) the following receiver output, $S_{\text{out}}\left(t\right)$:

$$\begin{gathered} S_{\text{in}}\left(t\right)\xrightarrow{\text{SLD}}\left[S_{\text{in}}\left(t\right)\right]^{2}\xrightarrow{\text{LPF}}\overbrace{\frac{A_{\text{dp}}{}^{2}+A_{\text{tgt}}{}^{2}}{2}+A_{\text{dp}}A_{\text{tgt}}\sin\left(2\pi f_{0}t_{\text{tgt}}\left(t\right)\right)}^{S_{\text{out}}\left(t\right)}. \\ \Rightarrow S_{\text{out}}\left(t\right)\approx A_{\text{dc}}+A_{\text{ph}}\sin\left(2\pi f_{0}t_{\text{tgt}}\left(t\right)\right) \end{gathered} \tag{3.1.8}$$

Where $A_{\text{dc}}=\frac{A_{\text{dp}}{}^{2}+A_{\text{tgt}}{}^{2}}{2}$, which given that $A_{\text{dp}}\gg A_{\text{tgt}}$ is essentially a dc level equal to the direct path signal power, sometimes referred to as the received signal strength indicator (RSSI). $A_{\text{ph}}=A_{\text{dp}}A_{\text{tgt}}$ is the phase signature envelope and $A_{\text{ph}}\sin\left(\psi\right)$, where $\psi=2\pi f_{0}t_{\text{tgt}}\left(t\right)$, is the modulation on top of the RSSI dc level. It can be seen here that if the value of $t_{\text{tgt}}\left(t\right)=\text{const}$ i.e. a stationary target, then the sin term is also a constant and the target just contributes to the received signal dc amplitude, as one would expect. Also from Figure 3.1-7, an expression for the target signal delay, $t_{\text{tgt}}\left(t\right)$, can be found:

$$t_{\text{tgt}}\left(t\right)=\frac{R_{\text{t}}\left(t\right)+R_{\text{r}}\left(t\right)-D}{c}, \tag{3.1.9}$$

where $R_{\mathrm{t}}(t)$ and $R_{\mathrm{r}}(t)$ are the transmitter to target and receiver to target ranges respectively and D is the baseline length. The numerator is the total extra distance travelled by the target signal w.r.t. the direct path, c is the speed of signal propagation (speed of light) and t indicates the dependence on time due to target motion. The argument of the sin function in (3.1.8) is the phase of the point-like target signature $\psi(t)$ as it travels through the system, and can be written in full using (3.1.9) as:

$$\psi(t) = 2\pi f_0 t_{\mathrm{tgt}}(t) = \frac{2\pi f_0}{c}\left(R_{\mathrm{t}}(t) + R_{\mathrm{r}}(t) - D\right). \qquad (3.1.10)$$

This describes the phase in the general sense, the dependence on time is indicated but this has to be calculated in relation to the target kinematics and initial conditions. The method of calculation of the ranges R_{t}, R_{r} and d is straight forward and described with the aid of Figure 3.1-8.

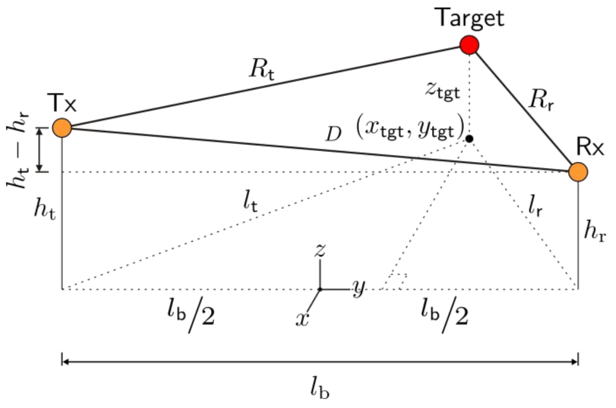

Figure 3.1-8. Variables to calculate ranges required for FSR phase signature calculation as target traverses the system. Time dependence is omitted for figure clarity.

The figure shows the Tx and Rx antenna masts, with heights h_{t} and h_{r} respectively, separated by a distance along the ground of l_{b}, centred on the coordinate origin and extending in either direction along the y axis. The target, depicted by its phase centre, is undergoing motion and as such has a time dependent position $\boldsymbol{p}_{\mathrm{tgt}} = \left(x_{\mathrm{tgt}}(t), y_{\mathrm{tgt}}(t), z_{\mathrm{tgt}}(t)\right)$. There are two further ground paths shown, $l_{\mathrm{t}}(t)$ and $l_{\mathrm{r}}(t)$, which correspondingly join the Tx and Rx antenna mast bases to the target ground coordinates $\left(x_{\mathrm{tgt}}(t), y_{\mathrm{tgt}}(t)\right)$. It can be seen that knowing l_{b}, the baseline distance D can be calculated thus,

$$D = \sqrt{\left(h_{\mathrm{t}} - h_{\mathrm{r}}\right)^2 + l_{\mathrm{b}}^2}\,. \tag{3.1.11}$$

It can therefore by similar means be shown that,

$$R_{\mathrm{t}}(t) = \sqrt{\left(h_{\mathrm{t}} - z_{\mathrm{tgt}}(t)\right)^2 + l_{\mathrm{t}}(t)^2} \tag{3.1.12}$$

and

$$R_{\mathrm{r}}(t) = \sqrt{\left(h_{\mathrm{r}} - z_{\mathrm{tgt}}(t)\right)^2 + l_{\mathrm{r}}(t)^2}\,, \tag{3.1.13}$$

where

$$l_{\mathrm{t}}(t)^2 = \left(\frac{l_{\mathrm{b}}}{2} + y_{\mathrm{tgt}}(t)\right)^2 + x_{\mathrm{tgt}}(t)^2 \tag{3.1.14}$$

and

$$l_{\mathrm{r}}(t)^2 = \left(\frac{l_{\mathrm{b}}}{2} - y_{\mathrm{tgt}}(t)\right)^2 + x_{\mathrm{tgt}}(t)^2\,. \tag{3.1.15}$$

To give an example of the form of the target phase signature, it is possible to consider the simplest case of a mid-point, perpendicular crossing of the baseline as shown in Figure 3.1-9.

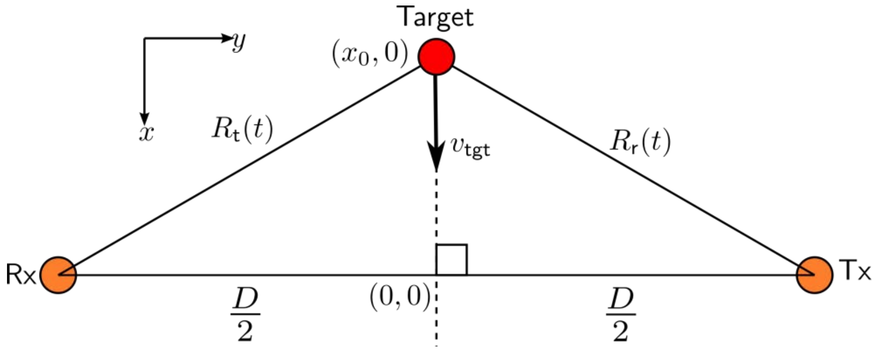

Figure 3.1-9. Plan view of target trajectory of mid-baseline, perpendicular crossing. Scenario used to highlight general features of target phase signature.

If the antennas and target height are all considered equal, the equations for the ranges $R_\mathrm{t}(t)$ and $R_\mathrm{r}(t)$ in (3.1.10) are given by:

$$R_\mathrm{t}(t) = R_\mathrm{r}(t) = \sqrt{\left(\frac{D}{2}\right)^2 + x_\mathrm{tgt}(t)^2}\,, \tag{3.1.16}$$

with

$$x_\mathrm{tgt}(t) = x_0 + v_{tgt}t\,, \tag{3.1.17}$$

where v_{tgt}, the target speed has purely positive x component. The phase and phase signature for this trajectory is shown in Figure 3.1-10 for a speed of 5 and 10 ms^{-1} crossing a 500 m baseline.

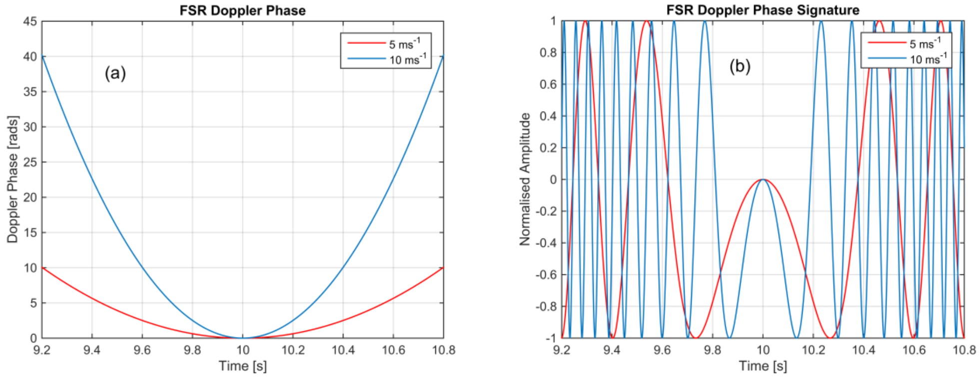

Figure 3.1-10. Doppler phase (a) and phase signature (b) for target mid-point crossing of 500 m baseline at 5 and 10 ms^{-1}.

It can be seen that the signature is a chirp like waveform and the phase progression can actually be described by the progress of the target through Fresnel zones [39] as shown pictorially in Figure 3.1-11.

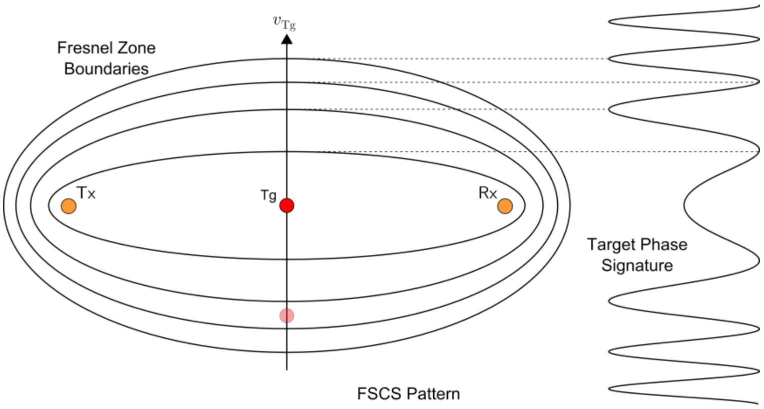

Figure 3.1-11. Target phase signature as a consequence of target motion through consecutive (constructive and destructive) Fresnel zones along the trajectory.

In the preceding discussion and examples the amplitude A_{ph} in (3.1.8) has been neglected in order to purely show the phase description of the signal (the amplitude is set to unity), now in truth the phase signature is modulated by an envelope given by the amplitude of the target scattered signal. This amplitude is both a consequence of the FSCS pattern and the signal propagation. Neglecting propagation effects for now, the next sub-section will concentrate on describing/estimating the contribution of the target FSCS pattern to the target phase signature envelope.

3.1.4.2 *TARGET SIGNATURE ENVELOPE – THE EFFECT OF FORWARD SCATTER CROSS SECTION*

This section is dedicated to estimating the effect of target FSCS on the Doppler signature envelope. When modelling the target signatures in FSR, in order to limit the complexity and variety of the simulations it is assumed that target has a uniform linear trajectory when crossing the FSR baseline. This is a reasonable assumption stemming from the consequence of having the relatively narrow FSCS patterns, visibility time (signature length) is generally in the order of seconds, it is not likely that any (at least ground based) target would make a significant manoeuvre or change of speed over this short time. The target is treated as a plate of given length and height traversing the baseline, complying with and representing the aperture approximation of the FSCS as described before in Section 3.1.2. Figure 3.1-12 shows as an example, a rectangular plate of height h_{tgt}, length l_{tgt}, travelling at velocity $\boldsymbol{v}_{\mathrm{tgt}} = (v_{\mathrm{x}}, v_{\mathrm{y}}, v_{\mathrm{z}})$ with a time dependent position $\boldsymbol{p}_{\mathrm{tgt}}(t) = (x_{\mathrm{tgt}}(t), y_{\mathrm{tgt}}(t), z_{\mathrm{tgt}}(t))$ of the phase centre of the target at it traverses the baseline.

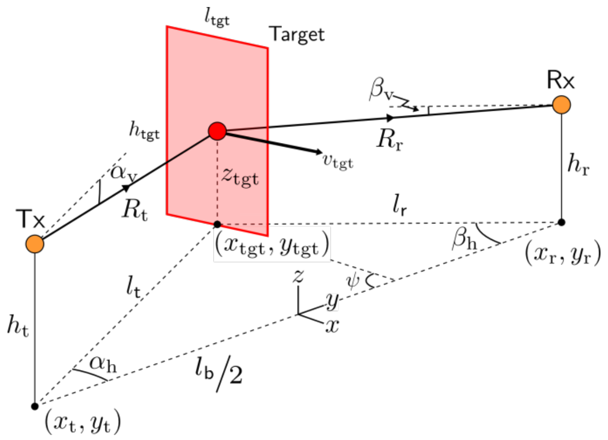

Figure 3.1-12. Rectangular plate target traversing the FSR baseline.

The angles α_{h} and α_{v} are the horizontal and vertical view angles of the transmitter to the target, β_{h} and β_{v} are the corresponding angles for the receiver, given by,

$$\alpha_{\mathrm{h}}(t) = \arctan\left(\frac{x_{\mathrm{tgt}}(t)}{\frac{l_{\mathrm{b}}}{2} + y_{\mathrm{tgt}}(t)}\right), \tag{3.1.18}$$

$$\beta_{\mathrm{h}}(t) = \arctan\left(\frac{x_{\mathrm{tgt}}(t)}{\frac{l_{\mathrm{b}}}{2} - y_{\mathrm{tgt}}(t)}\right), \tag{3.1.19}$$

$$\alpha_{\mathrm{v}}(t) = \arctan\left(\frac{z_{\mathrm{tgt}}(t) - h_{\mathrm{t}}}{l_{\mathrm{t}}(t)}\right) \tag{3.1.20}$$

and

$$\beta_{\mathrm{v}}(t) = \arctan\left(\frac{z_{\mathrm{tgt}}(t) - h_{\mathrm{r}}}{l_{\mathrm{r}}(t)}\right). \tag{3.1.21}$$

Where $l_t(t)$ and $l_r(t)$ have been previously defined in (3.1.14) and (3.1.15). ψ is the angle the target velocity vector (v_x, v_y) component makes with the line joining antenna bases, expressed by,

$$\psi = \arctan\left(\frac{|v_x|}{|v_y|}\right). \tag{3.1.22}$$

In order to calculate the FSCS in the direction of the receiver for a given point along the trajectory, the effective length l_{tgt}^{eff}, height h_{tgt}^{eff} and thus area A_{tgt}^{eff} of the target perpendicular to the incident wave must be calculated, this is highlighted in one dimension in Figure 3.1-13.

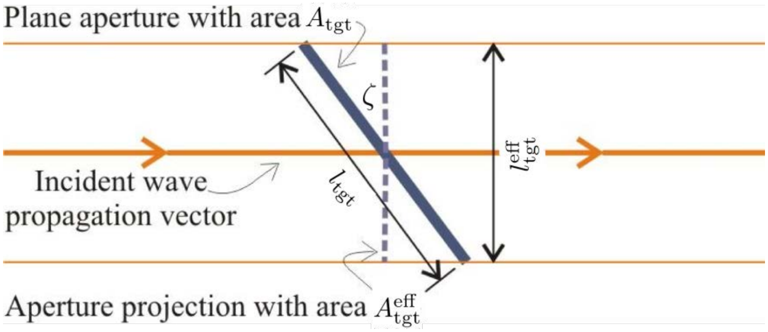

Figure 3.1-13. Idea of target effective dimension l_{tgt}^{eff} and area A_{tgt}^{eff}, perpendicular to the incident beam.

In Figure 3.1-13, ζ is the angle the target makes with the perpendicular to the incident wave beam. So as the plate target progresses in its motion, the FSCS directed towards the receiver is defined by the aforementioned transmitter and receiver view angle variation over time. Figure 3.1-14 shows the geometries required for calculation. Figure 3.1-14(a)-(c) show the plan view of three different parts of the target trajectory for a target originating in the $-x$ dimension, travelling with positive x and y velocity components, all other FSR trajectories can be derived from this due to symmetry. (d) gives the side on view of the trajectory. All variables relating to the figure have been previously described, except $\zeta_{h/v}$

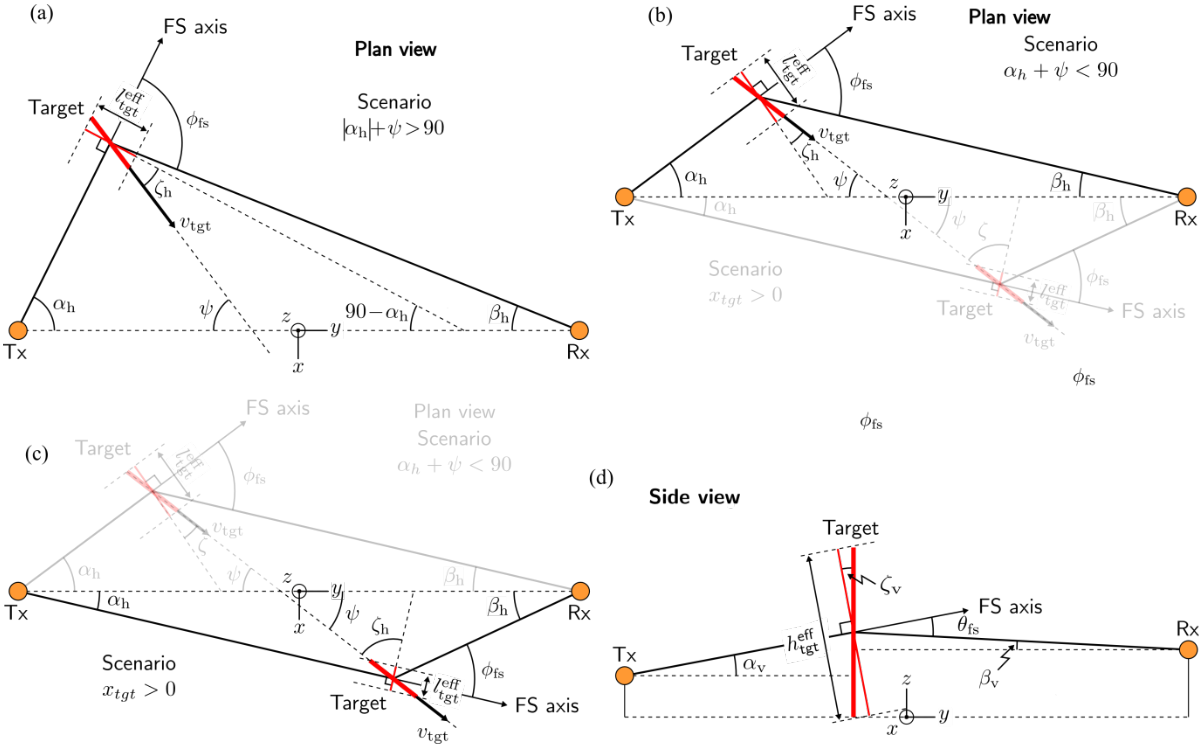

Figure 3.1-14. Geometries for the calculation of the received component of the FSCS pattern of a moving target, originating in the $-x$ dimension with positive x, y velocity components; (a) through (c) show plan views for different sections of the trajectory. Side on view parameters in (d).

Which relates to ζ in Figure 3.1-13 and $\theta_{\rm fs}$ and $\phi_{\rm fs}$ which are the azimuth and elevation angles from the FS axis to the receiver. These are in fact the FSCS pattern angles, corresponding to those in the aperture antenna descriptions in Section 2.2 and from the figure can be calculated as:

$$\phi_{\rm fs}(t)=\alpha_{\rm h}(t)+\beta_{\rm h}(t) \tag{3.1.23}$$

and

$$\theta_{\rm fs}(t)=\alpha_{\rm v}(t)+\beta_{\rm v}(t). \tag{3.1.24}$$

For completeness, Figure 3.1-14(a) shows the part of the trajectory where $|\alpha_h|+\psi>90^\circ$. In this case,

$$\zeta_{\rm h}(t)=\psi+\alpha_{\rm h}(t)-90 \quad \left(\text{for } \alpha_h(t)+\psi>90\right) \ [^\circ]. \tag{3.1.25}$$

Figure 3.1-14(b) shows the trajectory where $\alpha_h + \psi < 90°$ and (c) the continuation of this to $+x$. In these cases,

$$\zeta_{\mathrm{h}}(t) = 90 - \psi + \alpha_{\mathrm{h}}(t) \ [°], \tag{3.1.26}$$

which also accounts for the sign change in α_{h} as the target crosses the baseline. The geometry of Figure 3.1-14(d) gives,

$$\zeta_{\mathrm{v}}(t) = \alpha_{\mathrm{v}}(t). \tag{3.1.27}$$

Thus it is now possible to calculate the effective length $l_{\mathrm{tgt}}^{\mathrm{eff}}(t)$, height $h_{\mathrm{tgt}}^{\mathrm{eff}}(t)$ of the planar target over the course of the trajectory:

$$l_{\mathrm{tgt}}^{\mathrm{eff}}(t) = l_{\mathrm{tgt}} \cos\left(\zeta_{\mathrm{h}}(t)\right), \tag{3.1.28}$$

$$h_{\mathrm{tgt}}^{\mathrm{eff}}(t) = h_{\mathrm{tgt}} \cos\left(\zeta_{\mathrm{v}}(t)\right) = h_{\mathrm{tgt}} \cos\left(\alpha_{\mathrm{v}}(t)\right), \tag{3.1.29}$$

In any general measurement scenario, the shape of the target is *a priory* unknown, it is not possible to simulate the FSCS for all target shape possibilities and indeed not computationally efficient and so calculation of the received values of the FSCS are performed using the shapes with analytical patterns. The effective area of the aperture/plate target is dependent on the shape of target chosen, for the rectangular shape, it is given by

$$A_{\mathrm{rect}}^{\mathrm{eff}}(t) = l_{\mathrm{tgt}}^{\mathrm{eff}}(t) h_{\mathrm{tgt}}^{\mathrm{eff}}(t). \tag{3.1.30}$$

Or for an elliptical shaped target,

$$A_{\mathrm{elip}}^{\mathrm{eff}}(t) = \frac{\pi}{4} l_{\mathrm{tgt}}^{\mathrm{eff}}(t) h_{\mathrm{tgt}}^{\mathrm{eff}}(t). \tag{3.1.31}$$

It is now possible to write down the forms for the FSCS in the direction of the receiver for both a rectangular and elliptical shaped target using the equations for the aperture antenna patterns, (2.2.7) and (2.2.13), combined with the equation for the maximal FSCS (2.10.1) and those derived in this subsection. Such that for the rectangular target,

$$\sigma_{\text{fs}}^{\text{rect}}\left(t\right)=4\pi\left(\frac{A_{\text{rect}}^{\text{eff}}\left(t\right)}{\lambda}\right)^{2}\text{sinc}^{2}\left(\frac{kh_{\text{tgt}}^{\text{eff}}\left(t\right)}{2}\sin\phi_{\text{fs}}\left(t\right)\right)\text{sinc}^{2}\left(\frac{kl_{\text{tgt}}^{\text{eff}}\left(t\right)}{2}\sin\theta_{\text{fs}}\left(t\right)\right)\quad(3.1.32)$$

and for the elliptical target,

$$\sigma_{\text{fs}}^{\text{elip}}\left(t\right)=4\pi\left(\frac{A_{\text{elip}}^{\text{eff}}\left(t\right)}{\lambda}\right)^{2}\left[\frac{2J_{1}\left(k\sqrt{l_{\text{tgt}}^{\text{eff}}\left(t\right)^{2}\sin^{2}\theta_{\text{fs}}\left(t\right)+h_{\text{tgt}}^{\text{eff}}\left(t\right)^{2}\sin^{2}\phi_{\text{fs}}\left(t\right)}\right)}{k\sqrt{l_{\text{tgt}}^{\text{eff}}\left(t\right)^{2}\sin^{2}\theta_{\text{fs}}\left(t\right)+h_{\text{tgt}}^{\text{eff}}\left(t\right)^{2}\sin^{2}\phi_{\text{fs}}\left(t\right)}}\right]^{2}.\quad(3.1.33)$$

Now the received FSCS pattern of an extended target is calculable and the Doppler signature of a point target is known from (3.1.10) the two can be combined. Figure 3.1-15 shows the FCSC pattern (a) and that pattern as applied to the phase signature (b) of Figure 3.1-10 for a 2.5 m long, 1 m high rectangular target—(c) and (d) gives the equivalent when simulated with an elliptical target of the same dimensions. The full formation of the fundamental target signature can therefore be seen as being created from two processes, the progress of the target through Fresnel zones giving the phase signature and the diffractive processes (which are Fraunhoffer like in the far field) of the scattering from the 'aperture' target forming the signal envelope. This is shown pictorially in Figure 3.1-16, where the target progresses across the FSR baseline through the Fresnel zones causing the peaks and troughs in the phase signature, with the directive FSCS pattern providing the envelope modulation. The phase gives information on the target trajectory, and the envelope gives information on the target itself, size and even shape.

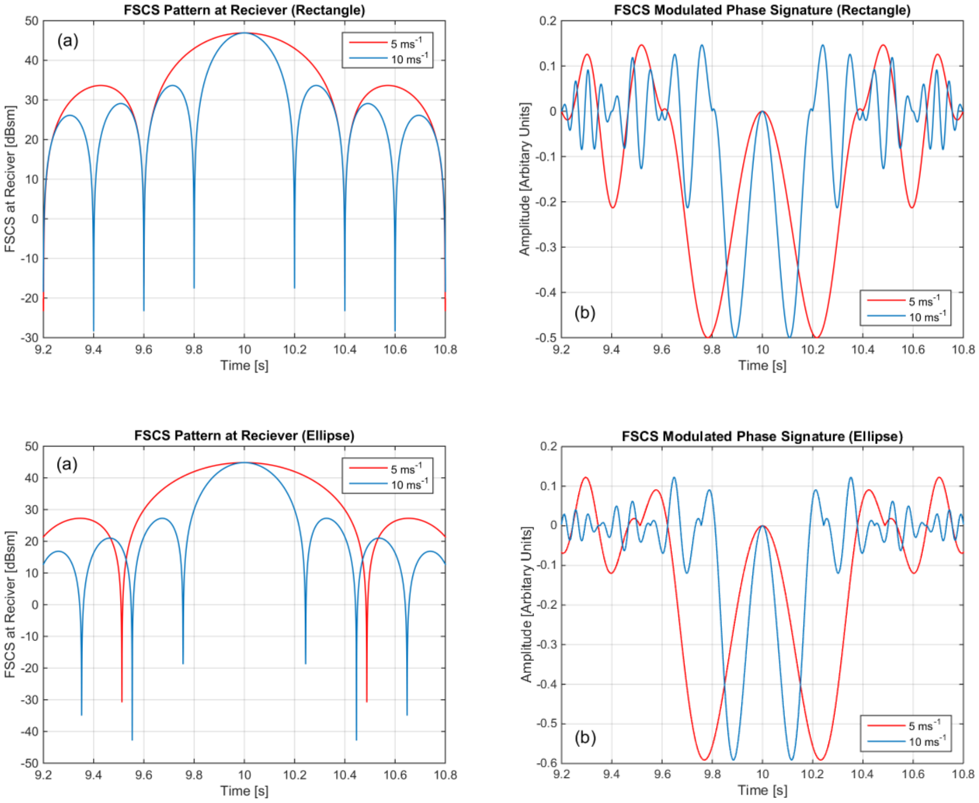

Figure 3.1-15. FSCS pattern at receiver (a)(c) and phase signatures from Figure 3.1-10 modulated according to FSCS pattern (b)(d).

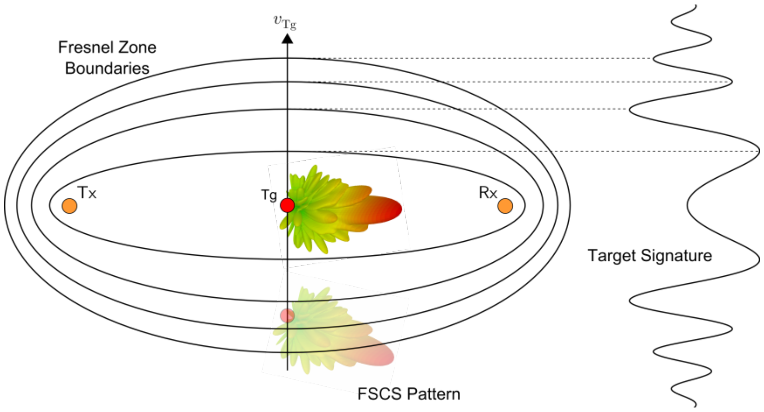

Figure 3.1-16. Target signature as a consequence of the constructive and destructive interference as the target travels through consecutive Fresnel zones combined with the envelope imposed by the FSCS (Fraunhofer like aperture diffraction) pattern.

3.1.5 VERIFICATION OF FORWARD SCATTER PHENOMENON IN A CONTROLLED ENVIRONMENT—EXPERIMENTAL STUDY IN ANECHOIC CHAMBER

A set of controlled FSR experiments were performed in an anechoic chamber. The main purpose of which was to confirm the phenomenological principles underlying FSR which have been described in this section (Section 3.1) thus far. The measurements and analysis shown here are a part of the author's contributions to publications [26] and [41]. By comparing signatures from absorbing and metallic targets with similar silhouettes, the independence of the shadow radiation from the actual target shape and material could be investigated. The targets used consisted of two types, cylinder and rectangular plate, each consisting of one metallic and one covered with absorbing material (Laird Technologies Q-Sorb RFSB 1062 [40]) with peak of absorption at 5.46 GHz (5.5 cm wavelength). The absorbing material will also help to reduce any bistatic reflections. The experimental setup is shown in Figure 3.1-17, where a polystyrene rail was setup along which to pull the targets to ensure the same trajectory on each test. Speed data for the target was measured through comparing timestamps on video recordings with distance markers on the rail—further details

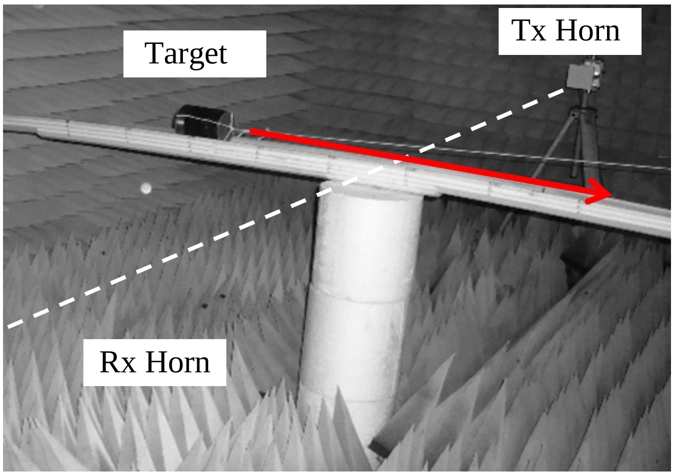

Figure 3.1-17. Anechoic chamber experimental setup to test FSR phenomenology. Red arrow shows direction of target motion, dashed line indicates the FSR baseline. Figure adapted from [26].

can be found in [26] and [41]. The Tx and Rx were positioned at distance of 4.25 m apart to provide far field operation. All targets have the same rectangular cross sections of 9 x 13 cm (height x length) in order to make effective comparisons between the recorded signatures. The dimensions also infer that the scattering regime for this experimental setup lies between the Mie and Optical regions. Recorded Doppler signatures—received signal strength indicator (RSSI) signals with leakage subtracted— are shown in Figure 3.1-18 (a) and (b) for absorbing and metallic cylinders and in Figure 3.1-19 (a) and (b) for absorbing and metallic plates. Using the previous sub-section signal model, a signature has been simulated for the plate for comparison in (c).

From comparison of Figure 3.1-18(a),(b) and Figure 3.1-19(a),(b) it can be seen that around the forward scatter region at 180° (the FS main lobe region), the amplitudes of the signatures for all target shapes and materials coincide very well with each other. The envelopes shown in Figure 3.1-18 are formed by applying a low pass filter to the signature magnitude, and are solely included here to highlight the main lobe region similarity between the absorbing and metallic targets. The similarity of the results of these comparative measurements validates the approximation that the target signal in the FS region is independent of the complete 3D object shape and material. It depends purely on the silhouette shape, agreeing with the 'Shadow Contour Theorem' stated in 3.1.1. As the bistatic angle tends away from the main lobe, in regions say less than 160° and greater than 200°, the amplitude of the signal from the absorbing cylinder in Figure 3.1-18 decreases. While for the metallic cylinder the amplitude remains reasonably constant. This difference indicates the transition from FS to bistatic reflections in the metallic case due to lack of absorbing cover, which supresses these reflections in the absorbing case.

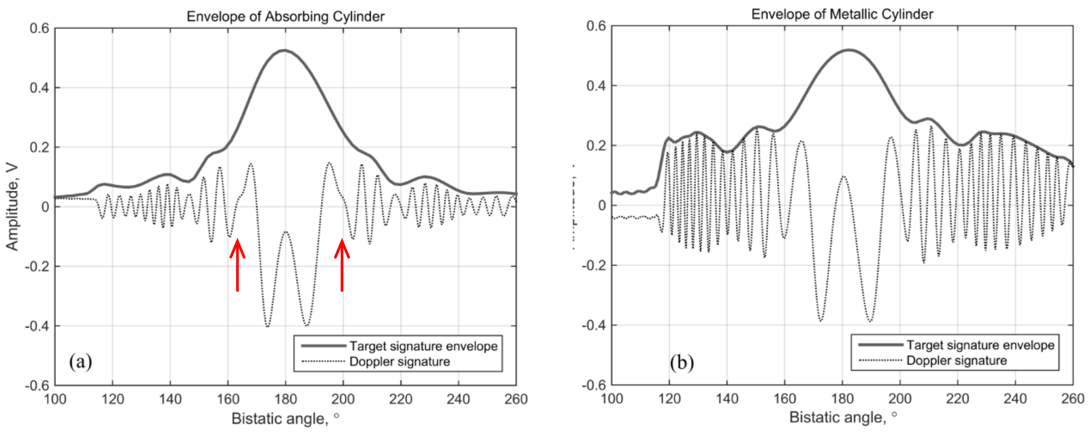

Figure 3.1-18. Experimental comparison of FSR signatures of similar dimension absorbing (a) and metallic (b) cylinders. Target signature envelope is formed by application of a low-pass filter to the Doppler signature magnitude. This is added to indicate similarity of the Doppler signal amplitude and structure in the forward scatter region. Phase discontinuities from FS main lobe to side lobe transition are arrowed in red Figure adapted from [26].

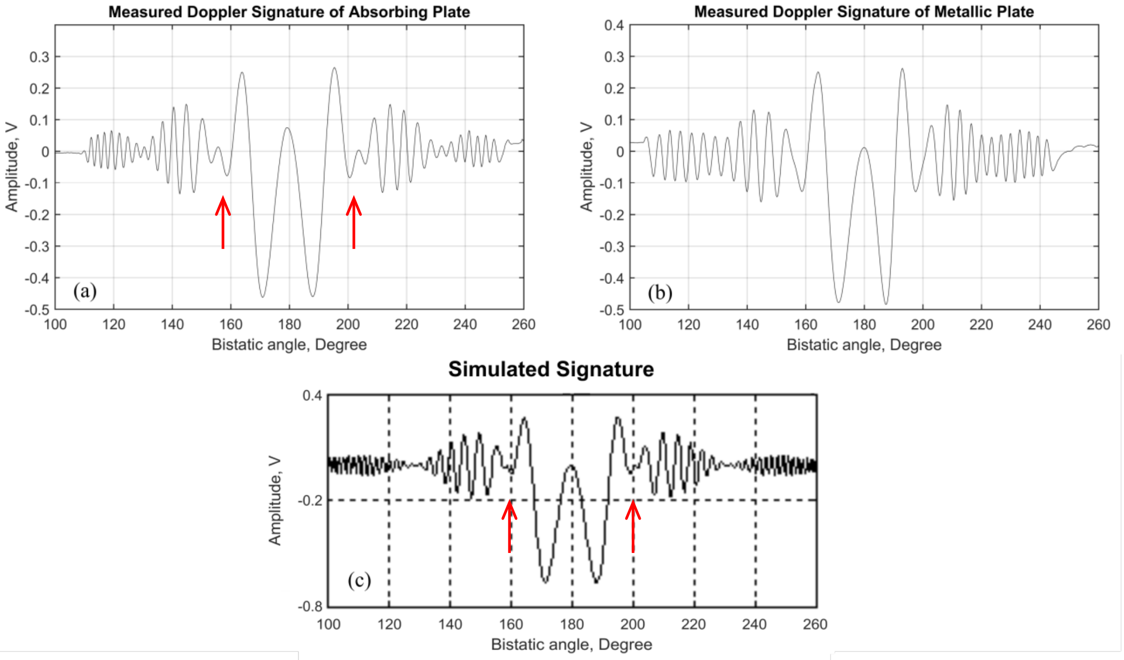

Figure 3.1-19.Experimental comparison of FSR signatures of similar dimension absorbing (a) and metallic (b) plates. Simulated signature for 'absorbing' plate (c), based on previously derived FSR signal model. Phase discontinuities from FS main lobe to side lobe transition are arrowed in red. Figure is adapted from [26].

This effect is less prevalent in the plate experiment (Figure 3.1-19) where the bistatic reflections are reduced due to the thinness of the target, and the signatures of absorbing and metallic structures maintain similarity over a wider angle. Phase discontinuities may be observable in the signals around 160° (and symmetrically 200°) which indicate transition between FSCS main and side shadow lobes, these are more obscured in the metallic cases due to the additional bistatic reflections. When they are visible, the discontinuities are marked on the figures with red arrows. One final remark is that the simulated signal of Figure 3.1-19(c) coincides with the measured signature of the absorbing plate, as would be expected from the shadow field based FSR signal model using a rectangular aperture target approximation. These measurements provide at least partial verification for its accuracy and use.

To highlight the benefit of using FSR to detect stealth targets, records have been made of the same cylinder targets using a monostatic radar configuration. Tx and Rx antennas were placed next to each other with enough separation to provide adequate isolation and the targets performed the same trajectory as in the previous experiments. The recorded signatures are found in Figure 3.1-20.

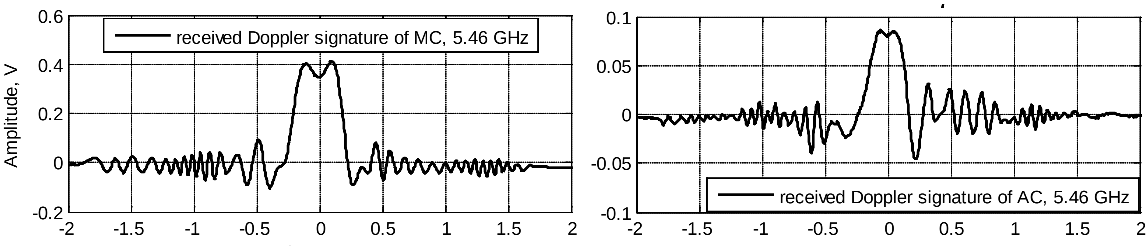

(a) (b)

Figure 3.1-20. Monostatic signatures of the metallic (a) and absorbing (b) cylinders. Figure adapted from [26].

A dramatic reduction of 14 dB of the peak backscattered power is seen when comparing the metallic and absorbing targets and highlights the difficulty posed by stealth targets in monostatic radar.

3.1.6 EFFECT OF TARGET DIMENSION ON SCATTERING

The previous descriptions of target signature formation in this section have been related to a specific scattering mechanism from the target i.e. Fraunhofer diffraction, from the equivalent aperture. Target signatures have however been measured in the maritime environment for cases where the receiver is not in the far-field region of the target due to the target size. The Fresnel parameter S can be used to classify the scattering region,

$$S = \frac{l_{eff}^{\;2}}{4\lambda}, \tag{3.1.34}$$

in which l_{eff} is the largest effective dimension of the target object. Thus in the Fraunhofer region $d \gg S$ and for the Fresnel diffraction region $d \approx S$, where d is the distance from target to receiver. Maritime target signatures were recorded for a 300 m base line at 7.5 GHz and the targets were approximately base line mid-point crossing. The experimental data gathering and subsequent analysis shown here are a part of the author’s contributions to publications [26] and [41]. The targets and corresponding signatures are shown in Figure 3.1-21. Figure 3.1-21(a) shows a small co-operative target (inflatable boat) estimated $S = 60$ m and so in the Fraunhofer diffraction region. It can be seen here that the direct path/leakage signal is essentially larger than and modulated by the scattered signal—as in the phenomenology/derivations thus far. A larger sail boat in (b) has an estimated $S = 160$ m, which is on the Fraunhofer/Fresnel diffraction boundary for the given baseline. The leakage signal is comparable to the target scattered signal. (c) defines the case where full signal blocking occurs (here $S = 630$ m). In (b) and (c) it is still possible to see the typical passage through the Fresnel zones at the leading and trailing edges of the target signature.

The largest targets are obviously detectable; however it is only the smaller target (a) for which any motion parameter data may be gained from the phase/Doppler structure of the signal.

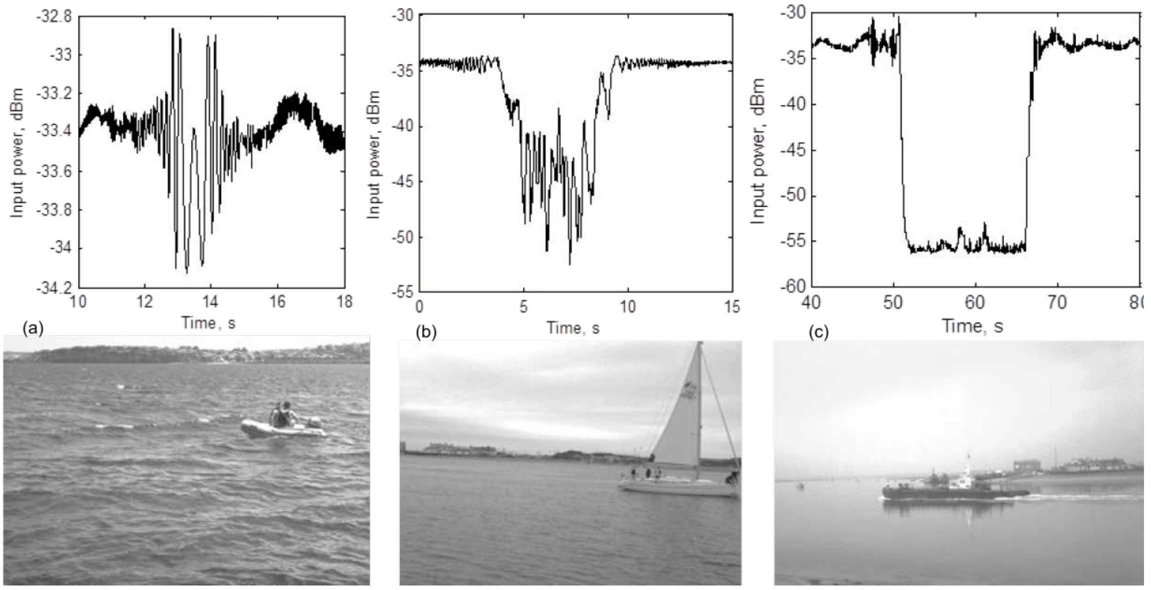

Figure 3.1-21. Recorded maritime FSR signatures of targets crossing the middle of a baseline of length *d* = 300 m. a) small inflatable boat, b) medium size yacht and c) large motor boat. Figure reproduced from [26].

The scattering mechanism also has dependence on the aspect angle of the target, as this will determine the dimension of the target presented to the FSR baseline. A long boat target for example, may present a much smaller target dimension if drifting sideways through the FSR baseline. The fundamental scattering mechanism may then change.

3.2 FORWARD SCATTER RADAR POWER BUDGET FOR SURFACE TARGETS

The previous section made an attempt to explain the major phenomenology behind FSR and the fundamental target signature formation. However for useful estimation of power budget, the effects of propagation must obviously be included. In this section a more in depth description of the signature formation is described with regard to estimating the received power, incorporating propagation losses/effects. The fundamentals of this analysis are related to the basic link budget models of free space and two-ray path propagation, but with further adaptation to not only include point to point links, but FSR targets as well. A similar description can be found in [42], however, the derivation is important in understanding propagation in FSR, here it is extended to take into account the full FSCS aperture description and potential effects to consider in propagation over the sea surface.

3.2.1 POWER BUDGET IN FREE SPACE

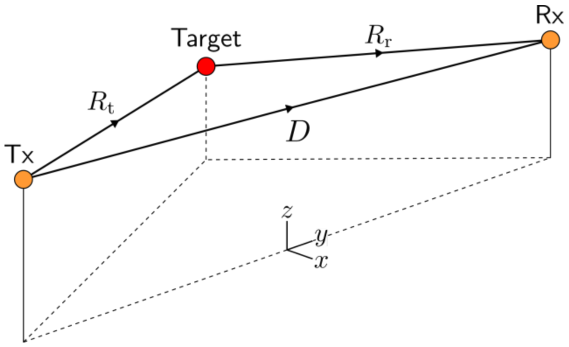

Figure 3.2-1. Free space propagation topology, consisting of two paths, one direct/leakage between antennas and one via target.

If we consider the scenario as in Section 3.1 and the diagram in Figure 3.2-1, the power budget calculation for free space propagation relies on two paths. One being the line of sight (LOS) between antennas, over a distance D, the other being the path via the target, with range $R_t + R_r$. The LOS signal power at the receiver input can be described by the standard free space communications point to point link budget equation. This is known as the Friis equation [43] and takes the form,

$$P_{\mathrm{lkg}}^{\mathrm{fsp}} = P_t G_t G_r \left(\frac{\lambda}{4\pi D}\right)^2 = P_t G_t G_r L_{\mathrm{fsp}}. \tag{3.2.1}$$

$P_{\mathrm{lkg}}^{\mathrm{fsp}}$ is the power at the receiver input/receive antenna output. In this radar analysis, we will term the direct path/LOS signal as the antenna leakage signal, labelled here as lkg and free space is abbreviated to fsp to avoid confusion with the use of fs for forward scatter. P_{t} is the transmitter power, $G_{\mathrm{t/r}}$ are the transmit and receive antenna gains, D is the baseline distance between antennas and λ is the wavelength of the transmitted signal. L_{fsp} is termed the free space loss. This equation is somewhat a misguiding, as it indicates that propagation through a vacuum has some loss properties which are dependent on wavelength, this dependence however comes from the definition of the receiving antenna gain (as given in Section 2.2) and (3.2.1) can be written thus,

$$P_{\mathrm{lkg}}^{\mathrm{fsp}} = \overbrace{\underbrace{\frac{P_{\mathrm{t}}}{4\pi D^2}}_{\substack{\text{Isotropic}\\ \text{source radiation}}} G_{\mathrm{t}}}^{\substack{\text{Power density at}\\ \text{distance } d \text{ from source}}} A_{\mathrm{r}} . \tag{3.2.2}$$

Where A_{r} is the receive antenna effective aperture/area.

$$A_{\mathrm{r}} = \frac{\lambda^2 G_{\mathrm{r}}}{4\pi} \tag{3.2.3}$$

The first part of (3.2.2) is the isotropic radiation factor, it gives the power density [Wm^{-2}] at a radial distance D from an isotropic source, i.e. the source power distributed over the surface area of a sphere of radius D. The antenna gain G_{t} increases (or indeed can decrease in a null) the power density in a given direction and then the effective area of the receiving antenna, A_{r}, intercepts a proportion of this.

The received power for the path to the receiver via the target can be found following the same procedure, however the antenna receiving aperture is replaced by the target cross section. One definition of the cross section is that it can be seen as the area over which if the intercepted power were re-radiated isotropically, then it would deliver the same power at the receiver as the target itself. Thus, on interception with the target, the signal can be seen as then re-radiating isotropically (spherically) towards the receiver which then again intercepts a proportion of the radiated power given by the antenna effective area. The power received at the antenna from the target scattered path is then given by,

$$P_{\mathrm{tgt}}^{\mathrm{fsp}} = \underbrace{\overbrace{\underbrace{\frac{\mathrm{P_t}}{4\pi \mathrm{R_t^2}}}_{\substack{\text{Isotropic}\\ \text{source radiation}}} \mathrm{G_t}\sigma}^{\substack{\text{Effective power}\\ \text{intercepted by target}}} \frac{1}{4\pi \mathrm{R_r^2}}}_{\substack{\text{Power density at receive antenna from}\\ \text{isotropic re-radiation from target}}} A_{\mathrm{r}} = \frac{\mathrm{P_t G_t G_r}\lambda^2\sigma}{(4\pi)^3 \mathrm{R_t^2 R_r^2}}. \tag{3.2.4}$$

This is the well-known free space bistatic radar equation (Section 2.4). Thus it is now possible to give forms for the amplitude parameters V_{lkg} and V_{tgt} in (3.1.8) through the blind use of ohms law. The instantaneous voltage amplitude V at the receive antenna output (input to receiver) is given by:

$$V = \sqrt{PZ}\ . \tag{3.2.5}$$

P is the instantaneous power and Z is the system impedance, in most common radar systems $Z = 50$ Ω. The free space case relates directly to the anechoic chamber experiments in section 3.1.

3.2.2 POWER BUDGET IN THE TWO-RAY PATH MODEL

The two-ray path propagation model [44] is the most basic model for incorporating multipath into calculation of propagation loss. In the two-ray path model, not only is the direct LOS signal considered as in the above example, but also a single ground specular reflected ray (under the assumption of flat ground). This multi-path propagation is vital for describing power budget over the sea surface

3.2.2.1 *LEAKAGE SIGNAL*

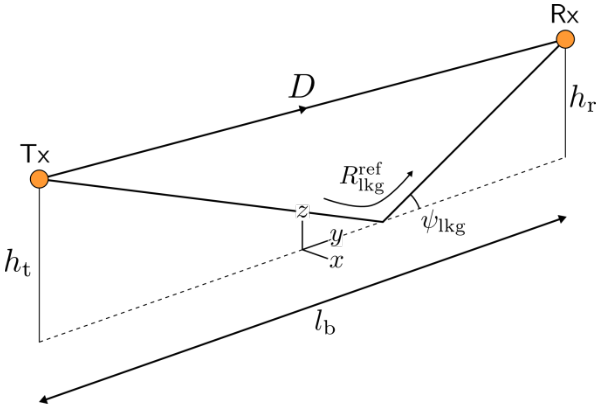

Figure 3.2-2. Geometry for leakage signal calculation in the two-ray path propagation model.

The scenario for the leakage signal, in this model which includes a ground reflected ray is shown in Figure 3.2-2; the field at the receiver is due to the sum of the direct path ray of length D and the ground reflected ray of length R^{ref}_{lkg}. The ground reflected ray travels a longer distance than the direct and therefore a comparative phase change is introduced due to its extra path length (much like the formulation of the target phase signature in Section 3.1). This extra distance travelled will also mean that the reflected ray amplitude will be reduced at the receiver in comparison to the direct path, the reduction depending on the antenna heights. There will also be phase and amplitude variation introduced by the specular surface reflection; these effects are described by the surface reflection coefficients.

The surface reflection coefficients [45], [44] are dependent on the grazing angle ψ (labelled as ψ_{lkg} in Figure 3.2-2), surface material properties and polarisation of the incident wave. For horizontally polarised waves, the reflection coefficient Γ_h is given by:

$$\Gamma_{\mathrm{h}} = \frac{\sin\psi - \sqrt{(\varepsilon_{\mathrm{r}} - ix) - \cos^2\psi}}{\sin\psi + \sqrt{(\varepsilon_{\mathrm{r}} - ix) - \cos^2\psi}}, \tag{3.2.6}$$

and for vertically polarised waves:

$$\Gamma_{\mathrm{v}} = \frac{(\varepsilon_{\mathrm{r}} - ix)\sin\psi - \sqrt{(\varepsilon_{\mathrm{r}} - ix) - \cos^2\psi}}{(\varepsilon_{\mathrm{r}} - ix)\sin\psi + \sqrt{(\varepsilon_{\mathrm{r}} - ix) - \cos^2\psi}}, \tag{3.2.7}$$

where $$x = \frac{\sigma}{2\pi f \varepsilon_0}. \tag{3.2.8}$$

In the above equations, ε_{r} and σ are the relative permittivity and conductivity [Sm^{-1}] of the surface material respectively. f is the wave frequency and ε_0 is the permittivity of free space, the factor $\varepsilon_{\mathrm{r}} - ix$ is also known as the complex relative permittivity. In order to have a visual insight into the behaviour of the reflection coefficient, some specific examples are calculated. The relative permittivity and conductivity for three surface types, dry ground, wet ground and sea water [43] are shown in Table 3.2-1.

Table 3.2-1. Table of relative permittivity's and conductivities for three surface 'materials'.

Surface Type	**Relative Permittivity** ε_{r}	**Conductivity** σ **[Sm^{-1}]**
Dry Ground	15	5×10^{-3}
Wet Ground (Average)	27.5	2×10^{-2}
Sea Water (Average)	81	5

Figure 3.2-3 shows the horizontal reflection coefficient magnitude (a) and phase (b) for the extreme cases of the shown surface types, dry ground and sea water at different frequencies.

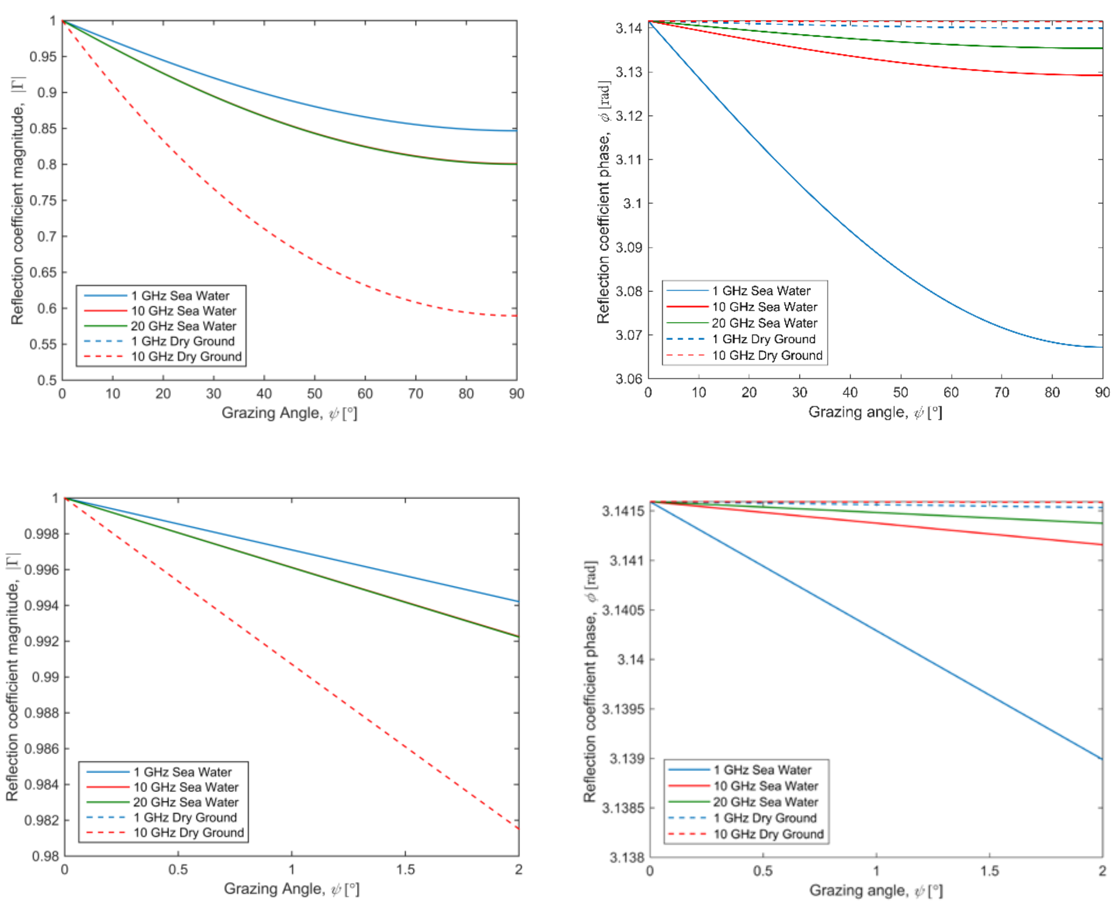

Figure 3.2-3. Reflection coefficient for dry ground and sea water. (a) shows magnitude and (b) phase for the three surface materials. Note that in the magnitude plots the 10 GHz and 20 GHz sea water curves are coincident, as too are the curves for dry ground. (c) showns zoomed magnitude and (d) the zoomed phase for small grazing angles.

It can be seen that for very low grazing—as is expected in the ground based FSR with grazing angles definitely below 2°—we can expect that for most surface types the reflection coefficient magnitude ρ is approximately 1 and the phase ϕ is approximately π radians i.e. the reflection coefficient $\Gamma = -1$. Even so, further derivations will include the use of the full reflection coefficient and after this, simplifications may be made.

To account for the interference of the propagating signals in the two-ray path model, it is important to consider not just the power, but the magnitudes and phases of the signals. The relationship between power density and the electric field strength magnitude (in the far field) in free space are related by the impedance of free space η, by,

$$E = \sqrt{P\eta}\ , \tag{3.2.9}$$

where $\eta = 120\pi$. So, if we reconsider the first part of (3.2.2) it is possible using (3.2.9) to write the electric field strength E_{dp} for the direct path ray (Figure 3.2-2) at a distance D from the source (transmitter),

$$\left|E_{\mathrm{dp}}\right| = \sqrt{\frac{P_{\mathrm{t}}G_{\mathrm{t}}}{4\pi D^2}\eta}\ . \tag{3.2.10}$$

Thus it is then possible to write a form of the oscillating direct path ray, when considering a CW transmitted signal,

$$E_{\mathrm{dp}} = \left|E_{\mathrm{dp}}\right| \mathrm{e}^{i(2\pi ft - kD + \phi_{\mathrm{i}})} = \left|E_{\mathrm{dp}}\right| \mathrm{e}^{-ikD}\ , \tag{3.2.11}$$

where ϕ_{i} is some initial phase term. It is possible to neglect this and any time dependence in the oscillatory part of the signal as all considered paths originate from the common transmitter and so oscillate with the same time dependence and have same initial phase. The signal for the ground reflected path in Figure 3.2-2 can be written in a similar way, this time including the reflection coefficient Γ and the total reflected path length $R^{\mathrm{ref}}_{\mathrm{lkg}}$ from Tx – ground – Rx,

$$E^{\mathrm{ref}}_{\mathrm{lkg}} = \sqrt{\frac{P_{\mathrm{t}}G_{\mathrm{t}}}{4\pi\left(R^{\mathrm{ref}}_{\mathrm{lkg}}\right)^2}\eta} \cdot \Gamma\left(\psi_{\mathrm{lkg}}\right) \mathrm{e}^{-ikR^{\mathrm{ref}}_{\mathrm{lkg}}} = \left|E^{\mathrm{ref}}_{\mathrm{lkg}}\right| \cdot \Gamma\left(\psi_{\mathrm{lkg}}\right) \mathrm{e}^{-ikR^{\mathrm{ref}}_{\mathrm{lkg}}}\ , \tag{3.2.12}$$

where,

$$R^{\mathrm{ref}}_{\mathrm{lkg}} = \sqrt{l_b^{\ 2} + \left(h_{\mathrm{t}} + h_{\mathrm{r}}\right)^2}\ , \tag{3.2.13}$$

with

$$l_{\mathrm{b}}^{\ 2} = D^2 - \left(h_{\mathrm{t}} - h_{\mathrm{r}}\right)^2 . \tag{3.2.14}$$

The grazing angle ψ, which is required for the calculation of Γ, can be found from Figure 3.2-2, using:

$$\psi_{\mathrm{lkg}} = \arcsin\left(\frac{h_{\mathrm{t}} + h_{\mathrm{r}}}{R_{\mathrm{lkg}}^{\mathrm{ref}}}\right) = \arctan\left(\frac{h_{\mathrm{t}} + h_{\mathrm{r}}}{l_{\mathrm{b}}}\right). \tag{3.2.15}$$

The total field at the receiver $E_{\mathrm{lkg}}^{\mathrm{trp}}$ is the sum of the two fields,

$$E_{\mathrm{lkg}}^{\mathrm{trp}} = E_{\mathrm{dp}} + E_{\mathrm{lkg}}^{\mathrm{ref}} = \left|E_{\mathrm{dp}}\right| \mathrm{e}^{-ikD} + \left|E_{\mathrm{lkg}}^{\mathrm{ref}}\right| \cdot \Gamma\left(\psi_{\mathrm{lkg}}\right) \mathrm{e}^{-ikR_{\mathrm{lkg}}^{\mathrm{ref}}}. \tag{3.2.16}$$

Commonly the above equation is simplified for calculation of low grazing angles, $D \gg h_{\mathrm{t}}, h_{\mathrm{r}}$, the reflection coefficient is approximated to $\Gamma = -1$ (independent of polarisation as shown previously), and due to the similar length of the two paths involved, $\left|E_{\mathrm{ref}}\right| \approx \left|E_{\mathrm{dp}}\right|$, resulting in:

$$\left|E_{\mathrm{lkg}}^{\mathrm{trp}}\right| = 2\left|E_{\mathrm{dp}}\right| \sin\left(\frac{2\pi h_{\mathrm{t}} h_{\mathrm{r}}}{\lambda D}\right) = 2\sqrt{\frac{P_{\mathrm{t}} G_{\mathrm{t}}}{4\pi D^2}\eta}\, \sin\left(\frac{2\pi h_{\mathrm{t}} h_{\mathrm{r}}}{\lambda D}\right). \tag{3.2.17}$$

Note that the antenna gains are assumed equal for both direct and ground reflected rays. Using (3.2.9) this can be re-converted into a power density at the receive antenna. Then as with the free space derivation, using the antenna effective area/gain relationship, the received power is given by:

$$\begin{aligned} P_{\mathrm{lkg}}^{\mathrm{trp}} &= \frac{\left|E_{\mathrm{lkg}}^{\mathrm{trp}}\right|^2}{\eta} A_{\mathrm{r}} = 4\frac{P_{\mathrm{t}} G_{\mathrm{t}}}{4\pi D^2} \sin^2\left(\frac{2\pi h_{\mathrm{t}} h_{\mathrm{r}}}{\lambda D}\right) \frac{G_r \lambda^2}{4\pi} \\ &= 4 P_{\mathrm{t}} G_{\mathrm{t}} G_r \left(\frac{\lambda}{4\pi D}\right)^2 \sin^2\left(\frac{2\pi h_{\mathrm{t}} h_{\mathrm{r}}}{\lambda D}\right) \end{aligned}. \tag{3.2.18}$$

Which for extremely low grazing (small arguments of the $\sin$ function), can be simplified further to give,

$$P_{\mathrm{lkg}}^{\mathrm{trp}} = P_{\mathrm{t}} G_{\mathrm{t}} G_r \left(\frac{h_{\mathrm{t}} h_{\mathrm{r}}}{D^2}\right)^2. \tag{3.2.19}$$

This is the standard equation for two-ray path propagation in communications, indicating an independence on frequency and an inverse 4th power law for distance.

3.2.2.2 *TARGET SIGNAL*

The target power model follows the same general outline as calculating the leakage power, and is shown in Figure 3.2-4. The target case involves the superposition of multiple two-ray path sections. As can be seen in the figure, there are two rays incident on the target, the direct signal from transmitter to target, R_t and the ground reflected ray, $R_\mathrm{t}^\mathrm{ref}$. Each of these produce two rays incident on the receiver, one direct from target to receiver, R_r, and one ground reflected, $R_\mathrm{r}^\mathrm{ref}$. Using the low grazing angle two-ray path leakage signal, described by (3.2.18), the target signal can be derived in a similar way to that of the target signal in the free space approximation. Instead of using the receiver antenna area A_r, the target FSCS is used in its place along with the appropriate ranges and heights, shown in Figure 3.2-4. The target then acts as the transmitter for the second two-ray path section and thus we can write down the equation for the target power at the receiver,

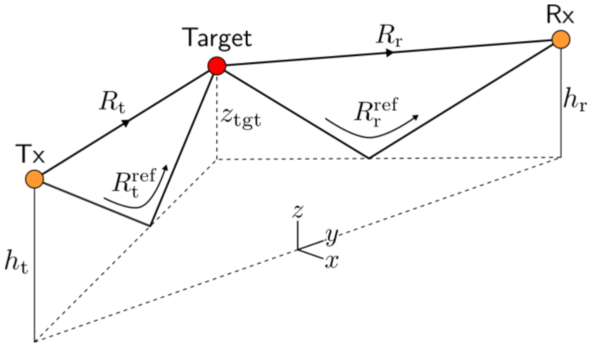

Figure 3.2-4. General outline of topology related to two-ray path calculation of received target power, indicating direct paths and ground reflected paths.

$$
\begin{aligned}
P_{\text{tgt}}^{\text{trp}} &= \overbrace{\underbrace{4\frac{P_{\text{t}}G_{\text{t}}}{4\pi R_{\text{t}}^{2}}\sin^{2}\left(\frac{2\pi h_{\text{t}}z_{\text{tgt}}}{\lambda R_{\text{t}}}\right)}_{\text{Power density at target}}\cdot\sigma_{\text{fs}}\cdot 4\frac{1}{4\pi R_{\text{r}}^{2}}\sin^{2}\left(\frac{2\pi z_{\text{tgt}}h_{\text{r}}}{\lambda R_{\text{r}}}\right)}^{\text{Power density at receive antenna}}\cdot\frac{G_{r}\lambda^{2}}{4\pi} \\
&= 16P_{\text{t}}G_{\text{t}}G_{r}\sigma_{\text{fs}}\frac{1}{R_{\text{t}}^{2}R_{\text{r}}^{2}}\frac{\lambda^{2}}{(4\pi)^{3}}\sin^{2}\left(\frac{2\pi h_{\text{t}}z_{\text{tgt}}}{\lambda R_{\text{t}}}\right)\sin^{2}\left(\frac{2\pi z_{\text{tgt}}h_{\text{r}}}{\lambda R_{\text{r}}}\right)
\end{aligned}
\quad . \tag{3.2.20}
$$

This derivation assumes equal antenna gains and FSCS for both paths. On simplification for extremely low grazing angles,

$$
P_{\text{tgt}}^{\text{trp}} = 4\pi P_{\text{t}}G_{\text{t}}G_{r}\sigma_{\text{fs}}\frac{h_{\text{t}}^{2}h_{\text{r}}^{2}z_{\text{tgt}}^{4}}{\lambda^{2}R_{\text{t}}^{4}R_{\text{r}}^{4}} \tag{3.2.21}
$$

Noting that now the received power goes like an inverse 8th power of the target range and has a 4th power dependence on the target height. It is also possible to derive the case for when the grazing angle is not so small and/or the reflection coefficient is not assumed to be -1. In order to clarify further, the scenario is split visually into four separate groups of rays, Figure 3.2-5(a) and (b) show the rays incident at the Rx due to the direct ray from Tx to target and Figure 3.2-5(c) and (d) shows those due to the reflected path from Tx to target. The total field at the receiver is the sum of the resultant fields these ray groups. It can be seen when comparing Figure 3.2-5(a) with (c) that the path from target to Rx, R_{r}, is the same length, but has differing contribution from the FSCS due to the slightly different target view angles—either α_{v} for (a) or ψ_{t} for (b) from the ground reflection point. The same type of effect occurs for $R_{\text{r}}^{\text{ref}}$ in (b) and (d). This variation in view angle gives different FS axis directions and thus different diffraction/scattering angles, $\gamma_{i,j}$'s, from the FS axis to the two receive paths and also potentially different target effective aperture size.

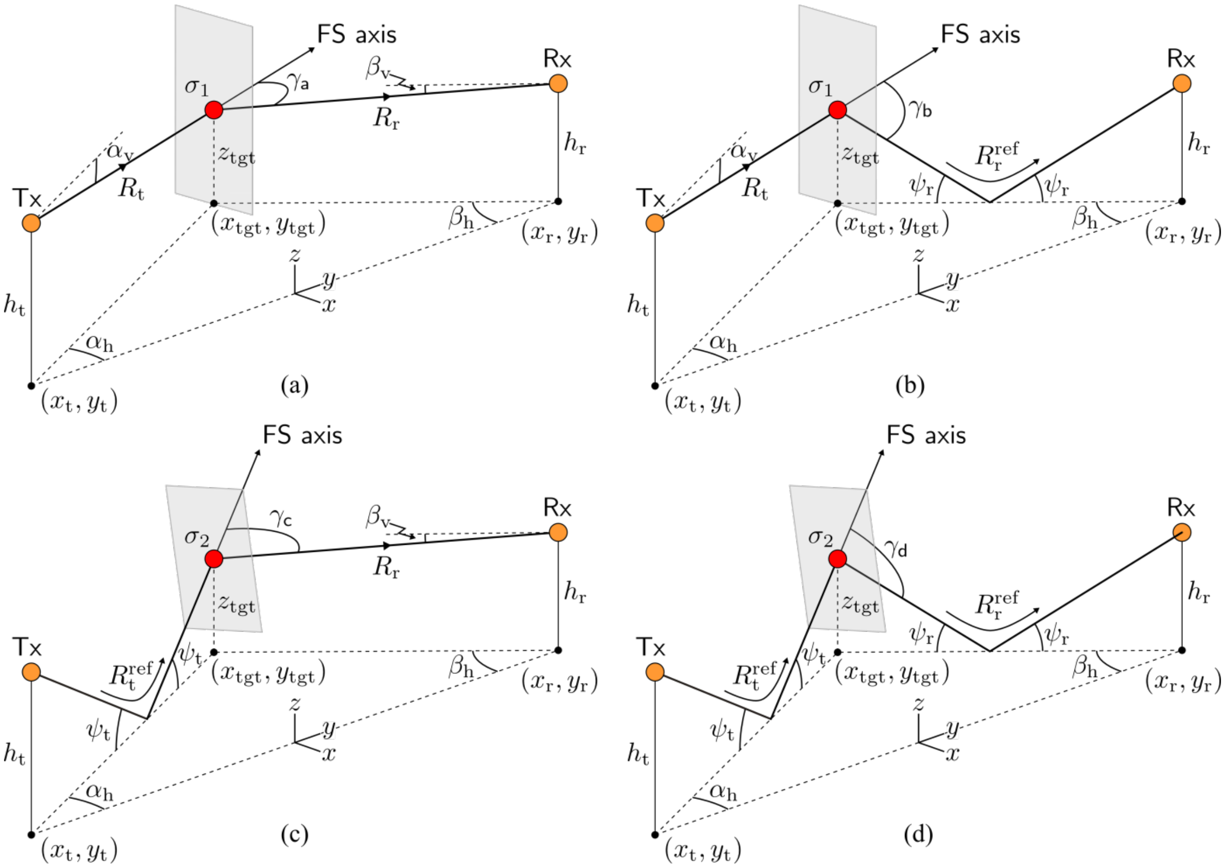

Figure 3.2-5. Parameters for calculation target two-ray path received power. (a) and (b) indicate the rays stemming from the direct path incident ray on target, (c) and (d) indicate the rays developed from the ground bounce incident path.

The scattering angles $\gamma_{i,j}$ are again actually composed of the azimuthal $\phi_{i,j}$ and elevation $\theta_{i,j}$ scattering angles, which correspond to the azimuth and elevation angles relating to the equivalent target aperture antenna pattern. The ray groups will be investigated separately, starting with ray group (a). The scenario in Figure 3.2-5(a) can be broken down further into two paths:

Path (a) $\quad \text{Tx}\xrightarrow{R_t}\text{Target}\xrightarrow{R_r}\text{Rx}$

The received field from path (a) is constructed from the free space target approximation in the same fashion as the leakage power was calculated for the two-ray path model. Using (0.3) and (0.8) an expression for the field at the receive antenna from path (a), $E_{\mathrm{r}}^{\mathrm{a}}$, can be written thus:

$$E_{\mathrm{r}}^{\mathrm{a}} = \sqrt{\frac{\mathrm{P_t G_t}\left(\alpha_{\mathrm{h}}, \alpha_{\mathrm{v}}\right)\sigma_1\left(\gamma_{\mathrm{a}}\right)}{\left(4\pi\right)^2 \mathrm{R_t^2 R_r^2}}}\eta \cdot \mathrm{e}^{-ik\left(R_{\mathrm{t}}+R_r\right)}. \tag{3.2.22}$$

The transmit gain dependence on the view angles of the target (or ground reflection point) is included for completeness. Following a similar logic it is possible to ‘write down’ the field at the receive antenna for each of the other paths, including reflection coefficients where applicable, i.e.,

$$E_{\mathrm{r}}^{\mathrm{b}} = \sqrt{\frac{\mathrm{P_t G_t}\left(\alpha_{\mathrm{h}}, \alpha_{\mathrm{v}}\right)\sigma_1\left(\gamma_{\mathrm{b}}\right)}{\left(4\pi\right)^2 \mathrm{R_t^2}\left(R_{\mathrm{r}}^{\mathrm{ref}}\right)^2}}\eta \cdot \Gamma\left(\psi_{\mathrm{r}}\right)\mathrm{e}^{-ik\left(R_{\mathrm{t}}+R_{\mathrm{r}}^{\mathrm{ref}}\right)}, \tag{3.2.23}$$

$$E_{\mathrm{r}}^{\mathrm{c}} = \sqrt{\frac{\mathrm{P_t G_t}\left(\alpha_{\mathrm{h}}, \psi_{\mathrm{t}}\right)\sigma_2\left(\gamma_{\mathrm{c}}\right)}{\left(4\pi\right)^2 \left(\mathrm{R_t^{ref}}\right)^2 R_{\mathrm{r}}^2}}\eta \cdot \Gamma\left(\psi_{\mathrm{t}}\right)\mathrm{e}^{-ik\left(R_{\mathrm{t}}^{\mathrm{ref}}+R_{\mathrm{r}}\right)}, \tag{3.2.24}$$

$$E_{\mathrm{r}}^{\mathrm{d}} = \sqrt{\frac{\mathrm{P_t G_t}\left(\alpha_{\mathrm{h}}, \psi_{\mathrm{t}}\right)\sigma_2\left(\gamma_{\mathrm{d}}\right)}{\left(4\pi\right)^2 \left(\mathrm{R_t^{ref}}\right)^2 \left(\mathrm{R_r^{ref}}\right)^2}}\eta \cdot \Gamma\left(\psi_{\mathrm{t}}\right)\Gamma\left(\psi_{\mathrm{r}}\right)\mathrm{e}^{-ik\left(R_{\mathrm{t}}^{\mathrm{ref}}+\mathrm{R_r^{ref}}\right)}. \tag{3.2.25}$$

Where,

$$\psi_{\mathrm{t}} = \arctan\left(\frac{h_{\mathrm{t}} + z_{\mathrm{tgt}}}{l_t}\right), \tag{3.2.26}$$

$$\psi_{\mathrm{r}} = \arctan\left(\frac{h_{\mathrm{r}} + z_{\mathrm{tgt}}}{l_r}\right), \tag{3.2.27}$$

$$R_t^{\mathrm{ref}} = \sqrt{l_t^{\,2} + \left(h_{\mathrm{t}} + z_{\mathrm{tgt}}\right)^2}\ , \tag{3.2.28}$$

$$R_r^{\mathrm{ref}} = \sqrt{l_r^{\,2} + \left(h_r + z_{\mathrm{tgt}}\right)^2}\ , \tag{3.2.29}$$

$$l_{\mathrm{t}}^{2}=\left(\frac{l_{\mathrm{b}}}{2}+y_{\mathrm{tgt}}(t)\right)^{2}+x_{\mathrm{tgt}}(t)^{2} \tag{3.2.30}$$

and $$l_{\mathrm{r}}^{2}=\left(\frac{l_{\mathrm{b}}}{2}-y_{\mathrm{tgt}}(t)\right)^{2}+x_{\mathrm{tgt}}(t)^{2}. \tag{3.2.31}$$

The total field at the receive antenna from the target $E_{\mathrm{tgt}}^{\mathrm{trp}}$ is therefore,

$$E_{\mathrm{tgt}}^{\mathrm{trp}}=E_{\mathrm{r}}^{\mathrm{a}}+E_{\mathrm{r}}^{\mathrm{b}}+E_{\mathrm{r}}^{\mathrm{c}}+E_{\mathrm{r}}^{\mathrm{d}}. \tag{3.2.32}$$

To take into account any dependence of receiver gain due to angle of ray arrival, it is necessary to consider independent antenna effective area factors for each of the fields, such that the instantaneous power at the output of the antenna is given by:

$$\begin{aligned}P_{\mathrm{tgt}}^{\mathrm{trp}}&=\frac{1}{\eta}\left|\begin{matrix}\sqrt{\dfrac{G_{\mathrm{r}}(\beta_{\mathrm{h}},\beta_{\mathrm{v}})\lambda^{2}}{4\pi}}E_{\mathrm{r}}^{\mathrm{a}}+\sqrt{\dfrac{G_{\mathrm{r}}(\beta_{\mathrm{h}},\psi_{\mathrm{r}})\lambda^{2}}{4\pi}}E_{\mathrm{r}}^{\mathrm{b}}+\ldots\\ \sqrt{\dfrac{G_{\mathrm{r}}(\beta_{\mathrm{h}},\beta_{\mathrm{v}})\lambda^{2}}{4\pi}}E_{\mathrm{r}}^{\mathrm{c}}+\sqrt{\dfrac{G_{\mathrm{r}}(\beta_{\mathrm{h}},\psi_{\mathrm{r}})\lambda^{2}}{4\pi}}E_{\mathrm{r}}^{\mathrm{d}}\end{matrix}\right|^{2}\\ &=\frac{\lambda^{2}}{4\pi\eta}\left|\begin{pmatrix}\sqrt{G_{\mathrm{r}}(\beta_{\mathrm{h}},\beta_{\mathrm{v}})}E_{\mathrm{r}}^{\mathrm{a}}+\sqrt{G_{\mathrm{r}}(\beta_{\mathrm{h}},\psi_{\mathrm{r}})}E_{\mathrm{r}}^{\mathrm{b}}+\ldots\\ \sqrt{G_{\mathrm{r}}(\beta_{\mathrm{h}},\beta_{\mathrm{v}})}E_{\mathrm{r}}^{\mathrm{c}}+\sqrt{G_{\mathrm{r}}(\beta_{\mathrm{h}},\psi_{\mathrm{r}})}E_{\mathrm{r}}^{\mathrm{d}}\end{pmatrix}\right|^{2}\end{aligned} \tag{3.2.33}$$

(Note the above is a sum, not a matrix). If we make certain assumptions, i.e. that the antenna beam width is much wider than the region we expect to observe FS or indeed it is omni-directional, we can remove the dependence of the Tx and Rx antenna gain on angle and assume each path experiences the same antenna gain.

3.2.2.3 *MODIFIED REFLECTION CO-EFFICIENT FOR SEA SURFACE SCATTERING*

For the case of sea surface scattering it is obvious there would not just be a single surface specular reflected ray, but multiple reflections from the many facets and slopes of the surface. Indeed the reflected signals can be seen as the combination of two scattering effects, known as coherent and incoherent (diffuse) [46], and are described pictorially in Figure 3.2-6.

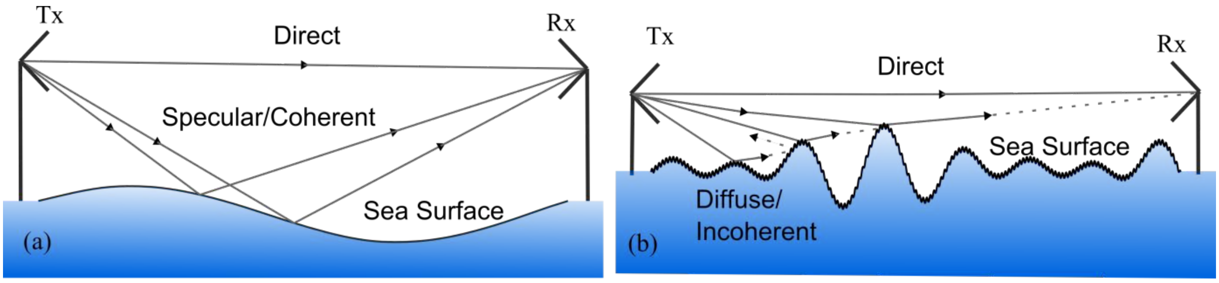

Figure 3.2-6 .Scattering behaviours from sea surface (a) specular/coherent scattering, (b) diffuse/incoherent scattering. Figure adapted from [47].

Figure 3.2-6 (a) shows the idea of coherent scattering from the smoother sea surface, whilst (b) shows the diffuse component arising from the rougher/choppier surface. The dominance of either coherent or incoherent scattering depends on the sea conditions and is discussed along with measurement in [47]. The discussion of scattering mechanism and the data collection work were part of the author's contribution to this publication. One other condition is defined, relating to low grazing angle systems in which intermittent loss of signal can occur due to wave blocking in high sea states. The specular/coherent scattering mechanism is the most important in terms of power budget analysis as it contributes to the average received signal power (and is coherent to the direct signal), whereas the incoherent part causes fluctuations around this.

The coherent reflected field was theoretically studied by Ament [48] and a form was proposed for a modified reflection coefficient Γ_{ament}, where:

$$\Gamma_{\text{ament}} = \rho_{\text{ament}}\Gamma = e^{-\frac{1}{2}g^2}\Gamma \ , \tag{3.2.34}$$

with Γ being the standard specular reflection co-efficient and

$$g = \frac{4\pi\sigma_\mathrm{h}}{\lambda}\sin(\psi_\mathrm{g}), \tag{3.2.35}$$

which is the Rayleigh roughness criterion [43] for reflections from rough surfaces, with σ_h being the standard deviation of the surface height about the mean and ψ_g the grazing angle. The coherent and incoherent fields were then experimentally studied by Beard [46] [49] in measurements of the sea surface and found that the experimental values of the coherent field were larger than those predicted by Ament. A modified expression was proposed by Miller, Brown and Vegh (MBV) [50] [51] ,

$$\Gamma_\mathrm{mbv} = \rho_\mathrm{mbv}\Gamma = e^{-\frac{1}{2}g^2} I_o\left(\frac{1}{2}g^2\right)\Gamma, \tag{3.2.36}$$

where Γ is the specular reflection co-efficient, g the Rayleigh criterion of Equation (3.2.35), I_0 is the zeroth order modified Bessel function and ρ_mbv is known as the MBV reduction factor. The MBV model is generally the most popular for use in radio wave propagation modelling [52]. In order to estimate the reduction factor for a given surface, the standard deviation of the surface height must be known. In the case of the sea surface, for a fully developed sea—one in which the wind has been blowing in the same direction for a long enough period of time, this can be approximated from the sea state/significant wave height/wind speed. These concepts and their relationship are discussed in more detail in Sections 4.1 and 6.1. The significant wave height $H_{1/3}$ (or H_s) is the mean wave height (trough to crest) of the highest third of the sea waves and the standard deviation of the heights σ_h is given by [53],

$$\sigma_\mathrm{h} = \frac{H_{1/3}}{4} \tag{3.2.37}$$

Needless to say, on inspection of (3.2.36), at the low grazing angles of the FSR system, it is expected that $\rho_{\mathrm{mbv}} = 1$. This infers that the power budget model should satisfy

3.3 SUMMARY OF FSR FOR SURFACE TARGETS

The investigation of the phenomenology behind forward scattering has provided an important insight into the scattering mechanisms at play in FSR. It has allowed estimates to be placed on the FS angular region for given target electrical dimensions and prediction of FSCS magnitude and main lobe widths. Using the phenomenological principles signal models have been produced for the FSR system, incorporating Doppler/phase signature creation and the envelope effect of the FSCS pattern upon this. A set of controlled experiments were performed which validated the FS principles. A target power budget model has been presented based on two-ray path propagation; this requires future confirmation against measured data. The models may then be used as a part of radar performance prediction.

The inclusion of a multi-path model is vital for the estimation of target power budget on the reflecting sea surface; multi-path reflection will have a great influence on measured FSR signals in the maritime environment. Indeed the model here is defined for a static surface, however the sea surface is constantly under motion and we can expect dynamically changing multipath reflections from the whole illuminated area of the surface. This dynamic multipath is the fundamental source of sea clutter in FSR. The continuously changing path differences between direct and surface reflected signals will cause varying interference behaviour at the receiver. Thus it may be expected that the multipath/clutter will cause an underlying oscillation to the received signals, modulated by the wave motion; the model will represent the average of this.

4 MARITIME FORWARD SCATTER RADAR

This section initially summarises the concept and requirement for the maritime FSR radar network, as was also explained within the thesis introduction. Following this a description of the prototype hardware that was designed and built by the author of this thesis[2] is provided. This equipment allowed an extensive experimental investigation to be performed and the gathering of a comprehensive database of maritime FSR measurements. An overview of the experimental targets and test sites used and ground truth measurements that were made during experimentation is provided.

4.1 MARITIME FORWARD SCATTER RADAR NETWORK CONCEPT

The fundamental concept of the maritime forward scatter radar is to provide perimeter protection in a maritime environment, for coastline, offshore interests such as wind farms and oil rigs and even exclusive economic zones. Utilising the benefits of increased cross section in the forward direction (FSCS) and long integration times to detect, in a high clutter environment, small even stealth low speed targets which may be being used for illegal activities. Due to the topology of FSR and the requirement for targets to cross the Tx-Rx baseline, FSR is ideally suited for surface target, tripwire-like applications. To enable remote offshore operation, the system is envisaged to be an easily deployable buoy mounted network of FSR sensors such as depicted in Figure 4.1-1.

---

[2] Through occasional consultation with Senior Research Fellow Dr. Edward Hoare

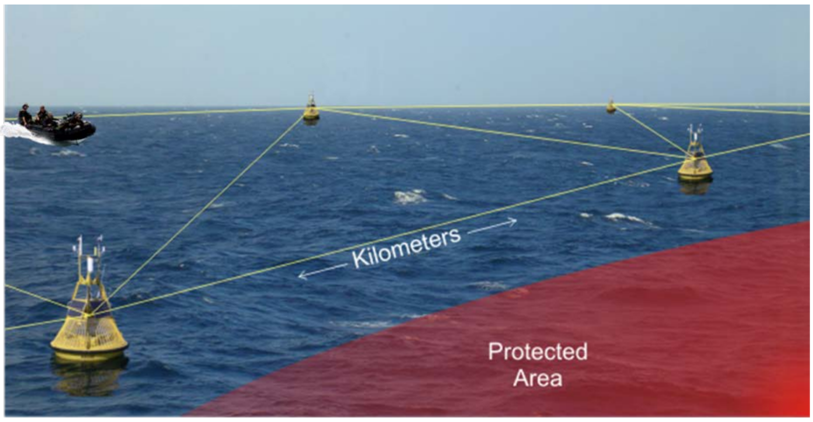

Figure 4.1-1. Example of buoy mounted maritime forward scatter radar network. Yellow lines show potential FSR baselines.

A buoy mounted system should have low antenna heights, this is not only due the need to maintain low grazing to ensure the use of the narrow increased FSCS, but also due to mechanical constrains on the floating/swaying structure. This platform motion would also limit the choice of antenna for the system. Full azimuth coverage would be required to form the network topology requiring a near omni-directional pattern or even a multiple azimuth sector horn arrangement. Antenna elevation beam widths would need to be wide enough to account for the swaying motion, or some form of antenna stabilisation would be required e.g. inertial measurement unit and servo control or even mechanical gimbal. Because the system will be remotely deployed, research should also be made into power supply demands and ways to lengthen battery life, for example the use of solar, wind and wave power.

The actual configuration of the network structure itself is not discussed here and this and the actual networking of these nodes are complex areas of research that a will need to be addressed. Fundamentally in order to setup the baselines in a networked system, each node must have knowledge of its position and the position of the surrounding nodes – this may be achieved through Global Navigation Satellite System (GNSS) positioning and node to node communication, where communication may be possible through modulation of the FSR transmit signal itself. Another important aspect to consider is inter-baseline/nodal signal interference. It would be understood that any transmitter/receiver may service many baselines, however in order to determine on which baseline a detection occurred something must uniquely identify this baseline to the receiver. This would infer the use of some form of channel access method, such as time-division multiple access (TDMA) or frequency-division multiple access (FDMA). FDMA would imply that each transmitter may have a slightly different transmit frequency; this method would require a level of frequency diversity in the receiver, increasing its RF complexity. The TDMA method would mean that each transmitter produced a burst in a different time slot and the receiver would recognise this from a pre-determined schedule. The synchronisation for this timing could be provided through the GNSS positioning system required for the buoy localisation. The number of timeslots and/or frequencies required would be related to the radius at which a transmitted signal can be received through the network and this would be a function of the required inter node spacing for a specific application.

Even though the final radar system is expected to be buoy mounted and have multiple nodes/baselines (multistatic), the start point of research must take the simplest component part to study. Indeed much of that covered in research thus far and that presented in this thesis is limited to the case of a single FSR baseline with stationary shore mounted antennas.

4.2 FORWARD SCATTER RADAR PROTOTYPE EXPERIMENTAL EQUIPMENT

In order to perform an experimental study of maritime FSR, it was necessary to design and build a test radar system. The fundamental system design was based around the need for a low cost ‘simple’ system design, allowing the extraction of the low Doppler frequencies that are observed in FSR. As previously explained in Section 3.1, FSR uses the direct path signal as a reference, this ultimately allows the extraction of the Doppler through the use of a non-linear element (NLE) and removes the need for a coherent transmitter and receiver. Given an element which functions in the appropriate frequency band, there is no need for any down conversion of the received RF signal. This all implies that the radar be a single channel system, moreover, due to the topology of FSR the requirement for a quadrature receiver is minimal. A quadrature receiver has two channels one termed in-phase (I) and the other termed quadrature phase (Q) which are related to each other by a 90° phase shift. For the purposes of discussion here, by looking at which channel lags or leads the other a determination of the sign of the Doppler frequency of the signal may be found. Symmetry in the FSR topology infers that there is ambiguity in the baseline crossing direction and angle, which cannot be resolved by knowing the sign of the Doppler. This lack of requirement of quadrature receiver makes the design much simpler, as stated, the transmitter and receiver do not need to be coherent, thus removing any need for connection (physical or remote e.g. GPS disciplined oscillator's) between the spatially separated nodes. Coherency still arises due to the direct path signal reception and minimal target scattered signal delays, over which time any transmit oscillator would not deviate in frequency by any considerable amount.

There are certain cases where a fully coherent quadrature FSR system would be required, i.e. situations where full signal phase information is required, such as in the Target Shadow Profile Reconstruction/Shadow Inverse Synthetic Aperture Radar application of FSR [28]–[30]. This process fundamentally requires the extraction and removal of the phase from the FS Doppler signature leaving what is essentially the FSCS pattern, which as shown previously (Section 3.1.2) is related to the target silhouette shape/profile. The profile may then be extracted by inverse Fourier transform.

4.2.1 TRANSMITTER AND RECEIVER DESIGN

The generic continuous wave (CW) transmitter and receiver architecture for the FSR system is found in Figure 4.2-1.

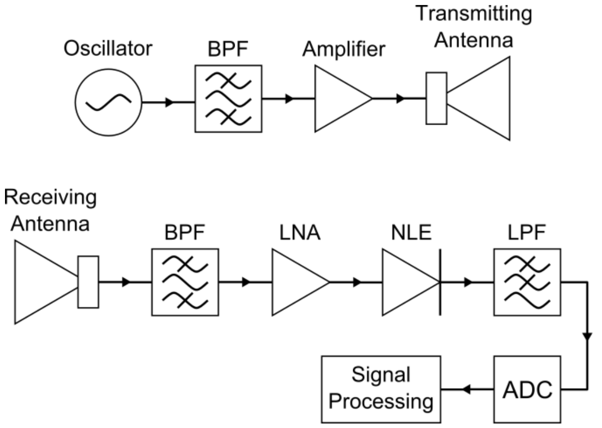

Figure 4.2-1. Generic design of FSR transmitter and receiver sections.

The transmitter section (upper Figure 4.2-1) simply consists of an oscillator with band pass filtering (BPF), amplification and transmit antenna. The receiver (lower Figure 4.2-1) consists of receive antenna, band pass filter (BPF) to reduce out of band noise, low noise amplifier (LNA) section into the non-linear element, low pass filtering (LPF) to remove any sum frequencies from the NLE and ensure no aliasing by the analogue-to-digital converter (ADC), which samples at a rate determined by the expected Doppler frequencies. The digitised data is stored on PC for post processing.

The actual hardware designed and produced was for CW operation at 7.5 GHz. The choice of 7.5 GHz was made such that smaller maritime targets (~1 m dimension) would be scattering in the upper Mie/optical regime. The choice was also swayed by the availability of RF parts and antennas within the radar group at this frequency. More recently a 24 GHz channel was added. This was to enable future investigation of the effect of higher frequency on the target detection from the increased but narrower lobed FSCS as well as effects on clutter characteristics. 24 GHz was chosen specifically due to the availability of (relatively) low cost commercial off the shelf components (COTS) and modules. It should be noted that no target measurement data at 24 GHz is presented in this thesis, the hardware is described here in order to show that thought has been put into investigating the fundamental effects of the radar parameters in FSR. Figure 4.2-2 contains the schematic of each of the radar channels.

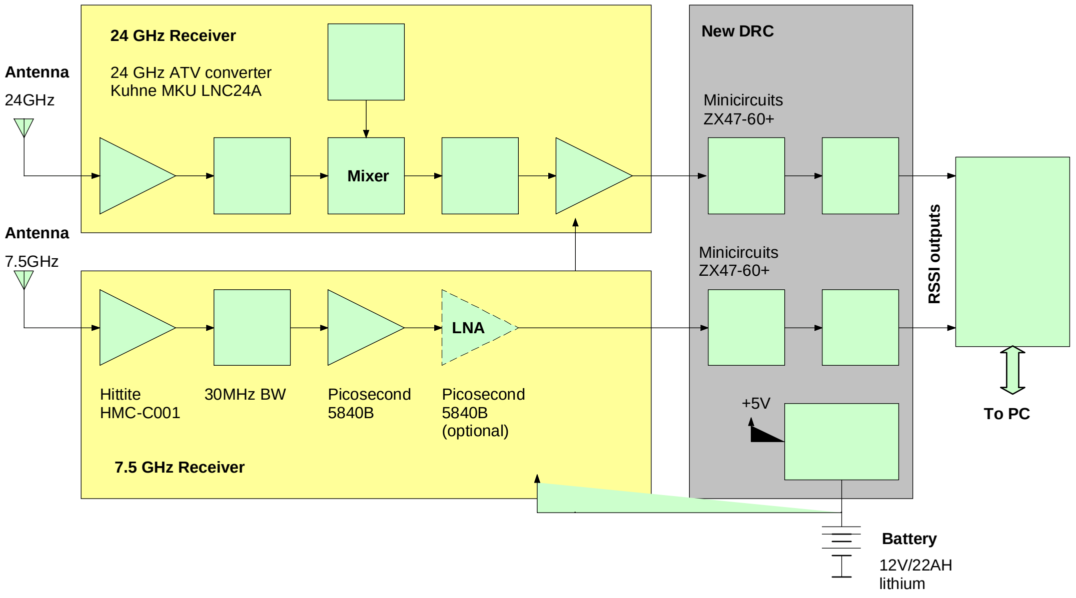

Figure 4.2-2. Schematic of the designed and manufactured 2 band Doppler receiver at 7.5 and 24 GHz used for maritime FSR trials.

The lower yellow section is the 7.5 GHz channel front end, which was designed and built by the author from COTS components. It has total gain of 60 dB at the output to the log detector, a noise figure of 2 dB, bandwidth of 30 MHz and dynamic range of 60 dB. The top yellow box in the figure is the 24 GHz receiver, which is a commercial amateur television (ATV) module from Kuhne Electronic [54] – MKU LNC 24A. This outputs an intermediate frequency of 1.1 GHz, has a gain of 45 dB, noise figure of 2.5 dB, bandwidth of 30 MHz and dynamic range of 60 dB. The gray part of the figure shows the NLE, which in the case of the most recent hardware for both channels consisted of a Mini Circuits ZX47-60+ logarithmic power detector [55]. This detector was chosen for its more than 60 dB dynamic band at frequencies up to 8 GHz, previous incarnations of the 7.5 GHz hardware utilised a Schottky diode detector – Herotek DHM124AB [56] which had only 40 dB dynamic range and less sensitivity and required addition hardware/gain on the diode output. The response curve of output voltage vs input power for the logarithmic detector is shown in Figure 4.2-3.

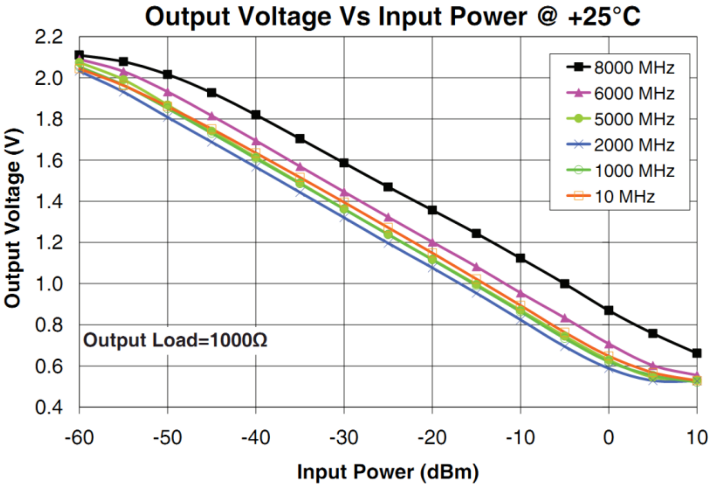

Figure 4.2-3. Data sheet response curve for Mini Circuits ZX47-60+ logarithmic detector.

For use with the maritime hardware it was necessary to perform similar calibrations at 7.5 GHz and 1.1 GHz in order to accurately relate the detector output voltages to the power received at the detector. This process was performed by attaching a calibrated signal generator to the detector input, varying the input power and recording the detector output voltage. The results of the calibration are found in Figure 4.2-4. When measuring signal data, it is essential that the output signals are in the 'linear' part of the response and are not undergoing saturation or indeed conversely too low or below the noise floor. This is highly dependent on the baseline range of testing and may require either additional amplification, or the use of attenuators. The output from the detector is of the form of a dc level (from the direct path signal) with Doppler variation imposed on top of this from the target scattered signals, as described in Section 3.1.4.1, and is referred to as the RSSI signal.

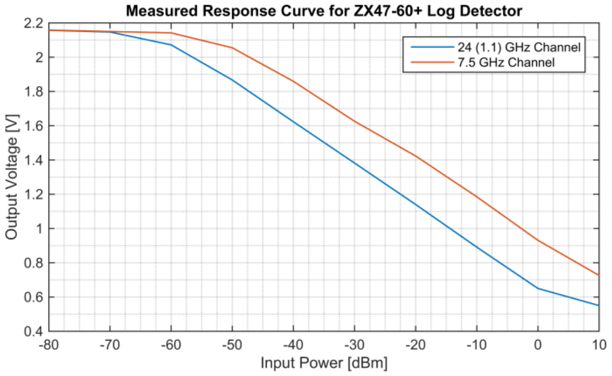

Figure 4.2-4. Response curve for logarithmic detector, measured at 1.1 GHz (IF output of 24 GHz receiver) and at 7.5 GHz.

The output RSSI signals are digitised with a Measurement Computing USB-1608FS USB ADC [57], with 16 bit resolution and maximum sample rate of 15 kS/s per channel. The ADC has multiple selectable voltage ranges enabling matching of the range to the received signal amplitudes, thus ensuring maximum bit depth is utilised. The digitised data is transferred to and stored on a laptop PC. An interface to MATLAB was developed to allow the visualisation of the digitised data as it was being collected, which greatly helps with system debugging in real time. Due to the low Doppler frequencies, low sample rates (generally a maximum of 200 Hz) are used, thus this system is capable of recording data for many hours continuously.

The transmit side of the 7.5 GHz system was built ‘in-house’ and had an output power of 26 dBm, the 24 GHz transmitter consisted of another Kuhne module (MKU ATV 24-2), with output power of 300 mW (~25 dBm). The FSR system requires very low power which would help to ensure long battery life when remotely deployed.

The complete maritime hardware itself is very compact and portable, transmitter and receiver sections each fit into a waterproof Peli case as shown in Figure 4.2-5.

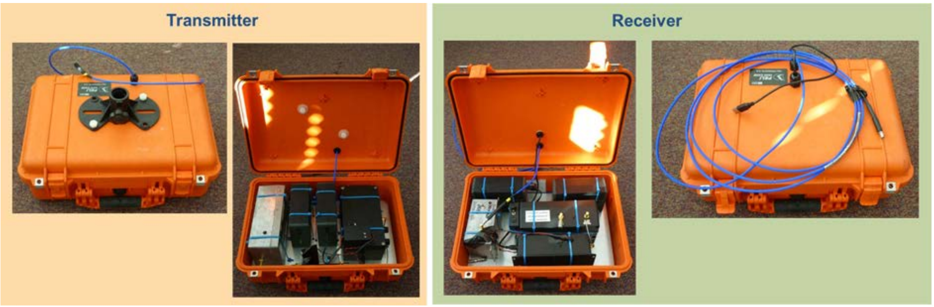

Figure 4.2-5. Prototype maritime forward scatter radar, contained in waterproof Peli cases.

4.2.1.1*Phase Noise Considerations*

It should be noted that the self-mixing receiver not only provides the extraction of the Doppler signature directly, but also overcomes a potential noise issue related to receiving low Doppler frequency signals – that being transmitter/synthesiser phase noise. Figure 4.2-6 shows the typical phase noise as a function of frequency offset from carrier for modern synthesisers, for carrier frequencies ranging from 500 MHz to 20 GHz.

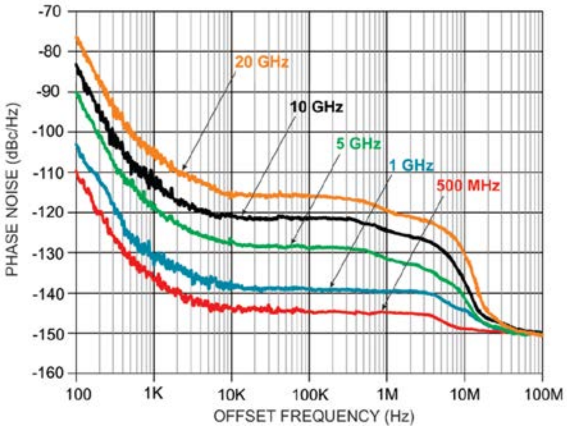

Figure 4.2-6. Typical phase noise level in modern synthesizers, showing phase noise levels as a function of frequency offset from the carrier for a range of carrier frequencies. Plot is taken from National Instruments QuickSyn Synthesisers web-site [58]**.**

The plot does not extend down to the very low offset frequencies; however, extrapolation can give an idea of the expected phase noise below 10 Hz. The phase noise level is estimated to be between –20 and –50 dBc/Hz for 20 GHz and –60 and –90 dBc/Hz at 500 MHz. Thus it might be expected that the transmitter phase noise may be a limiting factor in the FS mode. However with the use of the self-mixing receiver the leakage signal is acting as a heterodyne to the FS target signal. In FSR the target and leakage signals have near zero relative delay due to the very close vicinity of the target to the baseline, in this case the leakage and target phase noise will be correlated and converted to dc at the mixer output. Figure 4.2-7 shows frequency spectra from FS Doppler measurements performed at 7.5 GHz in an anechoic chamber, where a small rotating target was placed on the FSR baseline and spun at 4 different speeds ranging from 200 rpm – 600 rpm.

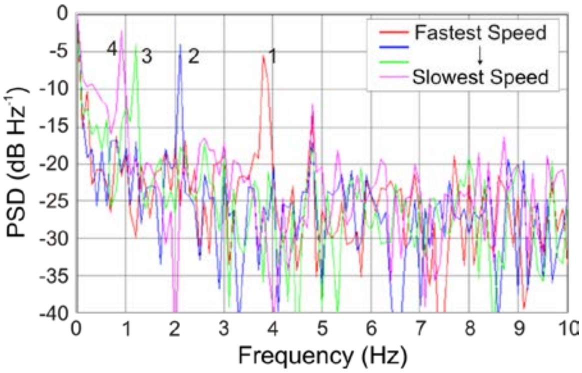

Figure 4.2-7. Spectra of measured Doppler signatures of a three-blade propeller rotated at four different speeds. Peaks indicate Doppler frequency of the rotating target for four speeds, ranging between peak 1, the fastest (200 rpm) and the slowest, peak 4 (60 rpm).

The figure shows four numbered peaks in the Doppler spectrum associated with the different fan speeds, peak 1 relates to the fastest speed and peak 4 the slowest as would be expected. More importantly, this experiment demonstrates that Doppler frequencies of less than 1 Hz can be measured, in practice, using this measurement technique. The static objects within the scene and the correlated phase noise reside in the dc (0 Hz) component and any residual phase noise extending out from this is not considerable enough to affect the 1 Hz Doppler measurement. The experiment was an attempt to validate the concept by measurement, the close-to-carrier phase noise of the 7.5 GHz transmitter would ideally be measured. However, the investigation of the influence of phase noise may be more important for the prototype 24 GHz system mentioned previously, and shown in Figure 4.2-2. The design was chosen due to the availability of low cost COTS components, but the superheterodyne receiver uses an internal dielectric resonator oscillator (DRO) for down conversion to 1.1 GHz. This oscillator will have an associated phase which is uncorrelated with the transmit signal, and produce an ac component on the detector output. The full investigation of these effects is part of future work.

4.2.2 ANTENNAS

Directional and omni-directional antennas were available for use with the 7.5 GHz radar system and are shown in Figure 4.2-8. The left hand image shows a pair of 20 dB horns with equal E and H-plane beam widths (±10°) and gain of 20 dB, which were the main antenna used. The middle image shows a pair of non-equal beam width horns (±6° H, ±30° V) also with a gain of 20 dB. These were produced so that in the future, measurements could be made to test the effects of increasing/reducing the illuminated area of the sea surface. The right hand image is of a pair of omni-directional azimuth antennas built at the University of Birmingham with an elevation beam width of ±30°and gain of 3 dB.

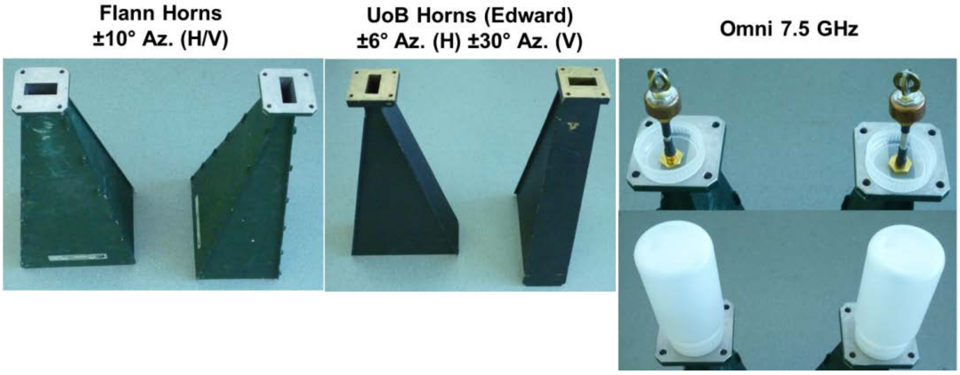

Figure 4.2-8. Examples of available 7.5 GHz antennas for the maritime FSR system.

4.2.3 WIDEBAND AND ULTRA-WIDEBAND HARDWARE DEVELOPMENT

A very preliminary study of ultra-wide band FSR has been performed by the author and aspects of this may be found in [60]–[62]. These papers discuss the concept of using ultra-wideband (UWB) signals in FSR [60],[61] and give a description of the experimental hardware (which is also described below)[60]. In [61] and [62] bistatic RCS simulations were performed in CST Microwave Studio [17]. The small inflatable and a jet-ski were modelled and the computed RCSs were compared to the aperture approximation of the FSCS described in the phenomenology section (3.1) and showed good agreement. Actual maritime measurements with this system were limited and mainly related to hardware testing, hence, only the above reference to the papers is included in the thesis for the interested reader to follow up.

The proposed benefit of UWB FSR is the introduction of a form of range resolution. Looking back at the equation for bistatic range resolution (2.5.2) in Section 2.5, to obtain resolution at very small bistatic angles requires very short pulse duration (large bandwidth), so UWB signals must be used. As explained in [60] and [61], the introduced range resolution may artificially limit the area of the sea surface from which returns are received to a very narrow elliptical region between the FSR transmitter and receiver. This would still allow reception of target signals through their directive FS main lobe, the actual discrimination in range of targets crossing the baseline would be no better than the CW system, but the size of the clutter patch would be substantially reduced. Signal-to-clutter ratio (SCR) would be enhanced whilst still permitting the use of omni-directional azimuth beam pattern antennas. The next stages of work in this area will be to collect UWB FSR data sets to prove the theory against the CW FSR data, thus as a precursor to enable this, an addition was made to the existing hardware. Pulsed wide-band (WB) and ultra-wide band (UWB) equipment was developed at a centre frequency of 7.5 GHz, which used Gaussian pulses with - 3 dB bandwidths of 100 MHz, 1 GHz and 3GHz as shown in Figure 4.2-9. Initially, the hardware composed of rather bulky equipment, using a Tektronix arbitrary waveform generator (AWG7102) with sample rate of 20 GS/s as a transmitter. As a receiver, a Tektronix digital phosphor (DPO72004) oscilloscope (DPO) with deep fast storage memory was connected to the output of the 7.5 GHz receiver described in Section 4.2.1—received raw pulse data was recorded at RF into the DPO memory. The devices are shown on the left hand side of Figure 4.2-10, the right hand image shows the receiver side of this setup being used (under cover due to rain) at one of the test sites (Langstone Harbour).

The recorded raw data from the oscilloscope can be used to reconstruct an equivalent Doppler signature as would be recorded from the standard FSR Doppler hardware, by implementing a square-law detector in software. A smaller portable variable PRF (1MHz, 100kHz and 10kHz), variable bandwidth (1 GHz, 100 MHz, 10 MHz) pulse modulated mode was designed (by the author, using salvaged test equipment parts) and added to the 7.5 GHz equipment to replace the DPO and AWG. This was included in the portable equipment shown in Figure 4.2-5 and required the development of a 3 GHz band width cavity BPF for the receiver front end to band pass the received 7.5 GHz UWB signals.

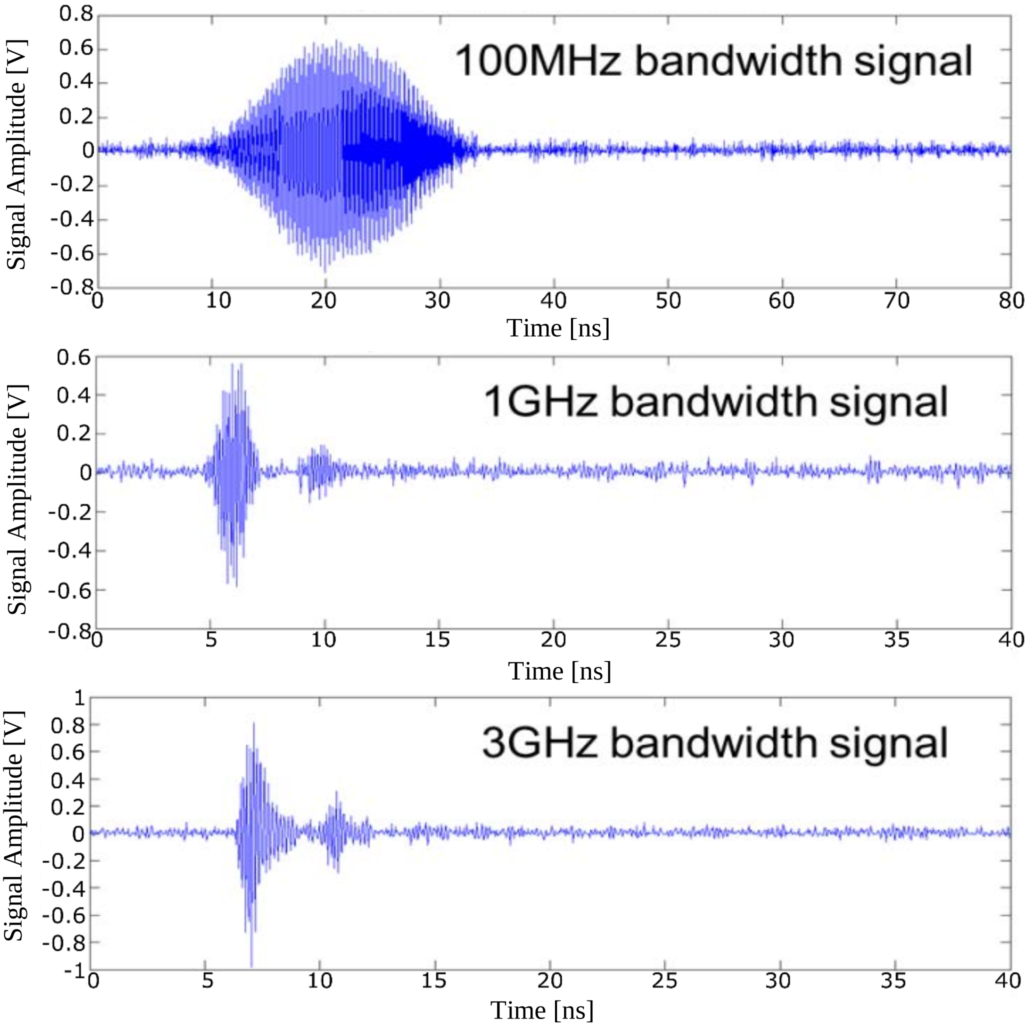

Figure 4.2-9. Examples of Gaussian pulsed signals used in WB and UWB maritime FSR. Raw data recorded on a digital phosphor oscilloscope.

Figure 4.2-10. Arbitrary waveform generator (AWG) and digital phosphor oscilloscope (DPO) used for UWB measurements (left hand images). Setup being used for initial UWB maritime measurements.

4.2.4 MOCK BUOY

As a preliminary stage of future investigation, to move from a stationary transmitter/receiver scenario to a single floating node, a ‘home made’ buoy was developed. This was created to test the effect off antenna motion on target and clutter signatures—shown in Figure 4.2-11. Only very preliminary trials were made in order to test the functionality of the system mounted on the ‘buoy’ and seaworthiness of the ‘buoy’ itself. No measurement results are presented here, rather it is included as an indication of where future research work will be required and how it may be accomplished, in order to develop a fully buoy mounted system.

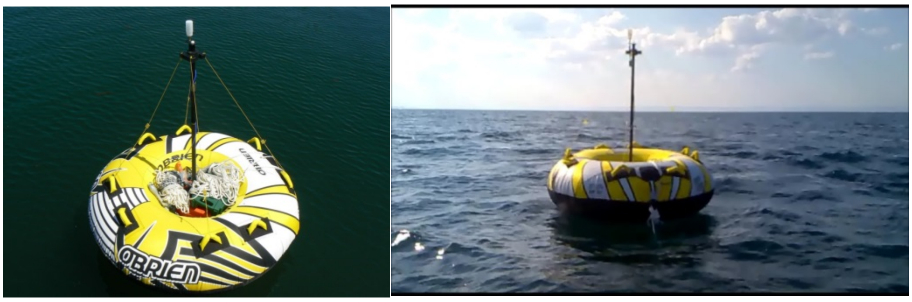

Figure 4.2-11. 'Buoy' mounted transmitter.

When anchored out in deep sea, the position of the ‘buoy’ was very stable, as seen from the GPS track in Figure 4.2-12, it only moved within a radius of 4 m over 6 hours.

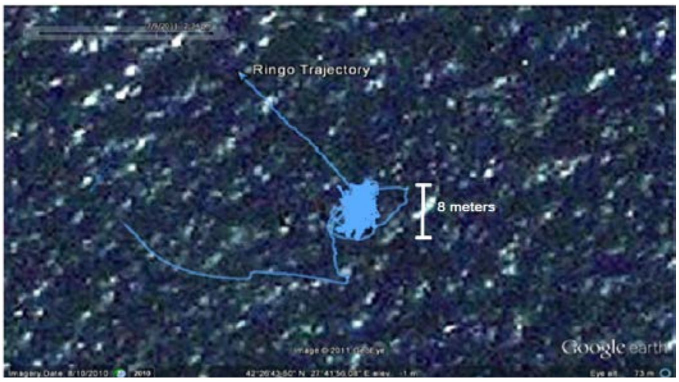

Figure 4.2-12. Six hour GPS track of the anchored ‘buoy’ in open sea.

4.3 CO-OPERATIVE TARGET

During trials, many targets of opportunity have been encountered, though the main target of experimentation and that which relates to data presented in this thesis, was the group’s small inflatable boat. The inflatable is 2.9 m long and approximately 1 m height with a person on board and is shown in Figure 4.3-1.

Figure 4.3-1. Small inflatable boat used for co-operative target measurements.

This co-operative target will be referred to from hereon in as the ‘MISL’ (Microwave Integrated Systems Laboratory) or ‘small inflatable’ boat.

4.4 MARITIME EXPERIMENTAL TEST SITES

From the outset, it should be stated that due to the logistical issues with testing out in deep sea, many of the trials performed to collect maritime FSR target and clutter data were performed in littoral environments. The need to have access to either side of a stretch of water to position transmitter and receiver means that inshore areas were more suitable for testing, thus deep sea test sites were unattainable. A number of test sites have been employed over the duration of the maritime FSR study, the author was responsible for assessing and identifying these as suitable for trials.

4.4.1 LANGSTONE HARBOUR

The main testing ground for the maritime FSR study was Langstone Harbour near Portsmouth and was initially chosen for ease of access to either side of the harbour entrance. The trials site is shown in Figure 4.4-1 with lines to indicate some of the baselines available.

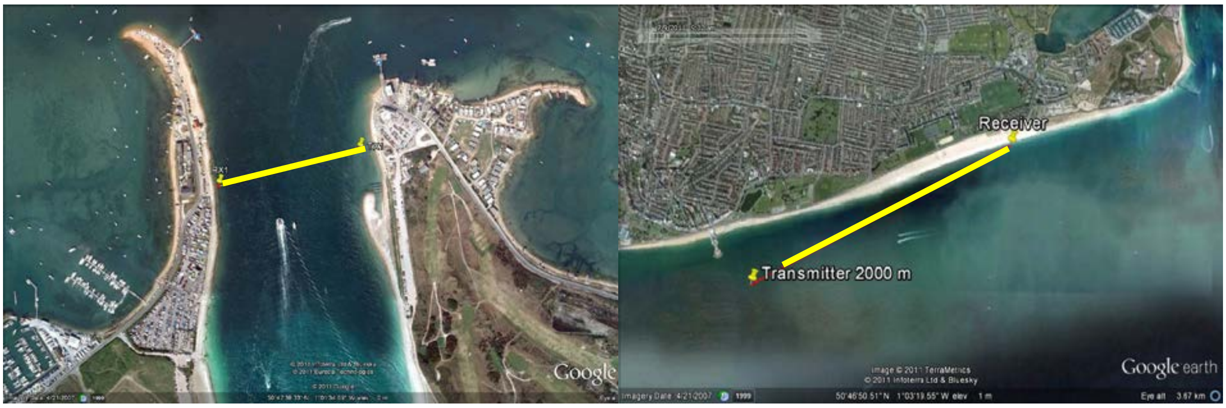

Figure 4.4-1. Langstone Harbour test site. Left image shows a baseline formed across the harbour, right shows the transmitter placed on a boat out at sea pointing back to the coastline.

Langstone provided baseline lengths ranging from 300 m to 750 m across the harbour entrance and longer ranges with the transmitter out at sea pointing back to the coastline. Measurements were made here involving the variation of many parameters, such as: sea state, target speed, target baseline crossing angle, baseline crossing point, antenna height and polarisation. The majority of results presented in this thesis were recorded at this test site.

4.4.2 CONISTON WATER

In order to provide some calm water trials and to access longer baselines in which the small inflatable boat could be used; Coniston water in the Lake District was chosen. Figure 4.4-2 shows a selection of the baselines used at this test site.

Figure 4.4-2. Examples of Coniston Water test site baselines.

4.4.3 OTHER TEST SITES

Other test sites were investigated and trials performed, these included such places as Weymouth, Sozopol in Bulgaria and Livorno in Italy for NATO-SET Group trials.

4.5 GROUND TRUTH AND ENVIRONMENTAL MEASUREMENTS

As with any experimental campaign, radar data is not the only required measurement and certain ground truth and environmental measurements were also made.

4.5.1 WEATHER AND SEA STATE

During trials, a weather station was employed to log the wind speed and direction, the device is shown attached to the group trials vehicle in Figure 4.5-1.

Figure 4.5-1. Weather station attached to test vehicle.

The use of such data may only provide a useful estimation for the given conditions of measurement which as shown were generally in a coastal littoral environment and so relating wind speed to the sea state which is a scale based on a developed deep sea is not necessarily appropriate. Also the wave direction was defined in the littoral cases by the fact that the waves were coming in shore from out at sea. It was deemed the best way to classify the sea state in the case of our experimental records was through estimation of the wave height, a table of sea state in relation to wave height and wind speed is shown in Table 6.2-1 in Section 6.1.

Tide tables were also utilised in order to estimate the sea level at the test site at the time of measurement.

4.5.2 VIDEO AND PHOTO IMAGERY

In all experimental trials, video and photographic recordings were made. These allowed documentation of non-cooperative targets, enabling estimation of their speed and sizes. Video was actually used post-measurement along with visual observation at the time of measurement in order to help define the wave height or associated ‘sea state’ for any given measurement. A video screen capture from trials is shown in Figure 4.5-2.

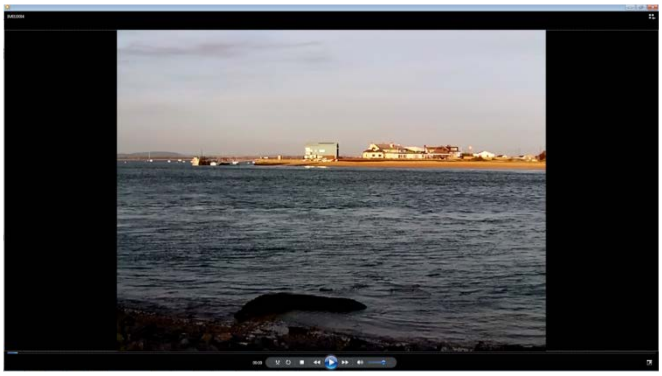

Figure 4.5-2. Example of video recording of trials at Langstone Harbour.

4.5.3 TRAJECTORY AND TOPOLOGY MEASUREMENT – GPS

In order to have an estimate of the inflatable boat target speed and trajectories along with knowledge of the Tx and Rx positions, a handheld GPS unit was used to record boat track data in the form of NMEA files and antenna positions in the form of waypoint files. The GPS positions have an root mean square positional accuracy of around 5 m (the best achievable with the standard GPS receiver used). An example of the layout of each file type can be found in Figure 4.5-3.

Initially great circle navigation formulae [59] were implemented in MATLAB™ and used to calculate all target trajectory parameters from GPS waypoint data for Tx and Rx positions and GPS track data from the inflatable boat. Trajectories were also calculated manually by constructing lines on Google Earth™ after importing GPS data. The trajectory parameters calculated via this method were comparable to the great circle method. Examples of the track data and waypoints as displayed in Google Earth™, are shown in Figure 4.5-4.

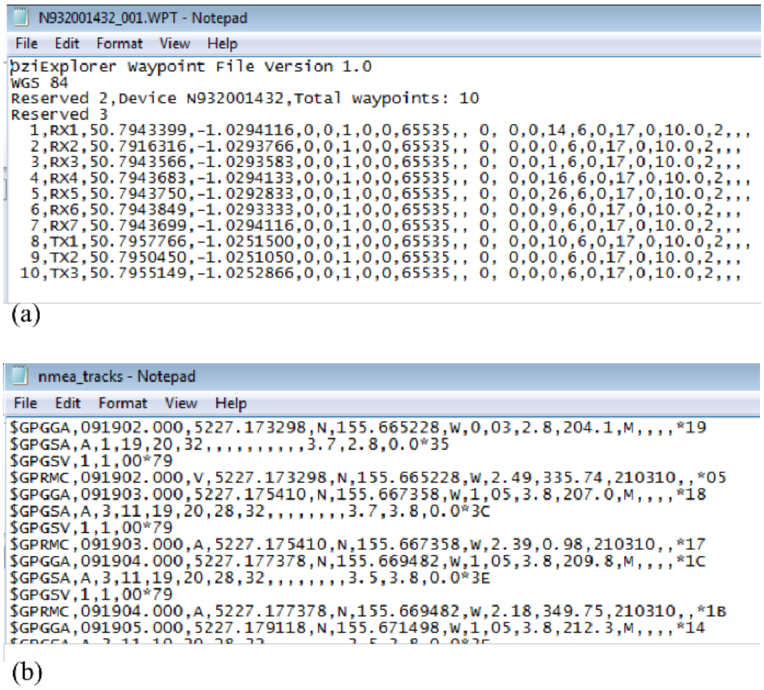

```
OziExplorer Waypoint File Version 1.0
WGS 84
Reserved 2,Device N932001432,Total waypoints: 10
Reserved 3
   1,RX1,50.7943399,-1.0294116,0,0,1,0,0,65535,, 0, 0,0,14,6,0,17,0,10.0,2,,,
   2,RX2,50.7916316,-1.0293766,0,0,1,0,0,65535,, 0, 0,0,0,6,0,17,0,10.0,2,,,
   3,RX3,50.7943566,-1.0293583,0,0,1,0,0,65535,, 0, 0,0,1,6,0,17,0,10.0,2,,,
   4,RX4,50.7943683,-1.0294133,0,0,1,0,0,65535,, 0, 0,0,16,6,0,17,0,10.0,2,,,
   5,RX5,50.7943750,-1.0292833,0,0,1,0,0,65535,, 0, 0,0,26,6,0,17,0,10.0,2,,,
   6,RX6,50.7943849,-1.0293333,0,0,1,0,0,65535,, 0, 0,0,9,6,0,17,0,10.0,2,,,
   7,RX7,50.7943699,-1.0294116,0,0,1,0,0,65535,, 0, 0,0,0,6,0,17,0,10.0,2,,,
   8,TX1,50.7957766,-1.0251500,0,0,1,0,0,65535,, 0, 0,0,10,6,0,17,0,10.0,2,,,
   9,TX2,50.7950450,-1.0251050,0,0,1,0,0,65535,, 0, 0,0,0,6,0,17,0,10.0,2,,,
  10,TX3,50.7955149,-1.0252866,0,0,1,0,0,65535,, 0, 0,0,0,6,0,17,0,10.0,2,,,
```

(a)

```
$GPGGA,091902.000,5227.173298,N,155.665228,W,0,03,2.8,204.1,M,,,,*19
$GPGSA,A,1,19,20,32,,,,,,,,,,3.7,2.8,0.0*35
$GPGSV,1,1,00*79
$GPRMC,091902.000,V,5227.173298,N,155.665228,W,2.49,335.74,210310,,*05
$GPGGA,091903.000,5227.175410,N,155.667358,W,1,05,3.8,207.0,M,,,,*18
$GPGSA,A,3,11,19,20,28,32,,,,,,,,3.7,3.8,0.0*3C
$GPGSV,1,1,00*79
$GPRMC,091903.000,A,5227.175410,N,155.667358,W,2.39,0.98,210310,,*17
$GPGGA,091904.000,5227.177378,N,155.669482,W,1,05,3.8,209.8,M,,,,*1C
$GPGSA,A,3,11,19,20,28,32,,,,,,,,3.5,3.8,0.0*3E
$GPGSV,1,1,00*79
$GPRMC,091904.000,A,5227.177378,N,155.669482,W,2.18,349.75,210310,,*1B
$GPGGA,091905.000,5227.179118,N,155.671498,W,1,05,3.8,212.3,M,,,,*14
```

(b)

Figure 4.5-3. Example of (a) waypoint file for Tx/Rx positions and (b) NMEA track data file for target position tracks.

Figure 4.5-4. Examples of GPS track data recordings of MISL boat target trajectory (blue lines) and waypoint markers for antenna positons (Tx/Rx).

5 SELECTED RESULTS FROM THE MEASUREMENT CAMPAIGN

This section presents a representative selection of results of from the FSR measurement campaign. Initially a summary of forward scatter radar clutter measurement results are made, looking briefly at spectral and statistical properties—these are vital to understand and predict target detection probabilities and false alarm rates within the clutter background. Following this, a comprehensive selection of target measurement results are presented for various different test parameters; which are described in more detail within the section. For each set of measurements a qualitative discussion of the results is provided and how they relate to the expected behaviour in FSR. This data set is required for future research to fully verify the target signature and propagation models described previously in this thesis. Also this data is vital (alongside the clutter data) for future work in predicting the radar performance. Finally a section describing initial work on signal processing to enhance target detection and predict target motion parameters is included. This is ongoing work and as such a discussion of the requirements for prediction of detection performance is presented.

The trials, trials data and results presented in this section were organised, collected and compiled by the author of this thesis. Measurements were conducted using the 7.5 GHz hardware designed and constructed, also by the author, and described in Section 4.2. The results here make up the first known comprehensive database of recorded maritime FSR target signatures.

5.1 MARITIME FORWARD SCATTER RADAR CLUTTER SUMMARY

Clutter in FSR is related to the change of the underlying surface and the surrounding environment, which in the case of maritime FSR is the dynamic sea surface. In the traditional radar case, range resolution and the use of directional antennas lead to clutter being received from only a limited area. In buoy mounted maritime FSR, it is expected that antennas with an omni-directional azimuth pattern will be used. This combined with the lack of range resolution infers that clutter will be received from a large area between the transmitter and receiver. The spatially distributed clutter will cause both bistatic and forward scatter signal interference and thus target detection in FSR will be performed against a background of strong Doppler modulated clutter. The main clutter related problems associated with target detection are: firstly, if the spectrum of Doppler modulated clutter overlaps with the target return spectrum and, secondly, general non-Gaussian behaviour of the clutter intensity distribution, where long tails of the distribution result in an increased false alarm rate. Statistical and spectral characteristics of FSR clutter need to be distinguished in order to develop effective detection algorithms. A general overview of statistical distributions in relation to radar and clutter may be found in Appendix A of [63] and discussion of distributions for sea clutter in bistatic radar may be found in [64].

By its very configuration the FSR channel is similar to an RF communication channel, therefore sea clutter can be described in terms of the fading of an RF channel over the sea surface. Forward propagation studies over the sea have been dedicated to characterising radio wave propagation [49], [68]–[74], coastal or ship-to-ship communications [51], [70], [75]–[78] as well as radar scattering at low grazing angles in [46], [49], [71]–[74], [77], [79]. In

[47] approaches developed for characterization of fading of RF channels were applied for analysis of FSR clutter at very low grazing angle. Both spectral and statistic properties were measured, analysed and results were compared to those of modelling. In particular, the dependence of scattering mechanisms – dominant specular reflections, diffused scattering and partial shadowing - on the sea state have been considered (as described briefly in Section 3.2). A brief overview of spectral and statistical properties of clutter related to the maritime environment is presented here, summarised from [47] and [66]. The author of this thesis was a co-author on these publications, responsible for the data collection, spectral analysis and providing initial clutter distribution analysis and the software for the distribution analysis. In summary:

- FSR sea clutter measured at very low grazing angles (less than 0.5º) exhibits, to a first approximation, a near constant frequency centred below 1 Hz. The spectrum rolls off of at approximately 35-40 dB per decade. Figure 5.1-1(a) shows clutter PSDs estimated from a variety of measurement parameters.
- The Rayleigh distribution is a good fit to the measured clutter intensity distribution. Figure 5.1-1 (b) and (c) show the measured distributions and corresponding Rayleigh distribution fits (straight lines on the Weibull scale) for different test sites and different sea states respectively.
- In fact both the clutter spectrum and shape of clutter distribution function are found to be independent of transmit receive baseline range, sea state and carrier frequency, within the range of limited experimental conditions.

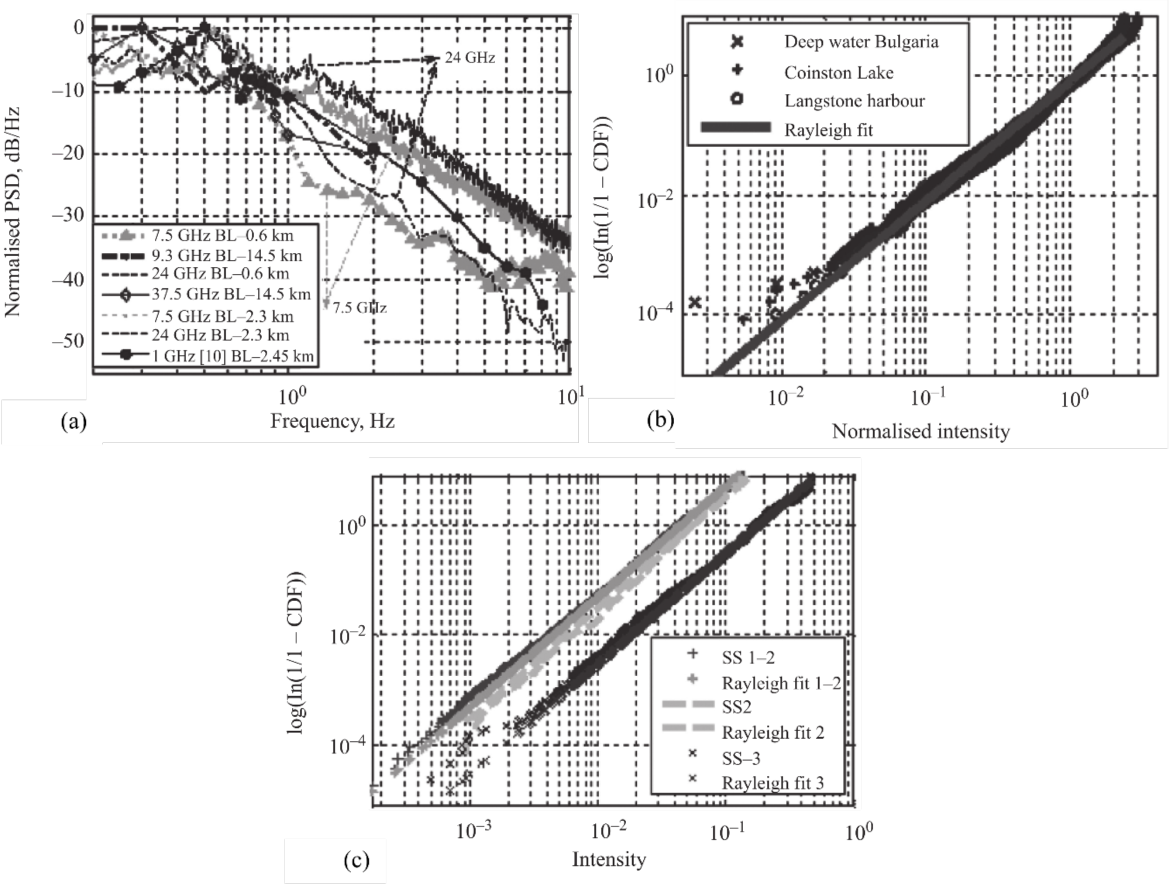

Figure 5.1-1. (a) Normalised PSDs of FSR sea clutter recorded at varying frequencies, ranges, sea states and test sites. (b) cumulative distribution function (CDF) of normalised FSR sea clutter from different test sites, plotted on Weibull paper along with a Rayleigh CDF fit (straight line). (c) gives comparison of CDFs for long term FSR sea clutter measurements in different sea states, with corresponding Rayleigh fits (straight lines). SS stands for Sea State by WMO/Douglas scale. Figures reproduced from [47].

5.2 TARGET MEASUREMENT PROGRAM EXPERIMENTAL RESULTS AND INITIAL PROCESSING

This section contains a set of representative results from the Maritime FSR measurement campaign. Measurements presented were measured under variation of baseline crossing angle, velocity, sea state, polarisation and range. The analysis of the results is limited at this time to showing target measurement results and corresponding spectra and is mainly qualitative at this stage of the research, relating the measured results to what we may expect in the FSR system topology. A section on initial work on quasi-coherent processing to estimate target motion parameters and improve target detection is included at the end, this work is a subject for extensive future investigation.

To give an example of a maritime FSR target signature, Figure 5.2-1 contains the first Doppler signature ever measured with the maritime FSR hardware, that of a rigid inflatable lifeboat target of opportunity.

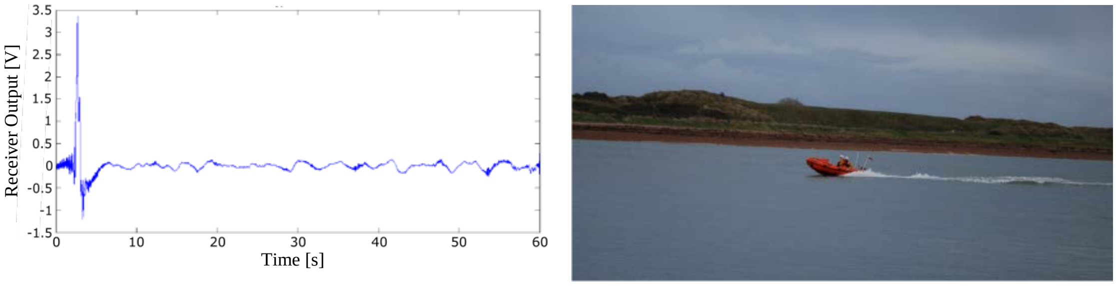

Figure 5.2-1. First target measurement with maritime FSR system, left hand side is the recorded Doppler signature, right hand side is an image of the lifeboat target.

The plot on the left side of the figure is the Doppler output from the detector i.e. the RSSI signal with dc offset (due to the direct path signal) removed. The target signature is at the beginning of the record, with clutter occupying the last 50 s of the record. The right hand side of the figure shows an image of the target.

5.2.1 VARIATION OF TARGET SIGNATURE WITH BASELINE CROSSING ANGLE

A set of experimental measurements have been performed to determine the variation of target signature with FSR baseline crossing angle. The measurements presented here were recorded at Langstone Harbour over a range of 298 m with antenna heights of 1 m using a 7.5 GHz CW signal. The target shown in each of the following measurements is the co-operative small inflatable boat target and using GPS track and waypoint data it is possible to retrieve the trajectories for the target in each measurement. Measurements were taken quite close in time to attempt to ensure a constant sea state. Efforts were made to achieve baseline crossing angles of 90, 45 and 22.5°, along with 0° directly along the baseline. The sea conditions make such trajectories hard to achieve precisely and the outcome was a set of measurements at 78, 52 and 34° and as close to along the baseline as possible.

5.2.1.1 *RECORDED SIGNATURES FOR 78° BASELINE CROSSING OF SMALL INFLATABLE BOAT*

Figure 5.2-2 shows the GPS track data corresponding to a 78° target-baseline crossing.

Figure 5.2-2. GPS track data for 78° target trajectory. Blue shows full track and red indicates section used for analysis.

The speed of the target was found to be 11 km h^{-1} (5.9 knots). The Doppler record is shown in Figure 5.2-3 and contains two inflatable boat signatures of which the second, highlighted in red, is related to the GPS data above.

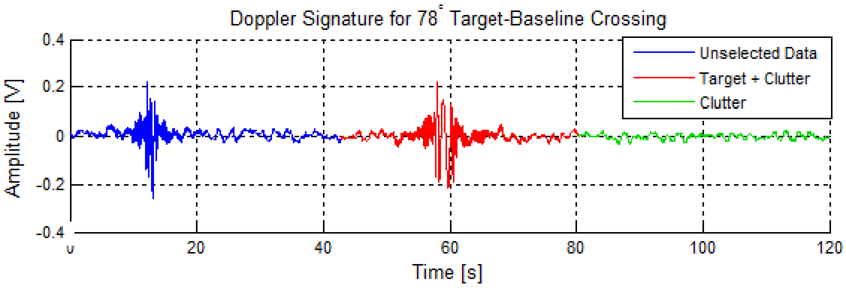

Figure 5.2-3. Doppler signature for two baseline crossings of the MISL boat. Red indicates target selection corresponding to a 78° crossing angle, green indicates a pure clutter selection, blue indicates data not selected for use in analysis.

The power spectral densities (PSD's) of the selected target (plus clutter) signature (red) and the selected clutter section (green) are shown in Figure 5.2-4 (in corresponding colours).

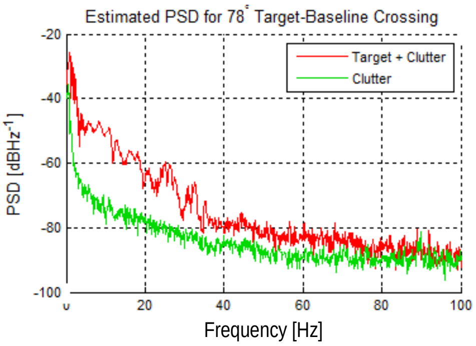

Figure 5.2-4. Power spectral density of target and clutter for a target-baseline crossing angle of 78°.

It can be seen both from time domain and PSD that the target signatures have a high SCR; the target is clearly visible above clutter and occupies a much wider spectral bandwidth.

5.2.1.2 *RECORDED SIGNATURES FOR 52° BASELINE CROSSING OF SMALL INFLATABLE BOAT*

Figure 5.2-5 shows the recorded trajectory for a target crossing the baseline at an angle of 52°.

Figure 5.2-5. GPS track data for target trajectory. Blue shows full track and red indicates section used for analysis.

In this case, the target speed is measured to be 10.6 km h^{-1} equivalent to 5.7 knots, which is similar to the speed of the target for the 78° crossing angle and so a good comparison. The Doppler record containing the target signature relating to the above trajectory is shown in

Figure 5.2-6. This record contains the target selected in red, the signature of a sailboat as it crossed the baseline in the blue section and a clutter selection in green. The PSDs for the target (plus clutter) and clutter selection are shown in Figure 5.2-7.

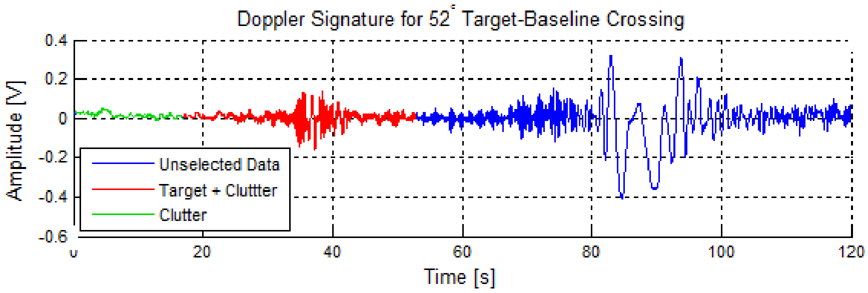

Figure 5.2-6. Doppler signature for baseline crossing of the MISL inflatable. Red indicates target selection corresponding to a 52° crossing angle and green indicates a clutter selection.

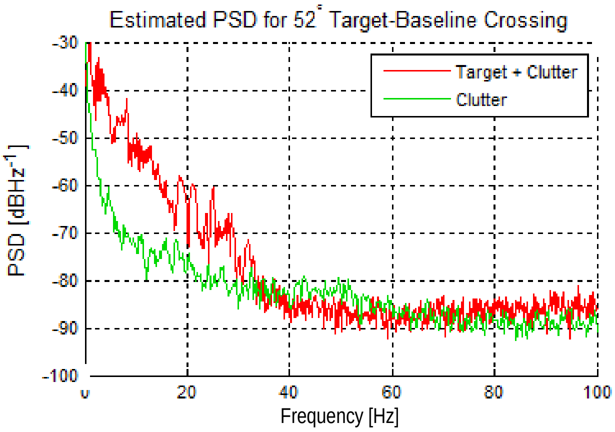

Figure 5.2-7. Power spectral density of target plus clutter for a target-baseline crossing angle of 52°.

Again the target is clearly separable from the clutter in both time and frequency domains. The Doppler spread of the target is still well removed from the clutter band.

5.2.1.3 *RECORDED SIGNATURES FOR 34° BASELINE CROSSING OF SMALL INFLATABLE BOAT*

Figure 5.2-8 shows the recorded trajectory for the target present in the Doppler signature in Figure 5.2-9. The GPS track of the target gives a velocity of 10.2 km h^{-1} or 5.5 knots.

Figure 5.2-8. GPS track data for target trajectory. Blue shows full track and red indicates section used for analysis.

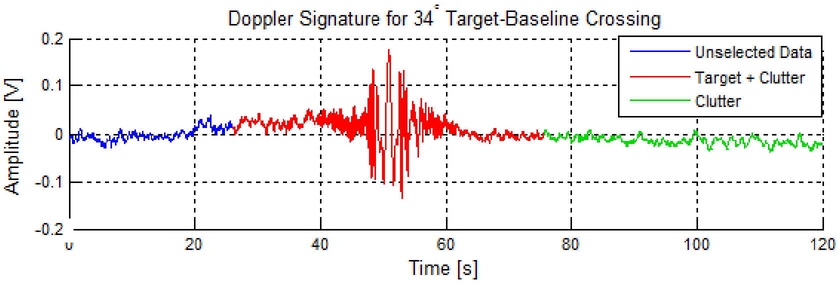

Figure 5.2-9. Doppler signature for baseline crossing of the MISL inflatable. Red indicates target selection corresponding to a 34° crossing angle and green indicates a clutter selection.

The PSD's of the selected target signature (red) and the selected clutter section (green) are shown in Figure 5.2-10. Yet again the target can clearly be seen above clutter, however it is noted that the spread of the target spectrum is reduced for the lower crossing angles – this is expected from the FSR topology—however the target is still separated from the narrow clutter.

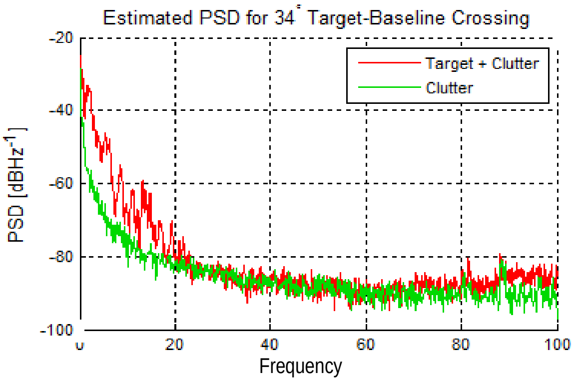

Figure 5.2-10. Power spectral density of target plus clutter for a target-baseline crossing angle of 34°.

5.2.1.4 *COMPARISON OF CROSSING ANGLE SPECTRA*

Figure 5.2-11 shows a comparison of all three target crossing angle PSDs plus one selected example of a clutter spectrum.

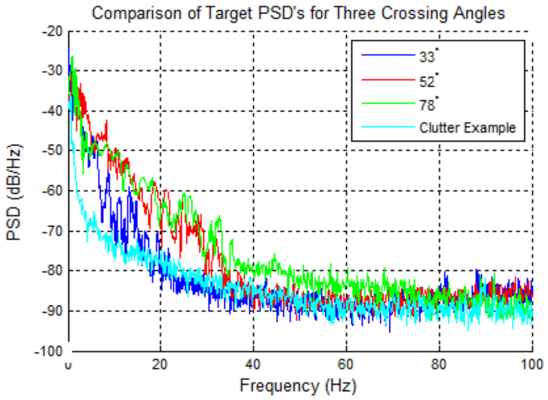

Figure 5.2-11. Comparison of target signature PSDs for target-baseline crossing angles of 78, 52 and 33°, alongside a selected example of clutter from one of the corresponding records.

5.2.1.5 *TARGET TRAJECTORY ALONG THE BASELINE*

At first thought one potential disadvantage of the FSR system is the non-detection of targets that are travelling directly along the baseline, where Doppler will be zero. Fundamentally this is not an issue for two main reasons. Firstly the target actually has to reach the baseline and in doing so has to approach from some larger angle; secondly attempting to maintain a trajectory directly along the baseline (especially in smaller craft) is extremely difficult. There is the added advantage that when the target is very near the baseline, even though the Doppler is small, the FSCS (forward scatter cross section) at these angles is at its greatest. Attempts have been made to record the MISL small inflatable travelling along the baseline with an effort to maintain as accurate a trajectory as possible. Figure 5.2-12 gives the GPS track for such a trajectory. It shows the difficulty involved in maintaining a straight line trajectory over the relatively short distance of 298 m even with complete visibility of transmitter and receiver as a guide.

Figure 5.2-12. GPS target track for attempted ‘along baseline 0°’ trajectory.

Figure 5.2-13 shows the signature recorded along this trajectory, towards the beginning of the signature, entry onto the baseline is noticeable as well as a baseline crossing (around 35-40 s), at the end, the boat makes some loops around the baseline and then moves away.

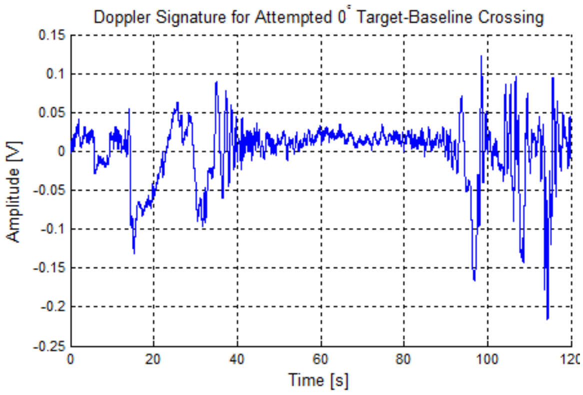

Figure 5.2-13. Doppler signature for attempted ‘along baseline’ trajectory.

5.2.1.6 *SUMMARY AND CONCLUSIONS FOR BASELINE CROSSING ANGLE RESULTS*

It can be seen from the PSDs in Figure 5.2-11, that he smaller the crossing angle, the narrower the target spectrum (when target speeds are more or less constant). This behaviour is expected from FSR geometry due to the velocity components of the target being larger with respect to transmitter and receiver at greater angles – thus higher Doppler.

The smaller the crossing angle the longer the observation time as the target occupies the region around the baseline for a longer time. This can be seen especially so by comparing the highlighted target signatures in Figure 5.2-3, Figure 5.2-6 and Figure 5.2-9; observing the relative widths in the time domain. It should be noted though that for the given parameters, in each case, the target Doppler spread is still well separated from the clutter spectrum even at such low speeds, making detection possible.

The potential difficulty posed by targets traversing along the baseline with zero Doppler is not realistic as essentially the targets need to travel to the baseline initially, also maintaining such a trajectory on the sea is difficult.

5.2.2 VARIATION OF TARGET SIGNATURE WITH BASELINE CROSSING VELOCITY

To determine the variation of target signature with respect to target velocity, Doppler recordings were made of the MISL inflatable boat target crossing the FSR baseline approximately mid-way at 90°, with 1m antenna heights using a CW 7.5GHz signal. Various target speeds have been measured over the full period of our trials, here two speeds are shown, 10 knots and 5 knots which have been recorded when travelling with and against the tide in Langstone Harbour.

5.2.2.1 *RECORDED SIGNATURE FOR 10 KNOT TARGET VELOCITY*

Recorded/measured Doppler data for the small inflatable boat target is found in Figure 5.2-14 (a), red indicates the target signature and green the clutter which are then used to form the PSD's in (b). The signature denotes the boat travelling with the tidal flow into the harbour. In Figure 5.2-14 (b) the spectral width of the target signature is effectively wide due to the relatively high speed of the target, noticeable above the clutter/noise level up to approximately 60Hz.

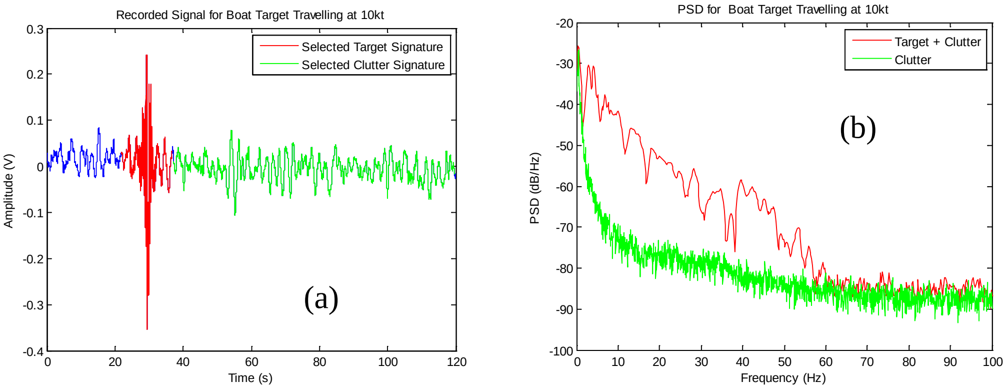

Figure 5.2-14. Doppler signature (a) and PSD (b) for sea clutter and target with speed of 10 knots.

Figure 5.2-15 is the image of the target trajectory as measured by the GPS tracker. The blue line shows the complete measured trajectory and the red, the trajectory used to measure target speed and baseline crossing parameters. The speed is estimated at an average of 9.8 knots (10.5 knots across the baseline), with a crossing angle of 68°, crossing a 276m baseline 106 m from the transmitter Tx.

Figure 5.2-15. GPS tracks showing the measured target trajectory for the signature in Figure 5.2-14.

5.2.2.2 *RECORDED SIGNATURE FOR 5 KNOT TARGET VELOCITY*

Figure 5.2-16(a) and (b) are the corresponding Doppler data and PSDs from measurement relating to a slower target velocity, where the target is competing against the tide.

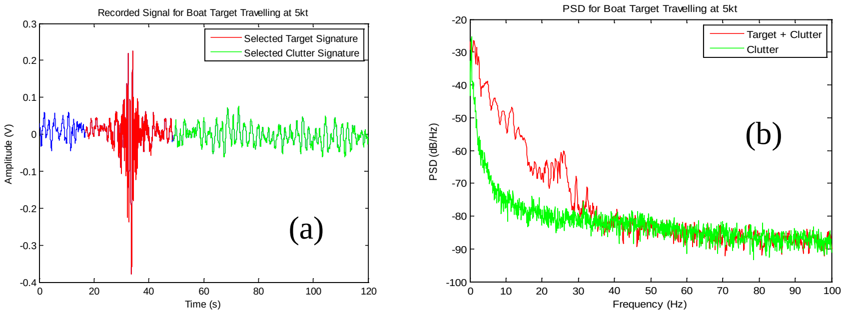

Figure 5.2-16. Doppler signature (a) and PSD (b) for sea clutter and target with velocity 5 knots.

Figure 5.2-17 indicates the target trajectory as measured by the GPS tracker. The blue line shows the complete measured trajectory and the red, the trajectory used to measure target speed and baseline crossing parameters. The speed is estimated at an average of 4.8 knots (5.4 knots across the baseline), with a crossing angle of 83°, crossing a 276m baseline 127m from the transmitter Tx.

Figure 5.2-17. Map showing the measured target trajectory (red line) for the signature in Figure 5.2-16. Yellow line is the FSR baseline.

5.2.2.3 COMPARISON OF SPECTRA AND SIGNATURE FROM DIFFERENT TARGET VELOCITIES

Figure 5.2-18 shows the comparison of the PSD’s of the two target speeds.

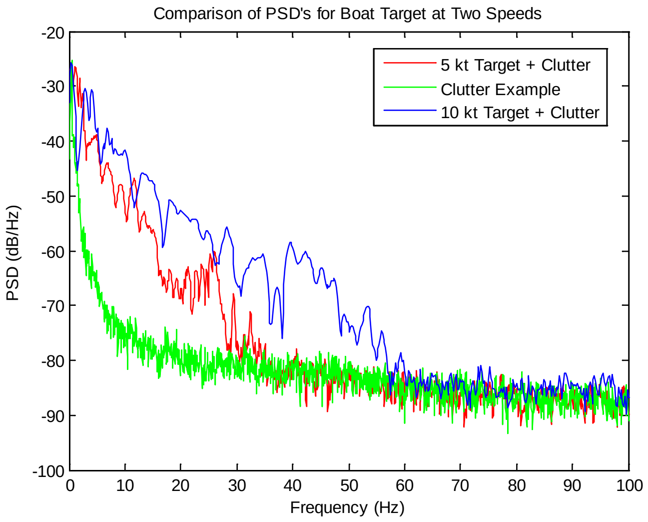

Figure 5.2-18. PSD comparison for boat target moving at speeds of 5kt and 10kt.

The figure indicates that the spectral width of the target signature at 5 kt is about half as wide as for the 10 kt as one would expect. The target spectra are visible above the clutter level up to a frequency of approximately 30 and 60 Hz for the different speeds. Zoomed versions of the time domain target signatures are found in Figure 5.2-19 and it can also be seen that the signal durations are also related by a factor of 2 (approximately).

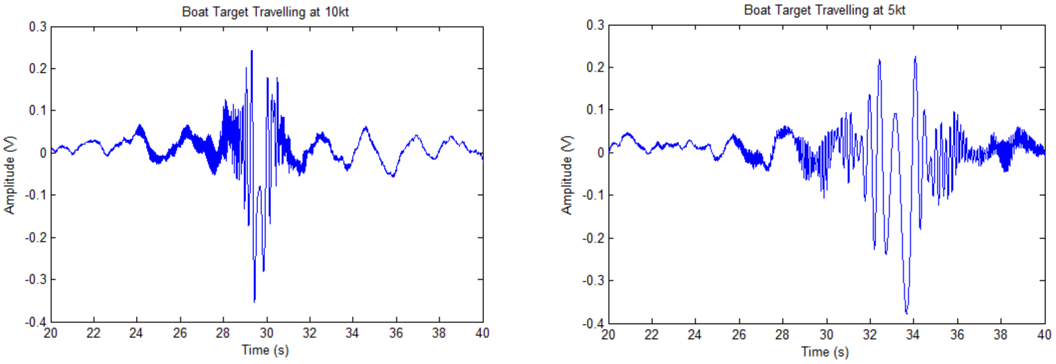

Figure 5.2-19. Zoomed target signatures at 5 and 10 knots, indicating relationship between signal duration.

5.2.2.4 *SUMMARY AND CONCLUSIONS FOR TARGET VELOCITY VARIATION RESULTS*

As expected, the bandwidth of the PSD is greater for the faster moving target. This is (as expected) in proportional to the speed being two times faster and all other conditions being reasonably equal. This proportional speed difference is also visible in the target signatures themselves, with the slower speed target having a twice longer duration signature in than the faster target, purely because the target has spent longer in the vicinity of the baseline. The target is still well separated from the clutter even for such a low speed as 5 knots.

It is reassuring that the measured amplitudes of the received signals are very similar due to the target FSCS (forward scatter cross section) remaining constant, slight fluctuation occurs due to the underlying clutter.

5.2.3 TARGET DETECTABILITY AS A FUNCTION OF SEA STATE

Data has been collected in what might be termed different ‘sea states’, though in the littoral environment of Langstone Harbour it is very difficult to classify in terms of real sea state as defined by the WMO (World Meteorological Organisation), which requires that the area of surface to be classified is large and has been exposed to external conditions for a long period of time. During the course of our trials, the surface conditions have visibly changed due to factors including tidal flow of varying strengths and weather conditions influencing waves coming into the harbour – though we cannot say there is a direct relationship between wind speed and surface conditions measured inside the harbour.

It has been possible using video recordings of the trials to select a few measurements in which we can say we have different sea states. The actual values of sea state are estimated and this is a very objective process. However we can at least separate lowest visual sea state from highest and some value in between.

Measurements shown here have been made using a 7.5 GHz CW signal, with a baseline range of approximately 300 m.

5.2.3.1 *TARGET SIGNATURES AT LOWEST ESTIMATED SEA STATE (1-2)*

Figure 5.2-20 shows the Doppler signature of the MISL boat and sphere target for motion over what is deemed to be a low sea state of 1-2, along with corresponding video capture stills of the sea surface during the measurement. The measured wind speed and direction was 1.4 km h^{-1} Westerly.

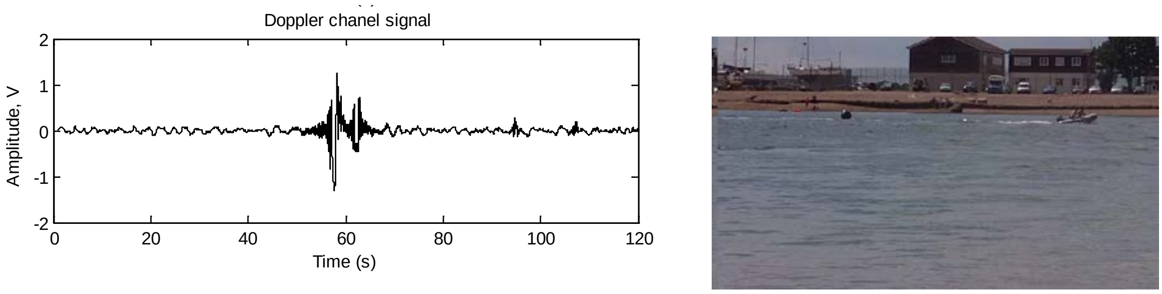

Figure 5.2-20. Recorded Doppler signature and image of lowest sea state (1-2) – including boat and sphere target.

Target and sphere are clearly visible over the sea clutter at around 60 s into the record.

5.2.3.2 *TARGET SIGNATURES AT MID ESTIMATED SEA STATE (2-3)*

Figure 5.2-21 shows a recorded target signature and still capture image of the sea surface for what is estimated to be somewhere in between the lowest and highest sea states in the available data, an approximate sea state 2-3.

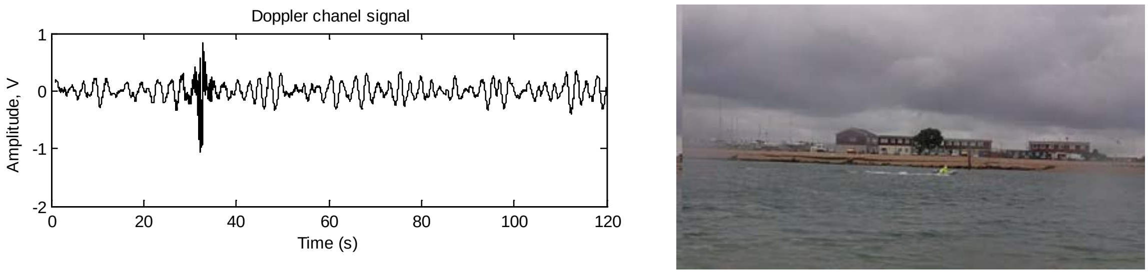

Figure 5.2-21. Recorded Doppler signature and image of sea state 2-3.

Target is still highly visible within the clutter (around 30 s), but much less so than the lower sea state case in Figure 5.2-20.

5.2.3.3 *Target Signatures at Highest Estimated Sea State (3)*

Figure 5.2-22, Figure 5.2-23 and Figure 5.2-24 represent the case of what are deemed to be the highest sea state measurements, around sea state 3.

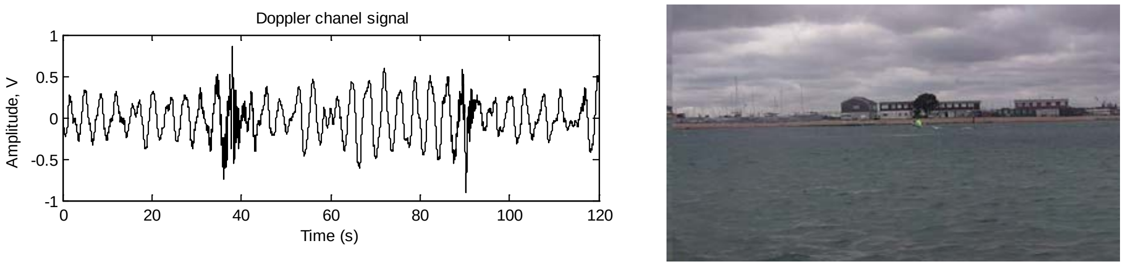

Figure 5.2-22. Recorded Doppler signature and image of sea state (3), target is visible at around 35-40 s and 90 s.

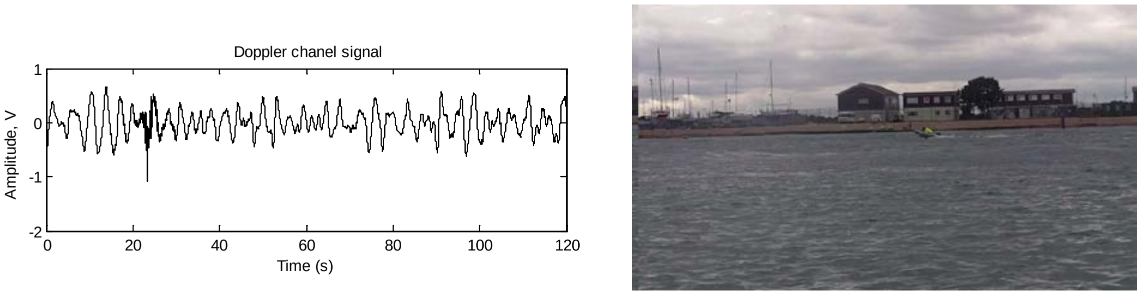

Figure 5.2-23. Recorded Doppler signature and image of sea state (3), target is visible at around 22 s.

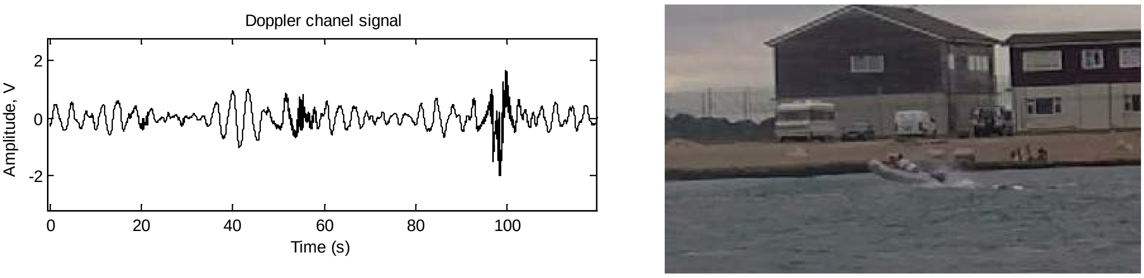

Figure 5.2-24. Recorded Doppler signature and image of boat jumping from the surface in highest sea state (3), target is visible at around 50-60 s. A larger boat target crosses the baseline at 100 s.

All measurements contain the MISL inflatable and it can be seen in the still captures that the small inflatable has left the water's surface - giving an indication of the roughness. The wind speeds and directions measured during the records are 3.4 km h^{-1} W, 4.4 km h^{-1} SW and 3.7 km h^{-1} SW respectively. Visually the target signatures become less visible within the clutter as we reach sea state 3 as you would expect, as the clutter amplitude rises, but target amplitude remains the same. Even though spectral plots would be ideal, it is visually clear that the density of the target signature oscillations (Doppler frequency) are separating the target from the clutter. As the clutter resides in quite a narrow bandwidth (<1 Hz) as presented in Section 5.1, with the use of a simple (non-optimised) 2 Hz HPF much of this can be removed to give good signal to clutter ratios without the need for a whitening filter designed around the measured clutter spectrum. Figure 5.2-25 shows a filtered version of Figure 5.2-23, an estimated sea state 3 record. The improvement through clutter reduction is clear.

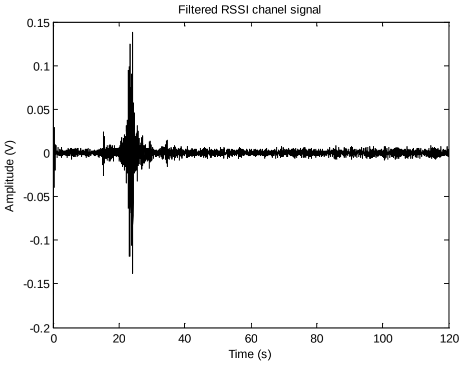

Figure 5.2-25. Target signature from Figure 5.2-23 after application of 2 Hz HPF to remove clutter.

5.2.3.4 *SUMMARY AND CONCLUSIONS FOR SEA STATE VARIATION*

Video, photographic, written and weather data have been collected during the majority of trials which have enabled the approximation of the sea state for certain Doppler records. Though this can quite subjective it still enables the selection of records for which the sea surface clearly has different roughness.

Even though the clutter amplitude rises, the narrow clutter spectrum means that still in high sea states, it may not overlap completely with the lower power target spectrum, thus allowing the use of a HPF for clutter removal, still leaving adequate signal power for detection.

5.2.4 EFFECTS OF POLARISATION ON TARGET SIGNATURE

Measurements have been performed to estimate the system performance with respect to varying antenna polarisation. The horns used in the trials presented here are equal beam width in both planes (±10°), ensuring no effect of antenna pattern when changing polarisation.

The MISL small inflatable boat is used as the target and measurements are made using a CW 7.5GHz signal with 1m antenna heights. On inspection of the recorded GPS track data the target trajectories for each measurement have similar baseline crossing points and angles, the speeds are in the range 10-12 knots. Absolute peak signal value for the target and received dc signal level are indicated, the dc level gives an indication of the received signal (leakage/direct path) strength and is removed from signatures shown before plotting.

Doppler data for a target recorded with both the receiving and transmitting antennas having vertical polarisation is shown in Figure 5.2-26 (a). The red highlight indicates the inflatable boat target signature and green a section of clutter. Figure 5.2-26 (b) shows the corresponding PSDs for these sections of the signature. The absolute peak signal value for the target and received dc signal level are indicated, as before, the dc level is removed from signatures shown before plotting. The same target is recorded for H-H polarisation depicted in Figure 5.2-27, (a) showing the Doppler signature and (b) the PSDs of the selections.

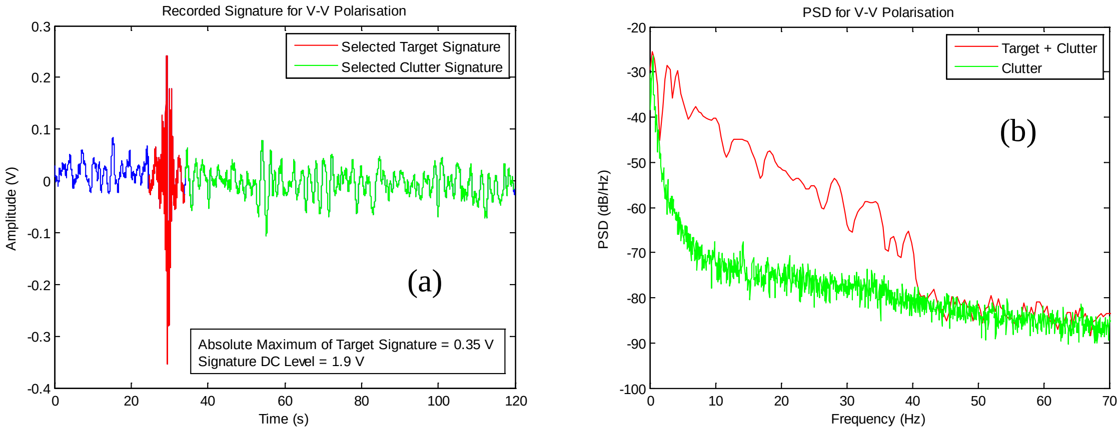

Figure 5.2-26. Doppler signature (a) and PSD (b) for target and clutter recorded with V-V polarisation.

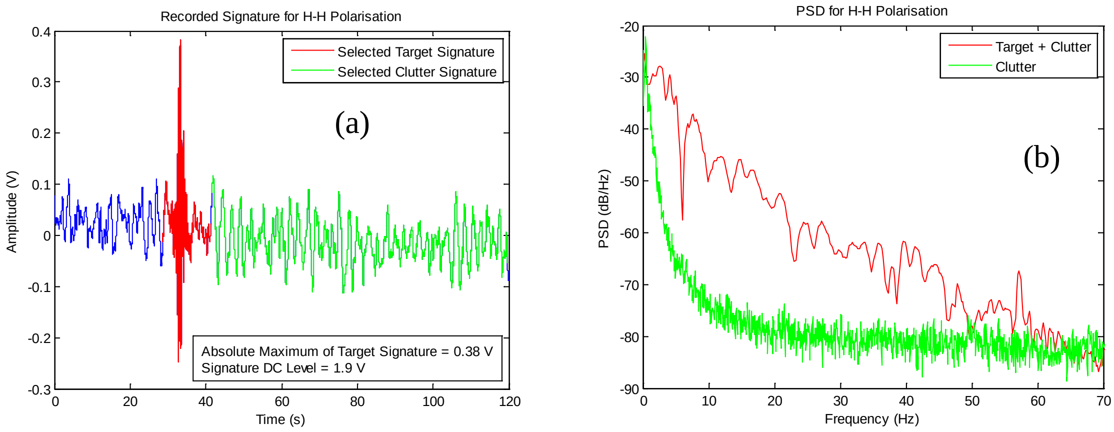

Figure 5.2-27. Doppler signature (a) and PSD (b) for target and clutter recorded with H-H polarisation.

Finally, the same target was recorded with cross polarisation H-V, shown in Figure 5.2-28, again with (a) showing the full and selected parts of the recorded Doppler signature and (b) the corresponding PSDs. Note that Figure 5.2-28 also contains the signature of a larger boat crossing the baseline (blue section).

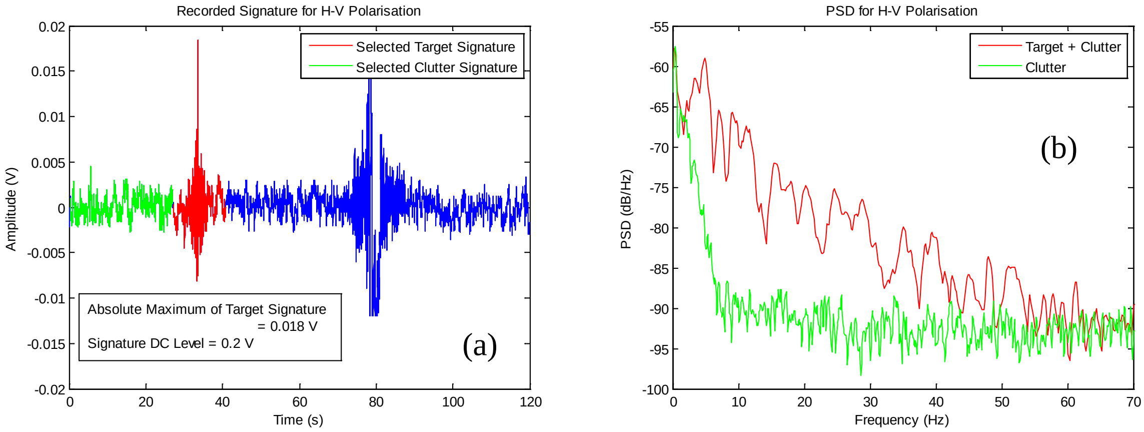

Figure 5.2-28. Doppler signature (a) and PSD (b) for target and clutter recorded with H-H polarisation.

It can be seen when comparing the co-polar measurements (note the different axis scales) that the target signature amplitudes and the direct path propagation amplitudes (dc levels) are reasonably coincident. Thus for the target signature, this implies no real dependence on polarisation. This is to be expected, as in FSR the propagation model is expected to be independent of the polarisation, due partly to the conductive surface material, but mainly the low grazing angles involved in the topology (Section 3.2). Due to the scattering mechanism in FSR being equivalent to diffraction from an aperture, at high frequencies we expect no depolarisation from the target scattering, and indeed the FSCS should not be dependent on the incident polarisation, as shown in Section 3.1. What is obvious is the dramatic drop in absolute signal power for the cross polarised case—the spectra showing a 25-30 dB reduction in power in relation to the co-polarised case (again note different axis scales in plots). This level of signature may be explained by the effect of antenna depolarisation, i.e. the antenna does not have perfect polarisation characteristics and will still receive a small amount of opposite plane polarised signal.

5.2.5 MEASUREMENT OF POTENTIAL DETECTION RANGE

In order to give insight into the potential detection range of the experimental system, the decision was made to test on the calmest surface possible. Therefore it was decided to move from sea to lake based trials, thus this section contains information gathered from trials on Coniston Water in the Lake District. This test site also gave us the ability to ground mount the antenna's at a variety of ranges; this is not possible at the Langstone harbour test site.

The signatures shown in this section are all recorded using a CW 7.5 GHz signal and an antenna height of 1 m. The target used is the MISL small inflatable and signatures contain either one or two baseline crossings of the boat.

5.2.5.1 *TARGET DOPPLER SIGNATURES FOR 726 M BASELINE*

The signature for a target detected at a range of 650m is shown in Figure 5.2-29. As before, the red highlight indicates the target signature itself (with clutter) and the blue the background noise and clutter. It is noticeable when comparing this signature to others, there is some unknown source of interference contained in the record; however the target signature is still visible between 50 and 60 s into the record.

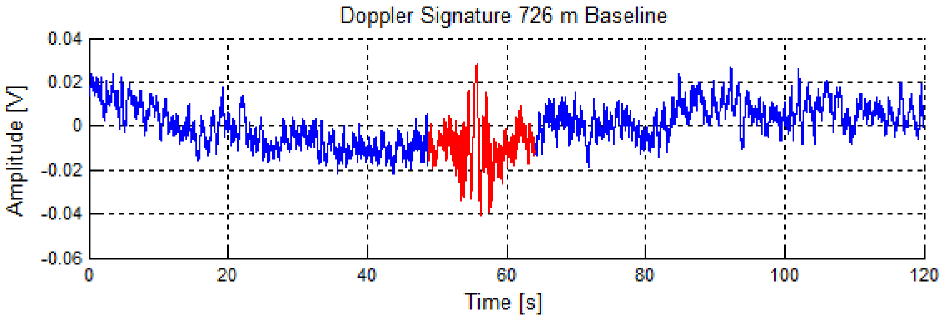

Figure 5.2-29. Doppler signature recorded with a 726 m baseline, target signature highlighted in red.

Figure 5.2-30 shows the GPS track data for the target trajectory in Figure 5.2-29. The target crossed 370 m from the transmitter (356 m from the receiver) at an angle of 82° to the baseline, with a velocity of 12.5 kmh^{-1} or 6.8 knots. The blue line shows the full trajectory and the red the section used for the GPS track analysis.

Figure 5.2-30. GPS track data for target trajectory. Blue shows full track and red indicates section used for analysis, green is the FSR baseline.

5.2.5.2 *TARGET SIGNATURES FOR 935 M BASELINE*

The Doppler signature for 2 consecutive target measurements over a 935 m baseline range is shown in Figure 5.2-31. The target signatures are highlighted in red and are reasonably well resolved visually. What is interesting to note here is the large amplitude, low frequency sinusoidal variation underlying the usual clutter variation. At the time of measurement a build-up of large long wavelength (swell like) undulations on the lake surface was seen. This was theorised to be due to combined wakes from multiple large passenger (sight-seeing) boats travelling on the contained body of water. The undulations essentially shifted the local mean surface height of the lake and this is the effect seen in the measurement. The multipath scattering from the surface is varying in unison with the slow surface height changes (the relative antenna heights are changing over time) giving what is a long term, 10 s – 15 s, periodic oscillation in the received signal power.

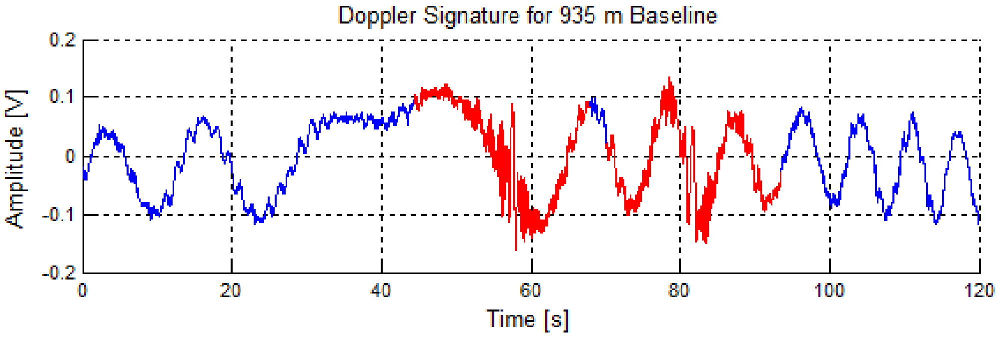

Figure 5.2-31. Doppler signature recorded with a 935 m baseline, two separate target signatures are highlighted in red.

The GPS track data sets used to calculate the target trajectory parameters for both target signatures in Figure 5.2-31 are presented in Figure 5.2-32. Blue showing full track and red the section used for analysis. The crossing points were 617 and 600 m from the transmitter, which makes this trajectory slightly off from a central baseline crossing, in a slightly more favourable position for detection. The crossing angles were 81 and 71° with velocities of 22.7 and 16.6 kmh^{-1}.

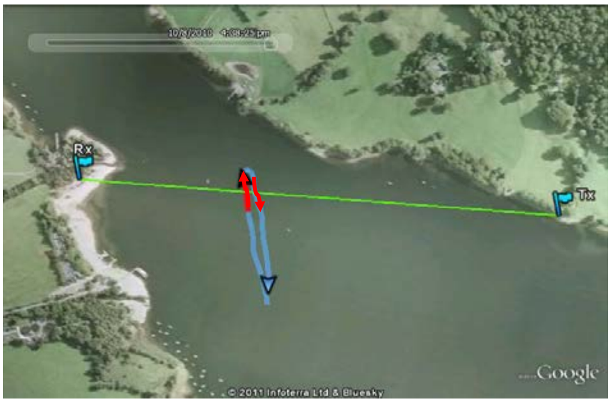

Figure 5.2-32. GPS track data for target trajectories. Blue shows full track, left red line highlights first target signature in Figure 5.2-31 right for second. Green line is the FSR baseline.

On implementation of a 2 Hz HPF for clutter removal, as was done for the high sea state case in 5.2.3.3, the two signatures are clearly visible as shown in Figure 5.2-33.

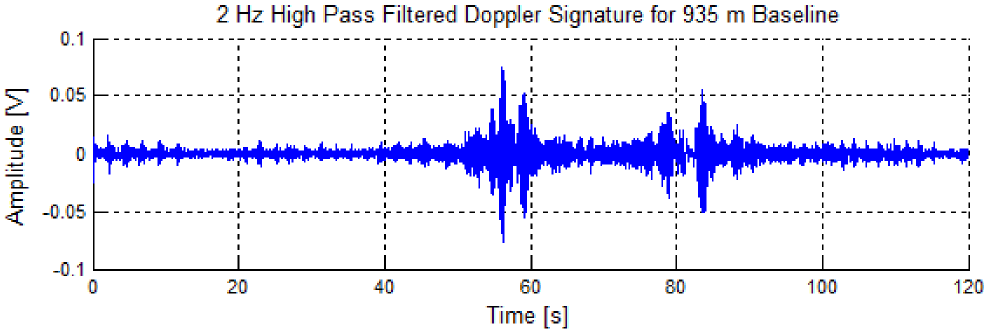

Figure 5.2-33. Doppler signature for a 935 m baseline, after application of a 2Hz HPF. Two target signatures are visible.

5.2.5.3 *TARGET SIGNATURE FOR 1287 M BASELINE*

The longest baseline measured was that of 1287 m. Figure 5.2-34 contains the received Doppler signature, where the target signal is highlighted in red and the corresponding target GPS track data is shown in Figure 5.2-35,

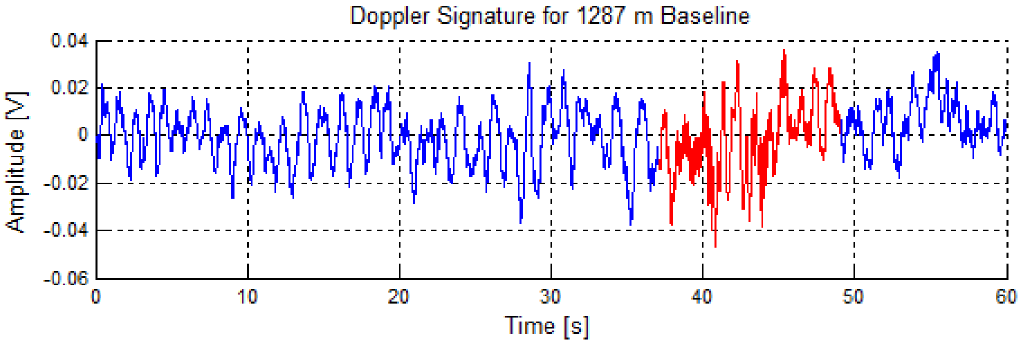

Figure 5.2-34. Doppler signature recorded with a 1287 m baseline, target signature highlighted in red.

Figure 5.2-35. GPS track data for target trajectory in Figure 5.2-34, Blue shows full track and red indicates section used for analysis.

The trajectory information gives the target-baseline crossing point at 643 m from the transmitter (almost exactly midpoint crossing), crossing angle of 81° and target speed of 22.6 km h^{-1} (12.2 knots). Still at this range the target signature is visible with no pre-processing performed on the data. Figure 5.2-36 shows the signal after being passed through the 2 Hz high pass filter.

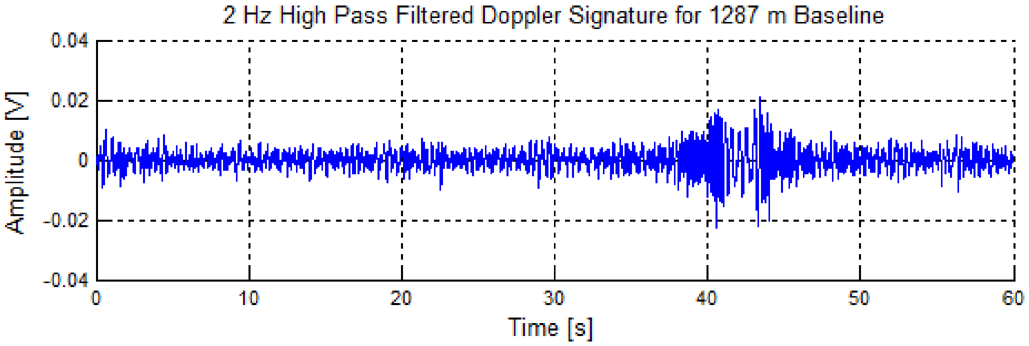

Figure 5.2-36. Doppler signature for a 1287 m baseline, after application of 2Hz HPF.

5.2.5.4 *SUMMARY AND CONCLUSIONS FOR TARGET DETECTION RANGE*

Data has been collected to show that it is possible to detect a small inflatable (2.9 m long) boat at a baseline range of approximately 1300 m, for the given smooth surface (~sea state 1) and radar parameters. These recorded signatures actually require no pre-processing to be visible, however it has been shown that the application of a HPF to remove the narrow band clutter can greatly improve the SCR/target visibility.

5.2.6 QUASI-OPTIMAL SIGNAL PROCESSING IN MARITIME FSR

Due to the lack of range resolution in FSR it is not possible, in the traditional sense, to track a targets position as it crosses the baseline. Target motion and trajectory parameters must therefore be inferred by other means. In [26] the process termed 'quasi-optimal' processing was introduced for the extraction of motion parameters in FSR and applied to experimental maritime target signatures[3]. The processing scheme, summarised here, relies on the creation of a database of pre-defined reference signatures, formed using the FSR target signature model in Section 3.1.4.1. The FSR signal model equation (3.1.8) is reproduced here with the dc term removed:

$$S_{\mathrm{ref}}(t) \approx A(t)\sin\left(2\pi f_0 t_{\mathrm{tgt}}(t)\right) \tag{5.2.1}$$

$A(t)$ is a time varying envelope, related principally to the FSCS, the argument of the sin function is the target Doppler where f_0 is the FSR operating frequency and

$$t_{\mathrm{tgt}}(t) = \frac{R_{\mathrm{t}}(t) + R_{\mathrm{r}}(t) - D}{c} \ . \tag{5.2.2}$$

$R_{\mathrm{t/r}}(t)$ are time varying target to transmitter/receiver ranges related to the target baseline crossing point and velocity and D is the baseline length. Using (5.2.1) a set of reference signatures can be produced, $S_{ijk}^{\mathrm{ref}}(t)$, which cover a range of expected target velocities $\left(v_{\mathrm{x}}^{i}, v_{\mathrm{y}}^{j}\right)$ and baseline crossing points y_{c}^{k}, where $i = 1 \ldots N_{v_{\mathrm{x}}}$, $j = 1 \ldots N_{v_{\mathrm{y}}}$ and

---

[3] The author of this thesis contributed in part with the first author to the development of the 'quasi-optimal' processing in [26] and played the major role in the creation of the software for its application to measured target signals.

$k = 1 \ldots N_{y_c}$. The total number of references in the database is $N_{v_x} N_{v_y} N_{y_c}$. The estimation of target motion parameters is now just a case of sequentially correlating the references with the measured signals. The reference providing the maximum correlation output gives the trajectory parameters best matched to that of the target.

No mention has yet been made concerning the envelope term in (5.2.1). The target velocities and crossing points used to create reference functions can be expressed within some expected ranges, dependent on the expected target types. The amplitude envelope of the reference (and indeed the measured signals) is a function of the FSCS pattern and hence target profile shape. It is not reasonable to expect the database can be extended to include references for all possible target profile shapes. In [26], correlations were performed on a series of chirps with different window functions and frequencies. It was shown through example, that the correlation output is much less affected by the slowly varying envelope than it is by the faster sign-alternating phase, i.e. estimating the Doppler correctly is much more important than using the correct target profile shape. Hence, as the processing does not fully account for this envelope parameter it has been termed ‘quasi-optimal’. Figure 5.2-37 shows the application of the quasi-optimal processing to three recorded maritime signatures. The left panes show the target trajectory with respect to the baseline, the middle panes are the recorded signatures and the right panes show the best matched reference waveform from the processing. The figures show that the signal envelope of the recorded signature may appear very dissimilar to the reference e.g. in (b) and (c). In these cases it is due to the underlying clutter and potential non planar motion of the target over the sea. Even so, as shown in

Table **5.2-1**, which compares the measured and extracted target motion parameters, very good estimations of the target motion parameters can be obtained purely by the phase matching.

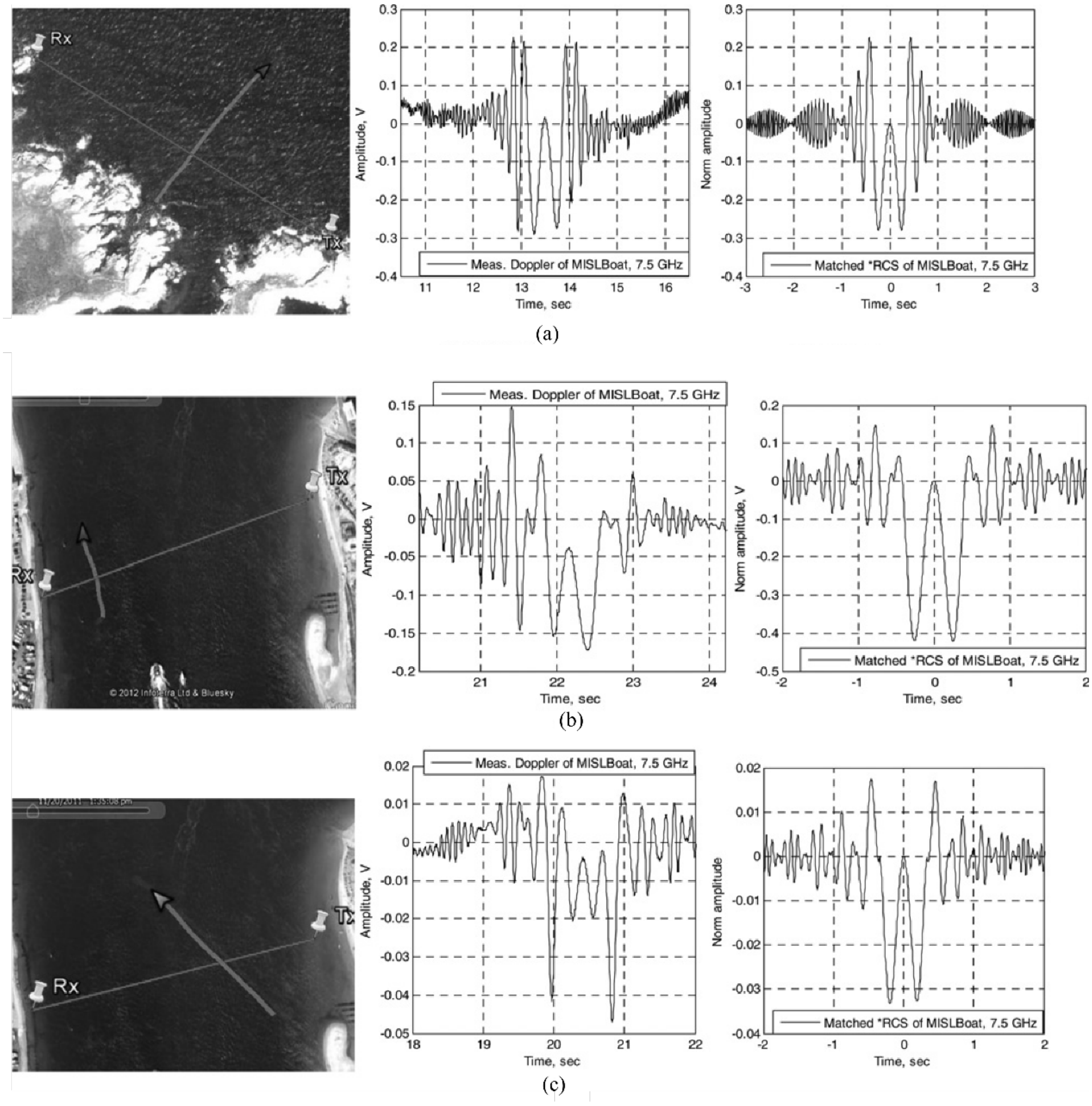

Figure 5.2-37. Example of measured maritime target signatures and matched waveforms from correlation processing. Left hand panes show the target trajectory, middle panes the recorded signature and right hand show the matched reference signal. (a) represents a target crossing the middle of a baseline perpendicularly, (b) a perpendicular crossing nearer to the receiver and (c) a crossing angle of around 60°. Reproduced from [26].

Table 5.2-1. Comparison of measured (GPS tracked) and extracted motion parameters for the target trajectories shown in Figure 5.2-37. Reproduced from [26].

	Baseline, m		Speed, v	Crossing angle φ,°	Crossing point, distance from the middle, m
(a)	350 (Bulgaria)	GPS recorded	10–10.3 knots (18.52–19.0756 km/h)	~90	12
		extracted	19.08 km/h	90.0	20.0
(b)	285 (UK)	GPS recorded	6.6–7 knots (12.2232–12.964 km/h)	~90	85.5
		extracted	13.32 km/h	90.0	80.0
(c)	262 (UK)	GPS recorded	9–10.3 knots (16.668–19.0756) km/h	~60	40
		extracted	17.64 km/h	60.0	60.0

The processing technique does require optimisation and future research may be based upon this. The generation of the database of signatures needs to be fundamentally investigated i.e. how to determine the optimal velocity component and crossing point increments used to create the database, and understand how this affects the accuracy in the estimations. It may not be as simple as creating as many references as possible. Ultimately the processing could use iterative refinement from an initial set of grossly spaced generated signatures to find upper and lower bounds of the parameters and then refine within these.

The quasi-optimal processing scheme was developed in FSR in order to provide a method of estimating target kinematics. However, the scheme is fundamentally the application of the correlation matched filter (Section 2.9), which is used to compress the signal and increase the SCR.

Figure 5.2-38 shows a Doppler signature consisting of two MISL inflatable crossings, one at around 55 s the other at 100 s overlapping with another larger boat. The sea state is an estimated sea state 3. Again, with the use of a 2 Hz HPF again the clutter components can be removed as shown in Figure 5.2-39. The target(s) positioned around 20 s in time were believed to be seagulls crossing through the FSR baseline close to one of the antennas.

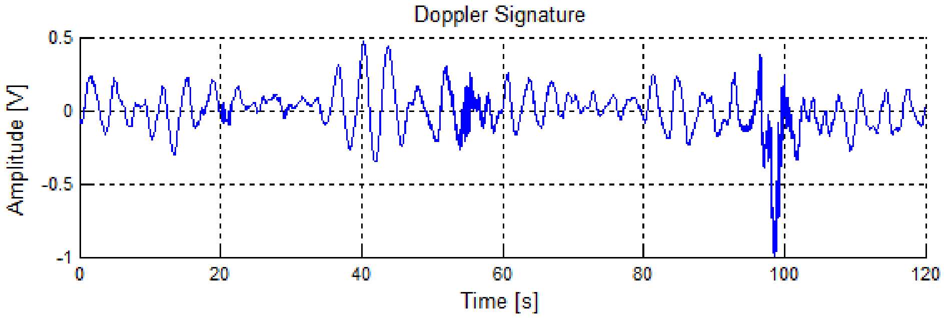

Figure 5.2-38. Doppler signature containing two inflatable boat crossings, one overlapping with a larger boat at around 100 s, in an estimated sea state 3.

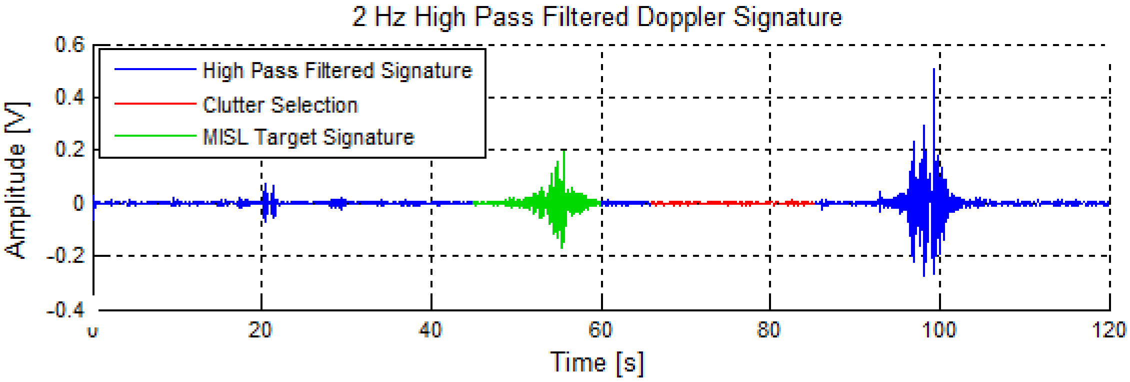

Figure 5.2-39. 2 Hz high pass filtered Doppler signature of Figure 5.2-38.

The red highlighted part of the Figure 5.2-39 indicates a section of filtered clutter of which the standard deviation is 0.003 V. The inflatable boat target signature, in green, has a maximum value of 0.20 V. This gives an estimated ratio of the standard deviation to maximum of 36.5dB. Applying the quasi-optimal correlation processing to this Doppler signature (after applying the same 2 Hz HPF filter to the reference database) yields the output shown in Figure 5.2-40. Green highlights the compressed target signature and red a section of clutter, visually selected with effort to avoid including the side lobes of compressed target signatures.

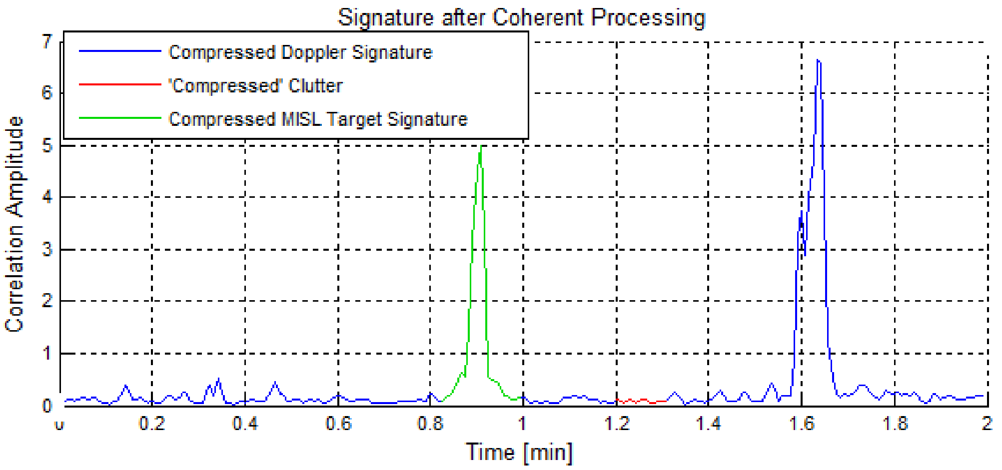

Figure 5.2-40. Measured target signatures after quasi-optimal correlation processing.

The standard deviation of the red highlighted clutter is now 0.023 and the compressed target signature peak is 5.0, giving a new ratio of 46.8dB. Thus after quasi-optimal processing the SCR has improved by 10dB. It should also be noteed that at around 1.6 mins into the record it is potentially possible to distinguish the smaller boat target from the larger, as there are two compression peaks.

The application of the quasi-optimal processing for improving target detection requires future investigation; here it is just shown as a concept applied to an example signature. Detection schemes as a whole need to be developed for the FSR system and its capabilities against low SCR (otherwise termed marginal) targets need to be assessed. At this time, the investigation of target detection algorithms and detection of marginal targets has not been considered (due to time constraints). It is however a priority for future work. In the first instance, the current target data set can be used to make estimates of the target statistics. Also if the proposed FSR target signal models can be verified against the data, they can be used for simulation of the statistics for many scenarios. The knowledge of the clutter and target statistics will allow the formation of receiver operating characteristic (ROC) curves. These are used to visualise the probability of detection, P_d, of targets with a given SCR for a given probability of false alarm, P_{fa} (probability of erroneous detection). The probability of false alarm is defined by the clutter statistics and a chosen detection threshold voltage, V_{t}, at the receiver output. It is calculated from the integral of the clutter probability density function (PDF), p_{c}, expressed in its basic form as:

$$P_{\mathrm{fa}} = \int_{V_{\mathrm{t}}}^{\infty} p_{\mathrm{c}} dV \qquad (5.2.3)$$

The detection probability is the same integral performed over the target signal plus clutter PDF, p_{s},

$$P_{\mathrm{d}} = \int_{V_{\mathrm{t}}}^{\infty} p_{\mathrm{s}} dV \qquad (5.2.4)$$

If the PDF for targets is known, then the probability of detection, P_{d}, can be found for the defined detection threshold. The sea clutter levels in FSR will however change over time due to, for example, variation in sea state. In practice a constant false alarm rate (CFAR) detector should be employed for automatic detection. A CFAR detector samples the clutter from the data as it is being collected and adjusts the voltage threshold according to the statistics; maintaining the chosen false alarm rate. There are many variants of the CFAR detector, one of the more common being the cell averaging-CFAR (CA-CFAR). The CA-CFAR takes the average statistical parameters of reference ‘cells’ of data on either side of a test cell. It then adjusts the detection threshold for that test cell accordingly. This is subject to investigation, but CA-CFAR would seem a good initial choice in FSR, as the clutter is generally observed to be homogenous over time (see previous experimental measurement results) i.e. the clutter in the reference cells would be representative of the clutter in the test cell. Changes in the FS clutter tend to occur over relatively long periods of time, allowing the CFAR time to adapt. The reader is directed to [63] for more information on CFAR and the fundamentals of radar detection.

5.3 SUMMARY OF MEASUREMENT CAMPAIGN RESULTS

This section presented a selection of results from a comprehensive measurement campaign to gather target and clutter data in Maritime FSR, in a variety of conditions. To the author’s knowledge it is a novel and unique dataset, which, as intended will provide data for the further investigation of the system.

Initially an overview of clutter spectral and statistical analysis was given, and it was seen that for a wide range of measurement parameters, the clutter spectral power is concentrated below 1 Hz and the statistics appear Rayleigh distributed. Target measurement results for varied scenarios were then presented; a qualitative analysis has been made at this stage to describe the effects seen in the context of FSR. For example, independence of polarisation, target spectra variation for different target kinematics.

A quasi-optimal correlation processing scheme was introduced, based on the earlier proposed signal models to provide estimation of target kinematic parameters in FSR. This was then applied to real data and showed good estimation of the motion parameters—this example may also give partial verification of the signal models. Target tracking/trajectory estimation is very important for any radar system. Due to the lack of range resolution in FSR, the only method by which any form of trajectory estimation is possible for a single baseline is through the use of this processing. The quasi-optimal correlation method is fundamentally related to matched filtering and is also crudely applied to target signatures to show improvement of the SCR. Now that the fundamentals of the processing have been laid down, optimisation and further examination should be carried out. The target detection performance of the FSR system, especially for low SCR (marginal) targets is one of the most important area of the system analysis and should be considered as high priority. Estimation of the performance requires knowledge of both clutter and target statistics in order to probabilities of false alarm and detection. Now that experimental target signatures have been collected, an estimation of target statistics may be made. Ultimately the signal model proposed in this thesis need to be shown to adequately reproduce the statistics. It can then be used to produce estimates for a wide range of parameters. The data should also be used to verify the power budget so that estimations can be made of the types/dimensions of target that will be considered marginal for given scenarios.

6 TARGET LINE OF SIGHT VISIBILITY IN HIGH SEA STATES

Due to the logistics of maritime testing, the majority of trials performed and data collected have been restricted to littoral waters, shore mounted antennas and the lower sea states (1-3 WMO). The outcome of this is that the line of sight (LOS) between antennas and antennas and target is rarely if ever lost due to wave blocking, i.e. the wave being high enough to block the radar/target scattered signals as in Figure 5.3-1. As mentioned in Section 4.1 the ultimate aim of the Maritime FSR system is to perform as a netted (multi-static) array of buoy mounted transceivers. In this situation, not only will the motion of the target contribute to blockage, but also the vertical and tilting motions of the antennas on their buoy mounts.

Until the time comes that it is possible to produce such experimental testing out in deeper waters with buoy mounted equipment, it is necessary to estimate to some degree what the level of wave blocking that will be present in the scenarios that are likely to be encountered i.e. sea conditions in which the small ‘difficult’ targets of interest would be at sea. In the long run, this can be an aid to estimating the target detection capability of the FSR system. This chapter presents a geometric (currently not electromagnetic) model that gives insight into the matter at hand and a selection of results from simulations based on the model. The model itself is a direct discrete synthesis of a deep sea surface onto which antennas and target models are placed and then the simulation is evolved through time to emulate an FSR baseline crossing. The target traverses the sea surface, under the influence of the surface height and the antennas sway and move according to the surface conditions at their base positions. During the traversal of the target, LOSs are estimated purely through the use of geometric rays drawn between antennas and target (as in Figure 5.3-1). At this stage the model is purely based on sea gravity waves (not capillary) as these are deemed to provide the most influence over LOS—the rest of this chapter describes the method used to generate the sea surface and the simulation model, followed by selected important results.

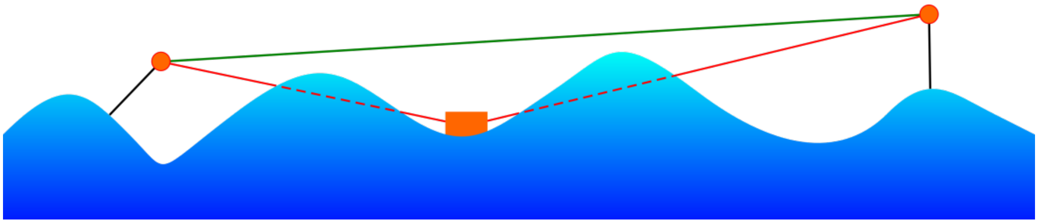

Figure 5.3-1. Antenna-target line of sight blocking due to high waves/sea state.

6.1 GENERAL METHOD FOR SURFACE SIMULATION

The computer-generated imagery (CGI) industry has been creating visually realistic simulations of the sea surface for computer games and movies for many years now and the methods used are useful for and indeed are now used in electro-magnetic scattering simulations.

The most commonly used method of sea surface simulation (due to its computational efficiency) involves the use of the inverse fast Fourier transform (IFFT) [80], [81]. The method is based on the assumption that the sea surface is composed as the sum of many sinusoids, (which relates to Airy's linear gravity wave theory [82]), with various amplitudes, frequencies, directions and phases. Thus the wave height, $\eta(\boldsymbol{x})$ at a position $\boldsymbol{x} = (x, y)$, at an instant in time, is given by

$$\eta(\boldsymbol{x}) = \sum_{\boldsymbol{k}} A(\boldsymbol{k}) e^{i\boldsymbol{k}\cdot\boldsymbol{x}} \tag{6.0.1}$$

Where $A(\boldsymbol{k})$ are the complex amplitudes (magnitude and phase) of the individual sinusoidal components specified by their wave vector $\boldsymbol{k}$. Here the sum for all $\boldsymbol{x} = (x, y)$ is to be performed computationally (and discretely) by the IFFT.

Some thought must be given to the choice of amplitudes and phases of the waves that are summed to construct the surface. Ocean waves in deep water are considered to be a Gaussian random process [83], irrespective of sea severity. Thus the measurements of surface displacement about the mean (over time, or a patch of sea) tend towards a Gaussian distribution; this and other statistical properties of the surface should therefore be reproduced in simulation. From the central limit theorem, the sum of a large number of random sinusoids should produce a Gaussian height distribution, provided the appropriate random variables are chosen for the construction of the individual sinusoids. There are two common methodologies adopted:

1. Non- deterministic spectral amplitude model (NSA)
2. Deterministic spectral amplitude (DSA)

These methods of Gaussian noise generation were originally developed by Rice [84] in his papers on the mathematical development of random noise, and are adopted in [85] to simulate random ocean waves.

The NSA model (also known as the random coefficient scheme) is derived from a representation of the surface height $\eta(x)$ through the discrete Fourier series in its quadrature form,

$$\eta(x) = \frac{a_0}{2}\sum_{n=1}^{N/2}(a_n \cos k_n x + b_n \sin k_n x)\,. \tag{6.1-1}$$

In which the d.c. component $a_0 = 0$ and the Fourier coefficients a_n, b_n are independent, normally distributed random variables with zero mean and a standard deviation σ_n defined by a prescribed discretised one sided energy density spectrum for the sea surface, $S(k_n)$, the choice of which will be discussed in the next sub-section. Thus the coefficients are given by,

$$\binom{a_n}{b_n} = \binom{\alpha_n}{\beta_n}\sqrt{S(k_n)\Delta k}. \tag{6.1-2}$$

Where α_n and β_n are normally distributed random variables with zero mean and standard deviation of 1 and Δk is the discrete wavenumber spacing of the energy density spectrum. These a_n, b_n can then be transformed into complex amplitudes A_n (one-sided) of the component waves in order to be used in the IFFT:

$$A_n = \left(\sqrt{{a_n}^2 + {b_n}^2}\right)e^{i\left(\mathrm{atan}\left(\frac{b_n}{a_n}\right)\right)} \tag{6.1-3}$$

Note the phase can actuallybe uniform random between 0 and 2π.

The DSA model (also known as the random phase scheme) uses the alternative form of the Fourier series,

$$\eta(t) = \frac{c_0}{2} \sum_{n=1}^{N/2} c_n \cos(\omega_n t - \theta_n)\,. \tag{6.1-4}$$

In this method, the Fourier coefficients c_n are determined directly from the energy spectrum, and are indeed the actual amplitudes of the wave components (hence the term deterministic),

$$c_n = \sqrt{2S(k_n)\Delta k}. \tag{6.1-5}$$

The phase term θ_n, is a uniformly distributed number in the range $[0,2\pi]$, thus the complex amplitudes (one sided) of the wave components of the surface are given by,

$$A_n = \left(\sqrt{2S(k_n)\Delta k}\right) e^{i\theta_n} \tag{6.1-6}$$

Which particular model to use is a matter of debate and there are arguments that the random phase method does not produce the correct statistics [86], though [87] argued that if enough frequency components are used, approximately 2000 comprising the main spectral peak, then the correct statistics are indeed reproduced. Essentially, the NSA model will reproduce surfaces more likely to be measured during say a single experimental trial as it randomly samples the energy spectrum, whereas the DSA model will reproduce a more average version as it directly uses the energy spectrum values – assuming the considered energy spectrum is one previously formed as an average from an ensemble of measurements. The method chosen for simulation in this thesis is the DSA, it requires the generation of only a single random variable and the number of samples chosen for the IFFT will be more than adequate.

6.2 EMPIRICAL SEA WAVE SPECTRA

In order to generate a model of the sea surface, as explained above, a description in terms of its energy density spectrum is required, both with regards to frequency/wavenumber and indeed direction. The most commonly used spectra are empirically derived from experimental data. This data is obtained from many sources, be that oceanic, lake/reservoir or wave tank, and measured in a variety of ways - wave buoys (of which there are many variations), ship based apparatus, wave staffs. The list is quite extensive and each experimental method for each developed spectrum cannot be discussed here and should be investigated as the reader requires, though an overview can be found in the more general ‘ocean wave’ texts such as [53] and [88].

There are two distinct parts of a full directional wave spectrum, the point spectrum and the directional spreading function. The point or uni-directional wave spectrum (as it assumes all wave energy is travelling in a single direction – the wind direction) is derived from wave recordings made at a single point on the sea surface, and essentially describes the combination of the wave energy from all directions at that point. The directional spreading functions (or directional energy distribution), are produced by combining data measured at multiple points on the surface and describe the actual angular distribution of the waves. The method of creating the spectra and directional function from measured data traditionally involved the Fourier transform of both auto and cross correlation functions, by use of Weiner-Kinchine theorm, more simple methods essentially boil down to performing the FFT of the time series data, again deeper methodological descriptions can be found in the more general texts [53], [88].

Two of the most commonly used point sea spectra will be discussed here, each is used for a different phase in the wave generation process, either fully developed or developing. The point must be made that these models are specifically only valid for what are termed gravity waves, which are generally accepted to be the sea waves with wavelength $\lambda > 2$cm and for which the restoring force is gravity, as opposed to capillary waves for which the restoring force is surface tension. Having said this, the method of measurement used in the data collected to form the spectrum may have a cut off at a much longer wavelength value than this boundary.

6.2.1.1 *PIERSON-MOSKOWITZ SPECTRUM FOR FULLY DEVELOPED SEAS*

The Pierson-Moskowitz (P-M) spectrum [89] describes the point sea wave spectra for a fully developed sea. This is the final stage of wave development where the energy losses from wave actions such as wave breaking and the dissipation to capillary waves equal the energy being supplied by the wind. The spectrum was originally given in terms of angular frequency ω by,

$$S_{\mathrm{PM}}(\omega) = \frac{\alpha g^2}{\omega^5} e^{-\beta\left(\frac{\omega_0}{\omega}\right)^4}, \tag{6.2-1}$$

where α is the Phillips constant, with value 0.0081. β has the value 0.74 and $\omega_0 = g/U_{19.5}$, where $U_{19.5}$ is the wind speed measured at 19.5 m above sea level. Examples of the Pierson-Moskowitz spectrum for different wind speeds, $U_{19.5}$, are shown in Figure 6.2-1.

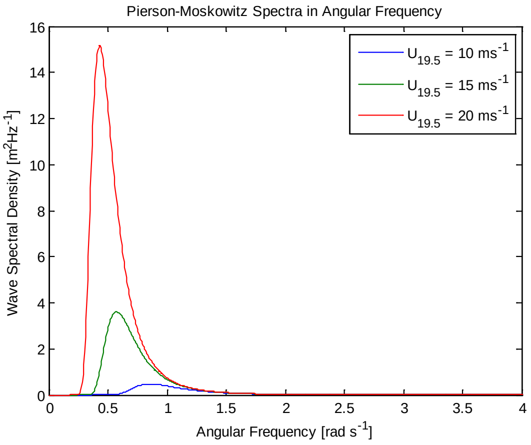

Figure 6.2-1 Pierson-Moskowitz point sea spectra in terms of angular frequency for differing wind speeds

Being a single peaked spectrum, we can find the modal wave frequency by differentiating (6.2-1),

$$\frac{\mathrm{d}S_{\mathrm{PM}}(\omega)}{\mathrm{d}\omega} = \alpha g e^{-\beta\left(\frac{\omega_0}{\omega}\right)^4}\left(\frac{4\beta\omega_0^4}{\omega^{10}} - \frac{5}{\omega^6}\right). \tag{6.2-2}$$

The modal frequency ω_{m}, occurs when $\mathrm{d}S_{\mathrm{PM}}(\omega)/\mathrm{d}\omega = 0$, thus from (6.2-2)

$$\frac{4\beta\omega_0^4}{\omega_{\mathrm{m}}^{10}} = \frac{5}{\omega_{\mathrm{m}}^6}, \tag{6.2-3}$$

$$\omega_{\mathrm{m}} = \omega_0 \sqrt[4]{\frac{4}{5}\beta} = \frac{g}{U_{19.5}} \sqrt[4]{\frac{4}{5}\beta}. \tag{6.2-4}$$

The knowledge of the modal frequency is not necessarily important; however it can be useful as a visual check to ensure any simulated sea surfaces correspond to the expected bulk wave frequency.

The wave spectrum can also be written in terms of significant wave height. This is useful when associating the spectrum with a sea state (SS). The sea state is a method of classifying the severity of a sea. Common definitions are the world meteorological organisation (WMO) code (Table 3700 in [90]) which adopts the Douglas sea state scale. The scale defines a number from 0 to 9 along with a significant wave height $H_{1/3}$ and description of the surface characteristic, the WMO codes are reproduced in Table 6.2-1.

Table 6.2-1. WMO Sea State Code.

Code Figure (Sea State)	Significant Wave Height, $H_{1/3}$ [m]	Descriptive Terms
0	0	Calm (Glassy)
1	0-0.1	Calm (Rippled)
2	0.1-0.5	Smooth (Wavelets)
3	0.5-1.25	Slight
4	1.25-2.5	Moderate
5	2.5-4	Rough
6	4-6	Very Rough
7	6-9	High
8	9-14	Very High
9	Over 14	Phenomenal

The significant wave height is the average height of the 1/3 highest waves (this being what it is supposed we actually measure when estimating wave heights visually).

So to obtain relationships for the significant wave height, firstly we integrate the point spectrum (6.2-1), using the substitution $u = -\beta\left(\frac{\omega_0}{\omega}\right)^4$

$$\int_0^\infty S_{\mathrm{PM}}(\omega)\mathrm{d}(\omega) = \frac{\alpha U_{19.5}^4}{4\beta g^2}, \tag{6.2-5}$$

then by assuming the spectra is narrow banded (surface has a Rayleigh height distribution) and given that the integral of the wave spectrum gives the variance (zeroth moment) of the wave height field [53], [88], i.e.

$$\int_0^\infty S_{\mathrm{PM}}(\omega)\mathrm{d}(\omega) = \sigma^2, \tag{6.2-6}$$

we therefore know the integral is also given by:

$$\int_0^\infty S_{\mathrm{PM}}(\omega)\mathrm{d}(\omega) = \left(\frac{H_{1/3}}{4}\right)^2. \tag{6.2-7}$$

Equating (6.2-5)and (6.2-7), after some rearrangement it is found that

$$U_{19.5} = \sqrt[4]{\frac{\beta g^2 H_{1/3}^2}{4\alpha}}, \tag{6.2-8}$$

which can if needed, be substituted into ω_0^4 in (6.2-1).

It should also be noted that (6.2-8) gives the relation between the significant wave height and the wind speed for the Pierson-Moskowitz wave spectrum. The modal angular frequencies and significant wave heights for the spectra in Figure 6.2-1 are, 0.86, 0.57 and 0.43 rad s^{-1} and 2.1 m (SS 4), 4.8 m (SS 6) and 8.5 m (SS 7) respectively with increasing wind speed.

The Pierson-Moskowitz spectral formulation is very useful in its simplicity, however fully developed seas require a specific fetch (distance) and duration of wind blowing over the surface, these conditions are listed in Table 6.2-2. In order to describe situations where these conditions are not met (and they rarely are it seems) another commonly used spectral form is the JOint North Sea WAve Project (JONSWAP) formulation.

Table 6.2-2. Condition for fully developed sea.

Wind Speed (in single direction) [km/hr]	Fetch [km]	Wind Duration [hrs]
19	19	2
37	139	10
56	518	23
74	1313	42
92	2627	69

6.2.1.2 *JONSWAP SPECTRUM FOR UNDEVELOPED SEAS*

The JONSWAP spectrum was created to describe developing seas, a sea where the energy equilibrium between wave and wind is not yet reached. The state of development is described using the wind speed and fetch, the fetch being the distance over which a persistent wind has been blowing, the JONSWAP spectrum in terms of frequency is given by [91]:

$$S_{\mathrm{JS}}(f) = \alpha \frac{g^2}{(2\pi)^4} \frac{1}{f^5} e^{-1.25(f_{\mathrm{m}}/f)^4} \gamma^{e^{-(f-f_{\mathrm{m}})^2/2(\sigma f_{\mathrm{m}})^2}}. \tag{6.2-9}$$

Where: $\gamma = 3.30$ (shape parameter).
$\alpha = 0.076\bar{x}^{-0.22}$ (scale parameter).
$\bar{x} = g\,x/\bar{U}_{10}^2$ (dimensionless fetch).
$x =$ fetch length [m].
$\bar{U}_{10} =$ mean wind speed at 10 m above sea level [ms^{-1}].
$g =$ gravitational constant [ms^{-2}].
$f_{\mathrm{m}} = 3.5\frac{g}{\bar{U}_{10}}\bar{x}^{-0.33}$ (modal frequency).

$$\sigma = \begin{cases} 0.07 & f \leq f_{\mathrm{m}} \\ 0.09 & f > f_{\mathrm{m}} \end{cases}$$

The JONSWAP form contains an additional parameter to the PM spectrum, the peak enhancement parameter γ. In truth the value of the parameter is quite spread and it can be considered to be Gaussian distributed with a γ value of 3.3 as the average (typical sea), the so called standard 'JONSWAP Spectral Formulation' is known by the use of the parameters above. They can be changed to suit particular sea measurement data if required. So in comparison to the Pierson-Moskowitz spectrum assuming we use the standard values of γ and σ we can vary not only the wind speed, but the fetch also; spectral plots are shown in Figure 6.2-2, highlighting the effects of variation of the two parameters.

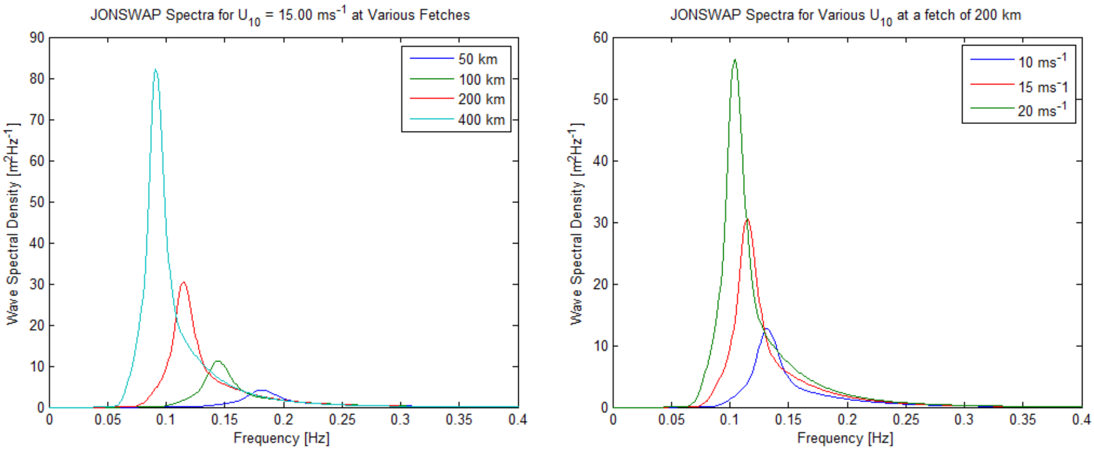

Figure 6.2-2 JONSWAP spectra for varying fetch at constant wind speed and varying wind speed at constant fetch.

It can be seen that the wave energy, which is proportional to the variance of the wave height and hence area under curves in Figure 6.2-2 (from (6.2-6)), increases as the fetch increases, as the sea is pushed more towards a fully developed equilibrium state.

Again, this spectral form can be written in terms of significant wave height $H_{1/3}$, again using the narrow banded spectrum approximation (as for the Pierson Moskowitz spectrum).

However there is no analytic solution to the integral of $S_{\mathrm{JS}}(f)$ and so this is performed for specific values of γ, the following relationship between fetch and wind speed was found,

$$\bar{U} = kx^{-0.615}H_{1/3}^{1.08}. \tag{6.2-10}$$

$$\Rightarrow H_{1/3} = \sqrt[1.08]{\frac{\bar{U}}{kx^{-0.615}}}. \tag{6.2-11}$$

Where the value of k has been derived for various values of the shape parameter γ; for $\gamma = 3.30$, $k = 83.7$ [92].

6.2.1.3 *COMPARISON OF SPECTRAL FORMULATIONS*

In order to compare both the JONSWAP and Pierson Moskowitz spectrum they should both be dependent on the same variable; as most directional spreading functions (which will be discussed later) are defined in terms of linear frequency this will be chosen as the common variable and the Pierson Moskowitz spectrum shall be transformed. The method of transformation is relatively simple, to maintain integral equality of the spectrum (and thus conserving wave energy on transformation), the equality

$$\int_0^\infty S_{\mathrm{PM}}(\omega)\,\mathrm{d}\omega = \int_0^\infty S_{\mathrm{PM}}(f)\,\mathrm{d}f \tag{6.2-12}$$

must be satisfied and thus,

$$\int S_{\mathrm{PM}}\big(\omega(f)\big)\frac{\mathrm{d}\omega}{\mathrm{d}f}\mathrm{d}f = \int S_{\mathrm{PM}}(f)\,df, \tag{6.2-13}$$

where $\omega(f) = 2\pi f$, $\mathrm{d}\omega/\mathrm{d}f = 2\pi$, therefore from the definition of the Pierson Moskowitz spectrum(6.2-1) and to put in terms of modal frequency f_{m} (from ω_{m} using (6.2-4)):

$$S_{\mathrm{PM}}(f) = 2\pi \cdot S_{\mathrm{PM}}(\omega = 2\pi f) \tag{6.2-14}$$

$$\Rightarrow S_{\mathrm{PM}}(f) = \frac{\alpha g^2}{(2\pi)^4 f^5} e^{-\frac{5}{4}\left(\frac{f_{\mathrm{m}}}{f}\right)^4}, \tag{6.2-15}$$

where

$$f_{\mathrm{m}} = \frac{\omega_{\mathrm{m}}}{2\pi} = \frac{g}{2\pi U_{19.5}} \sqrt[4]{\frac{4}{5}}\beta. \tag{6.2-16}$$

It should also be considered that there is a discrepancy in the definition of the wind speed, for the Pierson-Moskowitz spectrum the wind speed is specified 19.5 m above the sea surface whereas for the JONSWAP it is 10 m. Therefore the wind speed should be adjusted, and the chosen adjustment is to define the 10 m speed. Under certain atmospheric assumptions it can be shown [93] that $U_{19.5} = 1.076 \cdot U_{10}$. A comparison of the P-M and JONSWAP spectrum for a single wind speed but varying fetch is shown in Figure 6.2-3.

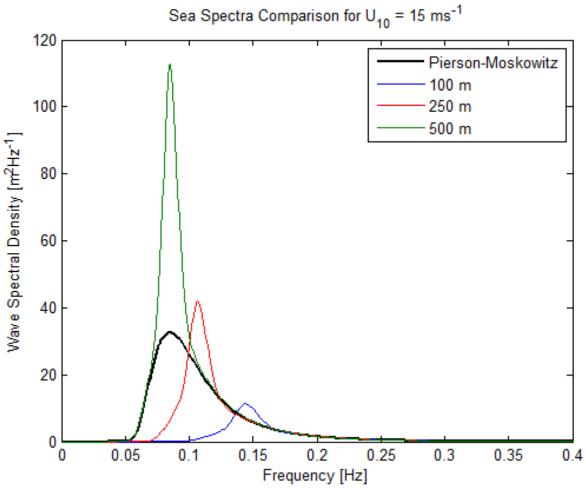

Figure 6.2-3 Pierson-Moskowitz and JONSWAP Spectral comparison for fixed wind speed and variable fetch.

What should be taken from Figure 6.2-3 is that, from Table 6.2-2, at 500 km fetch the JONSWAP spectrum (green line) should signify a fully developed sea, in some way tending towards the PM spectrum (black line) – it is not so simple as this, as adjustments may need to be made to the value of γ for this situation. Needless to say the JONSWAP formulation does not tend towards the PM as the fetch increases and remains overly peaked. This effect has been discussed and reconciled in other more recent spectral forms which have merged the two scenarios, for example the Donelan spectrum [94]. Suffice to say the PM spectra should be used for fully developed and JONSWAP for developing seas.

In this thesis the analysis is constrained to the use of the PM spectrum which thus restricts simulation to the fully developed sea, and allows us to therefore compare similar aged seas for various wind speeds, giving a well-defined basis for comparison of results.

6.2.2 DIRECTIONAL SPREADING FUNCTIONS

Just knowing the spectrum of the waves at a single point is not useful for constructing a 2-D surface profile; knowledge about the direction of travel of the various wave components is also required. This comes in the form of the empirically derived directional spreading functions.

6.2.2.1 *COSINE-SQUARE SPREADING FORMULA*

The most basic spreading function was proposed in [95] and is known as cosine-square spreading. It is basic in that it has no dependence on wave frequency, only angle and takes the form:

$$D(\theta) = \frac{2}{\pi}\sin^2(\theta) \quad \text{for} -\frac{\pi}{2} < \theta < \frac{\pi}{2} \tag{6.2-17}$$

Where θ is the spreading angle and $\theta = 0$ is the direction of motion of the bulk of the waves i.e. what would generally be considered the prevailing wave/wind direction. A plot of the function is shown in Figure 6.2-4. The factor of $2/\pi$ is a normalisation factor to meet the requirement for all directional spreading functions - the integral over all angles is unity,

$$\int_{0}^{2\pi} D(f,\theta) = 1, \qquad (6.2\text{-}18)$$

this property maintains that the total energy at a point (from the point spectrum) remains unchanged no matter which direction the waves arrive from.

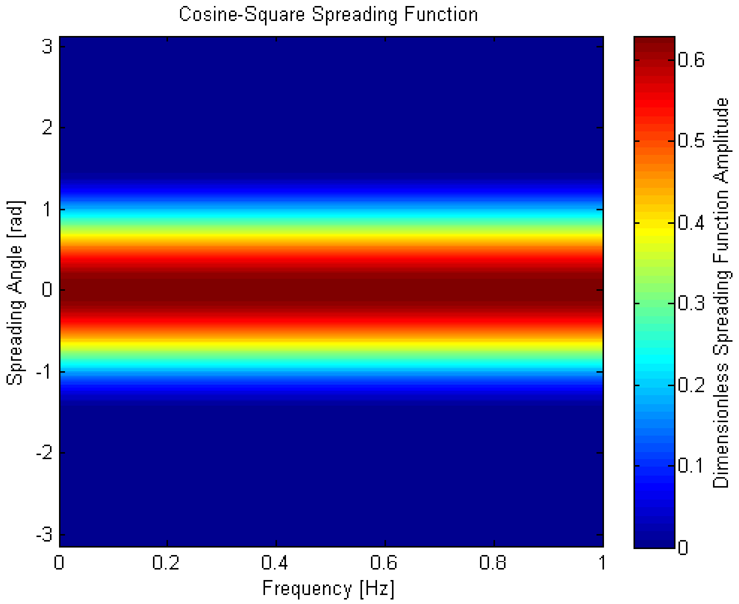

Figure 6.2-4. Cosine^2 directional/energy spreading function

This function may be relatively unrealistic as it has no dependence on frequency, a more complex generalised form for the directional spreading function is the Longuet-Higgins formulation.

6.2.2.2 *LONGUET-HIGGINS DIRECTIONAL SPREADING FORMULATION*

The Longuet-Higgins spreading function [96] is also dependent on the wave frequency (and thus by implication, the wind speed and fetch):

$$D(\theta,f) = \frac{2^{s-1}}{\pi}\frac{\Gamma(s+1)^2}{\Gamma(2s+1)}\left|\cos\frac{1}{2}(\theta-\bar{\theta})\right|^{2s}. \qquad (6.2\text{-}19)$$

Where, as in the cosine-square function, θ is the spreading angle, $\bar{\theta}$ is now the prevailing wind/wave direction. Γ is the gamma function and s is a function of frequency f for which others such as Mitsuyasu [97] and Hasselmann [98] have then proposed (through analysis of their sea data) forms.

6.2.2.3***MITSUYASU SPREADING***

Mitsuyasu *et al*. suggest the following for the parameter s in equation (6.2-19).

$$s = \begin{cases} s_m(f/f_{\mathrm{m}})^5 & f \le f_{\mathrm{m}} \\ s_m(f/f_{\mathrm{m}})^{-2.5} & f > f_{\mathrm{m}} \end{cases}$$

$$s_m = 11.5(2\pi f_{\mathrm{m}} \bar{U}_{10}/g)^{-2.5}$$

f_{m} = modal frequency of wave spectrum.

$\bar{U}_{10}$ = mean wind speed 10 m above sea surface.

An example of the Mitsuyasu spreading function for $f_{\mathrm{m}} = 0.8$ Hz and $\bar{U}_{10} = 15$ ms^{-1} is shown in Figure 6.2-5.

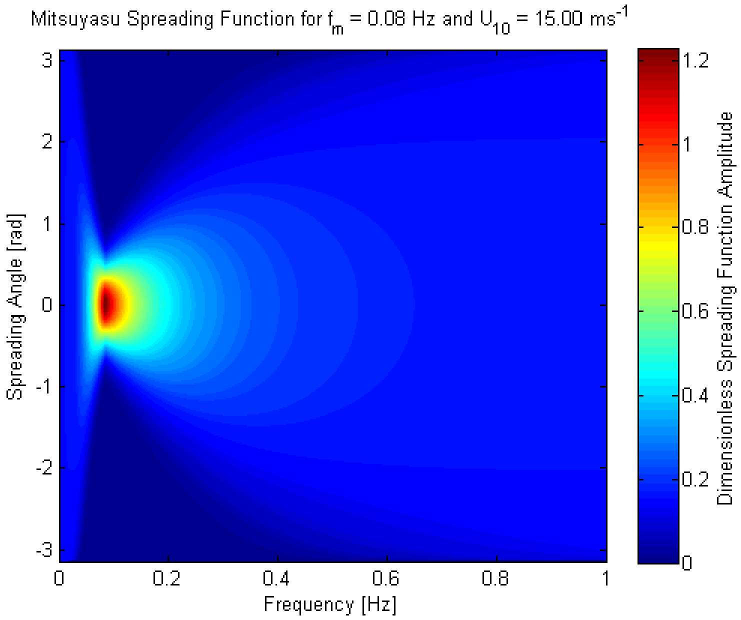

Figure 6.2-5 Mitsuyasu directional/energy spreading function

6.2.3 DIRECTIONAL WAVE SPECTRA

Now we have both point spectra and spreading functions, due to their construction, the two are combined by multiplication to form a full frequency directional wave spectrum (termed from now on as the directional wave spectrum). Firstly this can be shown in the same co-ordinates as the spreading spectra in section 6.2.2, a function of (f, θ). It is then required that we express the wave spectrum in terms of spatial frequencies or wavenumbers and for this a dispersion relationship is required.

6.2.3.1 *Directional Wave Spectrum in Angular and Frequency Domain*

The directional wave spectrum $E(f, \theta)$ is given by:

$$E(f,\theta) = S(f)D(f,\theta). \qquad (6.2\text{-}20)$$

Figure 6.2-6 shows the full wave spectra for the Pierson-Moskowitz spectrum with both cosine-square and Mitsuyasu spreading functions for a wind speed of U_{10} of 15 ms^{-1}.

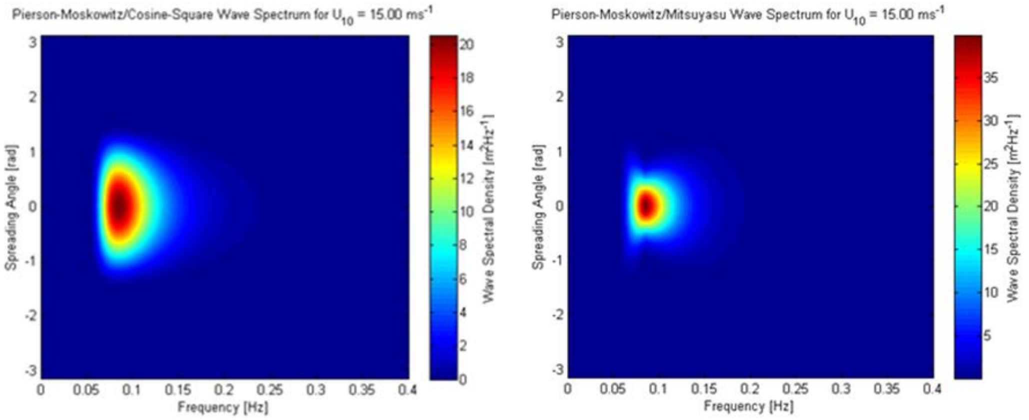

Pierson-Moskowitz/Cosine-Square Wave Spectrum for U_{10} = 15.00 ms^{-1}

Pierson-Moskowitz/Mitsuyasu Wave Spectrum for U_{10} = 15.00 ms^{-1}

Figure 6.2-6. Pierson-Moskowitz spectra with both cosine-square and Mitsuyasu spreading.

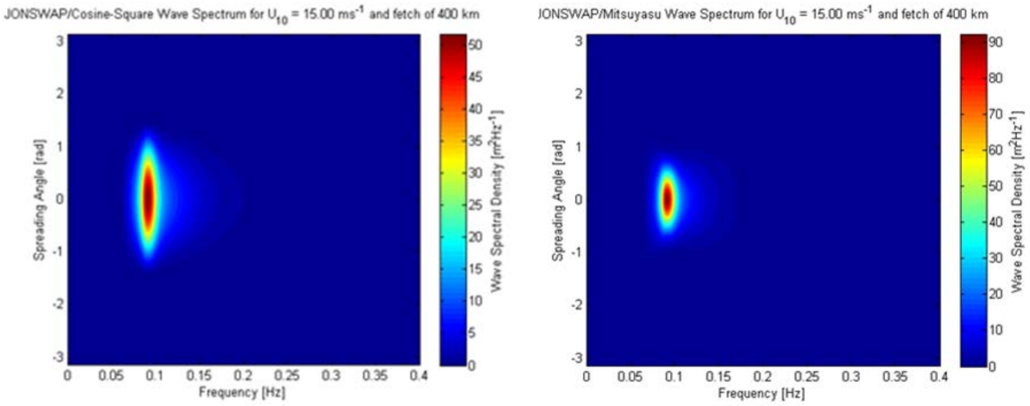

Figure 6.2-7. JONSWAP spectra with both cosine-square and Mitsuyasu spreading.

Figure 6.2-7 shows the JONSWAP spectra with both spreading functions at the same wind speed for a fetch of 400 km.

It can be seen that the cosine-square spreading is much wider than the Mitsuyasu. For further simulation, due to its handling of the effects of wave frequency (and it is deemed more realistic), the Mitsuyasu spectrum will be used.

6.2.3.2 *DIRECTIONAL WAVE SPECTRA IN ANGULAR AND SPATIAL FREQUENCY DOMAIN*

In order to create a modelled 2D sea surface (eventually through the use of the FFT), the wave spectra is required to be expressed in spatial frequency (or indeed wave number). In order to do this, the dispersion relation must be known. For gravity waves (linear wave theory-small displacements) the dispersion relation is well known,

$$\omega = \sqrt{gk\tanh(kh)}, \tag{6.2-21}$$

$$k = \frac{2\pi}{\lambda}. \tag{6.2-22}$$

In which ω is the angular wave frequency, k is the wavenumber, g is the acceleration due to gravity, h is the water depth and λ is the wavelength (this does not describe the capillary waves which are not included in these simulations). When only considering the deep sea, i.e. $h > \lambda/2$, (6.2-21) can be reduced to

$$\omega = \sqrt{gk}. \tag{6.2-23}$$

Converting this to linear frequency f, to match the definitions we have used for the sea spectra by again using the substitution $\omega = 2\pi f$,

$$f = \frac{1}{2\pi}\sqrt{gk}. \tag{6.2-24}$$

It would be appropriate to stop there and leave this dispersion relation in terms of frequency and wavenumber. However in order to make things simpler (to save further scaling of the FFT for MATLAB algorithms), we will also convert the wavenumber to spatial frequency. The spatial frequency $\nu = 1/\lambda$. Substituting this into (6.2-22) then (6.2-24) gives the dispersion relation in terms of f and ν:

$$f = \sqrt{\frac{g\nu}{2\pi}} \tag{6.2-25}$$

Now we can transform the full wave spectrum $E(f,\theta)$, into the spatial frequency domain $E(\nu,\theta)$. Again preserving the integral equality,

$$\int E(\nu,\theta)\,\mathrm{d}\nu\mathrm{d}\theta = \int E(f,\theta)\,\mathrm{d}f\mathrm{d}\theta = \int E(f(\nu),\theta)\frac{\mathrm{d}f}{\mathrm{d}\nu}\mathrm{d}\nu\mathrm{d}\theta \tag{6.2-26}$$

and from (6.2-25)

$$\frac{df}{d\nu} = \frac{1}{2}\sqrt{\frac{g}{2\pi\nu}} \tag{6.2-27}$$

Thus

$$E(\nu,\theta) = \frac{1}{2}\sqrt{\frac{g}{2\pi\nu}}\,E\left(f = \sqrt{g\nu/2\pi}\,,\theta\right) \tag{6.2-28}$$

Indeed this operation could also be carried out separately the point spectrum $S(f)$, to give $S(\nu)$, then $D(f,\theta)$ would just require the substitution of (6.2-25) and will still remain normalised over angle due to its construction. No transformation is required for the cosine-square spreading as it is not a function of frequency. Figure 6.2-8 shows an example of the PM spectrum with Mitsuyasu spreading the same as in Figure 6.2-6 however now in terms of spatial frequency and angle.

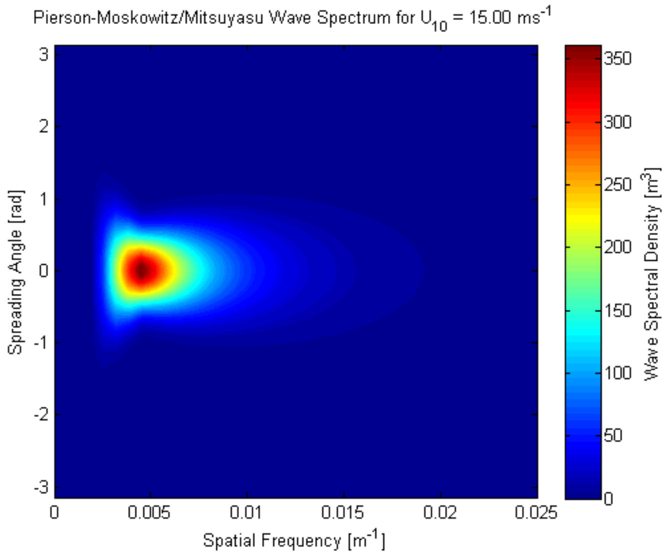

Figure 6.2-8 PM wave spectrum in terms of spatial frequency and Mitsuyasu spreading angle.

6.2.3.3 *Wave Spectrum in Spatial Frequency Vector Domain*

The final conversion required is essentially a conversion from the polar co-ordinates of spreading angle and spatial frequency magnitude into the rectangular/Cartesian co-ordinates of spatial frequency (x and y) vector components.

It is commonly known in order to change integration variables from polar co-ordinates r, θ to Cartesian x, y that

$$\mathrm{d}x\mathrm{d}y = r\,\mathrm{d}r\mathrm{d}\theta,$$

or in the case of the variables used above,

$$\mathrm{d}\nu_x \mathrm{d}\nu_y = \nu \,\mathrm{d}\nu \mathrm{d}\theta,$$

where ν_x,ν_y are the vector components of the spatial frequency. Hence

$$\int E(\nu_x,\nu_y)\,\mathrm{d}\nu_x \mathrm{d}\nu_y = \int E(\nu_x,\nu_y)\nu\,\mathrm{d}\nu \mathrm{d}\theta = \int E(\nu,\theta)\,\mathrm{d}\nu \mathrm{d}\theta \tag{6.2-29}$$

and thus

$$E(\nu_x,\nu_y) = \frac{1}{\nu} E(\nu,\theta) \tag{6.2-30}$$

or from the original temporal frequency defined spectrum,

$$E(\nu_x,\nu_y) = \frac{1}{2\nu}\sqrt{\frac{g}{2\pi\nu}}\,E\left(f = \sqrt{g\nu/2\pi}\,,\theta\right). \tag{6.2-31}$$

An example of the spectrum calculated in Figure 6.2-8, now in terms of spatial frequency vector components is shown in Figure 6.2-9.

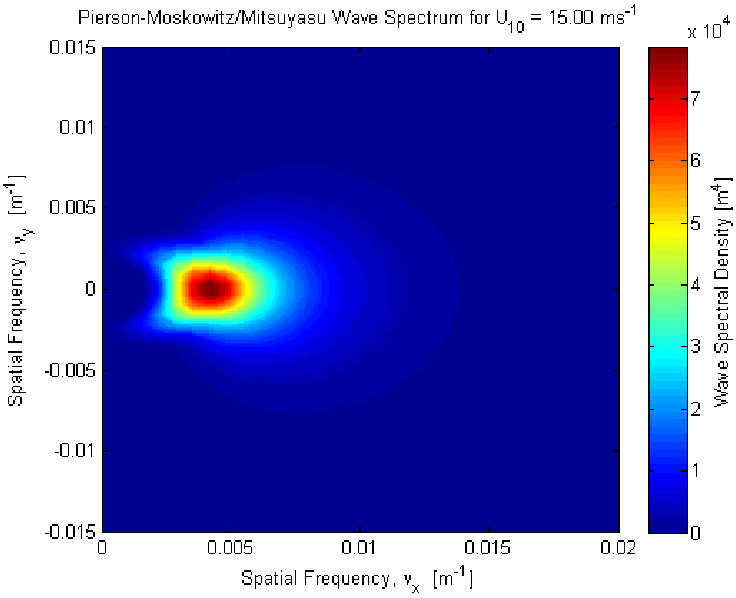

Figure 6.2-9. P-M/Mitsuyasu directional wave spectrum in terms of vector spatial frequency.

Spectra of this sort can then be used in an IFFT to produce a representation of the sea surface. Thought must now be given to the sampling methodology used.

6.3 CREATING AND EVOLVING THE SURFACE THROUGH THE IFFT

Essentially from the directional spectra we have the energy distribution of the different spatial wave components that make up the surface. Next to be considered is the spectrum/ surface sampling, the conversion of the energy spectrum to an amplitude spectrum (and the addition of random phase terms) and then the evolution of the created surface in time.

6.3.1 SPECTRUM SAMPLING AND ARRAY FORMATION

The task when using the IFFT to produce a surface is one of obtaining the required spatial resolution through selection of the spatial sample rate. It must be ensured, through the Nyquist criteria, that the sample rate is enough to encompass all the spectral content required. The surface then has to be of appropriate dimension to ensure good frequency resolution in the spectrum, however, the IFFT size should be reasonable so simulation times are not excessive.

To this end it is appropriate to begin with deciding what spatial frequency content is required in the spectrum. As stated before, the spectra described thus far are only suitable to describe gravity waves; this immediately imposes a lower wavelength cut-off in the spectrum of 2 cm. However the methods used to determine these spectra were not designed to measure down to this wavelength, for example in the JONSWAP experiment the measurement equipment lowest wavelength cut off was 1.5 m. It may be justified to say that as the wave physics should still be the same and it can be assumed the spectra are good down to the capillary length, but due to gravity capillary interactions, this may not be the case. So to avoid the inclusion of the shorter wavelengths, it was decided to remove them from the spectra – cutting off below 1.5 m. The removal of these higher frequency waves will not affect our optical line of sight calculations or have great effect on the surface energy due to their very small amplitudes. The cut–off does not introduce any sharp discontinuities in the spectra, as the spectral amplitudes are very low in this region.

Now that the minimum wavelength/maximum spatial frequency is decided ($\mathrm{v}_{\max} = 1/\mathrm{l}$), the surface sample rate minimum $\mathrm{R}_{\mathrm{x,y}}^{\mathrm{samp}}$ can be set according to the Nyquist criterion,

$$R_{x,y}^{\mathrm{samp}} \geq 2\nu_{x,y}^{\max} \tag{6.3-1}$$

In order to reproduce the spectrum well in the spatial domain, it is chosen to over-sample the surface, at a rate of $R_{x,y}^{\mathrm{samp}} = 3\nu_{x,y}^{\max}$ and with the cut off spectrum, this adds no higher physical frequency content. The spatial sample spacing $\Delta_{\mathrm{x,y}}$ is given by $1/R_{x,y}^{\mathrm{samp}}$, thus for a given surface of length L_x and breadth L_y the spatial vectors can be formed[4] :

$$\begin{aligned} x &= [0\ \Delta_{\mathrm{x}}\ 2\Delta_{\mathrm{x}}\ \cdots L_x\ ] \\ y &= \left[0\ \Delta_{\mathrm{y}}\ 2\Delta_{\mathrm{y}}\ \cdots L_y\ \right] \end{aligned} \tag{6.3-2}$$

where the surface dimensions in terms of number of samples in x and y direction $n_{x,y}$, is given by:

---

[4] The sample spacing is chosen such that the required spatial dimension is an integer multiple of that spacing.

$$n_{x,y} = \frac{l_{x,y}}{\Delta_{\mathrm{x,y}}} + 1. \tag{6.3-3}$$

As the number of samples in the spatial frequency and spatial domain are one to one for the FFT/IFFT, this allows us to define our spatial frequency vectors v_x and v_y, which consist of $n_x$and n_y samples and range over:

$$\frac{-R_{x,y}^{\mathrm{samp}}}{2} \leq v_{x,y} < \frac{R_{x,y}^{\mathrm{samp}}}{2} \tag{6.3-4}$$

where the equality sign on the left depends on whether $n_{x,y}$are odd or even and a matrix of spatial frequencies is created from these vectors and the directional spectrum is calculated at these points and is similar to Figure 6.2-9.

It should be noted that if a specific spatial sampling is required this could be used as the start point of the above method, instead of a required minimum wavelength. Indeed it must be made sure that the number of samples $n_{x,y}$ in the spectrum is enough to effectively sample the spectrum and there are enough components to allow the representation of a Gaussian process as discussed in the previous section. This can be altered by increasing the spatial sampling rate for a given surface size or increasing the surface size for a given sample rate. One form of check is to compare the expected/theoretical value of the integral of the continuous energy spectrum (6.2-7) to that calculated from the created discrete one (by summing the area under the discrete spectrum) – these should be similar if sampled properly and also hint that the spectrum generation has been performed correctly (a sanity check). It is known that for speed reasons the IFFT dimensions should be a power of 2^n, thus as a compromise between speed and adequate spectrum sampling it would be preferable to use an IFFT size of 2048 x 2048 points if other constraints allow. Needless to say, for any set of comparative measurements, all parameters are kept constant.

6.3.2 CONVERSION TO AMPLITUDE SPECTRUM AND ADDITION OF RANDOM PHASE.

It should be re-emphasised, that the spectrum is not actually in terms of wave amplitude as required for IFFT procedures, but wave energy. The amplitudes a_{ij} of the individual wave spectrum components are found by:

$$a_{ij} = \sqrt{2E(f_i, \theta_{ij})\Delta f_i \Delta\theta_{ij}} = \sqrt{2E(v_x^i, v_y^j)\Delta v_x^i \Delta v_y^j} \tag{6.3-5}$$

as in (6.1-6) and where Δ signifies the spacing of the discrete variables in the spectrum. Following this conversion each component is then multiplied by a random phase factor $e^{i\phi_{ij}}$ where ϕ_{ij} is uniformly distributed between $[0,2\pi]$ again as in the DSA scheme (6.1-6).

The IFFT is then performed on the matrix of complex amplitudes to produce a spectrum for a given instant in time, an example surface is shown in Figure 6.3-1.

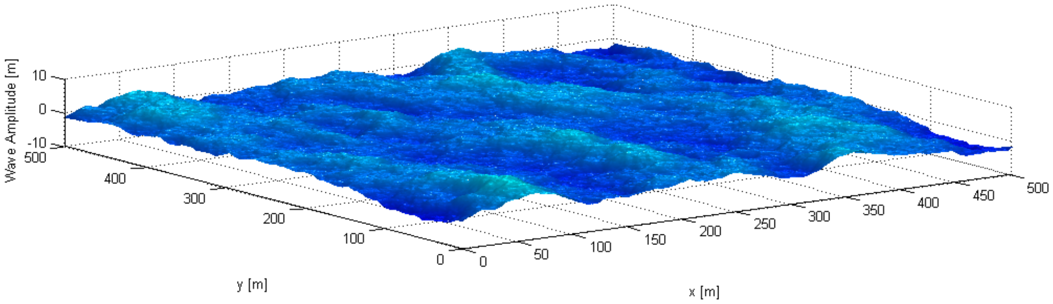

Figure 6.3-1 Example of surface produced from a JONSWAP/Mitsuyasyu wave spectrum for wind speed of 15 m/s and 400km fetch.

6.3.3 SURFACE EVOLUTION

In order to evolve the surface over time, the original phase spectrum is taken and each component ϕ_{ij}^{ori} progressed in phase according to the dispersion relation and a given time step Δt, such that the new phase ϕ_{ij}^{new} is given by:

$$\phi_{ij}^{\mathrm{new}} = \phi_{ij}^{\mathrm{ori}} + \omega_{ij}\Delta t = \phi_{ij}^{\mathrm{ori}} + \sqrt{2\pi\nu_{ij}g} \cdot \Delta t\,. \tag{6.3-6}$$

The process is slightly more complicated as it is performed on the vector values of spatial frequency separately in x and y and then combined and sign considerations must be made depending if frequency values are negative or positive.

6.4 ANTENNA MOTION MODEL

For this analysis the antenna is chosen to be omni-directional. It is expected that for such a radar system this would be the case as it removes the need to maintain any directional antenna pointing, which would in practice be challenging on the rough undulating surface without the use of stabilising equipment.

6.4.1 ANTENNA MAST DIRECTLY ON SEA SURFACE

To attempt to model the motion of an antenna mounted on a rigid mast directly on the varying surface, the gradient of the surface under the antenna position is used to perform a rotation about the x and y axes. Firstly, the base of an antenna of height $\mathrm{h_{ant}}$ is located at a point in the x-y plane $\mathrm{P_{ant}}(\mathrm{x_p}, \mathrm{y_p})$. The x and y components of the surface gradient $\Delta\mathrm{F_x}, \Delta\mathrm{F_y}$ are found at this point (discretely on the surface mesh), i.e.

$$\Delta F_x = \left.\frac{\partial F}{\partial x}\right|_{x_p,y_p} ; \quad \Delta F_y = \left.\frac{\partial F}{\partial y}\right|_{x_p,y_p} , \tag{6.4-1}$$

where F is the surface height function. These surface gradients are then related to corresponding tilt angles in the x and y directions, as illustrated in Figure 6.4-1.

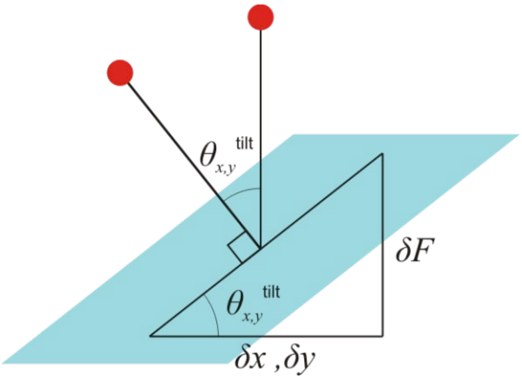

Figure 6.4-1. Illustration of gradient and tilt angle calculation for an antenna mounted on a surface.

Therefore the tilt angles $\theta_{x,y}^{\text{tilt}}$ are simply given by the arc-tangent of the gradient components,

$$\theta_x^{\text{tilt}} = \operatorname{atan}(\Delta F_x); \quad \theta_y^{\text{tilt}} = \operatorname{atan}(\Delta F_y) \tag{6.4-2}$$

Some precautions must be taken to ensure that the sign of each angle is correct. It is at this point where it is possible to invoke a form of antenna stabilization to the simulation by limiting the values of $\theta_{x,y}^{\mathrm{tilt}}$ to some value, for example 5° or indeed to simulate stabilisation by averaging out the surface over a given ‘buoy base’ area and taking the tilt from this.

The next process is to rotate the antenna about the base by the two tilt angles. The rotation is performed by using the standard rotation matrices $R_x(\theta)$ and $R_y(\theta)$, with the total rotation matrix $R_{\mathrm{tot}}\left(\theta_x^{\mathrm{tilt}}, \theta_y^{\mathrm{tilt}}\right) = R_x\left(\theta_y^{\mathrm{tilt}}\right) R_y\left(\theta_x^{\mathrm{tilt}}\right)$. This is acted on the vector $[0,0,h_{\mathrm{ant}}]$, to give the rotated antenna position w.r.t the origin A_{rot},

$$A_{\mathrm{rot}} = R_{\mathrm{tot}}\left(\theta_x^{\mathrm{tilt}}, \theta_y^{\mathrm{tilt}}\right)[0,0,h_{\mathrm{ant}}]^T. \tag{6.4-3}$$

This is then translated to the original antenna position to give the final rotated antenna position $P_{\mathrm{rot}}(x_r, y_r, z_r)$where

$$P_{\mathrm{rot}} = A_{\mathrm{rot}} + [x_p, y_p, h_p^{\mathrm{surf}}]^T, \tag{6.4-4}$$

h_p^{surf} is the surface height at $P_{\mathrm{ant}}\left(x_p, y_p\right)$.

It is understood that the order of rotation does indeed matter normally, however for sufficiently small time steps in simulation, it is expected that the angular changes will be very small and thus the rotation matrices commute.

6.5 SIMULATION TARGET MODEL

The target model chosen for these simulations is a rather simplified one. It consists of treating the target as a point, which is placed at half the true target height above the surface. The method of testing if the target is visible by the antennas will be explained in the next section, however there needs to be some definition of a potential target visibility region.

6.5.1 POTENTIAL TARGET VISIBILITY REGION

In order to ensure this is a simulation related to FSR, there is a need to specify when it may be possible to view the target in relation to some FSR parameter. The parameter chosen is to define the potential visibility region by use of the FSCS main lobe.

It is possible to use a simplified model of cross section in the forward scatter direction, wherein the target is replaced by a rectangular aperture of equivalent length and height, this is then treated as a secondary antenna [62], as described in Sections 2.10 and 3.1. In this case the radiation pattern (in power units) takes the form of a sinc^2 function; it is chosen that the main lobe width will be defined by the half power points (full width half maximum). In this simulation only the horizontal plane of the FSCS pattern will be used, thus the sinc^2 function depends only on the length l of the target object, thus

$$\mathrm{sinc}^2\left(\frac{\pi l}{\lambda}\sin\theta\right) = \frac{1}{2}, \tag{6.5-1}$$

where λ is the wavelength of the radiation striking the target and θ is the half cross section width. This is solved numerically such that,

$$\frac{\pi l}{\lambda}\sin\theta = 1.392\ ;\ \theta_{\mathrm{fs}} = 2\,\mathrm{asin}\left(\frac{1.392\lambda}{\pi l}\right), \tag{6.5-2}$$

in which θ_{fs} is the width of the FSCS main lobe. To decide if the target is potentially observable it is now just a case of ensuring that the main lobe is visible by the antennas during the target trajectory. This simple concept is highlighted in Figure 6.5-1, (a) indicating the non-visible scenario and (b) the visible.

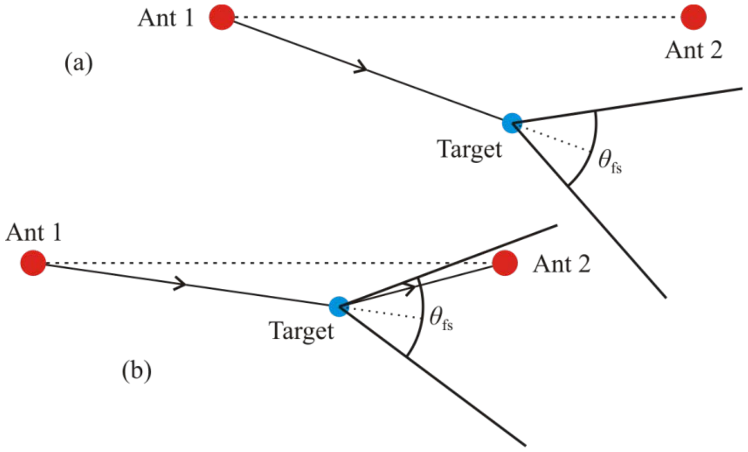

Figure 6.5-1 Illustration of potential target observation scenarios, (a) when target is not potentially visible and (b) when it is – plan view of surface.

There are three things that should be noted, firstly, using the -3dB (half power) point may be overly stringent due to the usually large gains in cross section in the FS direction, it severely restricts the lobe widths and available target viewing time (depending on target size). Secondly using just the FSCS pattern in one plane (horizontal) is not entirely accurate as it does not account for any pitch and roll of target. Finally, at present the model of potential target visibility is mapped purely to a flat plane, using only the x and y values of both target and antenna base as references, not accounting for any antenna motion. The latter two are approximations that make simulation easier by allowing us to define *a priori* the regions of potential observability before running the simulation.

6.5.2 SURFACE TARGET MOTION

The target is modelled with constant vector velocity $\boldsymbol{v}_{\text{tgt}}(v_x, v_y)$ with respect to the planar ground surface (or, in essence, the sea bed). Given a start position vector $\boldsymbol{P}_{\boldsymbol{0}}^{\text{tgt}}(x, y)$, the position vector $\boldsymbol{P}_{\text{tgt}}(x, y)$ at a later time t is simply found by the standard kinematic equation,

$$\boldsymbol{P}_{\text{tgt}} = \boldsymbol{P}_{\boldsymbol{0}}^{\text{tgt}} + \boldsymbol{v}_{\text{tgt}} \cdot t. \tag{6.5-3}$$

The z component of the target position is (as stated previously) given by the modelled sea surface height interpolated at the calculated $\boldsymbol{P}_{\text{tgt}}$, plus half the target height.

6.6 ESTIMATING TARGET VISIBILITY THROUGH LINE OF SIGHT

Now the positions of the target and antenna are known in relation the surface and each other, also the window of potential visibility is calculated. Thus, the actual target visibility by means of LOS can now be estimated, through the tracing of rays between the target and each antenna – fundamentally a purely geometrical approach. As described in Section 3.1.4.1, in FSR it is also required that there is mutual LOS between antennas to provide the reference signal, the target is deemed visible if and only if all three LOS's exist simultaneously. Thus, three 3-D rays are formed, see Figure 6.6-1; one from transmitter to the target $\boldsymbol{a}_{\text{tx-tgt}}$, another from the target $\boldsymbol{a}_{\text{tgt-rx}}$ to receiver, the third from transmitter to receiver

$$\begin{aligned} \boldsymbol{a}_{\text{tx-tgt}} &= \boldsymbol{P}_{\text{tgt}} - \boldsymbol{P}_{\text{tx}} , \\ \boldsymbol{a}_{\text{tgt-rx}} &= \boldsymbol{P}_{\text{rx}} - \boldsymbol{P}_{\text{tgt}} , \\ \boldsymbol{a}_{\text{tx-rx}} &= \boldsymbol{P}_{\text{rx}} - \boldsymbol{P}_{\text{tx}} , \end{aligned} \tag{6.6-1}$$

where the $\boldsymbol{P}$'s are the position (vectors) of the target and antennas. These vectors then allow the interpolation of the surface heights along their corresponding x, y paths. If the surface height is greater than each vector's z value at any point – this would imply a surface intersection and thus loss of one or more of the LOSs, as depicted in Figure 14. The interpolation is carried out at a finer resolution along the vector path than the resolution of the surface itself and must be fine enough such that the ray does not ‘pass through’ a wave without realising an intersection. On the other hand, the fineness greatly effects the simulation time, the spacing used is 0.10 m.

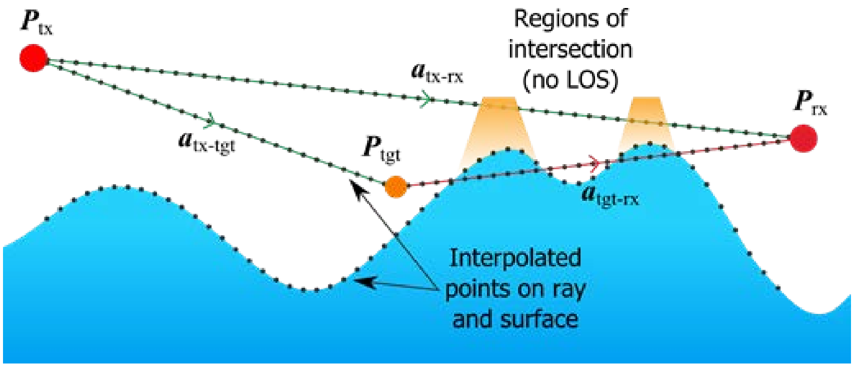

Figure 6.6-1. Line of sight vectors between target and antennas and antennas themselves. Loss of line of sight occurs between receiver (rx) and target (tgt) due to ray path intersection with surface.

During a simulation run this process is carried out at every time step, evolving the surface, moving the target and antennas and then observing if the three LOS’s exist or not, with the output for the particular time step being a logical 1 or 0 for each of the three rays. An example of the estimation of line of sight on a generated surface is shown in Figure 6.6-2. The target is classed as visible in a given time step all three rays are logical 1 i.e. have LOS for that time step.

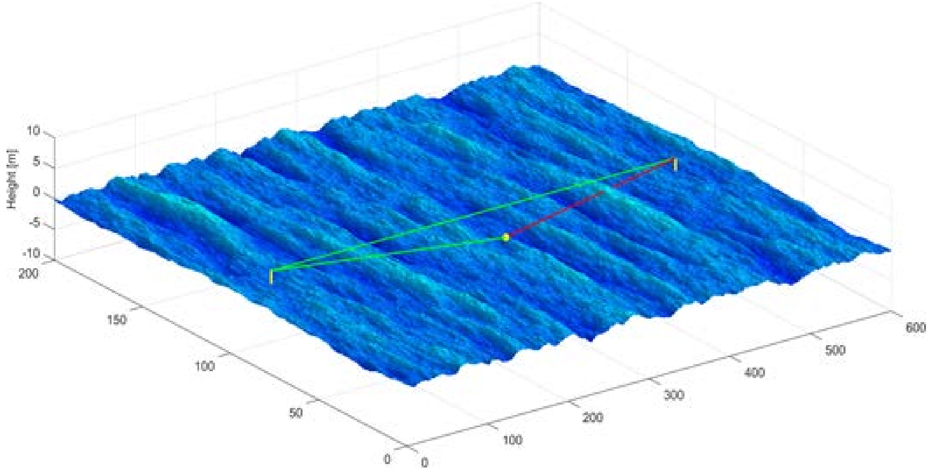

Figure 6.6-2 Example of line of sight evaluation on the simulated surface, green lines show available line of sight from transmitter to receiver and transmitter to target, red shows lack of line of sight from target to receiver.

6.7 SIMULATION PARAMETERS

There are many scenarios that can be investigated, with this in mind, the simulations for this thesis have been restricted to some fundamental target trajectories, wind conditions and sea states/significant wave heights. The target trajectory considered in each simulation is a perpendicular mid-point crossing of the baseline and three basic wind directions are considered. The first is a wind direction parallel to the baseline (cross wind for target), the second is the wind perpendicular to the baseline (head/tail wind for target) and thirdly, wind at 45° to the baseline. Note that for the last two cases the wind can be travelling with or against the target direction of travel, so in all a total of 5 wind directions are simulated— topologies are presented in Figure 6.7-1. The target dimensions in the simulations are based

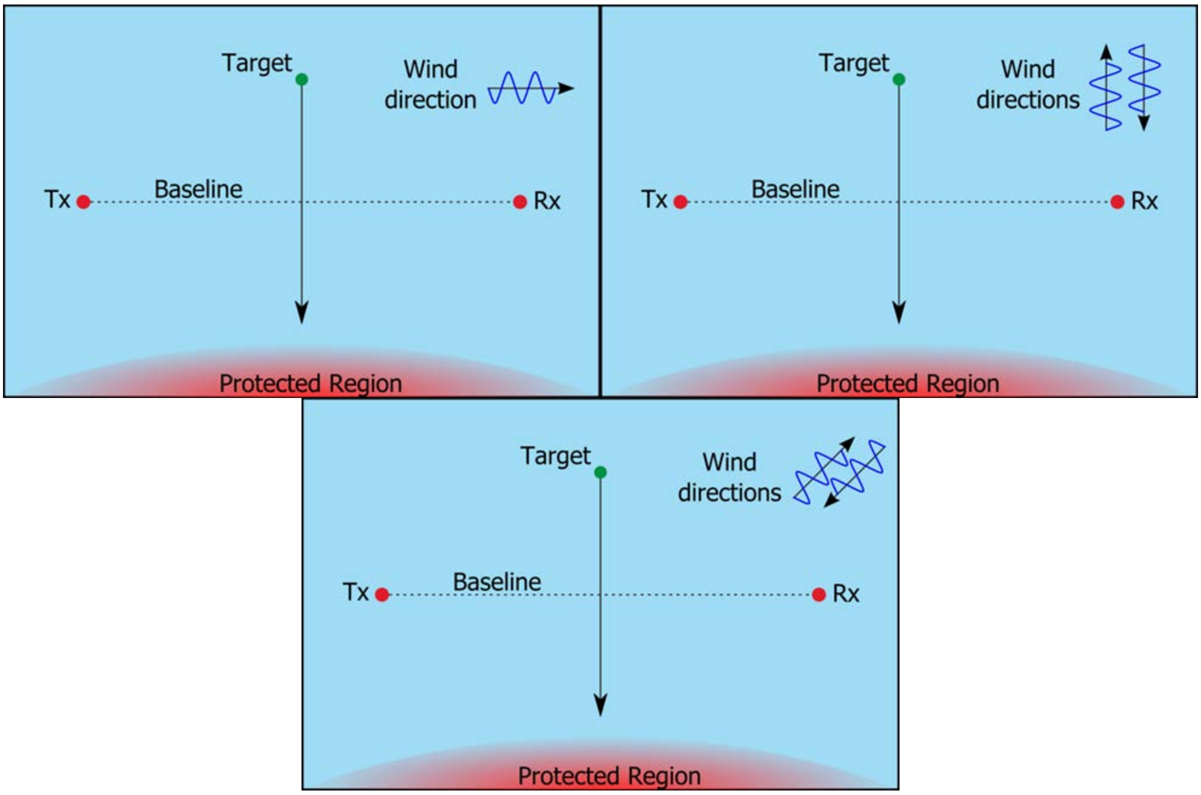

Figure 6.7-1. Simulation topologies, perpendicular crossing of baseline with winds (a) parallel, (b) perpendicular with and against target and (c) at 45° to the baseline with and against target direction.

upon the standard small inflatable boat target used in much of the experimental maritime FSR investigation i.e. of length 2.9 m and 1 m height [65] as introduced in Section 4.3, though a sub-set of simulations are carried out with 2 m height for comparative reasons; the target speed chosen is a low to medium speed of 4 ms^{-1} for all simulations. Again conforming to the experimental investigation, the radar frequency used (along with the target length) in order to calculate the potential visibility time is 7.5 GHz.

The wave spectrum chosen for use in the simulation is the P-M spectrum as stated in Section 6.2.1.3, it allows for a well-defined comparison of results; this is combined with the frequency dependent Mitsuyasu spreading function (Section 6.2.2.3). For each wind/baseline topology, five different wind speeds are chosen for the PM spectrum, giving significant wave heights of 0.5, 1, 2, 3 and 4 m (SS 2/3 – SS 5/6) as shown in Table 6.7-1. Along with this, four antenna heights of 1, 2, 3 and 4 m are simulated and three baseline lengths of 250, 500 and 1000 m. It should be noted that the small inflatable boat target under consideration would not be deemed seaworthy in a sea state above 3 (1 m significant wave height) and so any conclusions should be drawn in relation to this limit.

Table 6.7-1. Sea state descriptors for simulations with Pierson Moskowitz Spectrum.

Wind Speed U_{10} [ms^{-1}]	**Modal Wavelength [m]**	**$H_{1/3}$ [m]**	**WMO Sea State # (Description)**
4.5	20	0.5	2/3 (Smooth Slight)
6.4	40	1	3 (Slight)
9.0	80	2	4 (Moderate)
11.0	120	3	5 (Rough)
12.7	150	4	5/6 (Rough/Very Rough)

Each simulated baseline crossing will be divided into 0.02 s time steps in which to test for lines of sight and in total there will be 1000 runs (simulated baseline crossings) through each topology for each set of parameters for statistics, each new run starts with a new set of random spectral phases so as not to repeat the same sea surface on any given run.

6.8 ANALYSIS OF AVERAGE TARGET VISIBILITY TIME

In the following analysis, the target visibility time is expressed as a fraction of the potential visibility time, i.e. the number of time steps in the run (baseline crossing) in which full LOS occurs as a fraction of the total number of time steps in the run—this will be termed the '*fractional visibility time*'. Further to this, the fractional visibility time will be averaged over all of the 1000 runs per simulated scenario. Where necessary/appropriate, this can be easily converted into normalised or actual average visibility times with knowledge of the potential visibility time.

6.8.1 EFFECT OF WIND DIRECTION ON FRACTIONAL VISIBILITY TIME—AND VARIATION WITH SIGNIFICANT WAVE HEIGHT

The first variable that is considered in the analysis is how the wind direction affects the target visibility time. Figure 6.8-1 shows the fractional visibilities for the simulations with 2 m antenna heights over the range of wind directions and (a), (b) and (c) correspond to the different baseline lengths of 250, 500 and 1000 m respectively.

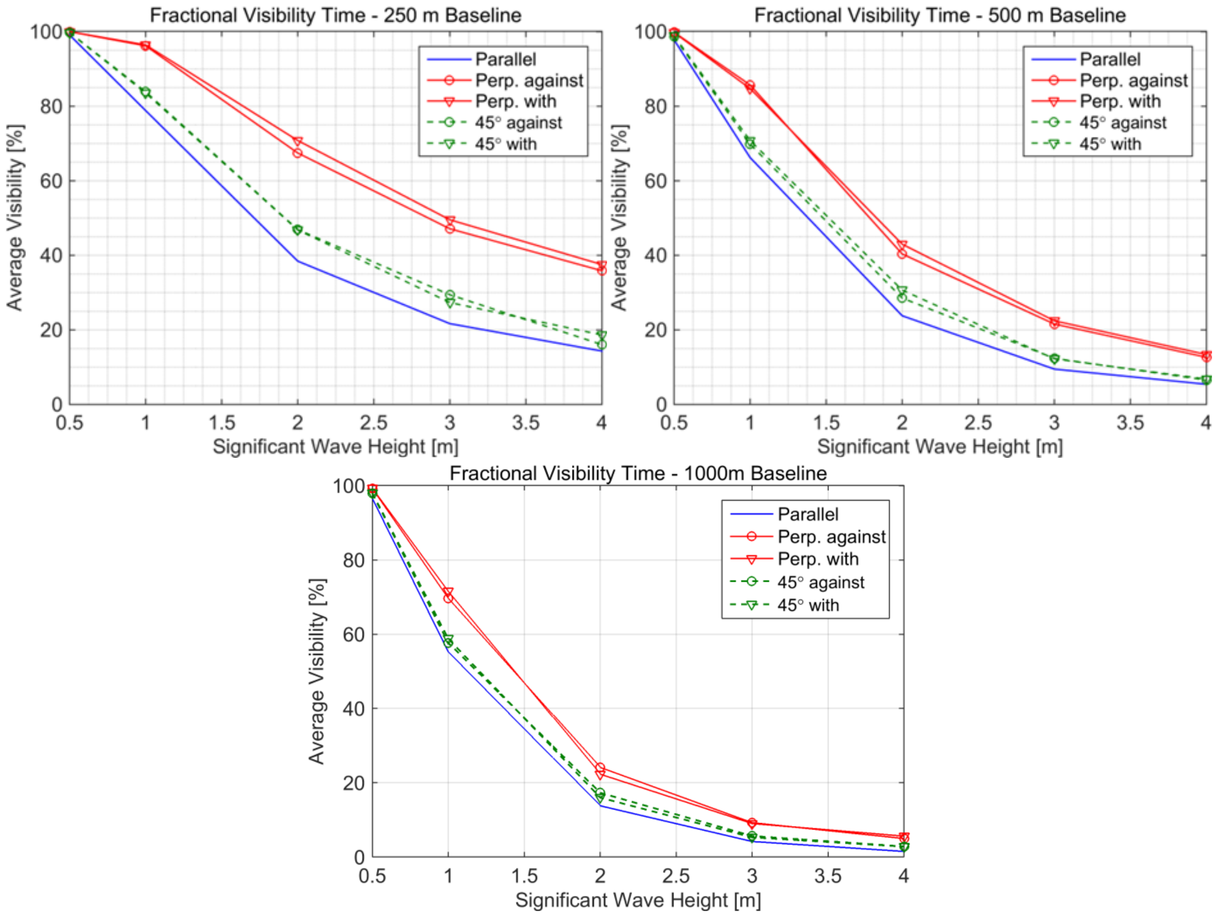

Figure 6.8-1. Dependence of fractional visibility time on the wind direction for 2 m antenna heights and baselines of (a) 250 m, (b) 500 m and (c) 1000 m.

It is immediately noticeable that there is a least and most preferable wind direction required to maximise the fractional visibility time of the target. The most favourable wind conditions are a wind perpendicular to the baseline (red lines in Figure 6.8-1), and as with the 45° winds (green lines), there is not much difference in visibility time with the wind being either with (triangles) or against (diamonds) the target motion; the least favourable wind is the wind blowing parallel to the baseline. These observations fit with the common sense view of the scenarios, the parallel wind would excite waves to oscillate up and down in between the antennas providing maximum wave blocking, whereas the perpendicular wind excites them such that the target and antennas would be oscillating more in synchronous with each other. The 45° case is an intermediate situation, though tending more towards the parallel case in terms of the effect on target visibility. A general comment can be made that after an initial separation of the curves when the significant wave height exceeds the target half height (0.5 m), as the significant wave height increases further, for significant wave heights greater than the antenna height (2 m), the difference in fractional visibility time between best and worst case wind conditions reduces. This can be assumed to be the effect of the increased blocking due to increased wave height dominating any effect of the wind conditions. For example, the 500 m baseline difference in fractional visibility reduces from 19% to 8% between significant wave heights of 2 – 4 m.

6.8.2 EFFECT OF BASELINE LENGTH ON VISIBILITY TIME

On viewing the plots in Figure 6.8-1, it is apparent that the rate of drop off of target fractional visibility time over increasing significant wave height is greater for the longer baselines. Ultimately the longer baselines have generally lower fractional visibility times for a given sea state, which fits again with the common sense view of increased number of wave peaks between antennas and target and antennas and thus greater amounts of blocking of LOS. However this is only a part of the picture, as the baseline length increases, the potential visibility time for the target crossing also increases, due to the geometry. It is therefore apparent that in order to compare results between baselines, it is necessary to normalise the potential visibility times.

Due to the defined target trajectory for the simulations presented here (perpendicular crossing of baseline), normalising the potential visibility times is relatively straight forward as they are proportional to the baseline length. Thus the 250 m baseline is given a normalised potential visibility time of 1, the 500 m baseline is therefore 2 and the 1000 m baseline is 4. Figure 6.8-2 shows the equivalent plots from Figure 6.8-1, but now with a normalised instead of fractional visibility time, which now allows the comparison of true effect of baseline length.

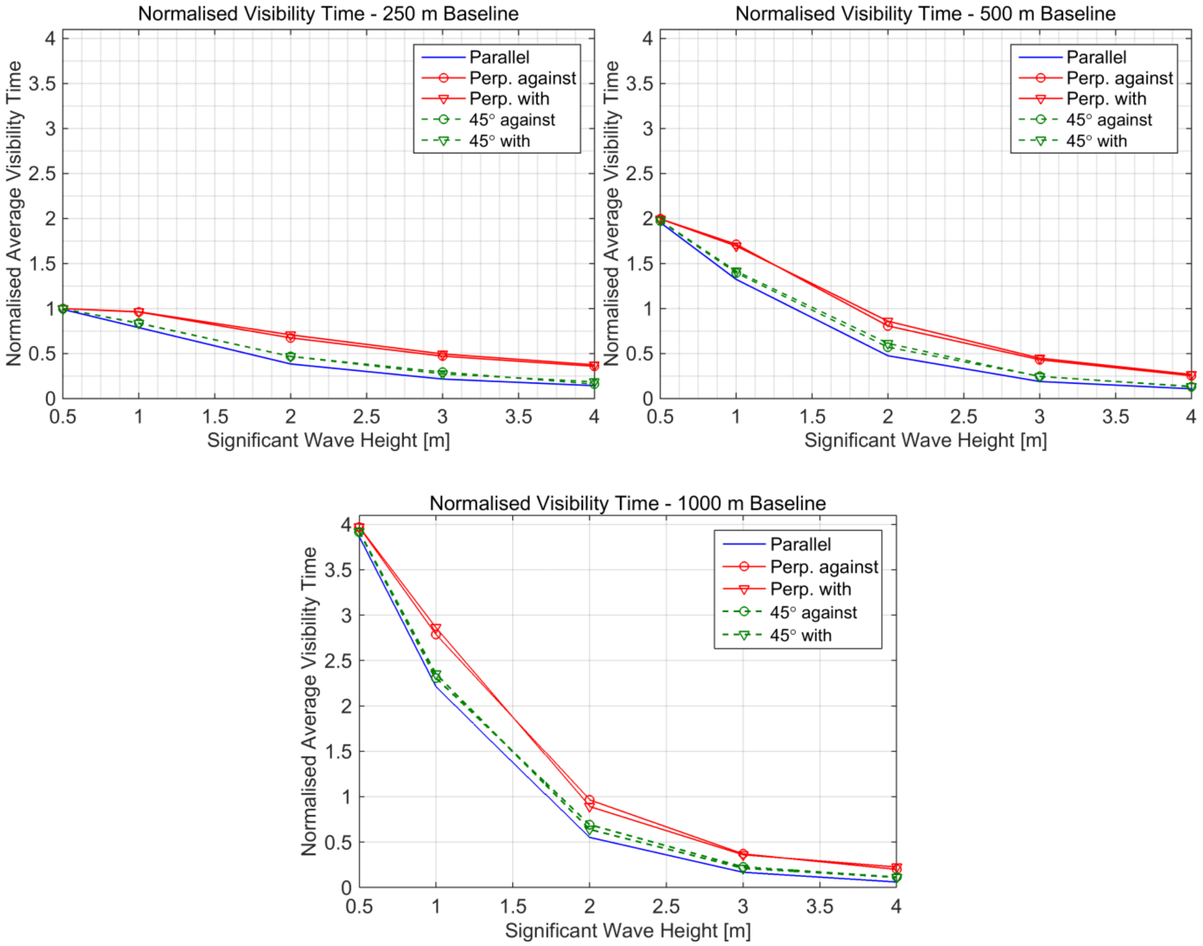

Figure 6.8-2. Dependence of normalised visibility time on baseline for baseline lengths of (a) 250 m, (b) 500 m and (c) 1000 m. Antenna heights 2 m.

It is clear that for significant wave heights less than the antenna height of 2 m, the reduction of fractional visibility time due to baseline length increase is more than compensated for by the increase in the potential visibility time. At wave heights greater than the antenna height it appears that there is no fundamental difference in the normalised visibility times with respect to the baseline length. The steeper falloff and lower fractional visibility times for the longer baselines cancel out any increase in potential visibility time. It must be stressed though that it is not so simple as to just increase the baseline and expect better visibility times for the lower sea states. This analysis assumes that the target can still be detected in a received power sense, but the increase of baseline length would obviously require increase in transmitted power.

If just the results at a significant wave height of 1 m (SS 3) are considered, it is possible to compare the best and worst case wind condition results over the range of baseline lengths, this is shown in Figure 6.8-3.

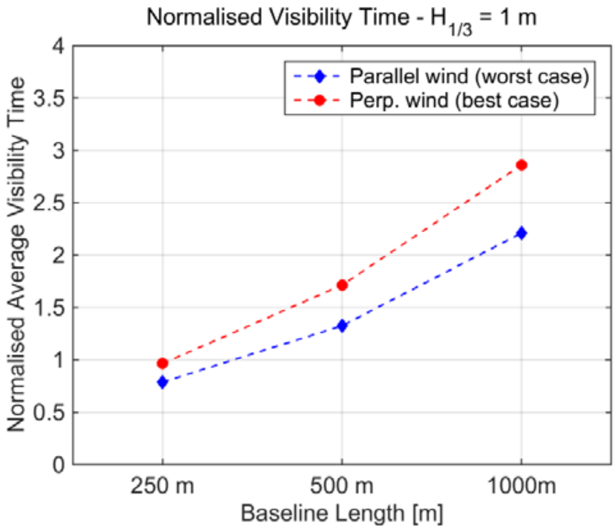

Figure 6.8-3. Normalised visibility time for various baseline lengths for 1 m significant wave height (SS 3) with best and worst case wind conditions – antenna height 2 m.

It can be seen from the figure that in going from 250 m baseline to 1000 m, it is possible to triple the average visibility time for the best and worst case (perpendicular and parallel) wind scenarios. Given that the visibilities are normalised to the 250 m baseline, it is possible to use the actual potential visibility time to define the absolute visibility time. Figure 6.8-4 shows the equivalent of Figure 6.8-3 however now with the absolute/actual visibility times.

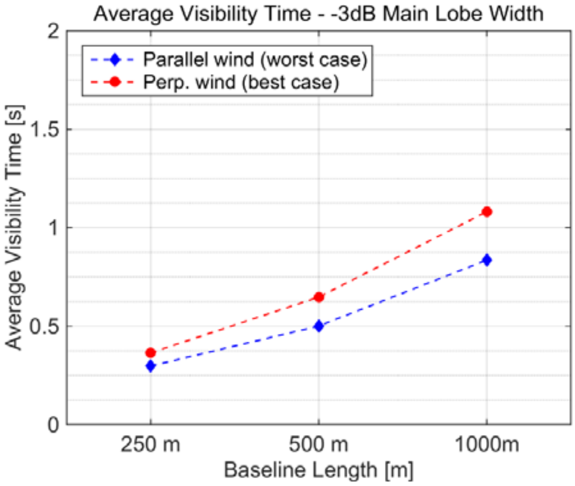

Figure 6.8-4. Actual visibility time [s] for various baseline lengths for 1 m significant wave height (SS 3) with best and worst case wind conditions – antenna height 2 m.

The plot indicates that assuming the target is detectable within the -3 dB main lobe of the FSCS pattern, with a baseline range of 1000 m it may be possible to achieve a target visibility time between 0.8 and 1.1 s dependent on the wind conditions. For 500 m basleine this reduces to between 0.5 and 0.65 s.

6.8.3 EFFECT OF ANTENNA HEIGHTS ON FRACTIONAL VISIBILITY TIME—AND VARIATION WITH SIGNIFICANT WAVE HEIGHT

In this section, the effect of antenna heights varying from 2 – 4 m on the fractional target visibility is discussed for the worst case wind scenario of the wind being parallel to the baseline again over a range of baseline lengths; plots are shown in Figure 6.8-5. As expected, the increase in antenna height does increase the fractional visibility time for a given baseline range as expected. However, as significant wave height increases, the effectiveness of the antenna height increase reduces, i.e. the separation between the blue and green lines (4 and 2 m antenna heights) tends to reduce. It may be expected that the taller antennas should maintain effectiveness in increasing target visibility to higher sea states, however there is interplay here between not only the antenna-antenna visibility, but the antenna-target visibility. Increasing the antenna heights at longer ranges does not necessarily help the antenna-target visibility as the look down angle is very shallow and remains shallow under antenna height increases which are small in comparison to the baseline range. In order to compare across the baseline ranges, again the visibility times should be normalised as described in the previous section, Section 6.8.2. The normalised visibility time plot equivalents of the plots in Figure 6.8-5 are shown in Figure 6.8-6

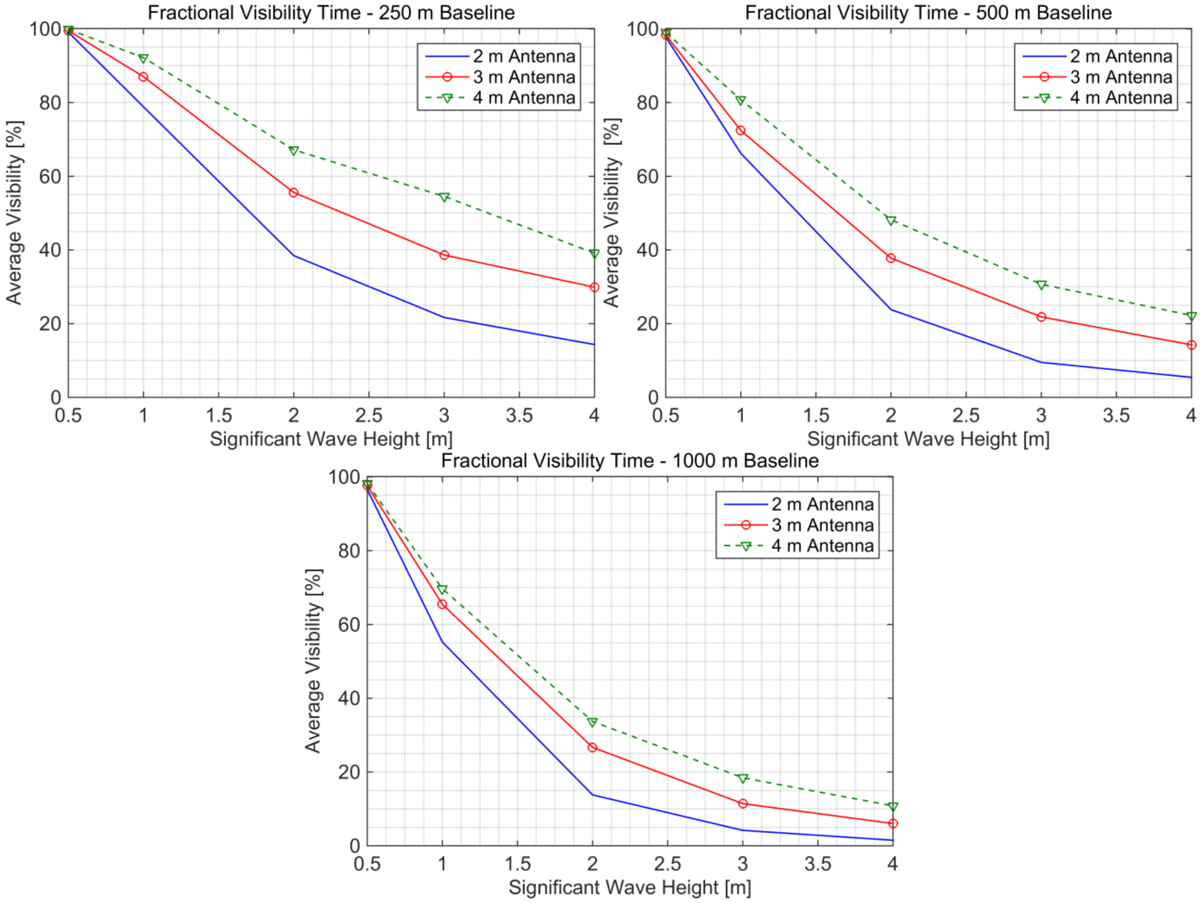

Figure 6.8-5. Dependence of fractional visibility time on antenna heights of 2 - 4 m, for baseline lengths of (a) 250 m, (b) 500 m and (c) 1000 m. Antenna heights 2 m, wind parallel to baseline (worst case).

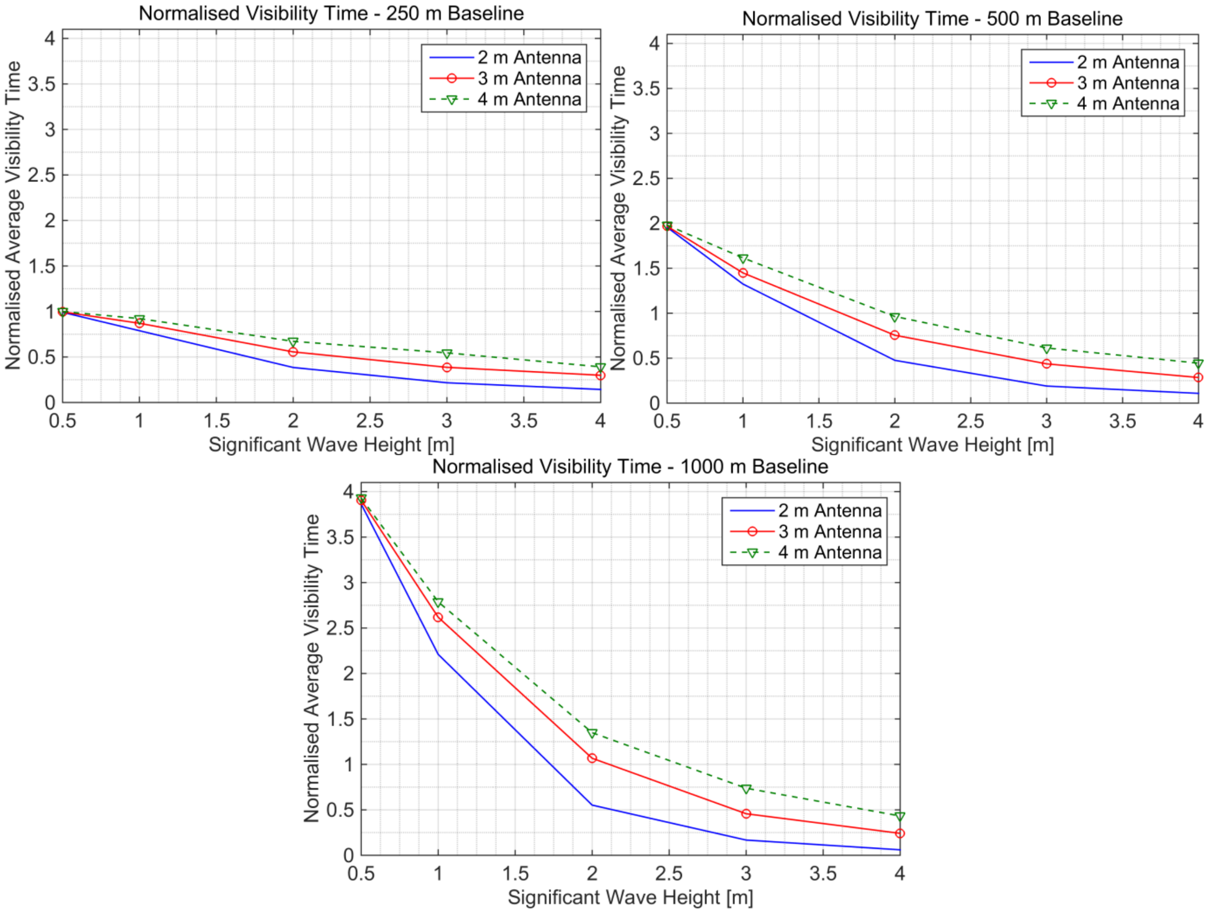

Figure 6.8-6.. Dependence of normalised visibility time on antenna heights of 2 - 4 m, for baseline lengths of (a) 250 m, (b) 500 m and (c) 1000 m. Antenna heights 2 m, wind parallel to baseline (worst case).

Once again from this, it is possible to focus on the results for SS 3 (1 m significant wave height) and plot the normalised and actual visibility times as a function of baseline length and antenna height, as in Figure 6.8-7. It can be seen, that if the target is detectable within the -3 dB main lobe of the FSCS pattern with a baseline range of 1000 m, it is possible to achieve target visibility time improvement of 0.8 to 1.1 s on increase of the antenna height from 2 m to 4 m. If detection is only achievable at 500 m then the target visibility time will be reduced to being between 0.5 and 0.6 s.

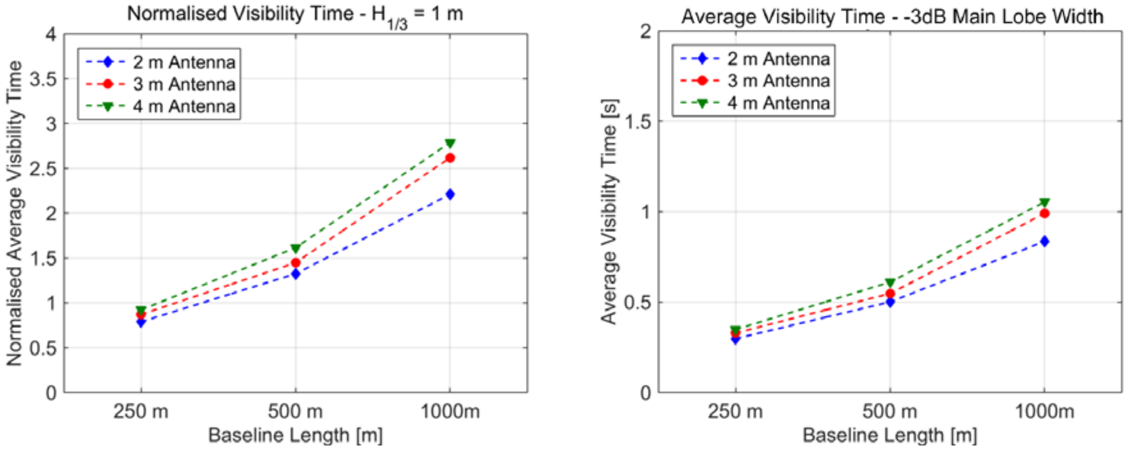

Figure 6.8-7. Normalised (a) and actual visibility time (b) for various antenna heights as a function of baseline lengths for 1 m significant wave height (SS 3) under worst case wind conditions – antenna height 2 m.

6.9 SUMMARY OF VISIBILITY SIMULATIONS

A sea surface simulator has been developed in order to estimate the availability of target LOS visibility in a buoy mounted maritime FSR. This was done in order to assess if the system had any potential capability in situations where wave blocking was expected and which were unmeasurable experimentally at this stage. The simulation uses empirical sea surface spectra and simple target and antenna models. Target visibility times have been estimated for a set of scenarios which include variation of wind direction, wave height, baseline length and antenna heights.

Fundamentally the simulations have shown that the FSR system would still maintain a certain level of target visibility in sea states where wave blocking is expected and warrants further research into these scenarios

The simulated average visibility times from the results range from between 0.3 s and 1.2 s over all scenarios. Comparing these visibility times (which in essence are the coherent integration times in FSR) to the coherent integration times for the monostatic radar in

Table **2.10-1**, it can be seen that they are still comparatively quite lengthy even with the effect of wave blocking. It should however be noted that the visibility estimations are all given under the assumption that adequate target power is received for detection over the given ranges, within the received clutter power.

The simulation work in this chapter has been described (more briefly) in the author’s publication [99]. Simulations looking at the effect on visibility by including a second parallel baseline can be found in [100]—also written by the author of this thesis. This paper simulated a target traversing different parallel baseline separations with 3 m height waves travelling perpendicular and parallel to the 500 m baselines. The fractional visibility times for a single baseline and for the combined baselines were calculated and it was found that for baseline separations above 12.5 m, the second baseline was acting as if it were statistically independent to the first[5]. For the worst case scenario of wind parallel to the baseline, a single baseline gave an average fractional visibility of 23% whereas the pair gave 39%.

It still remains to validate the simulation model through comparison with trials data. As stated in the introduction to this section, currently all the maritime FSR experimental data has been recorded in situations where wave blocking has not been observed. In order to gain confidence in the use of the model for extrapolating results to higher sea states, more measurements will be required. The reason for the simulation development was that experiments with small boats in high sea states are difficult to perform. Blocking can currently only be experimentally measured by reducing antenna heights during lower sea state measurements. A series of scaled down measurements may be performed i.e. target height, antenna height and wave height reduced, however maintain similar height ratios as in the simulations. There will of course be propagation related effects due to the reduction of

---

[5] This may also be confirmed by looking at the auto-correlation function and correlation length of the generated sea surface.

antenna height and these will need to be considered in more detail when planning such experiments. The evidence of blocking of line of sight will be apparent from a complete loss of received power at the detector output—implying a loss of direct path signal. The blocking time can be estimated from these received power outages and compared to the model.

The simulations themselves may be also be extended. Currently they only include the generation of wind driven (wind-sea) waves; it may be assumed that swell will have a role in any real sea measurement. Swell may be caused by very distant storms and will introduce long wavelength structures to the wave spectrum. The wave spectrum may become bi-modal, one peak from the local wind driven waves and the other from the distant swell (discussed in [101] and the references within). The addition of swell to the simulations and the investigation of its effects may be considered as future work. Ultimately, from a radar performance prediction point of view, it would be useful to assess target visibility from an electromagnetic point of view. Having had experience with commercial electromagnetic simulation software, it is noted that the generated faceted sea surface model lends itself to a multi-bounce ray tracing/geometrical optics simulation. Rays are launched at the surface and each hit point acts as a new Huygens source of waves; the simulation only requires that the appropriate level of surface detail is used. Generally it would be assumed that feature sizes of the order of a wavelength should be incorporated. The surface detail is not only governed by the range of spectral components used (surface sample rate), but also by the surface resolution and these parameters will need investigation. 3D target models such as the ones shown in [61] and [62] would be introduced onto the surface. The simulation would have to be stepped through time to build up a full received signal record similar to that measured. Computational time may be excessive for larger surfaces, though the use of GPU processing will help here. To decrease simulation times the surface area of the simulation may be reduced by considering smaller baselines and restricted angles. The surface may be considered a perfect electrical conductor due to the low grazing angle and surface conductivity, further reducing simulation complexity.

7 SUMMARY, CONCLUSIONS AND FUTURE WORK

7.1 SUMMARY

This thesis and the research work related to it, is dedicated to the study of Forward Scatter Radar (FSR) in the context of the marine environment and marine target measurements. FSR is a little (but growing) studied sub-class of bistatic radar, its application to the marine environment is a novel concept, which takes advantage of the benefits that FSR has to offer to overcome the problems associated with a high clutter environment such as the ocean. The study has involved a mix of theory/phenomenology, classic radar principles, hardware design and production, model development, simulation, extensive field trials (in what were at many times harsh environmental conditions), as well as initial (more qualitative) data analysis.

The thesis begins by setting the scene on why such a radar system would be required, and its application for persistent remote monitoring of maritime borders and assets. It is not necessarily seen as a replacement for the current sensing systems, but an addition. An introduction to common monostatic and bistatic radar principles, concepts and terminologies is provided in Section 2. FSR is then introduced and comparisons drawn between the three radar types in order to give context and highlight the benefits of FSR; such as increase in radar cross section in the forward direction and increased target coherent/visibility times. After the fundamentals of FSR had been introduced in a more conceptual manner, the phenomenology behind FSR was then discussed in Section 3.1, putting it in a more physical light through its description in terms of the Physical Theory of Diffraction. This is by no means described to a rigorous level, but to one which allowed the formulation of a fundamental signal model for FSR. This was based around two components, a Doppler component and an amplitude modulation component imposed by the FSCS. This description was then incorporated with the free space and two-ray path propagation models in the derivation of the power budget for FSR in Section 3.2. This is a more comprehensive signal description, whereby the two-ray path model introduces multi-path reflections into the model; a brief discussion of the multi-path effects on the sea surface was given—these are the underlying source of the clutter in maritime FSR. Section 3.1.5 presents results of experimental work performed in an anechoic chamber, in order to experimentally observe the effect of the FS Shadow Contour Theorem, i.e. that the FSCS is governed solely by the silhouette shape of the target. This was investigated by comparing the signature of similarly contoured metallic and absorbing targets. The result of the experimental measurements confirmed the effect.

After the more theoretical aspects of forward scatter and FSR had been discussed, the concept behind the expected application of this work, the maritime FSR network, was introduced in Section 4.1. A short discussion on how such a networked system may be practically implemented was provided. Following this, the core design of the FSR hardware was explained—the self-mixing receiver. This inherently uses the direct path signal between transmitter and receiver as a reference to extract the low frequency Doppler of targets crossing the FSR baseline. 7.5 GHz experimental hardware development and production was discussed in Section 4.2, including efforts to design and build hardware for future experimentation, in the form of additional multi-frequency and UWB systems. The trials methodology, a brief description of test sites and other experimental essentials was included, preceding the presentation of measurement results from comprehensive trials in Section 5.

An overview of maritime FSR clutter analysis was given, explaining the key aspects such as the narrow clutter bandwidth, concentrated below 1Hz, and its Rayleigh probability density. Both of which appear invariant to the experimental parameters used in the trials on which the analysis was performed. Following this a selection of target measurement results are presented, recorded with variation of certain parameters of the target, radar and radar topology. Initial analysis was performed on the data, mostly of a qualitative nature involving comparison of the spectra. The effect of changing target velocity and crossing angle were observed to fit with the expectation from theory, in general the very narrow clutter bandwidth does not completely overlap the target spectra. This allows the detection/visibility of the small boat target even at very low speeds and with trajectories at very narrow angles to the baseline. The visibility of targets in increasing sea states was studied, showing the expected degradation of visibility with increased sea roughness and clutter. Some initial processing was performed through the application of a 2 Hz HPF to remove clutter and this was shown to help improve the target visibility/SCR. Results to show the effect of the radar polarisation on the target and clutter signals have been presented. These fit with the expected behaviour corresponding to very low grazing angle measurements, and the forward scatter effect at optical frequencies. Finally some results of target measurements made over longer ranges were presented, it was seen that with the current maritime hardware it was possible to detect the small inflatable boat target over a baseline range of 1300 m. The target was crossing the mid-point of the baseline, which is the least preferable from a power budget perspective. The concept of ‘quasi-optimal’ processing was introduced in Section 5.2.6 and showed by application to data, that even though FSR has no range resolution, processing techniques can be applied to extract the target trajectory with good accuracy. In summary, the method uses signal correlation with a reference database in order to find the reference with the nearest matching trajectory parameters. The quasi-optimal processing is very similar to the matched filter correlator and so was also applied to a high sea state record (after a 2 Hz HPF clutter removal) to further increase the SCR. Following this, a discussion was provided of what needs to be done in order to predict the detection capabilities of the FSR system, its effectiveness against marginal (low SCR) targets and implement automatic target detection algorithms.

Finally due to the fact that the majority of experimental work had to be carried out in low sea state littoral waters, with stationary antennas, simulations were required in order to give some estimation of the FSR system capabilities in open sea conditions. The maritime FSR system is ultimately expected to function out in the deep sea in high sea states, with moving antennas, where wave blocking is expected to become an issue. This sort of environment is not however easily accessible for trials.

In Section 6, a 3D sea surface model was created through the use of empirical deep sea wave spectra. Antennas and targets were placed upon the animated surface, set in motion, and target line of sight visibility times were estimated for varying wind/wave speeds and directions. The simulations suggested that visibility can be maintained for between 0.3 s and 1.2 s for the given simulation parameters, which is encouraging. Discussion was included as to how the simulations may be extended to include electromagnetic effects and how to validate the model experimentally.

7.2 CONCLUSIONS

The work undertaken for the production of this thesis actually initiated research in the field of maritime FSR. It set out to fundamentally show through creation of an experimental system and collection of experimental data, that the concept of maritime FSR was practically feasible. The author collected the first ever database of maritime FSR target and clutter records for various environmental, radar and target parameters.

The introductory work in Section 2 provided essential comparison of radar basics to place FSR within the context of the more commonplace radar systems (and vice versa). The phenomenological description in Section 3.1 however gave a more comprehensive, required understanding of the physics underlying the FSR system. The benefit of the phenomenological research is apparent as it allows us to more completely define the operating region of FSR, based on expected target sizes and radar frequency. It also provided the information necessary to produce the FSR signal and power budget models. These incorporated the most important consequence of the forward scatter effect, known as the *'Shadow Contour Theorem'*. The signal amplitude in the forward scatter region is modulated by the diffraction pattern from the target object's silhouette shape; it is independent of the full 3D shape and material. This makes it very useful in detecting stealth targets. At this stage, neither model has been comprehensively compared to experimental data for verification. However, the signal simulated for comparison to the results of anechoic chamber experiments to verify the FS effect in Section 3.1.5 provided a good match to the measured signals in the FS region for which it was derived. It gave a near complete match to the rectangular absorbing target, which almost completely negates any bistatic scattering, which the FS signal model doesn't account for. This gives the signal model some credibility at least in controlled conditions. The models were derived in this work in order to gain insight into what to expect during measurement, provide correlation references for the quasi-optimal processing in Section 5.2.6 and more fundamentally create a starting point for future development and verification; and these goals were achieved.

As stated previously, one of the most important aims for this research was to create an experimental system to perform actual maritime FSR measurements; the other was to make the measurements themselves. Both of these aims were achieved, and both contribute to the field of research in novel and important ways. Now that the design of the FSR system has been considered, built and proven experimentally, it can be used for future FSR studies. The trials data, as mentioned before, is unique and of great importance for progressing the current research. The main effort in design has been into the development of a 7.5 GHz system, based around the 'self-mixing' receiver, this has been the mainstay of the experimental research in this thesis. Thought has been put into testing the effects of radar parameters on performance; the FS phenomenology gives an indication into how the radar parameters may affect the target signal. This made the case for the design and inclusion of a 24 GHz channel in the radar system. The higher frequency may enable better target detection due to the increased target FSCS, however the reduction in width of the FSCS main lobe may impact directivity towards the receiver. This requires experimental investigation, and it is currently unknown how the clutter amplitude will behave at this higher frequency. This hardware addition was included to ensure the progress of research into the next stages after the work in this thesis.

All the experimental data within the thesis was collected for the fundamental single baseline transmitter–receiver pair, and indeed this is where the research should start. Research effotr should however be put in alongside this, to ensure that the end goal of the FSR buoy mounted network is feasible from a practical point of view. Discussion has been included in Section 4.1 as an effort to identify some of the issues that may need exploring. Additionally to this however, an analysis of the potential performance improvements derived from the network should be made e.g. enhanced target tracking across multiple baselines.

A selection of data from the measurement campaign was presented in Section 5 in which clutter analysis results were presented in terms of the clutter spectra and distribution. The target measurement data at this time has not however received as in depth an analysis and is currently more at the qualitative stages. The proposed ‘quasi-optimal’ processing was applied to estimate target trajectory parameters for a set of data. The fact that this processing provides good trajectory estimation is another indication that the FSR signal model used to form the correlation database is credible. The improvements from both the HPF clutter removal and quasi-optimal processing were not quantified completely and were shown rather as proof of principle. The techniques warrant further investigation into their optimisation and assessment of performance. The generation of the reference signature database requires investigation into the optimum parameter spacing required for accurate motion parameter estimation, whilst limiting the size of the database.

Currently no investigation has been performed on the data to predict detection performance of the radar system. This is a very important part of the development of the maritime FSR system as a whole and has been discussed at the end of Section 5.2.6. The clutter characteristics in general are known, what is required next is an analysis of the target data in order to estimate target signal statistics, and for verification or improvement of the FSR signal models. With the appropriate signal model the target signal characteristics may be simulated for a wide variety of scenarios without the need for excessive measurement campaigns. All the experimental measurements show reasonably good SCRs with easily detectable targets, and this is useful for understanding the system functionality and signal/propagation model confirmation. However, what is really important is to understand the detection capabilities against marginal targets. Once the statistics are understood, determination of the probabilities of detection for given false alarm rates and SCRs can be found and thought can be put towards the application of CFAR automatic detection schemes. It also important to understand what type/size/shape of target is considered a marginal target in FSR and how this varies with radar and topology parameters e.g. baseline length. This requires experimental validation of the FSR power budget to estimate signal strength and consequently (using clutter data) SCRs for given targets.

With no method of testing deep sea functionality, simulations were required in order to predict if this system will function in its proposed environment and thus warrant further investigation. The simulations gave good insight into the effects of wave blocking and how the various model parameters affect this. These results also seemed to correspond to insight. This model has however reduced the complexity of the real sea scenario quite dramatically with the choice to only measure the direct line of sight visibility; it will also require experimental confirmation as to its accuracy. It was proposed in Section 6.9 that this may be accomplished by scaled down experimentation, i.e. reduce antenna and target heights in low sea state measurements. The model could also extended, such as including the effect of swell in to the wave spectra, which may have a large effect. Ultimately it would be ideal to use the simulated surfaces in an electromagnetic simulation, this was also discussed in Section 6.9. The faceted models suggest ray tracing techniques could be used, it would be the subject of future work to assess the feasibility from a computational point of view however. If simulations are possible and accuracy determined, they can provide another source of data to further the development of the FSR system.

7.3 FUTURE WORK

As with any research, the work remaining exceeds what has already been accomplished. The process of performing the research highlights many important tasks with which to proceed. This section summarises the most important next stages of research and is drawn from the conclusions section.

The most important area of future work is to perform analysis on the collected target signature database. This will involve FSR signal model verification through comparison with the recorded data, to test if the models accurately reproduce the measured spectra, statistics and expected power budget. The use of the clutter analysis work will be required for this and this process will also determine if any further clutter analysis is required. Alongside this, the measured data should be used to begin characterisation of the FSR target detection capabilities. Estimations of detection probabilities should be formed from the target and clutter statistics, the signal models can also be used to inform prediction for unmeasured scenarios. Marginal targets should be defined and the detection probabilities for these low SCR targets should be assessed. The use of automatic CFAR detection schemes should be investigated (initially CA-CFAR) and their performance evaluated.

Being that the hardware is already constructed, extensive experimentation should be made using the 24 GHz FSR system and compared to simultaneous 7.5 GHz measurements. This should be part of ongoing work investigating the optimisation of the FSR system, motivated in part by the FSR phenomenology.

Validation of LOS simulation models will require new data sets to be recorded with very low antenna heights in order for the measurement of wave blocking to be accomplished. This testing should be combined with and part of the 24 GHz measurements. Development of the model in terms of the addition of swell to the current simulation method and expansion of the model to consider electromagnetic scattering should be investigated.

The current clutter filtering and quasi–optimal processing methodologies should be progressed further, estimating performance and optimising filter characteristics and reference database creation.

Finally, some continued effort should be made into investigating the practicalities of networking nodes in the final system design. It is better to know the problems that may be faced before we face them.

REFERENCES

[1] M. J. Skolnik, *Radar Handbook*, 3rd ed. McGraw-Hill, 2008.

[2] N. J. Willis, *Bistatic Radar*, 2nd ed. SciTech Publishing Inc., 2005.

[3] H. D. Griffiths, C. Baker, and D. Adamy, *Stimson's Introduction to Airborne Radar*, 3rd ed. SciTech Publishing Inc., 2014.

[4] F. E. Nathanson, *Radar Design Principles*, 2nd ed. SciTech Publishing Inc., 1999.

[5] G. D. Hopkins, J. Ratner, A. Traille and V. Tripp, "Aperture Efficiency of Amplitude Weighting Distributions for Array Antennas," 2007 IEEE Aerospace Conference, Big Sky, MT, 2007, pp. 1-9.

[6] M. J. Skolnik, *Introduction to Radar Systems*, 3rd ed. McGraw-Hill, 2001.

[7] D. K. Barton, *Modern Radar System Analysis*, 1st ed. Artech House Inc., 1988.

[8] C. A. Balanis, *Antenna Theory - Analysis and Design*, 2nd ed. John Wiley, 1997.

[9] E. V. Jull, *Aperture Antennas and Diffraction Theory*. Institution of Engineering and Technology, 1981.

[10] T. A. Milligan, *Modern Antenna Design*, 2nd ed. Wiley-Blackwell, 2005.

[11] M. Born and E. Wolf, *Principles of Optics: Electromagnetic Theory of Propagation, Interference and Diffraction of Light*, 7th ed. Cambridge University Press, 1999.

[12] E. Hecht, *Optics*, 4th ed. Pearson Education Limited, 2013.

[13] Y. Kathuria, "Far-field radiation patterns of elliptical apertures and its annulli," *IEEE Trans. Antennas Propag.*, vol. 31, no. 2, pp. 360–364, Mar. 1983.

[14] G. B. Airy, "On the Diffraction of an Object-Glass with Circular Aperture," *Trans. Cambridge Philos. Soc.*, vol. 5, pp. 283–291, 1835.

[15] C. A. Balanis, *Advanced Engineering Electromagnetics*, 2nd ed. John Wiley, 2012.

[16] M. Cherniakov, *Bistatic Radars: Principles and Practice*, 1st ed. Wiley-Blackwell,

2007.

[17] “CST Microwave studio.” [Online]. Available: https://www.cst.com/Products/CSTMWS.

[18] P. Swerling, “Radar probability of detection for some additional fluctuating target cases,” *IEEE Trans. Aerosp. Electron. Syst.*, vol. 33, no. 2, pp. 698–709, Apr. 1997.

[19] P. Swerling, “Probability of detection for fluctuating targets,” *IEEE Trans. Inf. Theory*, vol. 6, no. 2, pp. 269–308, Apr. 1960.

[20] D. O. North, “An Analysis of the factors which determine signal/noise discrimination in pulsed-carrier systems,” *Proc. IEEE*, vol. 51, no. 7, pp. 1016–1027, 1963.

[21] V. S. Chernyak, *Fundamentals of Multisite Radar Systems*. 1998.

[22] P. Ufimtsev, “New Insight into the Classical Macdonald Physical Optics Approximation,” *IEEE Antennas Propag. Mag.*, vol. 50, no. 3, pp. 11–20, Jun. 2008.

[23] G. T. Ruck, D. E. Barrick, K. M. Stuart, and K. C.K, *Radar Cross Section Handbook*, 1st ed. Plenum Press, 1070.

[24] R. A. Ross, “FORWARD SCATTERING FROM A FINITE, CIRCULAR CYLINDER,” *Prog. Electromagn. Res. C*, vol. 2, pp. 207–215, 2008.

[25] P. Y. Ufimtsev, *Fundamentals of the Physical Theory of Diffraction*, 1st ed. Wiley-Blackwell, 2007.

[26] M. Gashinova, L. Daniel, V. Sizov, E. Hoare, and M. Cherniakov, “Phenomenology of Doppler Forward Scatter Radar for Surface Targets Observation,” *IET Radar, Sonar Navig.*, vol. 7, no. 4, pp. 422–432, Apr. 2013.

[27] M. Gashinova, L. Daniel, E. Hoare, V. Sizov , K. Kabakchiev and M. Cherniakov, “Signal characterisation and processing in the forward scatter mode of bistatic passive coherent location systems,” *EURASIP Journal on Advances in Signal Processing*,

December 2013, 2013:36.

[28] V. V. Chapurskiy and V. N. Sablin, “SISAR: Shadow Inverse Synthetic Aperture Radiolocation,” *Rec. IEEE 2000 Int. Radar Conf. [Cat. No. 00CH37037]*, vol. 0, pp. 322–328, 2000.

[29] S. Hristov, L. Daniel, E. Hoare, M. Cherniakov, and M. Gashinova, “Target Shadow Profile Reconstruction in ground-based forward scatter radar,” in *2015 IEEE Radar Conference (RadarCon)*, 2015, pp. 0846–0851.

[30] A. Myakinkov, A. Kuzin, M. Gashinova, V. Sizov, and M. Cherniakov, “Inverse Forward Scatter SAR,” in *Proc. Of International IEEE Conference Synthetic Aperture Sonar and Synthetic Aperture Radar*, 2010, vol. 32.

[31] J. Glaser, “Bistatic RCS of Complex Objects near Forward Scatter,” *IEEE Trans. Aerosp. Electron. Syst.*, vol. AES-21, no. 1, pp. 70–78, Jan. 1985.

[32] G. Mie, “Beiträge zur Optik trüber Medien, speziell kolloidaler Metallösungen,” *Ann. Phys.*, vol. 330, no. 3, pp. 377–445, 1908.

[33] H. C. Hulst van de, *Light Scattering by Small Particles*, 1st ed. Dover Publications Inc., 2003.

[34] P. Y. Ufimtsev, “The 50-Year Anniversary Of the PTD: Comments on the PTD’s Origin and Development,” *IEEE Antennas Propag. Mag.*, vol. 55, no. 3, pp. 18–28, 2013.

[35] H. M. Macdonald, “The Effect Produced by an Obstacle on a Train of Electric Waves,” *Philos. Trans. R. Soc. A Math. Phys. Eng. Sci.*, vol. 212, no. 484–496, pp. 299–337, Jan. 1913.

[36] W. Macke, “V. A. Fock, Electromagnetic Diffraction and Propagation Problems. (International Series of Monographs on Electromagnetic Waves, Volume 1) IX + 414

S. m. Fig. u. Tab. Oxford/London/Edinburgh/New York/Paris/Frankfurt 1965. Pergamon Press. Preis geb. $ 7 net," *ZAMM - Zeitschrift für Angew. Math. und Mech.*, vol. 46, no. 1, pp. 76–76, 1966.

[37] P. Y. Ufimtsev, "The 50-Year Anniversary Of the PTD: Comments on the PTD's Origin and Development," *IEEE Antennas Propag. Mag.*, vol. 55, no. 3, pp. 18–28, 2013.

[38] P. Y. Ufimtsev, *Theory of Edge Diffraction in Electromagnetics: Origination and Validation of the Physical Theory of Diffraction*, 1st ed. SciTech Publishing Inc., 2000.

[39] J. F. Seybold, *Introduction to RF Propagation*, 1st ed. 2005.

[40] "Laird Technologies." [Online]. Available: http://www.lairdtech.com/. [Accessed: 10-Feb-2016].

[41] M. Gashinova, L. Daniel, K. Kabakchiev, V. Sizov, E. Hoare, and M. Cherniakov, "Phenomenology of signals in FSR for surface targets detection," *Radar Syst. (Radar 2012), IET Int. Conf.*, pp. 1–6, 2012.

[42] V. Sizov, M. Cherniakov, and M. Antoniou, "Forward scattering radar power budget analysis for ground targets," *IET Radar, Sonar Navig.*, vol. 1, no. 6, p. 437, 2007.

[43] J. D. Parsons, *The Mobile Radio Propagation Channel*, 2nd ed. Wiley.

[44] T. S. Rappaport, *Wireless Communications: Principles and Practice*, 2nd ed. Prentice Hall, 2002.

[45] P. Z. Peebles, *Radar Principles*, 1st ed. Wiley-Interscience, 1998.

[46] C. I. Beard, "Coherent and Incoherent Scattering of Microwaves from the Ocean," *IRE Trans. Antennas Propag.*, vol. 9, no. 5, pp. 470–483, Sep. 1961.

[47] M. Gashinova, K. Kabakchiev, L. Daniel, E. Hoare, V. Sizov, and M. Cherniakov, "Measured forward-scatter sea clutter at near-zero grazing angle: analysis of spectral

and statistical properties," *IET Radar, Sonar Navig.*, vol. 8, no. 2, pp. 132–141, Feb. 2014.

[48] W. Ament, "Toward a Theory of Reflection by a Rough Surface," *Proc. IRE*, vol. 41, no. 1, pp. 142–146, Jan. 1953.

[49] C. Beard and I. Katz, "The dependence of microwave radio signal spectra on ocean roughness and wave spectra," *IRE Trans. Antennas Propag.*, vol. 5, no. 2, pp. 183–191, Apr. 1957.

[50] R. M. Brown and A. R. Miller, "Geometric-Optics Theory for Coherent Scattering of Microwaves From the Ocean Surface," 1974.

[51] A. R. Miller, R. M. Brown, and E. Vegh, "New Derivation for the Rough-Surface Reflection Coefficient and for the Distribution of Sea-Wave Elevations," *IEE Proc. H (Microwaves, Opt. Antennas)*, vol. 131, no. 2, pp. 114–116, Apr. 1984.

[52] T. S. Hristov, K. D. Anderson, and C. A. Friehe, "Scattering Properties of the Ocean Surface: The Miller–Brown–Vegh Model Revisited," *IEEE Trans. Antennas Propag.*, vol. 56, no. 4, pp. 1103–1109, Apr. 2008.

[53] S. R. Massel, *Ocena Surface Waves: Their Physics and Prediction*, 1st ed. World Scientific Publishing Co., 1998.

[54] "Kuhne Electronics." [Online]. Available: http://www.kuhne-electronic.de/en/home.html. [Accessed: 15-Feb-2016].

[55] "Mini Circuits ZX47-60." [Online]. Available: http://194.75.38.69/pdfs/ZX47-60+.pdf. [Accessed: 10-Feb-2016].

[56] "Herotek Schottky Diodes." [Online]. Available: http://www.herotek.com/datasheets/pdf/High_Sensitivity_Zero_Bias_Schottky_Detectors_100KHz-26.5GHz.pdf. [Accessed: 12-Feb-2016].

[57] https://www.mccdaq.com/usb-data-acquisition/USB-1608FS.aspx

[58] “National Instruments - QuickSyn Synthesizers.” [Online]. Available: http://ni-microwavecomponents.com/quicksyn-full. [Accessed: 10-Feb-2016].

[59] “Aviation Formulary V1.46.” [Online]. Available: http://williams.best.vwh.net/avform.htm. [Accessed: 10-Feb-2016].

[60] L. Y. Daniel, E. G. Hoare, M. Gashinova, A. Svintsov, M. Cherniakov, and V. Sizov, “Ultra-Wideband Forward Scatter Radar Fence for Maritime Surveillance - Initial Experimental Results,” *Radar Conf. 2010 IEEE*, pp. 526–531, 2010.

[61] L. Daniel, M. Gashinova, and M. Cherniakov, “Maritime UWB forward scattering radar network: Initial study,” in *2008 International Conference on Radar*, 2008, pp. 658–663.

[62] L. Daniel, M. Gashinova, and M. Cherniakov, “Maritime target cross section estimation for an ultra-wideband forward scatter radar network,” *2008 Eur. Radar Conf.*, no. October, pp. 316–319, 2008.

[63] M. A. Richards, "Fundmentals of Signal Processing," 2nd Ed., McGraw Hill Education, USA, 2014.

[64] K. Ward, R. Tough and S. Watts, "Sea clutter: Scattering, the K Distribution and Radar Performance," 2nd Ed., The Institution of Engineering and Technology, London, 2013.

[65] K. Kabakchiev, L. Y. Daniel, V. Sizov, E. G. Hoare, M. Gashinova, and M. Cherniakov, “Received Signal Characterization in Forward Scatter Radar for Maritime Application,” *Radar Symp. (IRS), 2011 Proc. Int.*, pp. 67–72, 2011.

[66] K. Kabakchiev, L. Daniel, M. Gashinova, E. Hoare, M. Cherniakov, and V. Sizov, “Radar parameters influence on the clutter in maritime forward scatter radar,” in *2014 11th European Radar Conference*, 2014, pp. 113–116.

[67] A. De Luca, L. Daniel, K. Kabakchiev, E. Hoare, M. Gashinova, and M. Cherniakov, "Maritime FSR with moving receiver for small target detection," in *2015 16th International Radar Symposium (IRS)*, 2015, pp. 834–839.

[68] R. Berry, "Radar Propagation at Very Low Altitude over the Sea," in *Radar-present and future*, 1973, pp. 140–145.

[69] P. D. L. Williams, H. D. Cramp, and K. Curtis, "Experimental study of the radar cross-section of maritime targets," *IEE J. Electron. Circuits Syst.*, vol. 2, no. 4, p. 121, 1978.

[70] V. Fabbro, C. Bourlier, and P. F. Combes, "Forward Propagation Modeling Above Gaussian Rough Surfaces by the Parabolic Shadowing Effect," *Prog. Electromagn. Res.*, vol. 58, pp. 243–269, 2006.

[71] V. A. Zujkov, Y. A. Pedenko, and V. B. Razskazovsky, "Characteristics of Radio Propagation in Sea Surface Layer, Propagation of Radio Waves of Millimeter and Centimeter Bands," in *Proc. of IRE AN USSR*, 1989, pp. 76–82.

[72] Y. Pedenko and V. B. Razskazovsky, "Multipath Propagation over Sea, Radiophysical study of the World Ocean," in *Proc. of IRE AN USSR*, 1992, pp. 32–50.

[73] C. Beard, I. Katz, and L. Spetner, "Phenomenological vector model of microwave reflection from the ocean," *IRE Trans. Antennas Propag.*, vol. 4, no. 2, pp. 162–167, Apr. 1956.

[74] J. R. Smith, S. J. Russell, B. E. Brown, P. M. Haldeman, D. D. Hayden, D. G. Morgan, R. D. Pierce, J. W. Shan, W. T. Stephens, and M. S. Mirotznik, "Electromagnetic forward-scattering measurements over a known, controlled sea surface at grazing," *IEEE Trans. Geosci. Remote Sens.*, vol. 42, no. 6, pp. 1197–1207, Jun. 2004.

[75] W. S. Ament, "Toward a Theory of Reflection by a Rough Surface," *Proc. IRE*, vol. 41, no. 1, pp. 142–146, Jan. 1953.

[76] D. E. Freund, N. E. Woods, H.-C. Ku, and R. S. Awadallah, “Forward Radar Propagation Over a Rough Sea Surface: A Numerical Assessment of the Miller-Brown Approximation Using a Horizontally Polarized 3-GHz Line Source,” *IEEE Trans. Antennas Propag.*, vol. 54, no. 4, pp. 1292–1304, Apr. 2006.

[77] T. S. Hristov, K. D. Anderson, and C. A. Friehe, “Scattering Properties of the Ocean Surface: The Miller-Brown-Vegh Model Revisited,” *IEEE Trans. Antennas Propag.*, vol. 56, no. 4, pp. 1103–1109, Apr. 2008.

[78] R. M. Brown and A. R. Miller, “Geometric-Optics Theory for Coherent Scattering of Microwaves from the Ocean Surface,” 1974.

[79] K. Anderson, S. Doss-Hammel, D. Tsintikidis, B. Brooks, M. Smith, P. Caffrey, A. Clarke, L. Cohen, A. De Jong, G. De Leeuw, M. Moerman, K. Crahan, K. Davidson, P. Frederickson, D. Dion, C. Friehe, D. Khelif, T. Hristov, J. S. Reid, S. Reising, and E. Terrill, “The RED Experiment: An Assessment of Boundary Layer Effects in a Trade Winds Regime on Microwave and Infrared Propagation over the Sea,” *Bull. Am. Meteorol. Soc.*, vol. 85, no. 9, pp. 1355–1365, Sep. 2004.

[80] G. Mastin, P. Watterberg, and J. Mareda, “Fourier Synthesis of Ocean Scenes,” *IEEE Comput. Graph. Appl.*, vol. 7, no. 3, pp. 16–23, Mar. 1987.

[81] S. Thon and D. Ghazanfarpour, “Ocean waves synthesis and animation using real world information,” *Comput. Graph.*, vol. 26, no. 1, pp. 99–108, Feb. 2002.

[82] G. B. Airy, *Tides and Waves*, vol. 3. 1841.

[83] P. Rudnick, “Correlograms for Pacific Ocean Waves,” in *Second Berkeley Symposium on Mathematical Statistics and Probability*, 1950, pp. 627–638.

[84] S. O. Rice, “Mathematical Analysis of Random Noise,” *Bell Syst. Tech. J.*, vol. 23, no. 3, pp. 282–332, Jul. 1944.

[85] H. Tuah and R. T. Hudspeth, “Comparisons of numerical random sea simulations,” *J. Waterw. Port, Coast. Ocean Div.*, vol. 108, no. 4, pp. 569–584, 1982.

[86] M. J. Tucker, P. G. Challenor, and D. J. T. Carter, “Numerical simulation of a random sea: a common error and its effect upon wave group statistics,” *Appl. Ocean Res.*, vol. 6, no. 2, pp. 118–122, Apr. 1984.

[87] S. Elgar, R. T. Guza, and R. J. Seymour, “Wave group statistics from numerical simulations of a random sea,” *Appl. Ocean Res.*, vol. 7, no. 2, pp. 93–96, Apr. 1985.

[88] M. K. Ochi, "*Ocean Waves - The Stochastic Approach*," 1st ed. Cambridge University Press, 1998.

[89] W. J. Pierson and L. Moskowitz, “A Proposed Spectral Form for Fully Developed Wind Seas Based on the Similarity Theory of S. A. Kitaigorodskii,” *J. Geophys. Res.*, vol. 69, no. 24, pp. 5181–5190, Dec. 1964.

[90] *Manual on Codes - International Codes, Volume I.1: Part A- Alphanumeric Codes*. World Meterological Organisation, 2014.

[91] K. Hasselmann, T. P. Barnett, E. Bouws, H. Carlson, D. E. Cartwright, K. Enke, J. A. Ewing, H. Gienapp, and H. Hasselmann, D.E. Kruseman, P. · Meerburg, A. · Müller, P. · Olbers, D.J. · Richter, K. · Sell, W. · Walden, “Measurements of wind-wave growth and swell decay during the Joint North Sea Wave Project (JONSWAP),” 1973.

[92] M. K. Ochi, “A Series of JONSWAP Wave Spectra for Offshore Structure Design,” in *International Conference on teh Behaviour of Offshore Structures*, 1979, pp. 75–86.

[93] S. A. Hsu, E. A. Meindl, and D. B. Gilhousen, “Determining the Power-Law Wind-Profile Exponent under Near-Neutral Stability Conditions at Sea,” *J. Appl. Meteorol.*, vol. 33, no. 6, pp. 757–765, Jun. 1994.

[94] M. A. Donelan, J. Hamilton, and W. H. Hui, “Directional Spectra of Wind-Generated

Waves," *Philos. Trans. R. Soc. London. Ser. A, Math. Phys. Sci.*, vol. 315, no. 1534, pp. 509–562, Sep. 1985.

[95] W. J. Pierson, G. Neumann, and R. W. James, "Practical methods for observing and forecasting ocean waves by means of wave spectra and statistics," 1955.

[96] M. S. Longuet-Higgins, "Observation of the directional spectrum of sea waves using the motion of a floating buoy," in *Ocean Wave Spectra*, 1st ed., Prentice-Hall Inc., 1963, pp. 111–136.

[97] H. Mitsuyasu, F. Tasai, T. Suhara, S. Mizuno, M. Ohkusu, T. Honda, and K. Rikiishi, "Observations of the Directional Spectrum of Ocean WavesUsing a Cloverleaf Buoy," *J. Phys. Oceanogr.*, vol. 5, no. 4, pp. 750–760, Oct. 1975.

[98] D. E. Hasselmann, M. Dunckel, and J. A. Ewing, "Directional Wave Spectra Observed during JONSWAP 1973," *J. Phys. Oceanogr.*, vol. 10, no. 8, pp. 1264–1280, Aug. 1980.

[99] L. Y. Daniel, M. S. Gashinova, and M. Cherniakov, "Target visibility estimation in a buoy mounted maritime forward scatter radar," in *2015 IEEE Radar Conference (RadarCon)*, 2015, pp. 0755–0760.

[100] L. Y. Daniel, M. S. Gashinova, and M. Cherniakov, "Target observability improvement in multi-static maritime forward scatter radar," in *2014 International Radar Conference*, 2014, pp. 1–6.

[101] W. Garcia-Gabin, "Wave Bimodal Spectrum based on Swell and Wind-sea Components," IFAC-PapersOnLine, Volume 48, Issue 16, 2015, Pages 223-228

APPENDIX A – AUTHOR'S PUBLICATIONS REFERENCED WITHIN THIS THESIS

Below is a list of the author's publications that are referenced within this thesis. The reference number is given and a brief overview of contribution (in italics). Papers are found in this appendix in the following order.

[26] M. Gashinova, L. Daniel, V. Sizov, E. Hoare, and M. Cherniakov, "Phenomenology of Doppler Forward Scatter Radar for Surface Targets Observation," *IET Radar, Sonar Navig.*, vol. 7, no. 4, pp. 422–432, Apr. 2013.

Provided measurement data. Contributed to production of signal models, application of quasi-optimal processing to measured data for target parameter estimation, anechoic chamber experimentation.

[27] M. Gashinova, L. Daniel, E. Hoare, V. Sizov , K. Kabakchiev and M. Cherniakov, "Signal characterisation and processing in the forward scatter mode of bistatic passive coherent location systems," *EURASIP Journal on Advances in Signal* Processing, December 2013, 2013:36.

Provided measurement data. Contributed to production of target models, electromagentic simulation, analysis of coherenet times.

[29] S. Hristov, L. Daniel, E. Hoare, M. Cherniakov, and M. Gashinova, "Target Shadow Profile Reconstruction in ground-based forward scatter radar," in 2015 IEEE Radar Conference (RadarCon), 2015, pp. 0846–0851.

Contributed to data collection and speed estimation (quasi-optimal processing) to estimate Doppler phases of signatures for extraction.

[41] M. Gashinova, L. Daniel, K. Kabakchiev, V. Sizov, E. Hoare, and M. Cherniakov, “Phenomenology of signals in FSR for surface targets detection,” *Radar Syst. (Radar 2012), IET Int. Conf.*, pp. 1–6, 2012.

Provided measurement data. Contributed to production of signal models, application of quasi-optimal processing to measured data for target parameter estimation, anechoic chamber experimentation.

[47] M. Gashinova, K. Kabakchiev, L. Daniel, E. Hoare, V. Sizov, and M. Cherniakov, “Measured forward-scatter sea clutter at near-zero grazing angle: analysis of spectral and statistical properties,” *IET Radar, Sonar Navig.*, vol. 8, no. 2, pp. 132–141, Feb. 2014.

Provided measurement data. Contributed to discussion of scattering mechanisms, spectral investigation and provision of initial software for statistical analysis.

[60] L. Y. Daniel, E. G. Hoare, M. Gashinova, A. Svintsov, M. Cherniakov, and V. Sizov, “Ultra-Wideband Forward Scatter Radar Fence for Maritime Surveillance - Initial Experimental Results,” *Radar Conf. 2010 IEEE*, pp. 526–531, 2010.

Contributed to all aspects of work.

[61] L. Daniel, M. Gashinova, and M. Cherniakov, “Maritime UWB forward scattering radar network: Initial study,” in *2008 International Conference on Radar*, 2008, pp. 658–663.

Contributed to all aspects of work.

[62] L. Daniel, M. Gashinova, and M. Cherniakov, “Maritime target cross section estimation for an ultra-wideband forward scatter radar network,” *2008 Eur. Radar Conf.*, no. October, pp. 316–319, 2008.

Contributed to all aspects of work.

[65] K. Kabakchiev, L. Y. Daniel, V. Sizov, E. G. Hoare, M. Gashinova, and M. Cherniakov, “Received Signal Characterization in Forward Scatter Radar for Maritime Application,” *Radar Symp. (IRS), 2011 Proc. Int.*, pp. 67–72, 2011.

Contributed to data collection, target area and cross section calculation.

[66] K. Kabakchiev, L. Daniel, M. Gashinova, E. Hoare, M. Cherniakov, and V. Sizov, “Radar parameters influence on the clutter in maritime forward scatter radar,” in *2014 11th European Radar Conference*, 2014, pp. 113–116.

Provided measurement data. Contributed to discussion of scattering mechanisms, spectral investigation and provision of initial software for statistical analysis.

[99] L. Y. Daniel, M. S. Gashinova, and M. Cherniakov, “Target visibility estimation in a buoy mounted maritime forward scatter radar,” in *2015 IEEE Radar Conference (RadarCon)*, 2015, pp. 0755–0760.

Contributed to all aspects of work.

[100] L. Y. Daniel, M. S. Gashinova, and M. Cherniakov, “Target observability improvement in multi-static maritime forward scatter radar,” in *2014 International Radar Conference*, 2014, pp. 1–6.

Contributed to all aspects of work.